PROBING DYNAMICS OF COMPLEX ORDERED PHASES IN

COLOSSAL MAGNETORESISTIVE TRANSITION-METAL OXIDES

USING COHERENT RESONANT SOFT X-RAY SCATTERING

by

JOSHUA J. TURNER

A DISSERTATION

Presented to the Department of Physics
and the Graduate School of the University of Oregon
in partial fulfillment of the requirements
for the degree of
Doctor of Philosophy

March 2008

University of Oregon Graduate School

Confirmation of Approval and Acceptance of Dissertation prepared by:

Joshua Turner

Title:

"Probing Dynamics of Complex Ordered Phases in Colossal Magnetoresistive Transition-Metal Oxides Using Coherent Resonant Soft X-ray Scattering"

This dissertation has been accepted and approved in partial fulfillment of the requirements for the Doctor of Philosophy degree in the Department of Physics by:

Roger Haydock, Chairperson, Physics
Stephen Kevan, Advisor, Physics
Stephen Gregory, Member, Physics
Eric Torrence, Member, Physics
David Johnson, Outside Member, Chemistry

and Richard Linton, Vice President for Research and Graduate Studies/Dean of the Graduate School for the University of Oregon.

March 22, 2008

Original approval signatures are on file with the Graduate School and the University of Oregon Libraries.

An Abstract of the Dissertation of

Joshua J. Turner   for the degree of   Doctor of Philosophy

in the Department of Physics   to be taken   March 2008

Title: PROBING DYNAMICS OF COMPLEX ORDERED PHASES IN COLOSSAL

MAGNETORESISTIVE TRANSITION-METAL OXIDES USING COHERENT

RESONANT SOFT X-RAY SCATTERING

This manuscript has been approved by the advisor and committee named below and by Richard Linton, Dean of the Graduate School.

Professor Stephen Kevan, Advisor

A growing interest in the physics of complex systems such as in the transition-metal oxide family has exploded recently, especially in the last 20 years or so. One notable effect is the change in electrical resistivity of a system by orders of magnitude in an applied magnetic field, coined the "colossal magnetoresistance effect". In efforts to understand these types of effects, there has been an unveiling of a rich variety of phenomena in the field of strongly correlated electron physics that has come to dominate the current scientific times. Most notable is the competition of myriad types of order: magnetic, lattice, charge and orbital all self-organize to display a fascinating array of phases on a variety of length scales. Furthermore, it has become apparent that new probes are needed to grasp some of this physics that transcends current condensed matter theory, where much of the behavior of these types of systems has remained unexplored. We have

developed a new technique to gain more information about the system than with conventional x-ray diffraction. By scattering highly coherent, low energy x-rays, we can measure manganite speckle: a "fingerprint" of the microscopic structure in the bulk. The coherence of the x-rays can further be used to elucidate new insight into the dynamics of these phases. We describe here a number of novel effects near the orbital order phase transition in a half-doped manganite. We observe a small fluctuating component in the scattered signal that is correlated with three effects: both a rapidly decreasing total signal and orbital domain size, as well as an abrupt onset of a broad background intensity that we attribute to the thermal production of correlated polarons. Our results suggest that the transition is characterized by a competition between a pinned orbital domain topology that remains static, and mobile domain boundaries that exhibit slow, spatiotemporal fluctuations. This study opens up a new chapter to the study of manganite physics as coherent x-ray scattering offers a new direction to understand the strange and exotic behavior demonstrated in the multifaceted manganites.

CURRICULUM VITAE

NAME OF AUTHOR: Joshua J. Turner

PLACE OF BIRTH: San Jose, CA

DATE OF BIRTH: May 14, 1979

GRADUATE AND UNDERGRADUATE SCHOOLS ATTENDED:

 University of Oregon, Eugene, OR

 Boston University, Boston, MA

 University of California at Santa Barbara, Santa Barbara, CA

DEGREES AWARDED:

 Doctor of Philosophy, Physics, March 2008, University of Oregon

 Master of Arts, Physics, May 2003, Boston University

 Bachelor of Science, Physics, June 2001, UC Santa Barbara

 Bachelor of Arts, Mathematics, June 2001, UC Santa Barbara

AREAS OF SPECIAL INTEREST:

 Coherent x-ray scattering techniques

 Complex and non-ergodic systems

 Highly correlated electron physics; orbital ordering

 Detector development

 Nanomagnetism and low dimensional magnetic systems

PROFESSIONAL EXPERIENCE:

 Research Scientist, Brookhaven National Laboratory, 2006 - 2008

 Research Scientist, Lawrence Berkeley National Laboratory, 1998 - 2008

 Research Assistant, UC Santa Barbara, 2000 - 2001

GRANTS, AWARDS AND HONORS:

Advanced Light Source Doctoral Research Fellowship, 2003-2004

Teaching Fellowship, University of Oregon, 2004 - 2005

Teaching Fellowship, Boston University, 2001 - 2002

Teaching Fellowship, UC Santa Barbara, 2000 - 2001

PUBLICATIONS:

J. J. Turner, K. J. Thomas, J. P. Hill, M. Pfeifer, K. Chesnel, Y. Tomioka, Y. Tokura, and S. D. Kevan, 'Orbital domain dynamics in a doped manganite', *New J. of Phys.* (accepted for publication).

J. J. Turner, K. J. Thomas, M. Upton, J. P. Hill, J. Jordan-Sweet, Y. Tomioka, Y. Tokura, and S. D. Kevan, 'Domain Mapping of a Ca-doped Manganite', *App. Phys. Lett.* (accepted for publication).

K. Chesnel, J. J. Turner, M. Pfeifer, S. D. Kevan, 'Probing Complex Materials with Coherent Soft X-rays' *App. Phys. A* (accepted for publication).

M. S. Pierce, C. R. Buechler, L. B. Sorenson, J. J. Turner, S. D. Kevan, E. A. Jagla, J. M. Deutsch, T. Mai, O. Narayan, J. E. Davies, K. Liu, J. H. Dunn, K. M. Chesnel, J. B. Kortright, O. Hellwig, and E. E. Fullerton, 'Disorder-induced microscopic magnetic memory' *Phys. Rev. Lett.*, 94:017202, 2005.

ACKNOWLEDGEMENTS

It is impossible to thank all the people who have been a source of inspiration, guidance, and encouragement through the course of this dissertation. I would like especially to thank my advisor Steve Kevan. It is hard to sum in a few words the gratitude for the expertise, training, and the skills you have passed on to me. Thank you for your way of approaching science and your ability to make light of challenging situations, not the least of which was letting me share your office, or allowing me to 'commute' to work from across the country.

Thanks to all the faculty, and staff at the University of Oregon, especially to all my committee members. Bonnie Grimm for bailing me out again and again, and always coming to the rescue, I probably would not have made it if it was not for you. In particular, Forest Patton - you were invaluable in showing me the ropes and helping me with countless questions and adjust to Eugene-life.

To Zahid Hussain, whom I could not rave enough about. Your help and support are extremely appreciated and could not be overstated. Thanks for continuing to offer me opportunity after opportunity, your guidance and advice, and your inspiration via Isaac Newton.

To everyone at the ALS, too many people to possibly name. S. Kellar, Xiang Zhou, Rudy K., Bob G., Tom Miller, John Pepper, Elke Arenholz, Soren Prestemon, Craig, Dave Atwood, Tim Kellog, Sujoy Roy, Mark Pfeifer, Keoki Seu, Bob Gunion, Eric Gullikson, and Yanwei. All these people had roles either in our work conducted at the lab to make it successful or in teaching me about physics or synchrotrons, vacuum practices, fixing what I broke, burned, or blew up, or helping me in countless other ways.

John Hill for your guidance and mentoring while at Brookhaven. It was an exciting time to be there and to learn from one of the world's experts in strongly correlated electron physics.

To everyone at (or fomerly at) Brookhaven Lab: Stuart Wilkins, Mary Upton, Jean Jordan-Sweet, Jessica Thomas, Marty Blume, and especially Arlene for always dropping anything to help me out - you are amazing! And how could I forget the BNL librarian Noreen O'Donnell, for looking up obscure unpublished journal articles for this dissertation from a century ago.

To all my pre-graduate school educators that helped to shape my education or passion or scientific awareness: Omer Blaes, Francesc Roig, Marie

This thesis is dedicated to the most beautiful woman in the world: my wife, Elizabeth. You are such a radiant and captivating woman. From the conversation at that coffee shop in Boston, to what seemed like an eternity of dating cross-country for two and a half years, to the all-nighters of me taking beamtime so that I could finish this dissertation, you have been the most amazing and incredible support. This could not have been done without you. Thank you for being my wife. Thank you for everything.

TABLE OF CONTENTS

LIST OF FIGURES

Figure   Page

Figure   Page

Figure   Page

Figure   Page

Figure   Page

Figure   Page

Figure   Page

Figure   Page

Figure   Page

LIST OF TABLES

CHAPTER I

INTRODUCTION

Pleasure in the job puts perfection in the work.
- Aristotle

Imagination is more important than knowledge...
- Albert Einstein

Condensed matter physics is the broadest, most active area of physics research. With the push towards nanotechnology and thin film material growth processes, new effects constantly emerge that challenge our basic notions of the physical laws that govern electrons in solids. Setting the stage for this new era was the discovery of non-BCS superconductivity which occurred at higher temperatures than previously predicted. The phenomenon of superconductivity was thought to be a closed chapter in the physics textbooks until this discovery in 1986 reopened it. As a direct result, a surge of experiments were conducted on other similar transition-metal oxide systems. Soon after, enormous changes in electrical resistivity under applied magnetic fields was observed, by orders of magnitude. This was a much larger effect than previously observed or expected, and became known as "colossal magnetoresistance effect" as it involved changes of a thousand-fold. With the excitement of CMR [1], an entire world emerged as the systems responsible for effects such as these came under more scrutiny [2, 3, 4]. It is these manganite materials that we have chosen to conduct experiments on, and which we discuss at length in this work.

One feature of interest is the rich variety of self-organizing phenomena that seem to coexist in the manganite systems. A diverse range of lattice, charge, magnetic, and orbital patterns compete with each other to dictate the ground state of these systems [5]. The strange and exotic behavior have been at the forefront of research efforts for not only the technological significance, but for

the novel approach that must be taken from a physics standpoint to understand the mechanisms driving these effects.

One example is the so-called orbital ordering (OO) effect. This is a periodic arrangement of certain electron orbitals for a given chemical lattice embedded in the material that produces a modulation of the *orientation* of the wavefunctions. This only arises for certain doping levels which then control the type of patterns that are created [6]. More importantly, this self-arrangement of wavefunctions is believed to be one of the proponents of colossal magnetoresistance. The mechanism has produced a wide search in understanding the physics of the mesoscopic texture that is widespread in manganites, but has remained to be poorly understood. The study and understanding of the orbital order mechanism we believe is the direct pathway for gaining a better understanding of these complex systems, especially through scattering techniques (See Fig. 3.1 [7]).

Another major theme in this dissertation is the technique used to study the types of complex order mentioned above. With the advent of lasers [8], science and technology has been completely revolutionized [9]. A similar trend has occurred in x-ray science with synchrotron particle accelerators used to generate higher energy electromagnetic radiation [10], though not to the same degree. One issue in particular for soft x-rays, light typically in the range from about 300 eV to 2-3 keV, is the flux. The Advanced Light Source at the Lawrence Berkeley Laboratory is one of the best sources in the world in terms of flux in this energy range, yet still has a long way to go to compete with lasers in the optical regime. Another aspect that is paramount to the work here is the coherence: the x-ray sources of radiation are usually fairly incoherent, limiting the type of coherence based experiments that are regularly conducted in the optical and lasing research communities [8]. This becomes another issue that must be addressed to perform coherent scattering experiments.

We have recently developed an experimental apparatus surrounded by a magnet (See Table 6.1 for instance [11]) designed to maximize these properties, among other things. The idea is to harness highly coherent soft x-rays to conduct x-ray analog experiments to that which has been accomplished for years with optical light. By using x-rays to measure coherent diffraction patterns, or 'speckle' patterns, we are able to gain more information about the systems under study. This gives structural information on the local topology of the system, but can also be used to study dynamics. Because the speckle patterns

are unique to the local configuration of the ordering or mechanism being studied, measurements of speckle patterns of different regions of the sample, or of the same region but at a different time, can be collected and compared. This method allows for the direct measurement of memory or dynamics of the precise structure of interest. Experiments such as this have been successful at the long wavelength limit of optical lasers, but only have just begun in the x-ray region. The use of coherent soft x-ray scattering gives an unprecedented ability to probe dynamics at important length scales that can not be reached by any other method.

Finally, though there is a great deal of intrigue here for the condensed matter physicist, there has been an incredible effort directed at the types of systems to study described above for their technological importance. We bridge this gap by using our coherent scattering technique and apparatus to study technologically important materials. For instance, the notion of using orbital occupancy arrangements as a gate mechanism in electronics, has lead a powerful march into the mesoscopic arena for understanding domain structure of this type. One example is in the switching frequency of orbital states compared to that in charge or semi-conducting devices, or even spin-gate valves for that matter, sometimes referred to as 'spin-tronics' technology. Because the orbital symmetry can be coupled to electrical conduction, the advantage for using 'orbitons' is in the switching frequency: typically faster than spin precession frequencies by a factor of 10^4 [12, 13]. This could completely revolutionize the electronics and computing industries.

The following work is organized as follows: First we go through a detailed description of the manganites. We touch upon the history, the current theoretical constructs, and describe the ordering mechanisms and nanoscopic phase separation structure. The end of the chapter even sets the tone for the rest of the dissertation by discussing a philosophical notion of mesoscopic phenomena and how it relates to the complex behavior of manganite physics. The next chapter is on scattering theory. Starting from first principles, it goes into the full quantum mechanic description of scattering to get at the foundation of the resonant scattering phenomenon. This subtlety is crucial to all the experiments described here. The following short chapter is a review of the properties of coherence and speckle: important for the special kind of resonant scattering that is conducted. This is followed by an extensive exposition on speckle statistics. This is important for the analysis of speckle and in the interpretation of data.

This is followed by another treatise on the experimental side of the project. This incorporates details of the chamber and beamline used for the majority of the work presented. Finally, main results related to the manganites are presented. This includes both incoherent and coherent scattering results followed by an outlook to the future of both sides: manganite physics on the one, and the future of coherent x-ray scattering on the other. There are in addition five appendices to clarify details throughout the work.

CHAPTER II

COLOSSAL MAGNETORESISTIVE MANGANITES

> Nature uses only the longest threads to weave her patterns, so that each
> small piece of her fabric reveals the organization of the entire tapestry.
> - Richard P. Feynman

The description of the colossal magnetoresistance effect has baffled physicists since its discovery. The puzzle currently remains one of the hot areas of strongly correlated electron research and in fact, the study of the broader class of self-organization in transition metal-oxides (TMO) is one of the most dominant scientific themes today in condensed matter research [14, 15, 16, 17, 18, 19]. Although the insight into these systems has grown over the last decade, a proper understanding and theoretical description of the physics responsible for colossal magnetoresistance (CMR) is still predominantly lacking. Here the physics of what is generally believed to be understood about these systems is described, and discussion is presented on what has not yet found a reasonable explanation. Overall, the central theme in the manganites is the elaborate and intimate relationship between charge, orbital, lattice, and spin order parameters. The complex coupling that takes place among these functions is what makes this system so interesting, and is precisely what we will shed some light on in the following chapters. We start with a brief history of the manganites including some of the technological ideas for innovations motivated by CMR. This is followed by discussion of the major system parameters and of the different classes or ordering. The early theory starting in the 1950's is presented, followed by the new theoretical developments. Some discussion on dimensionality and of one particular cubic family of manganites is considered. The chapter concludes with some philosophical notions on the future of mesoscopic physics. Namely, the idea that the true understanding of physics in condensed media may be due to a special region of phase space yet to be considered: that bounded by the microscopic and the macroscopic descriptions on either side.

1. History of Colossal Magnetoresistance

Most would start the story of colossal magnetoresistance in 1994, but the much lesser known first discovery of CMR - the dramatic change in resistance of a material upon an application of a magnetic field - was actually in 1989 by R.M. Kusters and the group at the High-Field Magnet Laboratory at Nijmegen University in the Netherlands [20]. K. Chahara et al. followed with measurements in 1993 [21] as well as the German scientist R. von Helmolt [22], all publishing data proving a magnetoresistance measurement of over an order of magnitude. Finally, in 1994, S. Jin measured the well-known thousandfold change in resistance due to a magnetic field, and coined the term 'colossal magnetoresitance' to characterize changes in resistance of orders of magnitude [23]. For an example, see Figure 2.1 taken from measurements by P. Schiffer et. al. [1].

Magnetoresistance has been a phenomenon theorized and studied for over a 100 years, dating back as early as 1879, when Edwin H. Hall made his famous discovery that now bears his name [24]. The Hall effect however involves a much different physics than what is now known as CMR. The Hall effect refers to how strong a transverse electric field affects a current flow in a conductor when a magnetic field is applied perpendicular to the plane containing both current and electric field vectors. The field causes a charge build up on one side of the conductor which in turn affects the flow of current. This Hall coefficient is just the ratio of this transverse electric field to the product of the current flow and magnetic field magnitude [25]. Magnetoresistance then has been known about in some capacity and observed for well over a century, just not to the degree that we will discuss here.

i. Magnetoresistance

Magnetoresistance, by definition, is more or less observed in all metals and semi-conductors, but it involves a change in resistance on the order of 1 % [26]. This can be made quantitative by the MR ratio, usually given by

$$\frac{R(0) - R(H)}{R(0)} * 100 \tag{2.1}$$

and is given as a percentage [2]. The difference in the numerator is just the difference in resistivity for the state with and without an applied magnetic field.
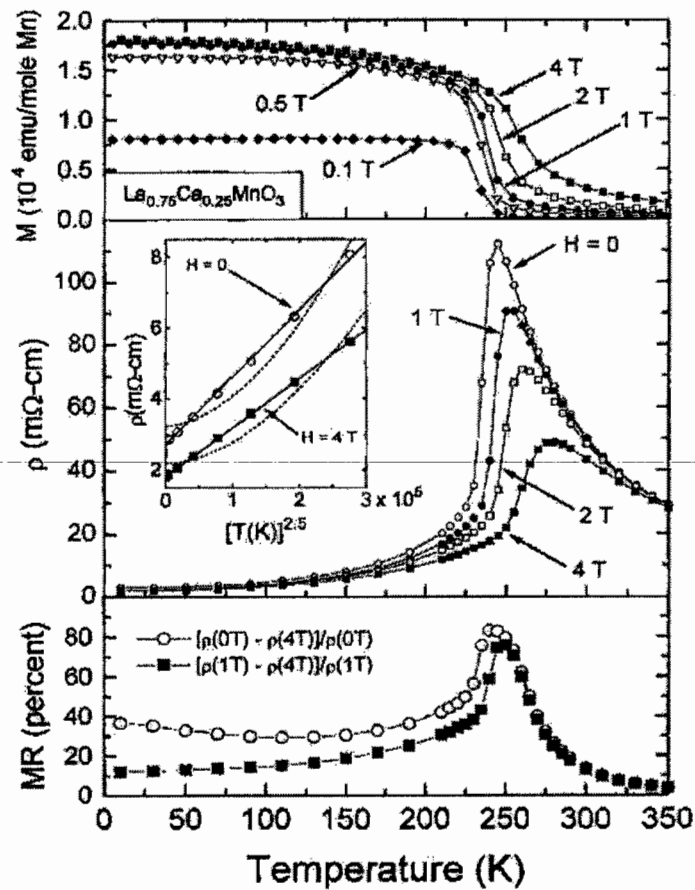
Fig. 2.1: **CMR Data for $La_{1-x}Ca_xMnO_3$ with x = 0.25** The magnetization, resistivity, and magnetoresistance of $La_{1x}Ca_xMnO_3$ with x = 0.25 is shown as a function of temperature for various fields [1]. The inset shows the resistivity at low T. The three plots clearly demonstrate the colossal magnetoresistance effect. The top shows the magnetization with temperature as a function of magnetic field. Right around 250 K, a well-defined Curie temperature can be observed. The second panel shows the resistivity also, with both temperature and field. Note that with a 4 Tesla field at about 250 K, the resistivity change is two orders of magnitude. The bottom panel shows the magnetoresitance data, defined by Equation 2.1.

ii.   Giant Magnetoresistance

A similar phenomenon, not to be confused with CMR is Giant Magnetoresistance (GMR). The GMR phenomenon has had an enormous technological impact on the computer hard drive industry and has received even more attention with the recent Nobel Prize award in physics, which was given for GMR in 2007. GMR was found by two independent European groups in 1988: Peter Gruenberg of the KFA research institute in Julich, Germany, and Albert Fert of the University of Paris [27]. They both saw resistance changes of 6% to 50% in composite materials. A common misconception on the differences between GMR and CMR is that it is only related to the order of change in resistance. While this is generally true, GMR is based on thin film technology, being discovered in multilayer Fe/Cr structures [28]. It typically takes place in fabricated systems that consist of ferromagnetic and non-magnetic metal layers, and it has been attributed to the difference in scattering cross-sections from the two different types of interfaces. The transfer of spin-polarized current will then depend on the arrangement of the metal arrays [28]. These structures are responsible for the new technology that the latest generation of read-heads for computer disk drives are all using - yet the physics is remarkably different from CMR. The phenomenon of CMR is a more intrinsic. Instead of using contrasting properties of different materials that are then combined, the physics is purely due to competing types of order within single crystal phases. From a physics point of view, CMR is much more interesting as it challenges our notion of electron behavior in solids.

One further note about GMR physics is that since the band structure of the ferromagnet layer is exchange split, the orientation of electron spin has a different density of states at the Fermi level. Scattering rates go like the density of states, so these rates and therefore resistivities are different for electrons of different spin [29].

iii.   Technology

There is a close relationship of GMR to the new field of magneto-electronics, or the poorly chosen name that some insist on referring to it by: 'spintronics'. This is the idea of designing electronics around the spin degree of freedom instead of the charge. CMR is thought to play a role in new forms of computing and electronics as well. There have been proposed applications to specialized magnetic sensors and for 'instant-on' personal computers by use of MRAM.
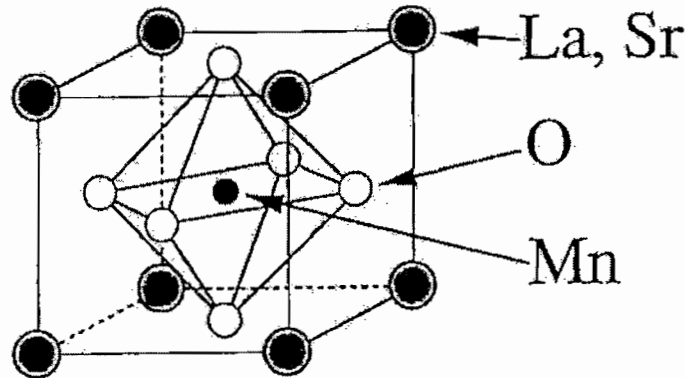
Fig. 2.2: **Typical Manganite Unit Cell** Arrangement of the ions in the perovskite structure of the manganite $La_{1-x}Sr_xMnO_3$, image take from [2]. Though the cation states are labeled La and Sr for this particular compound, the same basic perovskite structure is found in all manganites.

iv. First Studies

The *manganites* was a term first used by Jonker and Van Santen in their 1950 paper to describe a class of materials that all have the same manganese-oxygen network, but contain different mixtures of alkaline and rare earths to regulate the number of Mn electrons [30]. It was this beautiful first neutron scattering study that paved the way for a theoretical physics heyday that progressed over the next decade. The pioneering theory of De Gennes [31], Goodenough [32], Zener [33, 34, 35], and the team of Anderson-Hasegawa [36] demonstrated a deep understanding of the manganites. By the end of the decade, many regarded the manganites as well understood systems.

2. Manganite Parameters

i. Crystal Structure

The manganese-oxygen crystal structure in the manganites is perovskite-like. The essential component is a Mn ion surrounded by a oxygen octahedron. That is, six equidistant oxygen atoms surround the Mn center, shown in Figure 2.2, which occupy the faces of a cube. The four corners of the unit structure are where the cations reside that act as a charge reservoir for the Mn-O bond, a mixture of trivalent and divalent ions [37]. The crystal unit cell contains one Mn, one cation site, and three oxygen atoms. The Mn lattice forms a quasi-cubic

superlattice, but later discussion will include families with both orthorhombic and tetragonal crystal structures, for both cubic and bi-layer systems. Because the resonant scattering technique is only sensitive to a single atomic species, we tend to focus on the crystal structure of the Mn only. This is embedded in the full crystal structure of the compound, and plays an important role in the system properties.

ii. Doping

The parent compound $AMnO_3$ (where A is a rare-earth element), with $x = 0$, is an anti-ferromagnetic insulator due to super-exchange physics between Mn sites [38]. The parameter x is a measure of the doping of holes into the Mn d-states, effectively controlling the distortion of the octahedron [39]. The doped manganite is created by effectively substituting Mn^{4+} for some of the Mn^{3+}, creating manganese ions that have an empty e_g shell throughout the crystal. This is done physically by replacing rare earths, with alkaline earths which have one less valence electron. Electronically, this is equal to doping holes into the Mn e_g-band, giving rise to the formula $RE_{1-x}AE_xMnO_3$. This can also be written more explicitly as $RE^{3+}_{1-x}AE^{2+}_x[Mn^{3+}_{1-x}Mn^{4+}_x]O^{2-}_3$, where RE and AE are rare-earth and alkaline earth elements, respectively. This shows how the amount of substitution controls the mean Mn valence or hole number [40], where chemically, there must be $4 - x$ electrons per Mn ion on average [41]. In other words, x produces a vacancy in the electron state at a rate of x per Mn site. If one is not inclined to accept hole doping, then this can also be thought of as $1 - x$ electron band filling [16]. This doping scheme creates mixed valence states on the Mn lattice.

Another effect that doping produces is buckling of the Mn-O-Mn bonds. The average radius, $\langle r \rangle$, of these doped cations affects the distortion of the perovskite lattice. By choosing different elements with varying radii, one can control the amount of buckling of the Mn-Mn bonds. Conduction is based on the transfer integral between the Mn 3d-orbital and O 2p-orbital and is highly dependent on bond length; it is also sensitive to the bond angle. The overlap integral contains a factor that goes like

$$t_{ij} \sim (\cos \Phi)^2$$

where Φ is the bond angle deviation from π radians. So by substituting different rare earth ions, one can control the tilt of the oxygen octahedron, and effectively

manipulate the one-electron bandwidth [40]. This can be quantized by the tolerance factor:

$$f = \frac{1}{\sqrt{2}} \frac{\langle r_A \rangle + \langle r_O \rangle}{\langle r_{Mn} \rangle + \langle r_O \rangle} \qquad (2.2)$$

where $\langle r_A \rangle$ is the is averaged radius of the RE/AE atom, $\langle r_{Mn} \rangle$ the size of Mn, and $\langle r_O \rangle$ of oxygen [16]. This gives a value of 1 for a perfect cubic structure due to the fact that the $r_A - r_O$ length is longer than the $r_A - r_O$ length by a factor of $\sqrt{2}$ (see Figure 2.2). This allows one to mismatch the lattice and study the buckling of the bonds as a function of different rare earth ions.

iii. Orbital Structure

For the manganese oxides we will focus on the d-orbitals. Many properties of solids, from color to magnetism, are based on the energetics of the complex ion formation by the d-orbitals of transition metal compounds [42].

In free space, the d-levels of the manganese would be five-fold degenerate. In a solid, the crystal field effect from nearby ions acts to lift, wholly or partially, this degeneracy through hybridization or by electric Coulombic interactions [39]. In Figure 2.3, the five-fold degenerate d-orbitals are shown. These are simply constructed from the single-electron spherical harmonic wavefunctions, the basis functions for the angular part of the Hydrogen atom solution the the Schroedinger equation.

In manganites, the crystal field splitting is cubic because the structure is perovskite and so the Mn atom is enclosed by an octahedra of oxygen atoms, shown earlier. This geometry splits the 5-fold degenerate states into two sets: a lower energy, 3-fold set of t_{2g} orbitals and a higher energy, 2-fold degenerate set of e_g orbitals. Note that this crystal field splitting is only due to the geometry of the octahedra ligands. In the tetrahedra case for instance, the two sets are reversed energetically, since the e_g orbitals are then the furthest from the oxygens. Not only are they energetically more favorable in this case, but the overall tetrahedral crystal-field splitting is also much smaller than the octahedral case by a factor of 4/9 [43]. The two cases for the manganite crystal-field splitting are divided into two sets: the triply and doubly degenerate states.

The Triple Degenerate Electron States

The three lowest lying orbitals for the manganites, named the t_{2g} orbitals, are about 1 eV lower than the two higher lying e_g states. These three degenerate
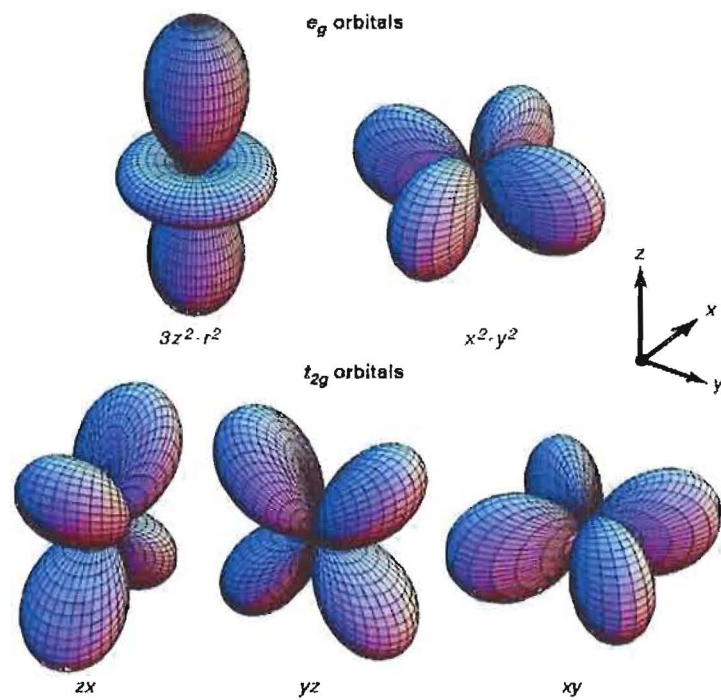
Fig. 2.3: **Structure of d-orbitals in manganites** This shows the single-electron wavefunctions for the d-shell in Mn. The e_g orbitals are higher in energy in the manganites and are shown at the top. The bottom three represent single particle t_{2g} states, and are oriented with electron cloud lobes directed in between the oxygen bonds. The images are taken from [3].

orbitals have a higher probability to be occupied by an electron before either of the e_g orbitals, and are named d_{xy}, d_{yz} and d_{zx} [16]. The three t_{2g} orbitals are the first to fill and are largely localized. They couple strongly ferromagnetically to each other and hybridize weakly with the O 2p states - strengthening the tendency to remain immobile. This tendency can be easily understood geometrically due to the t_{2g} orientation, which is at angles of $\pi/4$ radians, with respect to the oxygen orbitals (see Figure 2.3). Because of the repulsion between the electron orbitals and the negatively charged oxygen bonds, it takes the most energy to activate these electrons. We can treat this set as a core spin, of magnitude $S = |3/2|$. Other configurations of the t_{2g}'s are not relevant energetically, either a different number of electrons or a different spin configuration. These alternative configurations have much too high an energy and are dominated by the strong electron-electron interactions in the CMR materials [39]. Regardless of doping, each Mn site will normally always produce the spin-3/2 magnetic moment below the magnetic transition temperature.

The Double Degenerate Electron States

The two remaining e_g orbitals however point directly at the oxygen atoms (compare Figure 2.2 and Figure 2.3) and hence, hybridize strongly with the O 2p orbitals giving them strong itinerant characteristics [44]. These 2-fold degenerate orbitals are called $d_{x^2-y^2}$ and $d_{3z^2-r^2}$ and because of this hybridization, the bands are dispersive and contain the electrons responsible for the conduction in the ferromagnetic state [45]. Note that, as mentioned before, because the parameter x is between zero and one, each Mn atom will have either three or four d-electrons. The essential ingredient here is that this implies that there is a degree of freedom for the e_g orbitals. The states will have either none or one valence electrons available for filling, and assuming the presence of a local electron, the option of one out of the two orbital states.

3. The Main Classes of Ordering

One of the most interesting aspects of the manganites is the complex phase diagrams displayed with doping. The myriad types of ordering all compete to generate a delicate balance of phases and complex structure. Also puzzling is the correlation lengths of the respective order parameters. Order parameters are used to describe phases characterized by spontaneous symmetry breaking,

transforming according to the symmetry of the group that describes the system [46]. Though these can be represented by very complicated functions or even high-rank tensors for some ordering mechanisms, here we define them simply as the quantity, related to the ordering of the phase in question, which is non-zero below the transition and zero above [47]. The order parameters describing the different phases in the manganites are thought to be strongly coupled, yet the correlation lengths differ, usually drastically. This remains one of the fundamental puzzles to unravel in these types of systems. In this section the four main classes or ordering are discussed: charge, magnetic, lattice, and orbital.

i. Charge

By substituting alkaline earth atoms for rare-earths, the doping effectively changes the Mn lattice from d^4 to d^3, resulting in a mixture of Mn species that differ by at most one electron, on average. Below some ordering temperature, the Mn^{4+} ions will order - mostly due to Coulomb repulsion. A cartoon of this charge ordering is sometimes described as a 'checker-board-type' of ordering, shown in Figure 2.4, where each black square would represent Mn^{4+} charged ions, and white Mn^{3+}. Physically, this can be thought of as just being related to Hubbard-model physics. The point where the kinetic energy term in the Hamiltonian of the itinerant electrons decreases to the energy scale of the Coulomb repulsion is the point which localizes the carriers [48]. Because below this point, the Coulomb interaction of these sites dominates the energy decrease due to conduction, the electrons become affiliated with the respective Mn sites. The state becomes insulating solely due to the relative energies of kinetic and Coulomb terms [48]. Charge ordering is seen in many other types of transition-metal oxides such as cuprates and nickelates and can form many types of patterns such as stripes, or odd checkerboard-like configurations.

It should be noted however, that the figure is not to be taken literally. The cartoon is usually credited to Goodenough's work in 1955 [32] and recently has drawn a lot of attention. One feature is that resonant scattering studies conducted at the K-edge ($1s \rightarrow 4p$ transitions) have cast doubt on the unit valence difference between Mn^{3+} and Mn^{4+} sites. Nazarenko *et al.* for instance, has shown the percentage to be of order 12% [49]. It remains one of the many puzzles to understand precisely how these sites order globally, since the is doping of order 50% while the valence difference between Mn species is only of order 10%.
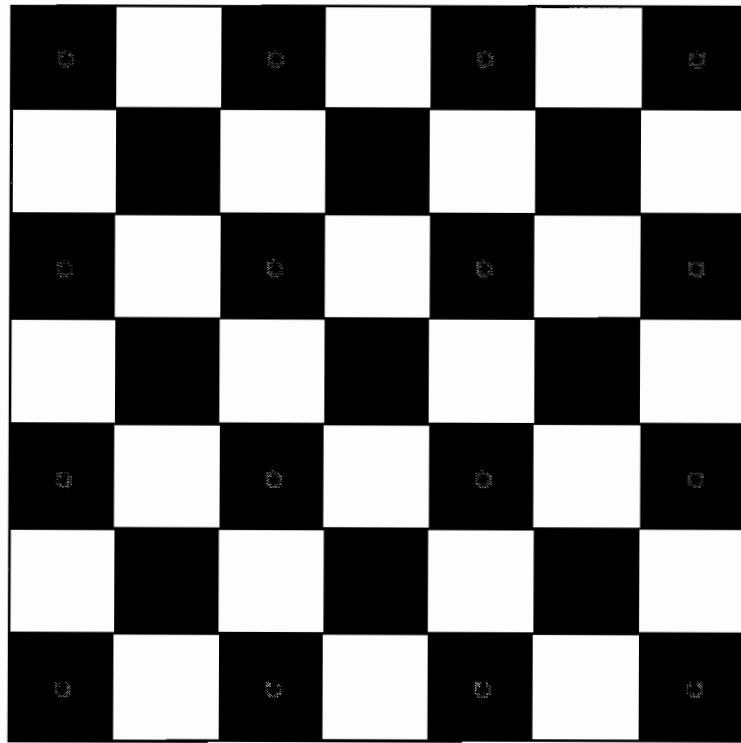
Fig. 2.4: **Charge Ordering for a Half-doped System** A 'checker-board-type' ordering is shown for a half-doped system. This represents the simplest case where there are equal number of sites that differ in charge by one unit. As the doping becomes incommensurate, the patterns formed can become much more complicated. When the Coulomb interaction between the 'extra' charged valence electrons dominates, the system must form a pattern that maximized the distance between charges in all directions.

The correlation length of the charge ordering is an interesting aspect that the doping effect has on the ordering as well. In many different types of x-ray scattering experiments, it has been measured to be resolution limited [5, 50]

$$\xi_{CO}^{-1} \leq l_R$$

This means the width of the Bragg peak, which is proportional to ξ_{CO}^{-1}, is so narrow in reciprocal space that it can not be measured within the resolution limit of the detector, l_R. That is, the ordering is longer-ranged than can be observed. The long-range ordering of the charge disappropriation seems to imply the strength and robustness of the Coulomb mechanism with respect to other, shorter-range mechanisms.

ii. Magnetic

Magnetic ordering is another important phenomenon to understand in the manganites. The most prevalent phase is ferromagnetism, which as we will discuss shortly, usually comes about through a coupling to conductivity by a method proposed by Zener [33, 34, 35]. This explains how ferromagnetism promotes electron transport, even though it is at odds with other phases, such as the ferromagnetic insulating state found in some doping regimes.

The basic ferromagnetism, antiferromagnetism, and paramagnetism come in many different forms, a sampling of which is shown in Figure 2.5. For instance, C-type magnetic structure consists of 1-dimensional ferromagnetic chains that are anti-ferromagnetically coupled to each other, A-type is ferromagnetic sheets in the a-b plane, anti-ferromagnetically ordered in the c-direction, and G-type is is anti-ferromagnetic in all three directions. The multiple types of magnetic order are also tuned by doping, and sometimes even include canted versions of the main ordered states.

As with the charge ordering, it is interesting to understand the correlation lengths of these different magnetically ordered states. For instance, correlation lengths of the magnetic ordering in $La_{0.5}Ca_{0.5}MnO_3$ were measured for both the Mn^{3+} and Mn^{4+} sites using x-ray scattering [51]. There it was shown that the correlation length for the d^3 species was larger than the d^4 by a factor of at least six [51]. This result emphasizes how important it is to understand what sets these length scales. The lower limit is given because the measurement of the Mn d^3 sites was, like the charge ordering mentioned earlier, resolution limited and in fact, probably differs by more. Measurements such as this emphasize how
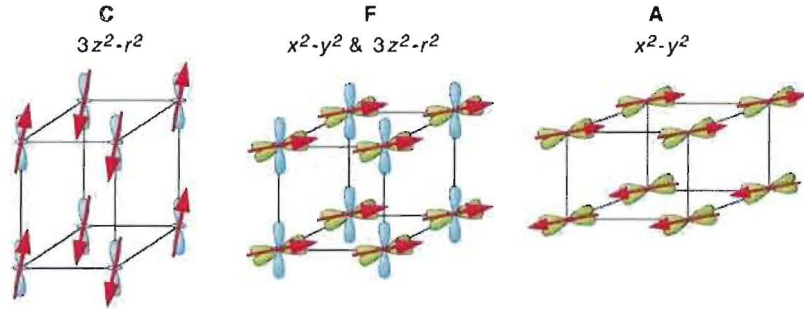
Fig. 2.5: **Sample of Complex Magnetic Structure** A few examples of the magnetic structure in the manganites. Some different types of orbital ordering are shown as well, taken from [3].

different the energetics can be that dictate the domain states for the different order parameters in these systems. This energy ultimately sets the size of the correlation lengths.

iii. Jahn-Teller

H. J. Jahn and E. Teller first came up with what is now used to describe the electron trapping in solids in 1948 [52] purely due to symmetry considerations. Strictly speaking, the effect now known as the Jahn-Teller effect does not imply a lifting of the degeneracy, but only an asymmetry corresponding to an instability of the lattice [53]. In the manganites, this instability of course does lead to a distortion of the local oxygen lattice around the immediate vicinity of the Mn, and effectively lifts the degeneracy of the two e_g d-states. Crystal-field splitting, as noted earlier, is responsible for lifting the degeneracy of the 5-fold degenerate d-states, but leaves a two e_g-state set with equal energies. The e_g splitting takes place due to the oxygen distortion, and this distortion can act as an anomaly that traps the electron, removing its itinerancy. This electron-phonon interaction was revisited as a way of describing the much higher resistivity that was seen in experiments, yet could not be recovered using the Zener formalism, a mechanism discussed in detail later. Its central importance was realized only after a seminal paper by 1995 by A. J. Millis and co-workers [41] argued its importance. This will be discussed in more detail later in the chapter in a subsection devoted to the photon-electron coupling of Section 5.

iv. Orbital

Intimately connected to the collective JT distortion is the so-called orbital ordering. Orbital ordering refers to the ordering of valence electron wavefunctions between sites that occupy a similar state. Due to a number of different interactions, a certain type of pattern can occur among the sites that share the same orbital occupational characteristics. This phenomenon is common in a number of different d- and f-electron systems and in some cases, is needed to understand novel types of magnetism [54]. It can occur in systems with either e_g or t_{2g} active degrees of freedom, systems with strong spin-orbit coupling such as the f-electron systems, and even in more exotic forms, such as multipole ordering, or systems, such as in the multi-ferroics [54].

Orbital ordering contains some of the most interesting physics in these types of systems for the complicated patterns it exhibits and its connection to other order parameters. For instance, in some manganites, charge stripes are thought to be induced by the orbital degree of freedom [55]. This ordering of the d-electrons is only observed in certain classes of transition metal oxides, such as nickelates or cobaltates. This class of ordering we have chosen to go into greater detail, and we will discuss the physical mechanisms for orbital ordering at length later in the chapter.

4. 1950's Theory

No discussion of the manganites would be complete without discussing the theoretical framework that was largely set up in the 1950's. In fact, it is commonly mentioned that the physics of the manganites was a closed chapter in physics knowledge almost 50 years ago, until the discovery of CMR reopened it. There are three main mechanisms to the microscopic physics of the manganites that we will briefly describe here. This physics is not only important for historical reasons, but the present understanding is largely attributed to pioneering works by these three main ideas.

i. Zener Mechanism - Double Exchange

The most important theoretical framework was proposed in a series of papers by Clarence Zener in 1951, connecting transport to magnetism [33, 34, 35]. This was the first description of the basic mechanism for the behavior of the manganese transition metal oxides and was based on what he called 'double

exchange' [33]. As mentioned earlier, the Mn ions in the doped manganites can be described by a $S = 3/2$ core spin due to the strong coupling of the t_{2g} orbitals, and a smaller valence spin-1/2 per ion from the e_g. This can be taken to be the case in general, since there is always a crystal field splitting of the d-states of Mn in perovskites. The underlying Mn lattice is composed of a matrix of Mn^{4+} (or with an electronic structure d^3) and Mn^{3+} (d^4) for a doped system. In the first paper, ferromagnetism is described to manifest due to the strong Hund's coupling between the on-site t_{2g} and e_g spins [34]. The reasoning was that the kinetic energy of the conduction electrons would be lower for a polarized background of spins aligned parallel to them [14]. The term 'double exchange' (DE) arose in a second paper [33] and refers to the mechanism of conduction: the simultaneous transfer of a conduction electron that only happens between the two *different* types of species. With two neighboring Mn sites, the single e_g electron present on one of the d^4 sites can be transfered to the opposite Mn site by way of a spin-preserving transfer via the oxygen ion. Physically, this means an oxygen valence electron on the site connecting to two manganese atoms, with the same spin as the e_g, transfers to the d^3 Mn site at the same time as an e_g moves from the d^4 to the vacancy on the oxygen. This is a qualitative explanation, as Zener himself proposed a *simultaneous* transport of both events [33], incurring the name 'double' exchange. The two ideas are usually taken together in the literature, and both the strong Hund's rule coupling with the ferromagnetic hypothesis along with the double-exchange mechanisms are collectively referred to as 'double-exchange' [14], implying both aspects described by Zener.

We can write the Hamiltonian describing the DE and Hund's coupling effects as

$$H = -\sum t_{ij}^{ab} d_{ia\alpha} d_{jb\alpha} - J_H \sum S \cdot d_{ia\alpha}^{\dagger} \sigma_{\alpha\beta} d_{i\beta\alpha} \qquad (2.3)$$

where the J_H coefficient gives the strength of the on-site Hund's coupling, the a, b indices label the orbital states, and α and β the spins. The t_{2g} spin is labeled as S, the e_g spin by the Pauli spin matrix, and of course the $d_{ia\alpha}$ and $d_{ib\beta}^{\dagger}$ operators annihilate and create electrons for sites located at i and j, respectively.

It should be noted of course that the ferromagnetic relationship between neighboring Mn sites is opposite than what would be expected from basic super-exchange [38]. In systems that are well-described by double-exchange, the Hund's coupling J_H is much stronger than the intersite super-exchange coupling J_{AF} that exists between Mn-Mn t_{2g} spins. As Zener mentions, if J_H is

so large that the electron can not be found on an ion with the wrong spin and the spin does not change upon transfer, conduction only happens between ferromagnetically aligned sites.

ii. Anderson-Hasegawa Mechanism - Transfer Integral

In 1955, Anderson and Hasegawa came up with a relation to take double-exchange one step further [36]. Their formalism treated the oxygen motion as a second-order process: a transfer of the oxygen valence electron to the d^3 site first, followed by the e_g electron motion from the d^4 site to replenish the oxygen vacancy. This produced the same effect: a spin-preserving transfer of an electron between manganese atoms. Most notably, their description of the transport of the outer electron involved treating the core spin structures as *classical* unit vectors [36]. Again, in the limit where J_H exceeds t_{ij}, the hopping interaction takes the form of

$$t_{ij} \sim t_0 \cos\left(\frac{\theta_{ij}}{2}\right)$$

where θ_{ij} is the relative angle between the neighboring spins [16]. As an electron goes from site i to site j, its probability amplitude is maximized for a spin that is quantized parallel to the core spin of site i to having its spin quantized parallel to its new ion location on site j [39]. The bandwidth then goes like the quantum mechanical overlap integral of the two spin states. Also note that according to this relation, the matrix element is *minimized* for nearest neighbor t_{2g} spins to be aligned antiferromagnetically, although quantum fluctuations assure us that the amplitude never fully go to zero [39].

Band theory calculations parametrized by t_{ij} give, to good approximation, negligible transport between sites i and j for any two sites that are not nearest neighbors. The Mn sites are too far apart for a direct atomic orbital overlap, which is why the intermediate oxygen atom must act as a catalyst for the hopping. It is interesting to note however, that some of the most successful Hamiltonians to date that describe this process convincingly are 'manganese-only' Hamiltonians; that is, without any explicit inclusion of oxygen [15].

It should be noted that De Gennes followed suit five years later with a mean-field approximation that lead to a wide spread belief in the spin canted state of A-type order [31]. Recently this structure has come under dispute due to multiple theoretical studies using Monte Carlo simulations, which demonstrate a state that is described in terms of phase separation, between ferromagnetic

and antiferromagnetic, or similarly hole-rich and hole-poor phases [15]. This will be discussed more in Section 5.

iii. Goodenough Mechanism - Semi-covalent Ordering

Also in 1955, Goodenough put forth his theory on semi-covalent bonding [32]. This is seen as the basic model for the ordering in the manganites and describes how covalent bonding between Mn and O can effect lattice distortions and indirect exchange coupling between Mn spins. This epitomizes the relationship between orbital ordering and magnetism. The typical CE-type ordering, sometimes referred to as the 'Goodenough' model was first proposed by J. B. Goodenough [32] only a few years after Zener's work. A CE-type ordering is shown in Figure 2.6, as there are more than one version of CE-type structure. 'CE-type' is a combination of two types of structures, C-type and E-type, and derives from the language of Wollan and Koehler [56], the first workers to study manganites with neutron diffraction. In their 1955 work, they discovered an array of new phases and it was here that the naming of different magnetic structures using letters began. The unit cell of a C-type phase for a cubic structure is two adjacent sites are spin up or $d_{3z^2-r^2}$, while the other two are spin down or $d_{x^2-y^2}$, in the example of either spin or orbital CE-ordering, respectively [14]. The plane consisting of these unit structures is anti-ferro-ordered to other planes stacked in the orthogonal direction. When a checkerboard pattern is made of alternating C-type and E-type unit cells, the 'zig-zag' configuration forms, as the example in Figure 2.6.

This Goodenough model originally assumed the specific pattern of charge ordering and used a single-orbital covalent bond model to project the orbital and magnetic structure [14]. Though mostly qualitative, it correctly gave the CE-structure for half-doped oxides. Two features to note in real systems. First, the c-axis or out-of-plane ordering does not contain an ordering wavevector. That is, the third dimension contains exact replicas of the ordering scheme in the a-b plane. This is why a strong d-d interaction can not simply be used: by assuming a long-range electron-electron potential U_{el-el}, charge ordering would be forced to occur along the c-axis as well. This was one hint as to the need for a more sophisticated model. The second feature is related to the zig-zag magnetic stripes. This particular pattern has been shown to lower the magnetic energy of the system in some recent theoretical models, which is why the ground state at half -doping has been projected to be the CE-phase [15].
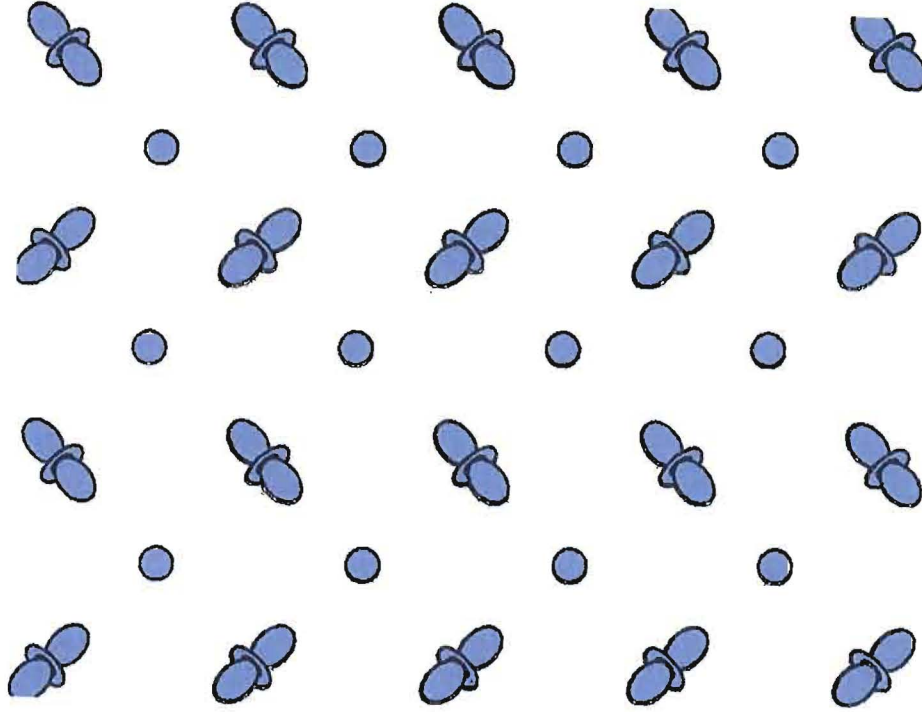
Fig. 2.6: **Orbital Ordering for the CE-type Structure** A cartoon is shown for orbital ordering at half-doping for a manganite system. The spheres represent the d^3 atom and the $d_{3z^2-r^2}$-type orbital are the d^4. In the perovskite structure, these orbitals are always elongated directly towards other Mn sites.

5. Current Theory

The theory developed regarding the manganites in the 1950's is crucial from a historical perspective, but also encompasses the basic physics of these systems at the present time. However, much progress has ensued since the discovery of colossal magnetoresistance in the early 1990's. In this section we will touch upon current work, leaving the special case of orbital ordering for the following section, where we immerse ourselves in the details. The summary on phase separation is largely taken from Dagotto [14] and the theory section by the same author in the book by Chatterji [15].

i. Phase Separation

One of the most intriguing theoretical developments is the generation of phase diagrams due to phase-separation which agree with a countless of experiments.

This is an energetic competition between different phases that compromise by reaching a heterogeneous state. This may or may not include differences in charge, but almost always includes a difference in symmetry breaking patterns between the two competitors. The term 'phase' is sometimes problematic for theorists or statistical mechanics. What is assumed here is that, while we are generally speaking of a 'small' number of electrons, thermodynamically speaking that is, we conclude that the behavior of the electrons in one phase is identical to a large, thermodynamic phase of the same character in the homogeneous limit.

Approximations such as the one-orbital model (based on a Goodenough-type bonding idea) or even the removal of oxygens have been shown to capture some of the basic idea. As unrealistic as these are, they are sometimes used for computational ease. Based on the 'charge-stacking' problem mentioned in the previous section, adjustment of the J_{AF} coupling out of the plane can reproduce the correct 3d structure.

But most exciting in the recent theoretical literature is the idea of a *universal* nanoscale inhomogeneity that is based on disorder, yet intrinsic to the system. This involves phases that are equal in electronic density, but differ in their magnetic characteristics. The condition is needed as it is hard to justify differing electronic densities between nano-phases. At such distances, the cost would be much to high in light of the domination of Coulomb interactions for these length scales. These mixed-phase structures are highly dependent on disorder. We must say a few words on disorder as that term is generically used for many different phenomena. Here, it refers to a random arrangement of the super-exchange interaction between Mn sites. That is, with a high variance of the doped cation radius, the Mn-O-Mn bonds can vary drastically depending on the location of the cations sites. Because of this, the super-exchange interaction is introduced as a random number per site-site coupling. This is transformed physically into random fluctuations in strength between the two coupling responsible for the competing phases: t_{ij} for the metallic ferromagnetic and J_{AF} for the insulating anti-ferromagnetic.

The cluster size that forms of the nano-phase separation is regulated by the disorder, and the results are independent of the nature of the competing ferromagnetic metal and antiferromagnetic insulating states, the distribution of random numbers, and the type of disorder considered. Near the phase transition, the fluctuations become even more important. Here, as the free energy of

the phases become nearly degenerate, the effect of the disorder plays an even more prominent role.

ii.   CMR Lattice Coupling

Another recent contribution pushing further the understanding of CMR is the strong electron-phonon coupling stemming from a Jahn-Teller (JT) splitting of the Mn^{3+} ion [41], suggested by Millis *et al.* This was an additional mechanism proposed to properly characterize CMR behavior. This corrected some ill effects, like giving the correct doping dependence, but most notably, it depicted the resistivity to the right order of magnitude in the paramagnetic phase - something that had not been done previously. The formation and conduction of polarons is thought to be the origination of the notably high conduction in the insulating state, above the transition temperature T_c, while the conduction in the metallic state is given by the DE mechanism we have described above. This addition to DE gave CMR a more sound footing. The self-trapping that occurs for the e_g-electron competes with the delocalization of electron hybridization and is controlled by a delicate balance of the tuning parameter, a dimensionless quantity used to describe the strength of the JT distortions [45]. This ratio λ, goes as

$$\lambda \sim E_p/t_{ij}$$

where E_p is the energy gained by the electron from phonon coupling in the absence of delocalization and t_{ij} is the kinetic energy of the conduction electron [57]. However, because this JT distortion involves the trapping of the lone outer electron, it is only possible on the Mn d^4 ion, as the d^3 is Jahn-Teller inactive. The occupation of one of the e_g orbitals is necessary for a distortion of the oxygen octahedron to create a polaron, acting as a quasi-particle. In fact, these states in this system have an unusually strong coupling with phonons. When this occurs, the Mn-Mn bonds can be stretched or contracted, lowering the cubic symmetry of the system. There are many different modes, but if an O atom moves closer, it will raise the energy of the orbitals overlapped with it, and lower the the energy of the shell whose corresponding O moves way from the Mn site. This Jahn-Teller effect then, leads to a frozen-in lattice distortion [39]. We will discuss polaron physics more when we describe our measurements in Chapter VII.

6. The Physics of Orbital Ordering

Now that the four main sources of ordering have been described qualitatively, and the basic ideas stemming from theory, from a half-century ago up until the present time, we take a more in-depth view on the mechanism of orbital ordering. Most of the work presented in this thesis focuses on this type of order, and there are some subtleties that are paramount to its understanding. This is one of the key phenomena in the manganites that may be responsible for the richness in the phase diagrams. Some of the most exciting and yet poorly understood functions in these systems are thought to be the direct consequence of orbital ordering, including ferromagnetically insulating states, stripes, or the asymmetry in the phase diagrams [58].

i. Jahn-Teller versus Orbital Ordering

One common misconception is the difference of the orbital ordering mechanism and of a 'collective' Jahn-Teller effect. Traditionally, these are thought to be one and the same, but only recently has that notion been challenged experimentally. First, though they can initiate or dictate each other, they are separate and different effects. By a 'collective Jahn-Teller' effect in this context, we mean a global, collective distortion of oxygen atoms. That is, the motion of oxygen atoms is not merely a statistically local effect, but behave as a collective mode: phonons mediated by oxygen sites. By orbital ordering here, we mean specifically the ordering of the e_g d-states of manganese. Because these two different effects can occur simultaneously, or even activate each other, there has not been much reason to differentiate the two. But as we shall see, this important phenomenon is just one of the many subtleties of the physics of the manganites.

To illustrate this difference, we can take two extreme cases to demonstrate the difference. In the Mn lattice of $CaMnO_3$, or PCMO with $x = 1$, every site has an unoccupied e_g orbital, and so any amount of distortion of the oxygen sub-lattice will not display an effect on the d-orbitals in a cubic crystal field. As these orbitals are largely unoccupied, the Jahn-Teller effect merely refers to the structural distortion of the oxygen lattice. On the other hand, in the case of $KCuF_3$, what minimal Jahn-Teller effect may exist does not however affect the orbital ordering. Both the orbital and magnetic structure is fully reproduced theoretically by taking into account the orbital exchange mechanism

only, and is also confirmed by experiments [53], to be discussed below. When this situation happens, the system is said to be 'Jahn-Teller ordered without a Jahn-Teller interaction' [53]. Because the JT effect is direct, and is a much stronger effect, a large degree of oxygen distortion will dominate the orbital structure due to large Coulombic effects between the oxygen valence and manganese d-shell electrons. However, in cases where there is little or no JT distortion of the oxygen lattice, the orbital Kugel-Khomskii super-exhange mechanism will completely determine the orbital structure. In this environment, there can be no distortion of oxygen atoms, yet a strong self-ordering of the e_g Mn orbitals.

ii. Mechanisms for Orbital Ordering

There are really three main contributions to the orbital ordering mechanism: a electronic-vibrational effect, a quadrupole effect, and an orbital super-exchange coupling [53]. The first two are manifestations of the JT effect, and the third is based on the Kugel-Khomskii idea. Since these effects can lead to the same symmetries, they have been difficult to distinguish experimentally. The first two are both direct consequences of Coulombic repulsion and so will be taken together. A distortion of oxygens towards a Mn site will act as a catalyst for the d-electron to occupy the orbital projected in orthogonal directions to the oxygen motion [53]. The third mechanism is a super-exchange-type mechanism similar to that discussed by P. W. Anderson in 1959 [38] for spin states. The Kugel-Khomskii formalism is a generalization of that idea to the orbital degeneracy found in Jahn-Teller systems, and is based on virtual transitions of electrons between sites through superposition wave functions that include not only the atomic-like d-orbitals, but the s and p wavefunctions of the oxygen mediators [53]. These different contributions can act jointly, or as we have see above, give contrasting results depending on the system. It is quite difficult theoretically to figure out which will be the predominant form for each specific case.

Now it may be asked: for a d^4 electron configuration on Mn, does the splitting give preference to the d-orbital occupied? In certain cases this is true. One can imagine that a volume preserving distortion of oxygens that expands the Mn-O distance vertically, and contracts the four Mn-O bonds in the plane necessarily gives preference energetically to the $d_{x^2-y^2}$ orbital, simply by Coulomb repulsion. The only normal modes that are relevant to splitting of the e_g orbitals must be even under inversion about the origin [14], giving only two that are relevant. The other four even-inversion normal modes do not act to lift the e_g degeneracy based

on symmetry, while all others give vanishing matrix elements in the perturbing potential [14].

In general, we can estimate the energies that characterize these effects. The Jahn-Teller splitting of the e_g levels is small compared to other terms, and is on the order of 0.2-0.3 eV. This is in comparison to the Hund's rule exchange between t_{2g} and the e_g which is about 0.8 eV, and the crystal-field splitting of these d-levels is about 2-3 eV [58].

The orbital degree of freedom controls the sign and magnitude of the spin exchange interaction [59]. Parallel orbitals are AF ordered while orthogonal ones are FM. This usually is accompanied by a JT-distortion of the oxygen octahedra, but in certain cases can occur with very little lattice distortion. This difference has been observed [60] recently and can be modeled as complex orbital wavefunctions which preserve the isotropy between all three principle directions [58]. Some theoretical discussion is given on this by Altarelli *et al.* [61].

7. Ruddlesden–Popper Phases

Up until this point we have only discussed the manganites in general, but as a result of a concentrated effort to study these compounds, material scientists are now able to make layered structures of manganites to introduce dimensionality to the plethora of parameters with which to study CMR. A phase diagram of one such system is shown in Figure 2.7. Much of the progress on this front has been due to the layered structures fabricated specifically for the study of high transition temperature copper oxide superconductors, which had paved the way for a large increase in preparative methods of crystal growth as well as the efficiency and quality of the specimens [62]. Later when CMR was discovered, by changing synthesis from chemical substitution to layered variants of the cubic perovskite, it was shown that CMR depends on dimensionality intricately [62].

The layered materials are generally known as RuddlesdenPopper phases and have the general formula, $A_{n+1}Mn_nO_{3n+1}$ where n is the number of corner shared MnO_6 octahedral sheets forming the layer [25]. The ability to control the number of MnO_2 sheets per unit cell allows one to construct a 2-dimensional system, which has actually been shown to enhance the CMR effect as well as lower the critical temperature [24].
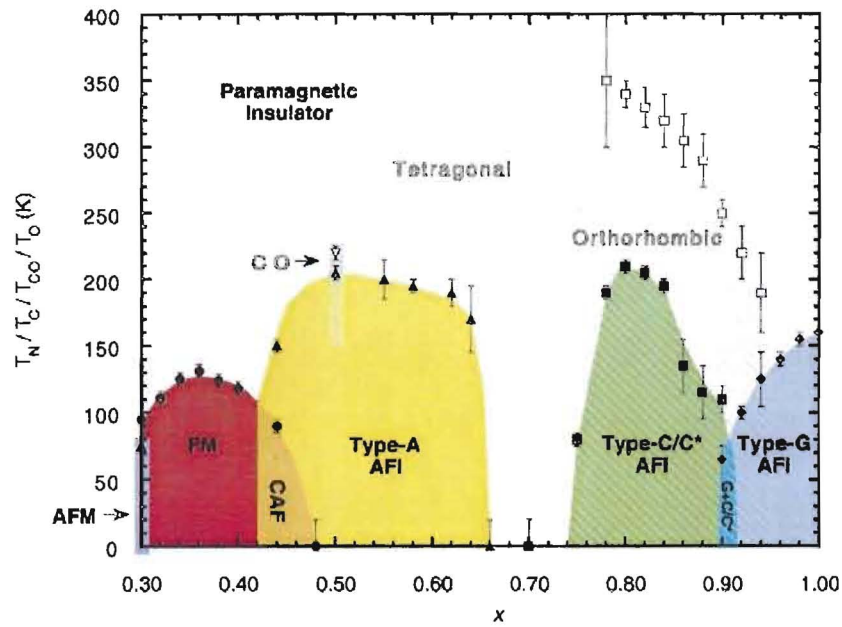
Fig. 2.7: **Bi-layer Phase Diagram** Phase diagram of the manganite bilayer $La_{2-2x}Sr_{1+2x}Mn_2O_7$. This is a 2-dimensional system that allows for a study of dimensionality in the manganites, taken from [4].

8.   Case Study: $Pr_{1-x}Ca_xMnO_3$

$Pr_{1-x}Ca_xMnO_3$ is one of the most exciting compositions of the manganite material for its doping simplicity. The Ca ion that is doped into the system has approximately the same radii as the Pr. The Pr^{3+} and the Ca^{2+} are 1.126 Å and 1.12 Å, respectively [63](or 1.30 Å and 1.34 Å based on another source [16]). This effectively removes the structural inhomogeneities and with it, the tolerance factor dependence. It is an ideal system for studying strictly doping dependence, as the bond angle or bond buckling, as well as any rotation of the oxygen octahedra, will play only a minimal role. It has a near cubic structure for high temperatures, and is one of the best examples of complex ordering that exhibits all the main features of charge, orbital, lattice, and magnetic phases: all occurring near half-doping.

PCMO is well-known also for its low band-width properties [14]. At all doping levels experimentally available, the ferromagnetic metallic phase is never realized without the application of a magnetic field [64] for any temperatures. The phase diagram is shown in Figure 2.8. An insulating state is found as the ground state of the system for all doping while only the magnetic ground state varies as a function of doping. Note the curious phase between the hole density of $x = 0.1$ and 0.3 shown on the horizontal axis: a ferromagnetic insulating phase. The coexistence of these two characteristics does not agree with the basic physics that we have discussed up until this point. In fact, many authors [58] attribute this to a region that must include some amount of orbital ordering to describe the behavior satisfactorily. The properties of this remain largely unexplored [14].

Another exciting attribute in the calcium-doped $PrMnO_3$ is the degree of the colossal magnetoresistance effect. Unlike any other system, this manganite can change in resistivity by 10 orders of magnitude [64]. The stability of the charge and orbitally ordered state at x = 0.5 is also robust [65]. At this doping level, it take up to 30 Tesla to destroy the ordering at low temperatures [66]. The large range where charge, magnetic, and orbital order exist in this sample near half-doping makes this an ideal candidate to study the interactions of these effects.
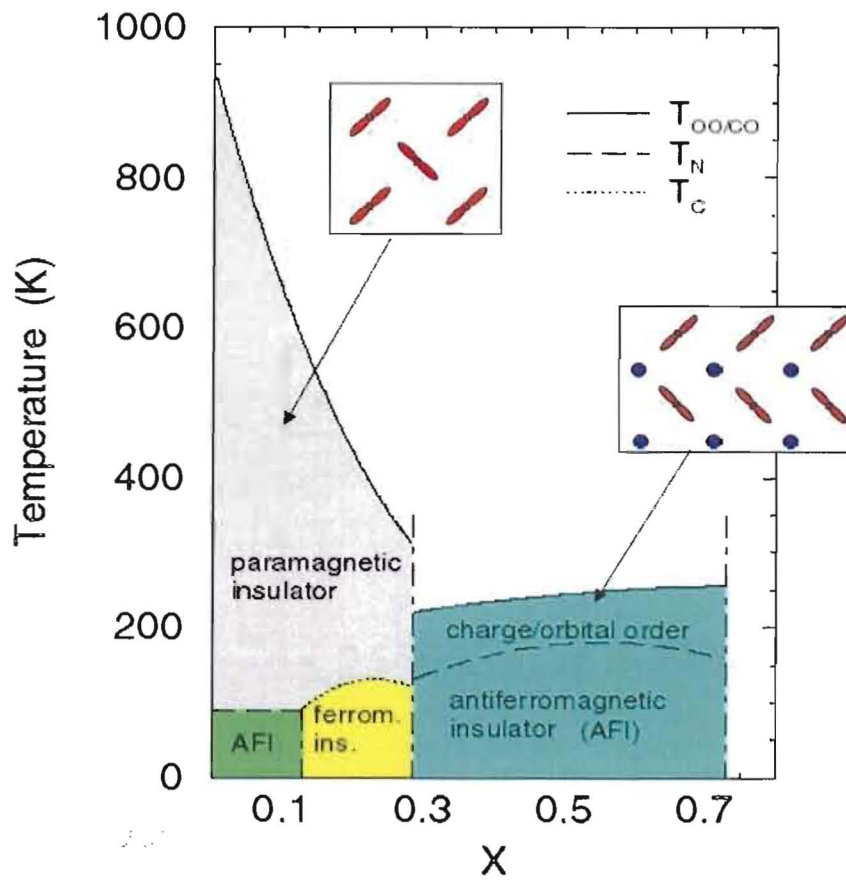
Fig. 2.8: **Phase Diagram for $Pr_{1-x}Ca_xMnO_3$** The zero-field phase diagram of the cubic manganite $Pr_{1-x}Ca_xMnO_3$ taken from [5] from measurements performed in [6]. This shows the global insulating phases of PCMO for all doping and the number of magnetic ordering phases present in the system. This system is known as the common example of a low-bandwidth manganite.

9.   The Middle-Way

In conclusion, we have mainly discussed two types of physics in the manganites: the macroscopic and microscopic. The colossal magnetoresistance effect was discovered because of the large macroscopic changes that are made to the properties of the system by changing other macroscopic entities. Following this we then looked at the microscopic physics of the behavior of the electrons, focusing on the Mn. Lastly, we would like to discuss mesoscopic physics. By mesoscopic, we mean the length scales that are too small to be described by thermodynamic principles, yet are larger than can be described with microscopic physics. In a paper from 2000, Robert Laughlin and co-authors describe this theory in what they call, 'the middle-way' [67]. The idea is that there are as-yet-undiscovered organizing principles at work on the mesoscopic scale, principles that could be responsible for the existence and/or universality of rules which organize behavior at long wavelengths. It is evident that properties for condensed matter - in which we have a large aggregate of particles - are caused by collective organizing principles that come out of quantum mechanics and the microscopic rules, but in every way, are really independent of them [67].

Soft x-ray techniques are the perfect match to explore these meso-phases on the length scale that, as we will explain in the following pages, we believe are crucial to CMR. Coupled with our abilities for simultaneous temporal studies, we are able to make a contribution to the understanding of CMR, but even on a much more general level, probe 'middle-way' principles that could be critical to our understanding at the heart of condensed matter physics.

Phase separation is likely in any system with a first-order phase transition, but manganites exhibit several first-order transitions between severely different electrical and magnetic regions [37]. Small perturbations of the microstructure allow phase transformations to occur, so coexistence is not a surprise [37, 68]. The peculiarity is that the coexistence is widespread: manganites exhibit a wealth of fascinating phase-separating behavior on a plethora of length scales. Mesoscopic phenomena, the range of structure we probe and describe in the following pages, approaches the type of length scales that beg for different physical descriptions. It is here that the properties are too complex for quantum descriptions, yet many-body concepts of thermodynamics no longer apply either [37]. Phase separation then, on this length scale is also known as 'texture within a phase' - mesoscopic structure that is emerging as some of the most intriguing and rich phenomena in this class of materials [37].

The mixed-phase tendencies have two origins: electronic phase separation between phases with different densities that lead to nano-scale coexisting clusters and disorder-induced phase separation with percolative characteristics between equal-density phases, driven by disorder near first-order transitions [2]. But something must be emphasized here: the physics of the mesostructure in manganites is dominated by intrinsic inhomogeneities of the Mn-oxides, believed to be a central issue to CMR [17]. This is not chemical homogeneities, but are attributed to equilibrium properties that still have yet to be fully understood [69]. There have been a number of studies that have shown different length-scale-types of phase coexistence [70, 71, 72, 73]. On the nanoscale however is both where it is poorly understood and where we are able to observe phase segregation the most readily, using the techniques described in the next chapter.

Another piece to the puzzle, as has been argued here, and seems to hold some of the most exciting secrets to this mystery, is the orbital ordering mechanism. From unexplainable states to puzzling properties, the orbital sector may hold the key to unraveling the physics of these compounds. For instance, many believe that phase segregation may be accompanied by orbital or other types of fluctuations, but this is still largely unexplored [16, 68, 73, 74]. In fact the orbital ordering mechanism has even lead to the idea of a novel type of electronics based on using the orbital degree of freedom instead of charge, or spin [75]. It is through studying the mesophases that these orbital fluctuations are elucidated in the following pages and allow a more complete portrait to be painted, and to obtain a deeper understanding of the colossal magnetoresistive effect in transition metal oxides.

CHAPTER III

RESONANCE AND 'EXCHANGE' SCATTERING

The light shines in the darkness, but the darkness has not understood it.
- John 1:5

In this chapter we will focus on the technique of x-ray scattering. We will start with a brief history of the subject, and then turn to resonant or 'exchange' scattering: the type of scattering used in all of the work presented here. This is sometimes referred to as magnetic scattering, but we refrain from that term here due to the many types of magnetic scattering that occur. These differences will be described in detail. Contrasting the previous chapter where we discussed the history and its relevance to the current state of the manganites, in this chapter we will skip the history and first start with the most challenging aspect of scattering theory: the derivation of the full quantum mechanical cross-section using 2nd order perturbation theory. The reason for this is really three-fold. First, this was first done in 1985 by M. Blume [76] and has not been in detail since. That derivation only consisted of a few lines, making it hard to follow in any depth. Second, there are actually a number of typographical errors in that paper, increasing the challenge to fully understand the quantum mechanics behind resonant scattering. Lastly, in the anomalous dispersion or resonant terms, only the magnetic contribution is worked out. The derivation here not only works out the explicit details, but generalizes the expression to include all the resonant terms, including Templeton-type terms. Following this, we will make a series of assumptions to simplify this relation for particular cases. We end with some specific discussion addressing a special case of resonant scattering: the resonant enhancement used to study orbital wavefunction modulations of electrons in strongly correlated electron systems.

1. Introduction

The famous example of a blue daytime sky and a red sunset at dusk (Fig. 3.1) are the most popular examples of scattering: the absorption and re-radiation of light in many directions by the molecules of the atmosphere [77]. Shortly after the discovery of x-rays by Wilhelm Rontgen in 1895, the first x-ray diffraction experiments were carried out on a crystal by Max von Laue in 1912 [78]. This confirmed two questions posed at that time: that x-rays were wave-like as well as the fact that crystals formed into periodic arrays of atoms. Since that time, x-ray diffraction has become an invaluable tool for the study of structure of a vast array of material properties, revolutionizing fields from physics to medicine, and changing the way we view and understand the world. However, while x-rays have been known about and studied for well over a hundred years, it is only in the last twenty or so years that we have had the knowledge and opportunity to take advantage of the multiple aspects of the interaction of photons with electrons, due mostly to the development of synchrotrons. X-ray scattering is typically thought to originate from the photon interaction with the charge density of the atoms of a system, as it does with optical light to yield the apparent color of the sky. Yet, as we shall demonstrate here from first principles, there are many new effects that arise by taking into account the full effect of the binding of electrons.

2. Scattering in Quantum Mechanics

The greatest advance in the technique of magnetic scattering is in the use of quantum mechanics. Though this was demonstrated previously, it was the seminal paper in 1985 by M. Blume that described the physics in detail. This lead x-ray scientists to use the resonance effect due to the difference in quantum energy levels of electrons in systems to greatly enhance magnetic effects in scattering. This has proved crucial to the study of magnetism and has spurred much interest in the properties of magnetically complex materials. The enhancement was first discovered as high as fifty-fold enhancement [79] and later shown to be six orders of magnitude [80].

i. Overview

To analyze resonant scattering, we will first start from first principles to evaluate precisely where the large enhancement of the scattering cross-section

Fig. 3.1: **Sunset** The sunset at Newport Beach demonstrating both the scattering of sunlight through a large volume of molecules in the atmosphere at the horizon and the scattering through a smaller volume at higher angles with respect to the observer. The large volume is what gives the redish color at smaller angles, as is the blue color for higher angles and smaller molecular volume. The difference in apparent color is based on the position of the observer only, with respect to the position of the sun and the number of molecules in the atmosphere between the two. Because near the horizon the light must travel further to the observer, the higher frequency light scatters more strongly as compared to the lower frequency, giving the appearance of an abundance of red colored light. The image was taken from [7].

originates. We begin with an arrangement of electrons in an electromagnetic field:

$$H = \sum_j \frac{1}{2m}(\mathbf{P}_j - \frac{e}{c}\mathbf{A}(\mathbf{r}_j))^2 + \sum_{ij} V(\mathbf{r}_{ij})$$

This is the basic textbook Hamiltonian with the electron given by charge e and mass m, and we have collected all electron-electron interactions into V_{ij} for the moment. The momentum operator is $\mathbf{P}_j$ and $\mathbf{A}(\mathbf{r}_j)$ is the vector potential given by

$$\mathbf{A}(\mathbf{r}_j) = \sum_{\mathbf{q}\alpha} \sqrt{\frac{2\pi\hbar c^2}{V\omega_{\mathbf{q}}}} \left[\hat{\epsilon}_{\mathbf{q}\alpha} c_{\mathbf{q}\alpha} e^{i\mathbf{q}\cdot\mathbf{r}_j} + \hat{\epsilon}^*_{\mathbf{q}\alpha} c^{\dagger}_{\mathbf{q}\alpha} e^{-i\mathbf{q}\cdot\mathbf{r}_j} \right] \tag{3.1}$$

where $\mathbf{r}_j$ is the position of the i-th electron of the system, q and α index the momentum and polarization states of the photon, ϵ is the polarization vector, and c and $c^{\dagger}$ are the photon annihilation and creation operators from quantum theory, respectively. It is worth noting that $\mathbf{A}(\mathbf{r}_j)$ is defined in terms of single powers of creation and annihilation operators. This linear form, means that for scattering to take place, the interaction must go as even powers of $\mathbf{A}(\mathbf{r}_j)$. This of course is not true for absorption or spontaneous emission computations, but in the quantum mechanical description of scattering, a photon must be absorbed and 'simultaneously' re-emitted. 'Simultaneously' simply refers to the fact that this is taken as a single quantum mechanical process.

At the final stage, we hope to obtain the cross-section of photon scattering from electrons in a crystal. This can be calculated with Fermi's golden rule from quantum mechanics:

$$W = \frac{2\pi}{\hbar} \left| \langle f | H' | i \rangle + \sum_{n=1}^{N} \frac{\langle f | H' | n \rangle \langle n | H' | i \rangle}{E - E_n} \right|^2 \delta(E_i - E_f)$$

This gives the transition rate for a transition from an initial quantum state to a continuum of states, and even though it bares Fermi's name, was mostly due to Dirac [81]. We show the relation at this stage because it is this expression we will work towards attaining and what we will use to finally calculate the cross-section for resonant or 'exchange' scattering. Also, it is worth noting that this equation only depends on the interaction part of the Hamiltonian H', and the eigenstates of the isolated, or non-interacting systems. This will motivate the main focus of this work, to calculate the amplitude due to this interaction term alone of the Hamiltonian.

ii. Hamiltonian

We start by writing down the full Hamiltonian of a set of electrons, which can be found in any basic graduate text in quantum mechanics [81]:

$$H = \sum_j \frac{1}{2m}(\mathbf{P}_j - \frac{e}{c}\mathbf{A}(\mathbf{r}_j))^2 + \sum_{ij} V(\mathbf{r}_{ij}) - \frac{e\hbar}{2mc}\sum_j \mathbf{s}_j \cdot \mathbf{B}$$

$$-\frac{e\hbar}{2mc^2}\sum_j \mathbf{s}_j \cdot \mathbf{E}(\mathbf{r}_j) \times (\mathbf{P}_j - \frac{e}{c}\mathbf{A}(\mathbf{r}_j)) + \sum_{k\lambda} \hbar\omega_k(c^\dagger(k\lambda)c(k\lambda) + \frac{1}{2})$$

which can be reformulated into

$$H = H_0 + H'$$

where we separate the Hamiltonian into an initial part and an interaction part. The initial part describes the system before an interaction take place while the interaction term describes the perturbation of the initial eigenstates (not necessarily the ground state). As we saw, Dirac's, or Fermi's golden rule is based on the interaction matrix elements in perturbation theory where we assume the interaction is only a 'small' perturbation of the original state. Using the usual definition of electric and magnetic fields $\mathbf{E} = -\nabla\phi - \frac{1}{c}\partial_t\mathbf{A}(\mathbf{r_j})$ and $\mathbf{B} = \nabla \times \mathbf{A}(\mathbf{r_j})$, we can rewrite the full Hamiltonian in terms of potentials as:

$$H = \sum_j \frac{1}{2m}(\mathbf{P}_j - \frac{e}{c}\mathbf{A}(\mathbf{r}_j))^2 + \sum_i e_i\phi(\mathbf{r}_i,t) + \sum_{ij} V(\mathbf{r}_{ij}) - \frac{e\hbar}{2mc}\sum_j \mathbf{s}_j \cdot (\nabla \times \mathbf{A}(r_j)) -$$

$$\frac{e\hbar}{2mc^2}\sum_j \mathbf{s}_j \cdot (-\nabla\phi(\mathbf{r}_i,t) - \frac{1}{c}\partial_t\mathbf{A}(\mathbf{r}_j)) \times (\mathbf{P}_j - \frac{e}{c}\mathbf{A}(\mathbf{r}_j)) + \sum_{k\lambda} \hbar\omega_k(c^\dagger(k\lambda)c(k\lambda) + \frac{1}{2})$$

First, notice the first term is actually four, due to the anti-commutator:

$$H_1 = \frac{1}{2m}\sum_j \mathbf{P}_j^2 + \frac{e^2}{c^2}\mathbf{A}^2(\mathbf{r_j}) - \frac{e}{c}\{\mathbf{P}_j, \mathbf{A}(\mathbf{r}_j)\}$$

where the sum is over all indices j for all electrons contributing to the scattering, and the brackets represent the anti-commutator since the vector potential and momentum operator do not commute. The fifth also contains four terms:

$$H_5 = -\frac{e\hbar}{2mc^2}\sum_j \mathbf{s}_j \cdot \mathbf{E}(\mathbf{r}_j) \times (\mathbf{P}_j - \frac{e}{c}\mathbf{A}(\mathbf{r}_j))$$

$$= -\frac{e\hbar}{2mc^2}\sum_j \mathbf{s}_j \cdot \mathbf{E}(\mathbf{r}_j) \times \mathbf{P}_j - \frac{e}{c}(\mathbf{s}_j \cdot \mathbf{E}(\mathbf{r}_j)) \times \mathbf{A}(\mathbf{r}_j)$$

$$= -\frac{e\hbar}{2mc^2}\sum_j \mathbf{s}_j \cdot (-\nabla\phi - \frac{1}{c}\partial_t \mathbf{A}(\mathbf{r}_j)) \times \mathbf{P}_j$$

$$+\frac{e^2\hbar}{2mc^3}\sum_j \mathbf{s}_j \cdot (-\nabla\phi - \frac{1}{c}\partial_t \mathbf{A}(\mathbf{r}_j)) \times \mathbf{A}(\mathbf{r}_j)$$

This spin-orbit term is of order $g = \frac{\hbar\omega}{mc^2}$, which is $\sim 10^{-3}$ for soft x-ray energies, since the electron rest mass is of order $500\,\mathrm{keV}$. Because of the value of this constant out front, we can neglect all but up to linear terms for this term. For instance, 2nd order in this term would give negligible contributions, lowering values by $g^2 = 10^{-6}$. This linear argument means we will only take this term up to first-order in the theory. Hence, only zeroth order or quadratic terms in the vector potential will contribute to the amplitude. Dropping terms that go like $\sim \mathbf{s} \cdot \mathbf{A}$ and $\sim (\mathbf{s} \cdot \nabla\phi) \times \mathbf{A}$, we are left with only two terms from the four-fold H_5 term:

$$H_5 = \frac{e\hbar}{2mc^2}\sum_j [\mathbf{s}_j \cdot \nabla\phi(\mathbf{r}_j)] \times \mathbf{P}_j - \frac{e}{c^2}\mathbf{s}_j \cdot [\partial_t \mathbf{A}(\mathbf{r}_j) \times \mathbf{A}(\mathbf{r}_j)]$$

iii.   Exact and Perturbative Hamiltonian Terms

Collecting all remaining terms, we can now separate terms to isolate the exact and perturbative terms. The former terms, denoted by H_0, are

$$H_0 = \frac{1}{2m}\sum_j \mathbf{P}_j^2 + \sum_{ij} \tilde{V}(\mathbf{r}_{ij}) + \sum_i e_i\phi(\mathbf{r}_i, t) \tag{3.2}$$

$$+\frac{e\hbar}{2mc^2}\sum_j [\mathbf{s}_j \cdot \nabla\phi(\mathbf{r}_j)] \times \mathbf{P}_j + \sum_{k\lambda} \hbar\omega_k(c^\dagger(k\lambda)c(k\lambda) + \frac{1}{2})$$

where we have the normal kinetic and Coulombic terms, the potential $\tilde{V}(\mathbf{r})$ that represents all other potentials seen by the particle other than Coulomb, and the part of the spin-orbit term that describes interactions between electrons only. The last term represents the interaction of photons with themselves, removing

it from the photon-electron interaction Hamiltonian. This is the term that is responsible for vacuum fluctuations. Collecting the remaining terms gives the perturbing potential:

$$H' = \frac{e}{2mc} \sum_j [\frac{e}{c} \mathbf{A}^2(\mathbf{r}_j) - \{\mathbf{P}_j, \mathbf{A}(\mathbf{r}_j)\}] - \frac{e\hbar}{2mc} \sum_j \{\, \mathbf{s}_j \cdot (\nabla \times \mathbf{A}(\mathbf{r}_j)) \quad (3.3)$$
$$+ \frac{e}{c^2} \mathbf{s}_j \cdot [\partial_t \mathbf{A}(\mathbf{r}_j) \times \mathbf{A}(\mathbf{r}_j)]\,\} + O(\mathbf{A}^3(\mathbf{r}_j)) + O(g^2)$$

This interaction Hamiltonian H' is the main result of this section. It represents all the terms we wish to calculate amplitudes for, as Fermi's golden rule only depends on matrix elements involving this perturbing Hamiltonian. We can split this into two interaction terms in order to deal with them separately: the first order $H^{(1)}$ and second order $H^{(2)}$ since the perturbing H can be written as $H' = H^{(1)} + H^{(2)}$.

3.   Perturbation Theory - Scattering to 1st Order

For the 1st order computation, the only interaction terms from H' that contribute to scattering are ones that are second order in $\mathbf{A}(\mathbf{r}_j)$:

$$H^{(1)} = \frac{e^2}{2mc^2} \sum_j \mathbf{A}^2(\mathbf{r_j}) - \frac{\hbar}{c^2} \mathbf{s}_j \cdot [\partial_t \mathbf{A}(\mathbf{r}_j) \times \mathbf{A}(\mathbf{r}_j)] \quad (3.4)$$

i.   First Term of 1st Order Scattering: Charge
The first term $H_1^{(1)}$ goes like

$$\sum_{\alpha,\mathbf{q}} \sum_{\alpha',\mathbf{q}'} \left[\hat{\epsilon}_{\mathbf{q}\alpha} c_{\mathbf{q}\alpha} e^{iq \cdot r_j} + \hat{\epsilon}^*_{\mathbf{q}\alpha} c^\dagger_{\mathbf{q}\alpha} e^{-iq \cdot r_j} \right] \left[\hat{\epsilon}_{\mathbf{q}'\alpha'} c_{\mathbf{q}'\alpha'} e^{iq' \cdot r_j} + \hat{\epsilon}^*_{\mathbf{q}'\alpha'} c^\dagger_{\mathbf{q}'\alpha'} e^{-i\mathbf{q}' \cdot r_j} \right]$$

or contains three types of terms:

$$e^{i(\pm q \pm q') \cdot r_j} [(\hat{\epsilon}_{\mathbf{q}\alpha} \cdot \hat{\epsilon}_{\mathbf{q}'\alpha'}) c_{\mathbf{q}\alpha} c_{\mathbf{q}'\alpha'} + (\hat{\epsilon}^*_{\mathbf{q}\alpha} \cdot \hat{\epsilon}^*_{\mathbf{q}'\alpha'}) c^\dagger_{\mathbf{q}\alpha} c^\dagger_{\mathbf{q}'\alpha'}$$

$$+ \hat{\epsilon}_{\mathbf{q}\alpha} \hat{\epsilon}^*_{\mathbf{q}'\alpha'} \{c_{\mathbf{q}\alpha}, c^\dagger_{\mathbf{q}'\alpha'}\}]$$

As mentioned briefly earlier, for a scattering process to occur, a photon must be absorbed, and then radiated, or in the language of quantum field theory, annihilated and then created (and vice versa). Hence, the result will include products of one creation and one annihilation operator. This leaves only cross-

terms as in the third term above. The final result for this term is:

$$\sum_{\alpha,\mathbf{q}} \sum_{\alpha',\mathbf{q}'} \left[(\hat{\epsilon}_{\mathbf{q}\alpha} \cdot \hat{\epsilon}_{\mathbf{q}'\alpha'}^*) c_{\mathbf{q}\alpha} c_{\mathbf{q}'\alpha'}^\dagger e^{i(q-q')\cdot r_j} + (\hat{\epsilon}_{\mathbf{q}\alpha}^* \cdot \hat{\epsilon}_{\mathbf{q}'\alpha'}) c_{\mathbf{q}\alpha}^\dagger c_{\mathbf{q}'\alpha'} e^{-i(q-q')\cdot r_j} \right] \quad (3.5)$$

The creation and annihilation operators adjust the number of photons in the quantization of the electromagnetic field. This is the same idea as the ladder operators in the harmonic oscillator problem, where the effect is to raise or lower the energy states of the system [82], aside from factors of $\hbar$ and 2π. We will denote a state explicitly as

$$|n; N_{k1,\epsilon1}, N_{k2,\epsilon2}, N_{k3,\epsilon3}...\rangle \quad (3.6)$$

where n represents the state of the solid, and $N_{k_i \epsilon_i}$ represents the number of photons in each mode, with wavevector k_i, and polarization ϵ_i. The operators $c_{q\alpha}$ and $c_{q\alpha}^\dagger$ then only operate on the mode with the index q and α. The results are derived in any introductory book on quantum mechanics (See for instance [82] or [81]) and are as follows:

$$c_{q\alpha} |n; ...N_{q-1,\alpha-1}, N_{q,\alpha}, N_{q+1,\alpha+1}...\rangle = \sqrt{N_{q,\alpha}} |n; ...N_{q-1,\alpha-1}, N_{q,\alpha} - 1, N_{q+1,\alpha+1}..\rangle \quad (3.7)$$

and for the creation operator

$$c_{q\alpha}^\dagger |n; ...N_{q-1,\alpha-1}, N_{q,\alpha}, N_{q+1,\alpha+1}\rangle = \sqrt{N_{q,\alpha} + 1} |n; ...N_{q-1,\alpha-1}, N_{q,\alpha} + 1, N_{q+1,\alpha+1}..\rangle \quad (3.8)$$

Using these expressions, we can then use Equation 3.5 to act on a arbitrary state. The result is

$$\sum_{\alpha,\mathbf{q}} \sum_{\alpha',\mathbf{q}'} \left[\hat{\epsilon}_{\mathbf{q}\alpha} \hat{\epsilon}_{\mathbf{q}'\alpha'}^* e^{i(q-q')\cdot r_j} \sqrt{N_{\mathbf{q}\alpha} N_{\mathbf{q}'\alpha'}} \delta_{\mathbf{q}\mathbf{q}'} \delta_{\alpha\alpha'} \right.$$

$$\left. + \ \hat{\epsilon}_{\mathbf{q}\alpha}^* \hat{\epsilon}_{\mathbf{q}'\alpha'} e^{-i(q-q')\cdot r_j} \sqrt{(N_{\mathbf{q}\alpha} + 1)(N_{\mathbf{q}'\alpha'} + 1)} \delta_{\mathbf{q}\mathbf{q}'} \delta_{\alpha\alpha'} \right.$$

where we have used the orthogonality of the photon part of the eigenstates, $\delta_{\alpha\beta} = \langle\alpha|\beta\rangle$. Note that the delta functions between 3d vectors are actually 3-dimensional, and so give constraints on all components of the vector.

Now we come to the beauty of this formalism. The delta functions however allow us to assign photon numbers to each state, and use the orthogonality of the photon states. In other words, what this means physically, is that if a

photon is absorbed, there is only an amplitude for the creation of a scattered photon with the same polarization and momentum eigenstate. If we assume there are a large number of photons N such that $N = N + 1$, the result is

$$< f|H_1^{(1)}|i > = \frac{2\pi\hbar e^2}{Vm} \sum_{q\alpha} \frac{N_{q\alpha}}{\omega_q} < f| \sum_j (\hat{\epsilon}_{\mathbf{q}\alpha}^* \cdot \hat{\epsilon}_{\mathbf{q}'\alpha'}) e^{-i(q-q')\cdot r_j}|i >$$

This term goes like the Fourier transform of the charge density and should be familiar. It is known as the Thompson term, and in general, is usually the most important term. In fact, x-ray scattering is usually referred to as the Fourier transform of the charge density, and only recently have the other terms in the expansion become important, as they have only been experimentally accessible with the advent of synchrotrons.

ii. Second Term of 1st order Scattering: Magnetic

Now the second term of Equation 3.4 in the interaction Hamiltonian is

$$H_2^{(1)} = -\frac{e^2\hbar}{2mc^4} \sum_j \mathbf{s}_j \cdot [\partial_t \mathbf{A}(\mathbf{r}_j) \times \mathbf{A}(\mathbf{r}_j)] \tag{3.9}$$

First note that $\partial_t \mathbf{A}(\mathbf{r}_j)$ has the form:

$$\partial_t \mathbf{A}(\mathbf{r}_j) = \sum_{\mathbf{q}\alpha} \sqrt{\frac{2\pi\hbar c^2}{V\omega_{\mathbf{q}}}} \left[(-i\omega\mathbf{q})\hat{\epsilon}_{\mathbf{q}\alpha} c_{\mathbf{q}\alpha} e^{i\mathbf{q}\cdot\mathbf{r}_j} + (i\omega\mathbf{q})\hat{\epsilon}^*{}_{\mathbf{q}\alpha} c_{\mathbf{q}\alpha}^\dagger e^{-i\mathbf{q}\cdot\mathbf{r}_j} \right]$$

Inserting this into Equation 3.9, we see that the consequence of this term is not much different than in Equation 3.5. The only difference is the cross-product is now transfered to the polarization product in front of the operators, as are the factors of $\pm i\omega$ from the time derivatives. The result, neglecting prefators, is

$$\sum_{\alpha,\mathbf{q}\alpha',\mathbf{q}'} [-i\omega_q(\hat{\epsilon}_{\mathbf{q}\alpha} \times \hat{\epsilon}_{\mathbf{q}'\alpha'}^*) c_{\mathbf{q}\alpha} c_{\mathbf{q}'\alpha'}^\dagger e^{i(q-q')\cdot r_j} + i\omega_q(\hat{\epsilon}_{\mathbf{q}\alpha}^* \times \hat{\epsilon}_{\mathbf{q}'\alpha'}) c_{\mathbf{q}\alpha}^\dagger c_{\mathbf{q}'\alpha'} e^{-i(q-q')\cdot r_j}] \tag{3.10}$$

The result is similar to the first term, but with the few differences in the operator mentioned above, and the spin operator is also retained as well. The final result is:

$$< f|H_2^{(1)}|i > = \frac{2\pi\hbar e^2}{Vm} \frac{N_{q\alpha}}{\omega_q} \frac{(-i\hbar\omega_k)}{mc^2} < f| \sum_j (\hat{\epsilon}_{\mathbf{q}\alpha}^* \times \hat{\epsilon}_{\mathbf{q}'\alpha'}) \mathbf{s}_j e^{-i(q-q')\cdot r_j}|i >$$

iii. Charge versus Magnetic

If we assume the number of magnetic scattering ions is equal the the charge scattering, a commonly quoted scaling relation is as follows [76]. Assuming the form factors are the same, then the relative difference in cross-section between these two terms is

$$\sigma = \frac{\sigma_{magnetic}}{\sigma_{electric}} = \left(\frac{\hbar\omega}{mc^2}\right)^2 \langle S \rangle^2$$

So magnetic scattering is proportional to the average spin density, and is smaller than the charge scattering by a energy ratio factor g^2, where g is the photon energy over the rest mass of the electron.

4. Perturbation Theory - Scattering to 2nd Order

Now we move on to 2nd order perturbation theory. As we will see, these are the terms that are responsible for exchange scattering, or as it was first named: anomalous scattering. That is, the effects from dispersion that arise when photon energies are near adsorption edges. The are four terms in the total Hamiltonian that have been collected into the interaction Hamiltonian H' in Equation 3.3. The two quadratic terms, the first and fourth terms, have been used in the first-order calculation and do not contribute to 2nd order because here we are only taking up to order g in the amplitude. Similarly, as mentioned earlier, the 2nd and 3rd terms that are linear in photon field $\mathbf{A}(\mathbf{r}_j)$ do not contribute to 1st order, but are the only terms that do in 2nd.

i. Feynman Diagrams

Feynman diagrams are a convenient way to visualize the interactions discussed here pictorially. The diagrams shown in Figures 3.2 and 3.3 are illustrations of possible quantum mechanical processes that take place in photon-electron scattering. The vertical axis is time, and the horizontal is position - reduced to one-dimension for simplicity.

Essentially, there are only two mechanisms by which to generate scattering in 2nd order perturbation theory. The most obvious, is when a photon is first absorbed. This process excites a core electron to an empty state, leaving a core vacancy. This process is followed by the radiation of a photon upon the electron decaying back to the original energy state. This process is shown in Figure 3.2. One interpretation of this process is that this allows 'forbidden transitions'. That is, if the first order amplitude for the transition of $< \psi_n | H' | \psi_0 >$ is zero,
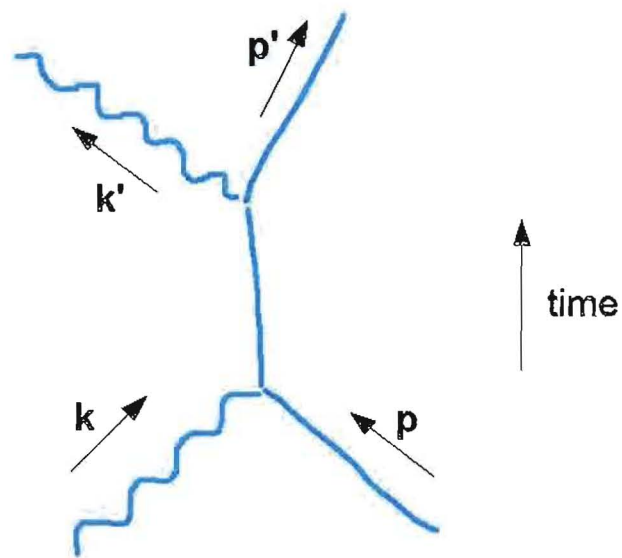
Fig. 3.2: **1st Feynman Diagram** The Feynman Diagram for the 2nd order process of a scattered photon by an electron state. The electron of momentum **p** first absorbs a photon of momentum **k**, changing the state of the system. This is followed by the emission of a photon **k'** at some later time. The result is an outgoing electron of momentum **p'**. The time axis is vertical in the diagram.

it can still occur in 2nd order in the two-step process: the absorption of the photon and excitation of the electron to an intermediate state, followed by the de-excitation of the electron and emission of the photon. Remember however, that this is a single quantum mechanical process. These virtual transitions must be summed over all possible states, in accord with the equation for the 2nd order matrix element:

$$\sum_m \frac{<\psi_n|H'|\psi_m><\psi_m|H'|\psi_0>}{E_0 - E_m + i\hbar\eta}$$

where η takes into account the core-hole lifetime and is dependent on the binding energies of the requisite electron energy states. The second contribution comes from the time-reversed process: the spontaneous emission of a photon and decay of an electron to a lower lying state, followed by the absorption of a photon and excitation of electron to its original state. This is shown in Figure 3.3 and must be included as it also contributes to the same scattering process.

ii. Photon and Electron-Momentum Coupling

The 2nd term in Equation 3.3 is the first of the two that contribute to 2nd order perturbation theory:

$$H_1^{(2)} = -\frac{e}{2mc}\sum_j - \{\mathbf{P}_j, \mathbf{A}(\mathbf{r_j})\}$$

In general, this anti-commutator term must be retained, but here we use the Coulomb gauge $\nabla \cdot A = 0$, and so we can write this simply as

$$H_1^{(2)} = \frac{e}{mc}\sum_j \mathbf{P}_j \cdot \mathbf{A}(\mathbf{r}_j) \tag{3.11}$$

or using Equation 3.1 for the operator $\mathbf{A}(\mathbf{r}_j)$

$$H_1^{(2)} = \frac{e}{mc}\sqrt{\frac{2\pi\hbar c^2}{V\omega_q}}\sum_{\mathbf{q}\alpha j}\left[(\mathbf{P}_j \cdot \hat{\epsilon}\mathbf{q}\alpha)c_{\mathbf{q}\alpha}e^{iq\cdot r_j} + (\mathbf{P}_j \cdot \hat{\epsilon}^*\mathbf{q}\alpha)c_{\mathbf{q}\alpha}^\dagger e^{-iq\cdot r_j}\right] \tag{3.12}$$

where we recall that our $N_{\mathbf{q}\alpha}$-notation is where $\mathbf{q}$ indexes the momentum of the photon state, and α its polarization.

1st Feynman Diagram

We are interested in the first Feynman diagram of this process, denoted by $H_1^{(2)}(f1)$, the absorption of a photon state $N_{\mathbf{q}\alpha}$ and the creation of a different photon state of momentum and polarization $N_{\mathbf{q}'\alpha'}$. For this possibility, the intermediate state vector is $\left|\phi_m; N_{\mathbf{q}\alpha} - 1; N_{\mathbf{q}'\alpha'} = 0\right\rangle$ where ϕ_m represents the electron state and the additional terms are to remind us that the there is one less $N_{\mathbf{q}\alpha}$ and none created yet. We can write this more explicitly as:

$$\sum_{m,\mathbf{q},\mathbf{q}'} \sum_{\alpha\alpha'} \left[\frac{\left\langle \phi_n; N_{\mathbf{q}\alpha} - 1; N_{\mathbf{q}'\alpha'} = 1 | H_{1b}^{(2)} | \phi_m; N_{\mathbf{q}\alpha} - 1; N_{\mathbf{q}'\alpha'} = 0 \right\rangle}{\sqrt{E_0 - E_m + i\hbar\eta}} \right. \tag{3.13}$$

$$\left. \cdot \frac{\left\langle \phi_m; N_{\mathbf{q}\alpha} - 1; N_{\mathbf{q}'\alpha'} = 0 | H_{1a}^{(2)} | \phi_0; N_{\mathbf{q}\alpha}; N_{\mathbf{q}'\alpha'} = 0 \right\rangle}{\sqrt{E_0 - E_m + i\hbar\eta}} \right]$$

Where we have used the subscripts $1a$ and $1b$ to differentiate between the two processes of the $H_1^{(2)}$ term: the absorption and the emission, respectively. This equation reminds us that the sum is over intermediate states, but it should be noted that this does not represent the full calculation unless the system is non-magnetic. We will describe this in detail later, but suffice it to say, we will calculate terms separately, and then sum at the end.

The first process of the first Feynman diagram is simply absorption of the photon by an intermediate state:

$$\sum_{m,\mathbf{q},\mathbf{q}'} \sum_{\alpha\alpha'} \frac{\left\langle \phi_m; N_{\mathbf{q}\alpha} - 1; N_{\mathbf{q}'\alpha'} = 0 | H_{1a}^{(2)} | \phi_0; N_{\mathbf{q}\alpha}; N_{\mathbf{q}'\alpha'} = 0 \right\rangle}{\sqrt{E_0 - E_m + i\hbar\eta}} \tag{3.14}$$

where $E_0 = \epsilon_0 + N_{\mathbf{q}\alpha}(\hbar\omega_{\mathbf{q}})$ and $E_m = \epsilon_m + (N_{\mathbf{q}\alpha} - 1)(\hbar\omega_{\mathbf{q}})$. Substituting these energies into the equations above or for the first absorption we have:

$$H_1^{(2)}(f1) = \frac{e}{mc}\sqrt{\frac{2\pi\hbar c^2}{V\omega_q}} \sum_{\alpha\alpha'} \sum_{m,\mathbf{q},\mathbf{q}'} \frac{1}{\sqrt{\epsilon_0 - \epsilon_m + \hbar\omega_{\mathbf{q}} + i\eta}} \left\langle H_{1b}^{(2)} \right\rangle \left\langle H_{1a}^{(2)} \right\rangle \tag{3.15}$$

where we have placed all constants in the operators outside of the summation. This is not in general true for momentum vectors, but here can be done for energy or frequencies, as will be argued shortly. The two separate matrix elements, $H_{1a}^{(2)}$ and $H_{1b}^{(2)}$, will be calculated explicitly below. Again, the notation $f1$ denotes the result for the first Feynman diagram only.
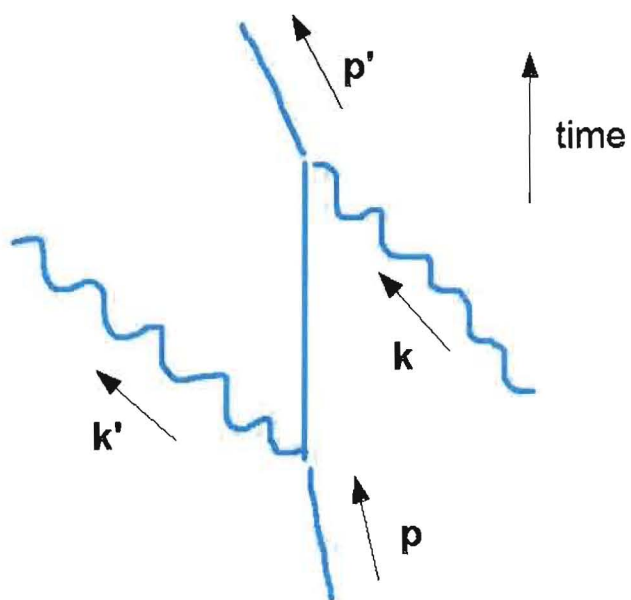
Fig. 3.3: **2nd Feynman Diagram** The Feynman Diagram for the time-reversed process of that shown in Figure 3.2. The system first emits a photon of momentum k', which is then followed by the absorption of a different photon k. The two processes must both be taken into account as they give contributions to the total amplitude quantum mechanically.

The operator matrix element $\left\langle H_{1a}^{(2)}(f1) \right\rangle$ can be expressed explicitly as

$$\left\langle \phi_m; N_{\mathbf{k}_\epsilon} - 1; N_{\mathbf{k}'_{\epsilon'}} \left| \sum_j \mathbf{P}_j \cdot (\hat{\epsilon}_{\mathbf{q}\alpha} c_{\mathbf{q}\alpha} e^{i\mathbf{q}\cdot r_j} + \hat{\epsilon}^*_{\mathbf{q}\alpha} c^\dagger_{\mathbf{q}\alpha} e^{-i\mathbf{q}\cdot r_j}) \right| \phi_0; N_{\mathbf{k}_\epsilon}; N_{\mathbf{k}'_{\epsilon'}} \right\rangle$$

remembering that the equation is still summed over polarizations, momenta, and the intermediate electron states as denoted in the previous equation. The constants and summations have been dropped here for clarity. By observing the $N_{\mathbf{k}'_{\epsilon'}}$ is unchanged, while the $N_{\mathbf{k}_\epsilon}$ decreases by one photon, we can see that, though summed over all possible photon states in the vector potential operator, the only term that survives is when $\mathbf{q}$ and α in the summation are equal to $\mathbf{k}$ and ϵ, respectively. Even then, only the annihilation operator on the left hand side gives a non-zero result:

$$\left\langle H_{1a}^{(2)}(f1) \right\rangle \sim \tag{3.16}$$

$$\left\langle \phi_m; N_{\mathbf{k}_\epsilon} - 1; N_{\mathbf{k}'_{\epsilon'}} = 0 \right| c_{\mathbf{k}_\epsilon} \left| \phi_0; N_{\mathbf{k}_\epsilon}; N_{\mathbf{k}'_{\epsilon'}} = 0 \right\rangle \tag{3.17}$$

$$= \sqrt{N_{\mathbf{k}_\epsilon}} \left\langle \phi_m; N_{\mathbf{k}_\epsilon} - 1; N_{\mathbf{k}'_{\epsilon'}} = 0 \middle| \phi_0; N_{\mathbf{k}_\epsilon} - 1; N_{\mathbf{k}'_{\epsilon'}} = 0 \right\rangle \tag{3.18}$$

$$= \sqrt{N_{\mathbf{k}_\epsilon}} \left\langle N_{\mathbf{k}_\epsilon} - 1; N_{\mathbf{k}'_{\epsilon'}} \middle| N_{\mathbf{k}_\epsilon} - 1; N_{\mathbf{k}'_{\epsilon'}} \right\rangle \left\langle \phi_m | \phi_0 \right\rangle \tag{3.19}$$

$$= \sqrt{N_{\mathbf{k}_\epsilon}} \left\langle \phi_m | \phi_0 \right\rangle \tag{3.20}$$

One note here regarding this last step is that the states discussed here are shorthand for tensor products of states. In other words, the state $|\alpha; \beta\rangle$ where α represents the state of the electron in the solid and β the state of the photon is actually a eigenstate of the form $|\alpha\rangle \otimes |\beta\rangle$, where each ket represents different subsets of Hilbert space. In the previous calculation, we invoke orthogonality between the photon states, and we are left with the inner product of electron states. So inner products only produce unity for orthogonal states in that space. In the simple example here, $\langle \alpha_1; \beta | \alpha_2; \beta \rangle = \langle \alpha_1 | \alpha_2 \rangle \langle \beta | \beta \rangle = \langle \alpha_1 | \alpha_2 \rangle$. Also, one important point is that we have only worked through the photon sector of the state. The last inner product is between electron states. The end result for the calculation of this matrix element is then

$$\left\langle H_{1a}^{(2)}(f1) \right\rangle \sim \left\langle \phi_m \left| \sum_j \mathbf{P}_j \cdot \hat{\epsilon}_{\mathbf{k}_\epsilon} e^{i\mathbf{k}\cdot r_j} \right| \phi_0 \right\rangle \tag{3.21}$$

Since the polarization and momentum summations have been dropped out of the expression, the only sum left is for the number of electrons in the volume of x-ray illumination. If we include all factors for completeness, both the constant out front from the operator and the energy dependence, we are finally left with:

$$\left\langle H_{1a}^{(2)}(f1) \right\rangle = \sum_{\mathbf{k}\epsilon} \frac{e}{mc} \sqrt{\frac{2\pi N_{\mathbf{k}\epsilon}\hbar c^2}{V\omega_k}} \sum_j \frac{\left\langle \phi_m \left| \sum_j \mathbf{P}_j \cdot \hat{\epsilon}_{\mathbf{k}\epsilon} e^{i\mathbf{k}\cdot r_j} \right| \phi_0 \right\rangle}{\sqrt{\epsilon_0 - \epsilon_m + \hbar\omega_{\mathbf{k}} + i\eta}} \quad (3.22)$$

This is the result for only the first part of the equation, the matrix element between initial and intermediate states and represents the absorption of the photon part of the calculation.

The second half of the calculation is done the same way to compute $H_{1b}^{(2)}(f1)$, the contribution from the intermediate state to the final state, and gives the matrix element for the subsequent photon emission.

$$\left\langle \phi_n; N_{\mathbf{k}\epsilon} - 1; N_{\mathbf{k}'\epsilon'} \left| \sum_j \mathbf{P}_j \cdot (\hat{\epsilon}_{\mathbf{q}\alpha} c_{\mathbf{q}\alpha} e^{i\mathbf{q}\cdot r_j} + \hat{\epsilon}^*_{\mathbf{q}\alpha} c^\dagger_{\mathbf{q}\alpha} e^{-i\mathbf{q}\cdot r_j}) \right| \phi_m; N_{\mathbf{k}\epsilon} - 1; N_{\mathbf{k}'\epsilon'} \right\rangle$$

Where in keeping consistent with out notation, the subscript $1b$ represents the second step in the two-step quantum process for the first term, $H_1^{(2)}$. We invoke a similar argument as before: the only non-zero contribution to this emission matrix element is when the k'th and ϵ'th creation operator acts on the state. This gives

$$\left\langle \phi_n; N_{\mathbf{k}\epsilon} - 1; N_{\mathbf{k}'\epsilon'} = 1 | c^\dagger_{\mathbf{k}'\epsilon'} | \phi_m; N_{\mathbf{k}\epsilon} - 1; N_{\mathbf{k}'\epsilon'} = 0 \right\rangle \quad (3.23)$$

$$= \sqrt{N_{\mathbf{k}'\epsilon'}} \left\langle \phi_n; N_{\mathbf{k}\epsilon} - 1; N_{\mathbf{k}'\epsilon'} = 1 | \phi_m; N_{\mathbf{k}\epsilon} - 1; N_{\mathbf{k}'\epsilon'} = 1 \right\rangle \quad (3.24)$$

$$= \sqrt{N_{\mathbf{k}'\epsilon'}} \left\langle N_{\mathbf{k}\epsilon} - 1; N_{\mathbf{k}'\epsilon'} | N_{\mathbf{k}\epsilon} - 1; N_{\mathbf{k}'\epsilon'} \right\rangle \left\langle \phi_n | \phi_m \right\rangle \quad (3.25)$$

$$= \sqrt{N_{\mathbf{k}'\epsilon'}} \left\langle \phi_n | \phi_m \right\rangle \quad (3.26)$$

where again, after applying orthonormal relations in the photon Hilbert space, gives:

$$\left\langle H_{1b}^{(2)}(f1) \right\rangle = \sum_{\mathbf{k}'\epsilon'} \frac{e}{mc} \sqrt{\frac{2\pi N_{\mathbf{k}'\epsilon'}\hbar c^2}{V\omega_{k'}}} \sum_j \frac{\left\langle \phi_n \left| \mathbf{P}_j \cdot \hat{\epsilon}^*_{\mathbf{k}'\epsilon'} e^{-i\mathbf{k}'\cdot r_j} \right| \phi_m \right\rangle}{\sqrt{\epsilon_0 - \epsilon_m + \hbar\omega_{\mathbf{k}'} + i\eta}} \quad (3.27)$$

It should be noted that we have kept the terms separate for reasons that will become clear later. Order is extremely important here: all terms should be summed that represent the same process. So as we have just calculated the $H_1^{(2)}(f1)$ Hamiltonian for the two separate processes with regard to the first Feynman diagram, this result is only correct for non-magnetic systems (when the spin term can be ignored). Without this limit, we must add the $H_2^{(2)}$ Hamiltonian to $H_1^{(2)}$ before summing over electron states and multiplying. By not paying attention to this detail, important interference terms are not correctly taken into account.

2nd Feynman Diagram

The second diagram for the photon-electron coupling for 2nd order scattering is given in Figure 3.3 and represents the time-reversed process. This transition amplitude is calculated in the same way and represents the second half of the total computation for this term. As can be seen from the diagram, the intermediate state has the form of $\left|\phi_m; N_{\mathbf{q}\alpha}; N_{\mathbf{q}'\alpha'} = 1\right\rangle$ and the energy terms in the denominator are now $E_0 = \epsilon_0 - N_{\mathbf{q}\alpha}(\hbar\omega_{\mathbf{q}})$ and $E_m = \epsilon_m + (N_{\mathbf{q}\alpha})(\hbar\omega_{\mathbf{q}})$. As we went through the first Feynman process in detail, here we just write the answer, due to the similarity of this calculation with the first diagram. The result for the 2nd Feynman diagram for the two processes is:

$$\left\langle H_{1a}^{(2)}(f2)\right\rangle = \sum_{\mathbf{k}'_{\epsilon'}} \frac{e}{mc} \sqrt{\frac{2\pi N_{\mathbf{k}'_{\epsilon'}}\hbar c^2}{V\omega_{k'}}} \sum_j \left[\frac{\left\langle \phi_m|\mathbf{P}_j \cdot \hat{\epsilon}^*_{\mathbf{k}'_{\epsilon'}} e^{-i\mathbf{k}'\cdot r_j}|\phi_0\right\rangle}{\epsilon_0 - \epsilon_m - \hbar\omega_{\mathbf{k}'} + i\eta}\right] \tag{3.28}$$

$$\left\langle H_{1b}^{(2)}(f2)\right\rangle = \sum_{\mathbf{k}_{\epsilon}} \frac{e}{mc} \sqrt{\frac{2\pi N_{\mathbf{k}_{\epsilon}}\hbar c^2}{V\omega_{k}}} \sum_j \left[\frac{\left\langle \phi_n|\mathbf{P}_j \cdot \hat{\epsilon}_{\mathbf{k}_{\epsilon}} e^{i\mathbf{k}\cdot r_j}|\phi_m\right\rangle}{\epsilon_0 - \epsilon_m - \hbar\omega_{\mathbf{k}} + i\eta}\right] \tag{3.29}$$

The only difference is a sign change of photon quantum in the denominator and a commutation in the operators in the numerator. This is because the system emits a photon first for this situation, meaning for a non-zero matrix element the annihilation operator must act first. Again, the sum over states has been left out as we must first compute the last term before combining all 2nd-order terms.

iii. Spin-Magnetic Field Interaction Term

The second and final contribution to 2nd order perturbation theory for scattering of photons from electrons is the spin-magnetic field Hamiltonian term.

$$H_2^{(2)} = -\frac{e\hbar}{2mc} \sum_j \mathbf{s}_j \cdot [\nabla \times \mathbf{A}(\mathbf{r}_j)] \tag{3.30}$$

Referring back to Equation 3.3, we note that the curl operator only acts on the plane wave part of the vector potential. This gives three components for each term. The result can be written as

$$\nabla \times \mathbf{A}(\mathbf{r}_j) = \pm i\mathbf{q} \times \mathbf{A}(\mathbf{r}_j)$$

depending on the direction of the plane wave. This part of the interaction Hamiltonian also has a term for each Feynman diagram, where each term consists of two separate matrix elements. Except for a negative sign and a factor of $\hbar$, the constant terms are the same as for the term that couples the photon to the electron momentum, calculated previously. Although there is vectorial difference, there is not an operative difference in this term. Meaning, that the dot product with the spin of each electron, and factors $i\hbar$ serve to change the magnitude of this amplitude with respect to the previous, and the curl of course changes the polarization dependence, but the structure of the operator is unchanged. So as discussed before, the single factor of the field operator will produce factors of $N_{\mathbf{k}\epsilon}$ when acting on the same states, with the same possible two time-reversed configurations of Feynman diagrams. The result contains terms that go as

$$\pm \mathbf{k} \times \hat{\epsilon}_{\mathbf{k}\epsilon}^*$$

or its complex conjugate. For instance, if we take the first diagram for this term for absorption of the photon by the system followed by emission of a different photon, remembering factors of $\hbar$ to keep consistent units, we can write this term $\left\langle H_2^{(2)}(f1) \right\rangle$ as:

$$-i\hbar C_{\mathbf{k}\mathbf{k}'\epsilon\epsilon'} \sum_{i,j,m} \left[\frac{\left\langle \phi_n | \mathbf{s}_i \cdot (-\mathbf{k}' \times \hat{\epsilon}_{\mathbf{k}'\epsilon'}^*) e^{-i\mathbf{k}' \cdot r_i} | \phi_m \right\rangle \left\langle \phi_m | \mathbf{s}_j \cdot (\mathbf{k} \times \hat{\epsilon}_{\mathbf{k}\epsilon}) e^{i\mathbf{k} \cdot r_j} | \phi_0 \right\rangle}{\epsilon_0 - \epsilon_m - \hbar\omega_{\mathbf{k}} + i\eta} \right]$$

where the subscript represents the second term of $H^{(2)}$ and the index $f1$ which Feynman diagram. We must make sure to keep track of the signs from the

positive and negative frequencies of the plane waves, and the constant $C_{\mathbf{kk}'\epsilon\epsilon'}$ is the same constant outside the summation from Equations 3.28 and 3.29, to allow us to keep track of differences in the constants.

However, as noted previously, this expression is not precise because we must take all terms of the Hamiltonian that contribute to 2nd order in this calculation. In other words, the full second order Hamiltonian equals the sum of the 2nd and 3rd terms from Equation 3.3, or the sum of both 2nd order terms

$$H^{(2)} = H^{(2)}_1 + H^{(2)}_2$$

The first Feynman diagram should include the full set of terms for each matrix element. The result is $\left\langle H^{(2)}(f1) \right\rangle$ equal to:

$$C_{\mathbf{kk}'\epsilon\epsilon'} \sum_{i,j,m} \left[\frac{\left\langle \phi_n | H^{(2)}_{1b}(f1) - i\hbar\, H^{(2)}_{2b}(f1) | \phi_m \right\rangle \left\langle \phi_m | H^{(2)}_{1a}(f1) - i\hbar\, H^{(2)}_{2a}(f1) | \phi_0 \right\rangle}{\epsilon_0 - \epsilon_m - \hbar\omega_{\mathbf{k}} + i\eta} \right]$$

with the second one the same accept for including the $f2$ terms instead of $f1$. It is worthy to note that closure can not be used here, as may be invoked naively since

$$\sum_n |\phi_n\rangle \langle\phi_n| = 1$$

because the sum over the intermediate states includes the energy state ϵ_n in the denominator: we will return to this shortly when approximations are instituted at the conclusion of the chapter.

5. Full Interaction Hamiltonian

The full expression then, including the two first-order terms as well as the sum over electron states over the two second-order terms, for both Feynman diagrams is finally:

$$\langle f|H'|i\rangle = \frac{2\pi\hbar e^2}{Vm} \frac{N_{q\alpha}}{\omega_q} \left\langle f \left| \sum_j (\hat{\epsilon}^*_{\mathbf{q}\alpha} \cdot \hat{\epsilon}_{\mathbf{q}'\alpha'}) e^{-i(q-q')\cdot r_j} \right| i \right\rangle$$

$$+ \frac{2\pi\hbar e^2}{Vm} \frac{N_{q\alpha}}{\omega_q} \frac{(-i\hbar\omega_k)}{mc^2} \left\langle f \left| \sum_j (\hat{\epsilon}^*_{\mathbf{q}\alpha} \times \hat{\epsilon}_{\mathbf{q}'\alpha'}) \cdot \mathbf{s}_j e^{-i(q-q')\cdot r_j} \right| i \right\rangle$$

$$+ C_{\mathbf{kk'}_{\epsilon\epsilon'}} \sum_{m,i,j} [A(\epsilon, \epsilon^*, k, k', \omega_k) + B(\epsilon, \epsilon^*, k, k', \omega_{k'})]$$

where $A(\epsilon, \epsilon^*, k, k', \omega_k)$ and $B(\epsilon, \epsilon^*, k, k', \omega_{k'})$ are given by

$$A(\epsilon, \epsilon^*, k, k', \omega_k) = \left[\frac{\left\langle \phi_n \left| \left[\mathbf{P}_i \cdot \hat{\epsilon}^*_{\mathbf{k'}_{\epsilon'}} - i\hbar \mathbf{s}_i \cdot (-\mathbf{k'} \times \hat{\epsilon}^*_{\mathbf{k'}_{\epsilon'}}) \right] e^{-i\mathbf{k'} \cdot r_i} \right| \phi_m \right\rangle \left\langle \phi_m \left| \mathbf{P}_j \cdot \hat{\epsilon}_{\mathbf{k}_\epsilon} - i\hbar \mathbf{s}_j \cdot (\mathbf{k} \times \hat{\epsilon}_{\mathbf{k}_\epsilon}) e^{i\mathbf{k} \cdot r_j} \right| \phi_0 \right\rangle}{\epsilon_0 - \epsilon_m - \hbar\omega_{\mathbf{k}} + i\eta} \right] \quad (3.31)$$

$$B(\epsilon, \epsilon^*, k, k', \omega_{k'}) = \left[\frac{\left\langle \phi_n \left| \mathbf{P}_j \cdot \hat{\epsilon}_{\mathbf{k}_\epsilon} - i\hbar \mathbf{s}_j \cdot (\mathbf{k} \times \hat{\epsilon}_{\mathbf{k}_\epsilon}) e^{i\mathbf{k} \cdot r_j} \right| \phi_m \right\rangle \left\langle \phi_m \left| \mathbf{P}_i \cdot \hat{\epsilon}^*_{\mathbf{k'}_{\epsilon'}} - i\hbar \mathbf{s}_i \cdot (-\mathbf{k'} \times \hat{\epsilon}^*_{\mathbf{k'}_{\epsilon'}}) e^{-i\mathbf{k'} \cdot r_i} \right| \phi_0 \right\rangle}{\epsilon_0 - \epsilon_m + \hbar\omega_{\mathbf{k'}} + i\eta} \right] \quad (3.32)$$

Just to reiterate: each term for 2nd order are added together, for each Hamiltonian in the full expression. There is one sum for each process in each of the Feynman diagrams. This expression is the main result of this chapter. It represents the full quantum mechanical matrix element for perturbation theory up to 2nd order. There is both a charge and spin dependence in the first two non-resonant terms, while the second two include both orbital and spin dependencies as well as the energy dependence seen in the denominator. The majority of current techniques that involve using some form of electromagnetic radiation to probe any type of media can be traced to this equation. We will discuss which terms become important in different limits in the next section.

Lastly, it should be noted that there is one final step to calculate the total cross-section: the actual quantity measured in experiments. This is done by first calculating the transition rate, which goes as the square of this matrix element. This is given by Fermi's golden rule [81]:

$$w_{i \to f} = \int dE_f \, \rho(E_f) \, \delta(E_f - E_i) \left(\frac{2\pi}{\hbar} \right) |H_{fi}|^2$$

where the integral is over the final energy state E_f and $\rho(E_f)$ is the density of states. This is over all terms of the full matrix element, where we have only

calculated up to 2nd order above, and will just take that as the full expression here. Higher order terms are negligible in all but a few special cases. Once the transition rate is attained, the cross-section can be computed. This is simply a relation between the differential cross-section and the transition rate:

$$\frac{\partial^2 \sigma}{\partial E \partial \Omega} = \frac{w * \rho(E_F)}{I_0}$$

where $\rho(E_F)$ is the density of states at the Fermi energy and I_0 is the incident flux. The total cross-section can then be derived from the matrix element calculated earlier.

6.   Approximations

To conclude, the full interaction Hamiltonian to 2nd order for the photon-electron interaction includes four main terms: two non-resonant, from 1st order theory, and two resonant, from 2nd order.

i.   Non-resonant Scattering

Away from resonance, the two resonant terms go like

$$\sim \frac{\hbar \omega}{mc^2}$$

or the square of this actually for the cross-section. At mentioned previously at soft x-ray energies, these terms are smaller by a factor of 10^{-6}. In this regime, only the first two terms give a non-negligible contribution to the scattering cross-section.

Thompson Scattering

Most well-known is the first term, as mentioned earlier, which is known to magnetic or resonant x-ray scientists as 'charge' scattering. This is the only term in the simplest 'kinematical' theory of x-ray scattering, referred to as Thompson scattering, and is due to the interaction of the photon field with electronic charge. This Thompson term is what gives rise to the more special case of Bragg scattering, when the states giving rise to the scattering have the necessary periodicity. Quantitatively, for incident photon energies far from the resonance energy of the system, and no magnetization density, these are the only terms left:

$$|\langle f\,|H'|\,i\rangle|^2 = \left[\frac{2\pi\hbar e^2}{Vm}\frac{N_{q\alpha}}{\omega_q}\right]^2 \left|\left\langle f\left|\sum_j(\hat{\epsilon}^*_{\mathbf{q}\alpha}\cdot\hat{\epsilon}_{\mathbf{q}'\alpha'})e^{-i(q-q')\cdot r_j}\right|i\right\rangle\right|^2$$

In fact, in most cases, even with a large magnetization density **S**, this will approximate the total cross-section for the same reason that we can neglect the resonant terms: the prefactor of photon energy over electron rest mass energy is small. Of order 0.1% in the soft x-ray regime. For this statement, we have assumed linear polarization as well. Because this condition usually holds, this is the reason scattering is commonly referred to in textbooks as 'the Fourier transform of the charge density'.

Magnetic Scattering

There are three clever ways to measure purely magnetic scattering. The first is simply due to geometry. When the spin-density has a different periodicity, magnetic scattering intensity can arise from points where the Bragg peaks are forbidden by the space group symmetry. For instance, in an anti-ferromagnetic or magnetic helical structure, where the periodicity is different then the Bragg scattering, enhancements will arise at forbidden reflections solely due to the $\mathbf{s}\cdot(\epsilon^*\times\epsilon)$ term. Only with the advent of high intensity synchrotron sources has the study of magnetism been possible with x-ray scattering.

The second way to measure magnetic scattering is through dichroism. This is done through complex polarization, or the lesser known condition of non-centrosymmetry. If we again neglect the resonant terms, the total cross-section only consists of the first two terms $H_1^{(1)}$ and $H_2^{(1)}$. If we have circular or elliptically polarized light, the cross term between these charge and magnetic amplitude terms will instead be real and can not be ignored in comparison to the charge term. This is simply due to the fact that we are taking the magnitude of a complex object and the inclusion of a complex polarization will give both real and sizable interference between charge and magnetic scattering. In this situation, magnetic signal can be significant, and is the reason circular dichroism has been so successful in recent years. There is a linear dichroic term, but it is significantly reduced compared to the circular dichroic term for the reasons mentioned above.

The third is by application of a magnetic field. Since the scattering amplitude depends on the polarization-spin relationship, a magnetic field can be

used to differentiate magnetic scattering from Thompson. For instance, with a ferromagnet where the magnetic structure is the same as that of the crystal, a field can be applied to saturate the magnetization density, and this charge contribution can be subtracted to retrieve the pure magnetic scattering.

ii. *The Born Approximation*

To approximate another case of scattering, we can take the energy to be elastic, and much larger than the excitations relevant to the solid: $\hbar\omega_k \sim \hbar\omega_k >> \epsilon_0 - \epsilon_m$. This is one of ranges of validity for the Born approximation and in this case, the two resonant terms reduce to a single commutator:

$$\left[\left\{\mathbf{P}_j \cdot \hat{\epsilon}^*_{\mathbf{k}'\epsilon'} - i\hbar\mathbf{s}_j \cdot (-\mathbf{k}' \times \hat{\epsilon}^*_{\mathbf{k}'\epsilon'})\right\} e^{-i\mathbf{k}'\cdot r_j}, \left\{\mathbf{P}_i \cdot \hat{\epsilon}_{\mathbf{k}\epsilon} - i\hbar\mathbf{s}_i \cdot (\mathbf{k} \times \hat{\epsilon}_{\mathbf{k}\epsilon})\right\} e^{i\mathbf{k}\cdot r_i}\right]$$

which is summed over i and j with a factor of $-\dfrac{C_{\mathbf{k}\mathbf{k}'\epsilon\epsilon'}}{\hbar\omega_k}$ out front.

This is due to the fact that since the photon energy is much greater than the difference in electron energy states, the intermediate states become negligible, and we can use the closure identity, or completeness relation, to remove the sum over the $|\phi_m\rangle$-states. This can be reduced to four separate commutators through the distributive property of commutators.

1st commutator

The first of the four terms is:

$$-\frac{C_{\mathbf{k}\mathbf{k}'\epsilon\epsilon'}}{\hbar\omega_k} \sum_{i,j} \left[\mathbf{P}_j \cdot \hat{\epsilon}^*_{\mathbf{k}'\epsilon'} e^{-i\mathbf{k}'\cdot r_j}, \mathbf{P}_i \cdot \hat{\epsilon}_{\mathbf{k}\epsilon} e^{i\mathbf{k}\cdot r_i}\right]$$

or ignoring the factors out in front of the summation and acting the momentum operator on the plane wave state:

$$\sum_j e^{i(\mathbf{k}-\mathbf{k}')\cdot r_j} \left\{[(\mathbf{k} - \mathbf{k}') \cdot \hat{\epsilon}^*_{\mathbf{k}'\epsilon'}](\mathbf{P}_i \cdot \hat{\epsilon}_{\mathbf{k}\epsilon}) - [(\mathbf{k} - \mathbf{k}') \cdot \hat{\epsilon}_{\mathbf{k}\epsilon}](\mathbf{P}_j \cdot \hat{\epsilon}^*_{\mathbf{k}'\epsilon'})\right\}$$

We will denote the sum $\mathbf{k} - \mathbf{k}'$ by $\mathbf{K}$, which not only simplifies, but will let us use some vector identities. The result is

$$\sum_j e^{i\mathbf{K}\cdot r_j} \left\{[\mathbf{K} \cdot \hat{\epsilon}^*_{\mathbf{k}'\epsilon'}](\mathbf{P}_j \cdot \hat{\epsilon}_{\mathbf{k}\epsilon}) - [\mathbf{K} \cdot \hat{\epsilon}_{\mathbf{k}\epsilon}](\mathbf{P}_j \cdot \hat{\epsilon}^*_{\mathbf{k}'\epsilon'})\right\}$$

Since this is the difference between two sets of dot products, we can use the vector identity $(A \times B) \cdot (C \times D) = (A \cdot C)(B \cdot D) - (A \cdot D)(B \cdot C)$, giving

$$(\mathbf{K} \times \mathbf{P}_j) \cdot (\hat{\epsilon}^*_{\mathbf{k}'_{\epsilon'}} \times \hat{\epsilon}_{\mathbf{k}_\epsilon})$$

or keeping track of the constants for this term, the final result is:

$$-\frac{C_{\mathbf{k}\mathbf{k}'_{\epsilon\epsilon'}}}{\hbar\omega_k} \sum_j e^{i\mathbf{K}\cdot r_j} (\mathbf{K} \times \mathbf{P}_j) \cdot (\hat{\epsilon}^*_{\mathbf{k}'_{\epsilon'}} \times \hat{\epsilon}_{\mathbf{k}_\epsilon})$$

2nd and 3rd commutators

Again if we ignore the overall constant in front of the total commutator, we have for the 2nd term:

$$\sum_{i,j} [-i\hbar\mathbf{s}_j \cdot (-\mathbf{k}' \times \hat{\epsilon}^*_{\mathbf{k}'_{\epsilon'}}) e^{-i\mathbf{k}'\cdot r_j}, \mathbf{P}_i \cdot \hat{\epsilon}_{\mathbf{k}_\epsilon} e^{i\mathbf{k}\cdot r_i}] \tag{3.33}$$

or

$$-i\hbar \sum_j e^{i(\mathbf{k}-\mathbf{k}')\cdot r_j} \mathbf{s}_j \cdot (-\mathbf{k}' \times \hat{\epsilon}^*_{\mathbf{k}'_{\epsilon'}}) \left\{ (\hat{\epsilon}_{\mathbf{k}_\epsilon} \cdot \mathbf{k}) - \hat{\epsilon}_{\mathbf{k}_\epsilon} \cdot (\mathbf{k} - \mathbf{k}') \right\} \tag{3.34}$$

This can be reduced considerably due to the orthogonality of electromagnetic waves. The dot product of wavevector $\mathbf{k}$ and polarization vector $\hat{\epsilon}_{\mathbf{k}_\epsilon}$ is always zero and just comes from Maxwell's equations. Note that this is only true when the momentum index matches the wavevector. This rule changes the last two terms:

$$-i\hbar \sum_j e^{i\mathbf{K}\cdot r_j} \mathbf{s}_j \cdot (-\mathbf{k}' \times \hat{\epsilon}^*_{\mathbf{k}'_{\epsilon'}})(\hat{\epsilon}_{\mathbf{k}_\epsilon} \cdot \mathbf{k}') \tag{3.35}$$

The third commutator is very similar to the 2nd, and we will just write the answer as

$$-i\hbar \sum_j e^{i\mathbf{K}\cdot r_j} \mathbf{s}_j \cdot (\mathbf{k} \times \hat{\epsilon}_{\mathbf{k}_\epsilon})(\hat{\epsilon}^*_{\mathbf{k}'_{\epsilon'}} \cdot \mathbf{k}) \tag{3.36}$$

4th commutator

The last commutator comes from the spin-spin term.

$$-\hbar^2 \sum_{i,j} e^{i(\mathbf{k}-\mathbf{k}')\cdot r_j} \left[\mathbf{s}_j \cdot (-\mathbf{k}' \times \hat{\epsilon}^*_{\mathbf{k}'_{\epsilon'}}), \mathbf{s}_i \cdot (\mathbf{k} \times \hat{\epsilon}_{\mathbf{k}_\epsilon}) \right] \tag{3.37}$$

or we can write this as

$$-\hbar^2 \sum_i e^{i\mathbf{K}\cdot r_j}(-i\hbar\mathbf{s}_i)[(-\mathbf{k}' \times \hat{\epsilon}^*_{\mathbf{k}'_{\epsilon'}}) \times (\mathbf{k} \times \hat{\epsilon}_{\mathbf{k}_\epsilon})] \tag{3.38}$$

using the spin commutation relations $[\mathbf{S}_i, \mathbf{S}_j] = \epsilon_{ijk}\mathbf{S}_k$.

Complete Result

The total commutator of the four terms above is finally given as

$$-\frac{C_{\mathbf{k}\mathbf{k}'_{\epsilon\epsilon'}}}{\hbar\omega_k} \left[\sum_j e^{i\mathbf{K}\cdot r_j}(\mathbf{K} \times \mathbf{P}_j) \cdot (\hat{\epsilon}^*_{\mathbf{k}'_{\epsilon'}} \times \hat{\epsilon}_{\mathbf{k}_\epsilon}) \right. \tag{3.39}$$

$$-i\hbar \sum_j e^{i\mathbf{K}\cdot r_j}\mathbf{s}_j \cdot (-\mathbf{k}' \times \hat{\epsilon}^*_{\mathbf{k}'_{\epsilon'}})(\hat{\epsilon}_{\mathbf{k}_\epsilon} \cdot \mathbf{k}') \tag{3.40}$$

$$-i\hbar \sum_j e^{i\mathbf{K}\cdot r_j}\mathbf{s}_j \cdot (\mathbf{k} \times \hat{\epsilon}_{\mathbf{k}_\epsilon})(\hat{\epsilon}^*_{\mathbf{k}'_{\epsilon'}} \cdot \mathbf{k}) \tag{3.41}$$

$$+i\hbar^3 \sum_i e^{i\mathbf{K}\cdot r_j}\mathbf{s}_i \cdot [(-\mathbf{k}' \times \hat{\epsilon}^*_{\mathbf{k}'_{\epsilon'}}) \times (\mathbf{k} \times \hat{\epsilon}_{\mathbf{k}_\epsilon})]$$

$$\tag{3.42}$$

or simply as

$$i\frac{C_{\mathbf{k}\mathbf{k}'_{\epsilon\epsilon'}}}{\omega_k} \sum_j \left[e^{i\mathbf{K}\cdot r_j}(\mathbf{K} \times \mathbf{P}_j) \cdot (\hat{\epsilon}^*_{\mathbf{k}'_{\epsilon'}} \times \hat{\epsilon}_{\mathbf{k}_\epsilon}) + \mathbf{s}_j \cdot \left[(\mathbf{k}' \times \hat{\epsilon}^*_{\mathbf{k}'_{\epsilon'}})(\hat{\epsilon}_{\mathbf{k}_\epsilon} \cdot \mathbf{k}') \right. \right. \tag{3.43}$$

$$\left. \left. -(\mathbf{k} \times \hat{\epsilon}_{\mathbf{k}_\epsilon})(\hat{\epsilon}^*_{\mathbf{k}'_{\epsilon'}} \cdot \mathbf{k}) - [(\mathbf{k}' \times \hat{\epsilon}^*_{\mathbf{k}'_{\epsilon'}}) \times (\mathbf{k} \times \hat{\epsilon}_{\mathbf{k}_\epsilon})]]] \right.$$

$$\tag{3.44}$$

` Collecting all terms, including the first two non-resonant terms, finally the full result for the amplitude is:

$$-C^2_{\mathbf{q}\mathbf{q}'\alpha\alpha'}\sum_{q\alpha}\frac{mN_{q\alpha}}{\omega_q}\sum_j(\hat{\epsilon}^*_{\mathbf{q}\alpha}\cdot\hat{\epsilon}_{\mathbf{q}'\alpha'})e^{-i(q-q')\cdot r_j} \tag{3.45}$$
$$+i\frac{C_{\mathbf{k}\mathbf{k}'\epsilon\epsilon'}}{\omega_k}\sum_j[e^{i\mathbf{K}\cdot r_j}(\mathbf{K}\times\mathbf{P}_j)\cdot\mathbf{B}+\mathbf{s}_j\cdot\mathbf{A}]$$

iii. Resonant Scattering

Finally, we will look at resonant scattering. This is when the photon energy matches the energy difference between electron energy levels. This is of course only possible in the second order terms where there can be a virtual excitation of an electron to a higher energy state followed by the emission of a photon upon the decay of the electron back to the same energy level. One point of contention is the terminology that we have avoided until now. We will briefly discuss the terminology for its relevance here, but it should be noted that later in this work the term 'coherent' refers to something much different. The discussion here is unique and should not be confused with the terminology in the rest of this dissertation.

Elastic scattering always refers to a zero transfer of energy to the system by the photons, or $|k| = |k'|$. This does not place any condition on the actual state of the system, but merely its energy. For the special case of the process described above, the term 'coherent amplitude' is used to describe the process where the state of the system returns to its original state. That is, in the notation we have been using $\langle f|A|i\rangle \to \langle i|A|i\rangle$ for amplitude A.

For the case of resonance $\hbar\omega \sim \epsilon_0 - \epsilon_m$ and only the 1st Feynman term contributes, and this term dominates all others.

$$\frac{-i}{\eta_m}C_{\mathbf{k}\mathbf{k}'\epsilon\epsilon'}\sum_{i,j}\left\langle\phi_n\left|\left[\mathbf{P}_i\cdot\hat{\epsilon}^*_{\mathbf{k}'\epsilon'}-i\hbar\mathbf{s}_i\cdot(-\mathbf{k}'\times\hat{\epsilon}^*_{\mathbf{k}'\epsilon'})\right]e^{-i\mathbf{k}'\cdot r_i}\right|\phi_m\right\rangle \tag{3.46}$$
$$\left\langle\phi_m\left|\mathbf{P}_j\cdot\hat{\epsilon}_{\mathbf{k}\epsilon}-i\hbar\mathbf{s}_j\cdot(\mathbf{k}\times\hat{\epsilon}_{\mathbf{k}\epsilon})e^{i\mathbf{k}\cdot r_j}\right|\phi_0\right\rangle$$

where we have added the subscript to η notation to emphasize the dependence on the energy width of the states being summed over. The demonstrates that

for resonant scattering, the cross-section will depend specifically on the lifetime for the energy states involved in the process. Resonant scattering is a useful tool because it is inherently sensitive to local electronic structure. That is, for a site whose electron is excited to a higher lying energy state, the amplitude necessarily depends on the precise electronic structure surrounding the atom. Hence, its real power is in minute differences in the vicinity of the scattering site.

7. Orbital Scattering

One final comment is on orbital scattering. In the previous section, we derived the full cross-section for the photon-electron interaction quantum mechanically. From this we saw each term in the interaction Hamiltonian giving charge scattering, magnetic scattering, and two anomalous energy terms. Concerning the anomalous terms, it is usually commented on that the prefactors for spin and orbital magnetic scattering are different, and hence in experiments these can be separated using the different polarization dependence of the two different effects [83]. However, an important part of this work is based on orbital scattering that is different from the orbital scattering discussed up until this point. We will differentiate these by using the term 'orbital magnetic scattering' to refer to that described above: a dependence in the cross-section of the angular momentum of the electron state. 'Orbital scattering' will be applied to the measurement of intensity due to orbital ordering and will described by the following.

Suppose we have an array of electronic states that all share the same angular momentum state, for instance the $d_{3z^2-r^2}$ state. The phenomenon of orbital ordering is a configuration where the electron state can have the same orbital momentum state, but the spatial orientation alternates between sites. In other words, there is a modulation of the orientation of the spatial part of the wavefunction of the electron density. This of course does not go under orbital magnetic scattering because all the scattering sites in question contain the same quantum number l. It is more closely related to charge scattering, but charge scattering is usually not dependent on either the shape of the wavefunction or energy, to first order. Orbital scattering emerges in the resonant terms in the scattering cross-section we have derived, and for all practical purposes, can not be measured unless very close to an absorption edge. In fact, in our measurements we have shown that away from the absorption edge, this intensity from orbital ordering rapidly disappears. It is only with the increase in signal that

occurs from the resonant enhancement that these types of experiments are even possible.

The key point here is the relationship between the orientation of the orbital and the polarization of the photon. To access orbital scattering from a modulation of electron wavefunctions, the sites must differ from each other in scattering amplitude. This is what separates it from scattering due to charge ordering. More precisely, it depends on the difference of the inner products between the polarization and the orientation of the orbital at each site [84], or:

$$\sim [(\epsilon_f^* \cdot \hat{a})(\epsilon_i \cdot \hat{a}) - (\epsilon_f^* \cdot \hat{b})(\epsilon_i \cdot \hat{b})]$$

where the $\hat{a}$ and $\hat{b}$ are the vectors describing the orientation of the orbital for two neighboring sites with different orbital orientations.

Since this contribution is only evident from 2nd order perturbation theory, there must be empty orbitals available of the correct energy level for the electrons to conduct virtual excitations into. So the modulation of charge distribution must be accompanied by partially filled electron shells in the intermediate energy levels that match the photon energy. For instance in dipole exchange scattering, if the d-shell had 5 spin-up electrons, the polarization that excites p-shell spin up electrons into the d-states would have a null amplitude. In this way, orbital scattering more aptly describes the empty electronic states around the scattering site, rather than the filled electronic orbitals themselves. This fact is what allows for a direct study of the electronic structure of the resonating atoms. Note that this could also take place between a periodicity in the spatial part of the wavefunction between different l-functions, but both types of orbital scattering mentioned in this section must be taken into account for that case.

CHAPTER IV

SPECKLE AND COHERENCE

In this chapter, we discuss coherent scattering and the resultant phenomenon that becomes the basic mode of study for the experiments described in this thesis: speckle patterns. After a short history and description of speckle, we discuss a general, now famous, experiment first completed by a British physician in the early 1800s. We point out the two main proponents of speckle pattern formulation: coherence and disorder. We continue with a discussion of the structure of speckle, though we leave the detailed analysis for the next chapter. The chapter concludes with some work on contrast, an essential tool for describing these types of diffraction events. The historical material is largely taken from the classic work by Dainty [85] and more recently, work by Goodman [86].

1. History

A speckle pattern is named after its most notable characteristic: a grainy, or 'speckled' structure produced by a large intensity variation. Any type of light, radiation, or stream of particles that contains a large degree of coherence will in theory be able to produce a speckle pattern if the medium being illuminated has a high enough degree of disorder. There are certain limits where this is true, but in general, when scattered coherent waves are able to interfere with each other, the possibility exists to form a speckle pattern.

The speckle phenomenon is typically credited [85] to have been first observed by Sir Isaac Newton described in his writings from 1675 [87]. Though this is not fully true, he did notice that 'the Air through which we look upon the Stars, is in a perpetual Tremor; as may be seen by the tremulous Motion on of Shadows caft from high Towers, and by the twinkling of the fix'd Stars.' [87]. Thus, he accredited the twinkling of the stars to the 'Tremors of the Atmosphere' [87]

over 400 years ago. When the light from stars propagates to some observer on earth, the atmosphere it transverses contains many index of refraction density variations. Since stars are so far away, they appear as point sources. This is notably different than planets which have a finite size, and hence, do not twinkle. The starlight then is highly coherent to the observer on earth and interference between resultant waves that are being detected by the human eye will fluctuate, and cause a twinkling phenomenon. Two necessary facts make the twinkling phenomena possible: the coherence of the source, and the density fluctuations, or disorder, of the atmosphere. So although he did not in fact observe a speckle pattern, or anything similar to a speckle pattern even, it is true that by stating the reason for the twinkling of the stars, Newton was the first to theorize on how speckle patterns might be formed. Even today, the twinkling of the stars is used as an illustration of the speckle phenomenon [85].

From Newton to the 1960s, when lasers became available, there are few examples on the thinking of, or study of speckle. Most notable are brief observations by Exner in 1877 [88, 89], von Laue in 1914 [90, 91, 92], and de Haas in 1918 [93]. Most impressive is the work by von Laue, who gave an almost complete description of speckle statistics including the autocorrelation function and probability density function.

i. Laser Speckle

After the the first commercial, continuous gas-laser was introduced, two independent groups [94] and [95] conducted laser speckle experiments in late 1962. It was noticed that shining a laser on a matte screen resulted in the same random grainy structure. The hypothesis suggested at this early stage was the following: highly coherent light reflected from some diffusing surface produces a complex and random, but stationary granular pattern [95]. To produce the necessary interference, the diffusing object must randomize the incident wavefront in phase, polarization, or both [95]. Oliver's statement in the 1962 paper was a correct explanation and is still used to this day. One reason this was not noted previously is that for the first time, lasers brought a large degree of coherence and made speckle experiments much easier to perform. Previous experiments has to fabricate some degree of coherence, usually by forming a virtual source by implementing an aperture for instance. The second attribute of lasers that made the discovery of speckle possible was the enormous increase in coherent flux. Because of these two features available with lasers, a series of

experiments occurred soon after, followed by a flurry of excitement in studying and measuring properties of speckle patterns.

The discover (or re-discovery) of the speckle phenomenon had such a large surge of excitement by workers in the field of lasers, a seminal book that reviewed the most interesting topics in the field was published in 1975 [85]. At this point in time, the main interest existed in basic statistical properties for partially and fully coherent light, speckle reduction and information processing, and applications.

The study of laser speckle has expanded outside the optical regime and grown to unprecedented heights. The application today is so vast, that an overview is not possible here. The field stretches from microwave and radar applications in ultrasound imaging in medicine to stellar speckle interferometry. As recently as a few months ago, new work has been conducted in astronomy by measuring radar speckle to measure the motion of the planet Mercury [96]. On the order of 1 km-size speckles were detected at the surface of the earth in a back scattering geometry by reflected coherent microwave radiation from the surface of the planet [96]. Since the speckle structure gives information about a specific region of the surface, scientists were able to measure the rotation of the planet by following the speckle motion across the surface of the earth, and hence make predictions about the composition of its molten core [96].

2.   Coherence

The coherence, separated into both longitudinal and transverse components, is a measure of how well the waves are in phase with each other. The best example of this is given by Atwood [97] in a analog to marching soldiers. If one imagines a large group of soldiers marching precisely in step with one another, where one person in the middle is responsible for calling out the directives. The soldiers on the outskirts of the group will hear the counts at a slight delay time, and hence be behind in their steps. One can even imagine a large enough group that the outer soldiers are too far to hear any audibles, and they are left trying to keep up by watching their neighbor. The length from the director to the soldier who is out of step would define the correlation length of the soldiers. As is the case with synchrotron radiation, coherence lengths of x-rays are never isotropic. In this, we can push the analog further in imagining a wind where some direction of the soldiers will hear to a much greater distance then in the direction perpendicular to the wind direction.

Thinking of photon fields traveling in waves, as the soldiers are stepping in sync with each other, we can define two directions of coherence of light. Longitudinal will refer to the direction of beam travel, while transverse will be the plane orthogonal to the wavevector.

For photons traveling in the same direction, the longitudinal coherence is a measure of how well the waves are in phase with each other in the direction of propagation, defining the extent to be when one wave become exactly π out of phase with another. Up to factors of 2π, we can derive this equation using a back-of-the-envelope calculation [97].

Given the longitudinal or temporal coherence length $\xi_l^{(1)}$ of the first wave to be $N\lambda$ for N full, periodic oscillations, we can write a second wave coherence length to be

$$\xi_l^{(2)} = (N - \frac{1}{2})(\lambda + \delta\lambda) \tag{4.1}$$

for a spectrally shifted wave covering the same distance. The $\delta\lambda$ represents the maximum bandwidth difference between the two waves, and the $N - \frac{1}{2}$ is how we have chosen to define where the wave becomes completely uncorrelated. A half-period of N being exactly shifted in phase by π.

Equating $\xi_l^{(1)}$ and $\xi_l^{(2)}$ we get

$$\lambda = \delta\lambda(2N - 1) \tag{4.2}$$

Now we solve for N and multiply by a factor of λ (remembering that $\lambda >> \delta\lambda$) to finally retrieve an expression for ξ_l

$$\xi_l = \frac{\lambda^2}{(\delta\lambda)} \tag{4.3}$$

describing the length where wavelengths of continuous bandwidth $\delta\lambda$ become substantially dephased. Longitudinal coherence then is directly related to how monochromatic the source is. This value is usually not a limiting factor in our experiments. Because of the long wavelength of soft x-rays (compared to high energy x-rays), the extinction lengths are usually fairly short, on the order of hundreds of nanometers. So even for backscattering, typical longitudinal coherence lengths from our moderate energy resolution monochromator ($\frac{\delta\lambda}{\lambda} = 0.2\%$) are a couple thousand nanometers.

If we take a plane orthogonal to the wavevector at some point along the direction of travel of light, the degree of how well the waves are in phase with

each other spatially in this plane defines the transverse coherence. Figure 4.1 shows the spatial correlation plane for some point along the **k**-vector. This value is a measure of how well the field is correlated across the wavefront.

Spatial coherence also has a simple intuitive picture based on Heisenberg's uncertainty principle [97]

$$\delta x \delta p \geq \frac{\hbar}{2} \tag{4.4}$$

For photons, $p = \hbar k$ where $|k| = 2\pi/\lambda$. Taking derivatives,

$$\delta k = -\delta \lambda \frac{2\pi}{\lambda^2} \tag{4.5}$$

Thus, $\delta k/k = |(\delta\lambda)/\lambda|$. For small bandwidth then, the momentum uncertainty translates to an uncertainty in angle. For small angles we can approximate this as

$$\delta x \delta p = \hbar(\delta k) = \hbar(\frac{2\pi}{\lambda})\delta\theta \geq \frac{\hbar}{2} \tag{4.6}$$

or for source $d = \delta x$, we get the 'diffraction-limited' equation

$$d * \theta = \frac{\lambda}{4\pi} \tag{4.7}$$

To calculate the spatial coherence length at some observation point R from the source, we simply get

$$\xi_t = \frac{\lambda R}{4\pi d} \tag{4.8}$$

Spatial coherence is a crucial component in our experiments. Any structure studied in an experiment must be carefully matched to the level of spatial coherence in a given study. Without the containment of the necessary structure within the coherence length of the wavefront, the scattered radiation from different points within the coherence volume of the sample will not interfere. All scattered radiation will add incoherently, and no interference will be observed.

If we define a coherence length of the system as the distance in real space where some type of correlation exists between scattering centers in the sample, the we can state the above assumption that the transverse coherence length much be much greater than the coherence length of the system as

$$\xi_{photon} > \xi_{system}$$

This relationship will change when we discuss statistics, but for the discussion here, it ensures that each scattering center within the coherence length will
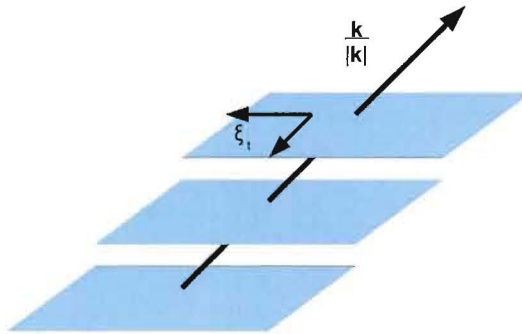
Fig. 4.1: **Spatial Correlation Planes**. Planes represent wavefronts orthogonal to photon propagation direction. Temporal coherence is a measure of correlated wavefields in the direction of wavevector **k**, while spatial coherence is related to how well correlations persist in the plane transverse to the wavevector. The planes shown here represent infinitesimal surface elements of a large spherical wave centered at the source.

scatter wave amplitudes with some finite probability to interfere. As the coherence length becomes smaller, on the order of the coherence length of the sample structure, or the length scale of the disorder, the interference fringes will 'wash out'. This is the result in *incoherent* scattering, or more precisely, scattering with small coherence length x-ray beams.

3. Spatial Filtering

A few words on spatial filtering are in order, one way to control the transverse coherence length. The use of a spatial filter, or pinhole, is to select a small region of in the incoming wavefront. Wavefields of radiation emitted from this filter then have a precise phase relationship across the wavefront. For instance, in the limit where the pinhole becomes a point source, the spherical wave that propagates from the new 'virtual' point source will exhibit a large degree of coherence across the wavefront. By reducing the angular extent of the rays, the transverse coherence is increased due to the inverse relationship discussed in the previous section. This can be seen from Equation 4.8 by taking the source size d to be the pinhole size. In fact, any source can be made coherent with the use

of an appropriate spatial filter. In other words, no matter how incoherent the source is, by using a small enough pinhole, sizable transverse coherence can be achieved. The challenge as we will see later, is the cost in flux, a severe issue especially in the soft x-ray regime.

To visualize the effect of spatial along with temporal coherence, Figure 4.2 shows both attributes and the consequences of each on filtered light. This illustrates the two types of filtering and how the spatial relates to the wavefront properties and the temporal to the energy resolution. The figure emphasizes the importance of both spatial and temporal types of filtering.

4. Young's Double Slit Experiment

Any two waves that arrive at the same point after traveling over different optical pathways will introduce a phase shift into the propagation. This is a well-known phenomenon from elementary physics, where the example usually is described in the form of the double-slit experiment, first completed in 1804 by the English scientist Thomas Young in the debate on whether light was a particle or a wave [98]. We will briefly review the main idea of the experiment here.

In this experiment, a monochromatic point source is used at a far distance from an opaque screen which consists of two small slits. Because of the large source-screen distance, the waves which impinge on the screen are to a first approximation plane waves. As long as the slits are spaced smaller than the coherence length of the light, which is infinite for perfectly plane waves, the resulting waves emitted through the far side of the screen will interfere with each other. According to Huygens's wavelet theory, each emerging wave from the opaque screen will act as a new source for wavelet generation that propagate to a detector a large distance away compared to the spacing of the slits. Because the two new 'virtual' sources are being illuminated with a coherent wavefront, the interference between the two new waves interfere with each other, just as water waves would from two separate rocks being dropped close together in a pond.

According to this simple experiment, the exact equation can be used to predict how the waves would interfere with each other for a detector screen that is in the far-field. For path lengths r_1 and r_2, when d is $< \lambda$, this is given by

$$r_1 - r_2 = d\sin(\theta) = m\lambda \qquad (4.9)$$
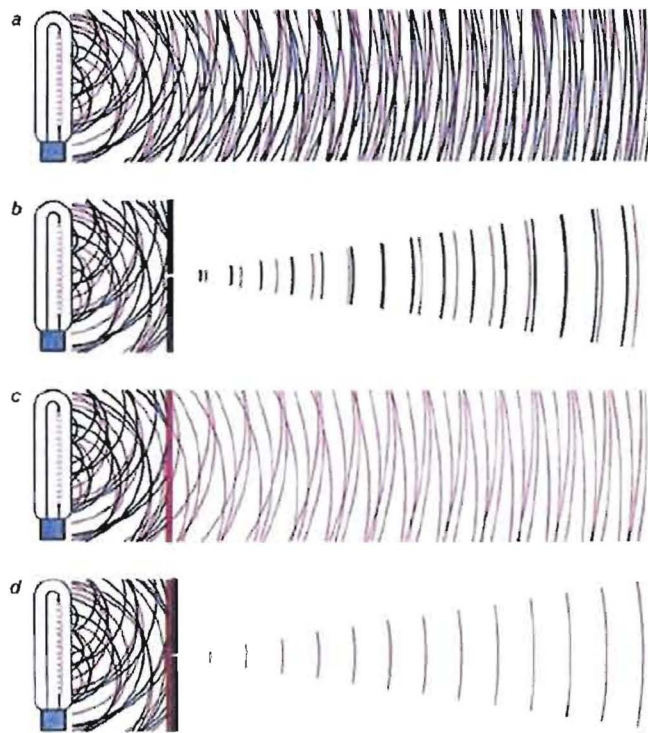
Fig. 4.2: **Spatial and Spectral Filtering**. (A) Unfiltered light. (B) Spatially, or transversely filtered light. A small portion of the wavefront it allowed through, but the bandwidth is quite large. (C) Spectrally filtered, or temporally filtered light. This is monochromatic light with a narrow bandpass, but many waves are present due to the incoherent nature of the source. It behaves as if there are many individual sources producing the same energy of photons. (D) Both spatially and spectrally filtered light [8].

for the wavelength of light λ, the spacing of the slits d, and the angle on the detector the light makes with the slit-detector distance, θ. This gives the degree of constructive and deconstructive interference. The detector screen shows a modulation of interference that goes like

$$I \sim \left[\frac{\sin(\xi_t)}{\xi_t}\right]^2$$

Young's two-slit experiment is usually used to describe the results of quantum mechanics, but at the time of the experiment, it served to change prevalent theory at the time, which was largely based on Newton's idea that light was corpuscular, and had not been challenged for the previous hundred years [98].

5. Disorder

What we are interested in however is the two dimensional generalization of the Young's two slit experiment. We can imagine a plane with a few random pinholes to represent two dimensional slits. The diffraction pattern of light scattered through an opaque screen is the simplest example of how to get strong, far-field interference scattering. Each speckle in the pattern represents the addition of all the wave amplitudes over all the scattering sources in the volume. In practice, this number N becomes large, the resultant speckle pattern takes a random looking characteristic, and indeed as we will see, we therefore must incorporate stochastic analysis to describe it.

The same idea of the random array of holes in a screen holds for reflections from disordered systems. Just as laser light has been used to study the roughness of surfaces, we can take advantage of the coherence properties of soft x-rays to study roughness of nm-scale structure. This provides a method to study surfaces through the Fourier transform of the height-height correlation function [99]. Fig.4.3 shows a speckle pattern generated by soft x-rays scattered in a low-angle, specular reflection geometry from a manganese-oxide thin film. Films of this sort are known to not only have surface roughness at this level, but also to have many length scales of heterogeneity in phase-separated regions, whether due to charge stripes as in cuprates, or mixed insulating and metallic phases in the colossal magnetoresistive manganites. Optically, this film has an extremely smooth surface. That is, by eye, the surface looks like a mirror. The scattering is charge-channel and is largely due to surface-only roughness. The coherent diffraction from the pinhole spatial filter is evident in the observation
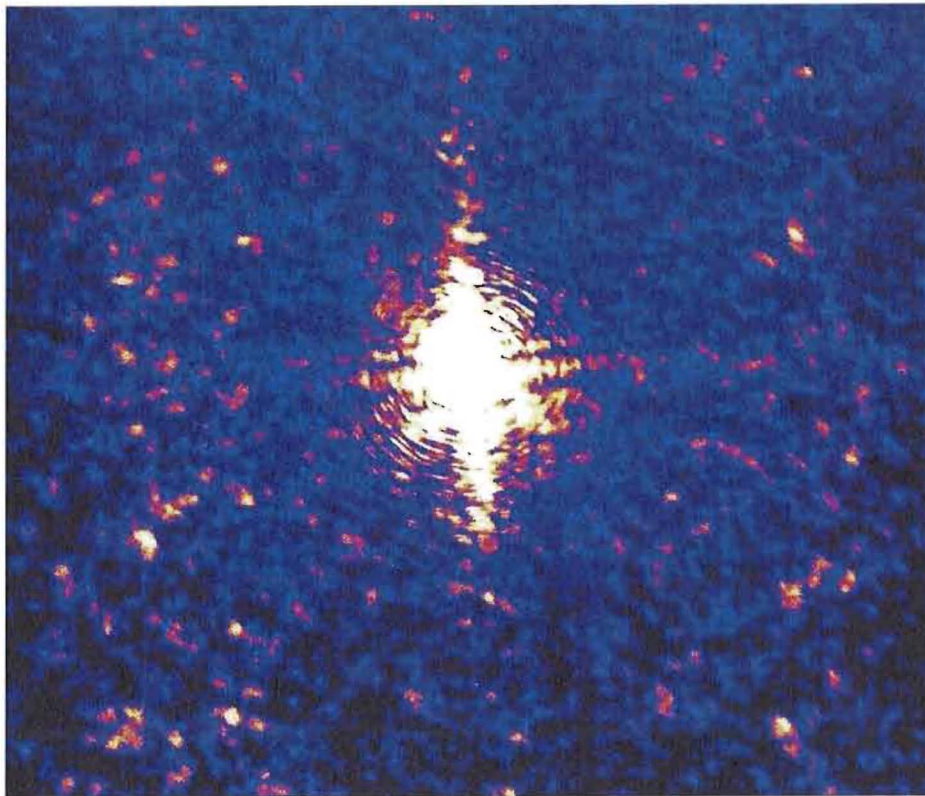
Fig. 4.3: **Charge Scattering from a Metal-Oxide Surface.** Speckle pattern formed from charge scattering due to surface roughness. The coherent diffraction from the pinhole spatial filter is evident in the observation of Airy fringes centered on the specular beam. The reflection just redirects the beam and images the far-field diffraction from a circular aperture. At higher values of momentum-transfer, the diffuse scattering is speckled, demonstrating a large degree of roughness on nm-scale wavelengths.

of Airy fringes around the peak. The specular component of the beam preserves its phase and the rings are similar to typical far-field diffraction patterns measured from a circular aperture. The diffuse scattering surrounding this region is heavily speckled, demonstrating a large degree of roughness on nm-scale wavelengths. If the sample approached a smooth surface with a roughness length scale much less than the soft x-ray wavelength, the film would act increasingly as a plane mirror for this energy of photons. In this case, the speckle would diminish and the specular component would be accompanied by true, concentric Airy rings.

Furthermore, there is a slight diffuse ring near the outer edge of the image. Since this is due solely to charge scattering in this instance, the ring is a measure of the average correlation length of surface RMS roughness. Typically, roughness is random, but in this case there seems to be some order in structure on the surface. We used an Atomic Force Microscope (AFM) to measure an ordering on the surface. Fig.4.4 shows an AFM image of the surface. We can see how the particles on the surface are rampant and could be due to the laser ablation growth process of the film itself [100].

Though these examples only involve surface roughness, as the structure at the surface is the only contributing factor to the structure factor, we can measure speckle pattern from any mechanism that has spatial fluctuations on the order of this wavelength. We will show later, this is true for many mechanisms and can vary from ferromagnetic domains in multilayers to orbital-ordering domains in transition-metal single crystals.

6. Speckle Structure

Figure 4.5 shows a scaled, zoomed-in image of Figure 4.3. The light and dark contrasting elements group together in regions dubbed 'speckle', where the region or size of the speckle is a function of x-ray energy, geometry of the experiment, and coherence length of x-rays that illuminate the sample. To be more precise, the equation for the average size of the speckle, or coherence areas, goes like

$$s \sim \frac{\lambda R}{\xi} \tag{4.10}$$

where s is the radius of the speckle, R is the distance from the sample to the detector, and ξ is the spatial coherence length of the beam at the sample. This is similar to the solution of the first zero in a Bessel function, except for

Fig. 4.4: **AFM Image of thin film surface.** The figure shows an Atomic Force Microscopic image of the surface responsible for the charge scattering in Fig. 4.3. The full frame is about 1.0 μm squared.
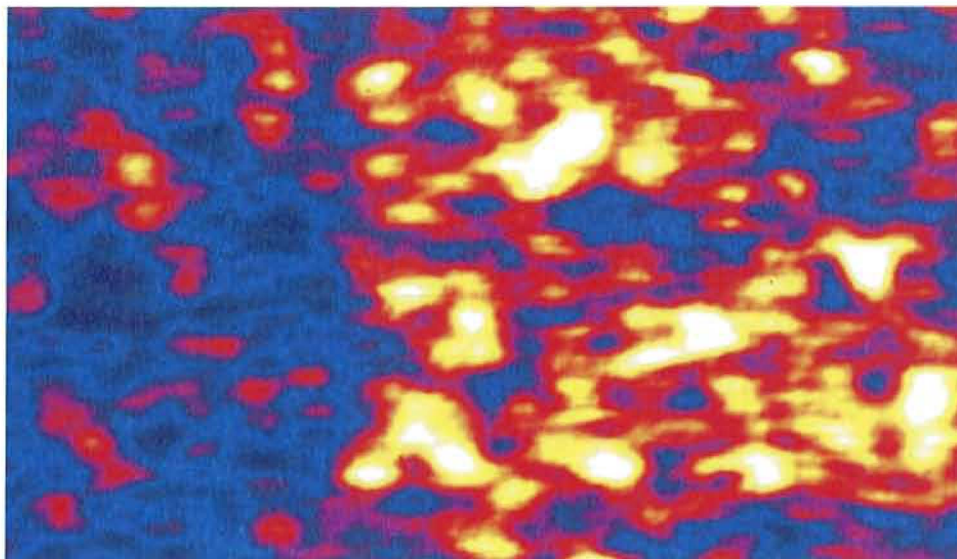
Fig. 4.5: **Speckle structure**. Close-up view of speckle pattern showing the large speckle size, give by equation 4.10. The size varies considerably over the region of the diffraction pattern as the equation is merely an estimate of the average speckle size for a given set of experimental parameters.

factors of 1.22. There is no need for precision of this level here since speckle is a random phenomenon. Because of this fact, we are only able to define parameters statistically to begin with. In fact the size of each individual speckle will vary considerable, and only through the autocorrelation function, can we extract an *average* coherence area size. We will discuss the autocorrelation measure of the average speckle width later in the next chapter, but here we just note the approximation in equation 4.10 for making an estimation of the speckle size which becomes important in detector and beamline design.

One other thing to note in equation 4.10 is the linear dependence on λ. In the last 15 years, with the onset of interest in speckle starting with laser studies, x-rays have become a popular method of speckle generation. However, a brief search through the literature will confirm that while although x-rays are important for the study of small-scale structure, the speckle size in general is much smaller. This can be seen in the most recent reports such as [101]. The issues that are raised where speckle size becomes important are two-fold.

First, in these hard x-ray examples, the detector resolution becomes critical. Usually, for a typical geometry, R is a couple meters, the coherence-defining pinhole is about $20\,\mu$m, and the wavelength is $2\,$Å. This gives a speckle size that

is comparable to the current detector resolution for a charge-coupled device (CCD) detector. In this case, the speckle structure is barely resolved. Deconvolution then of detector resolution from data becomes a necessity, and adds a considerable amount of issues in the analysis of these types of complex pictures.

Secondly, with small coherence areas, the signal per speckle becomes an issue. By noting the speckle size in Figure 4.5 is on the order of 15 x 15 pixels, we have typical counts of 50 counts per pixel-sec., or $\sim 10^3$ counts per second on average, per speckle. In dynamics experiments, signal-per-speckle really becomes the key quantity to maximize. So from a practical view point, soft x-rays bring a much higher resolution to the speckle structure, as well as increase the signal-to-noise ratio compared to hard x-rays by a factor of 10 or so. As we will see shortly, this particular energy range also has fundamental importance in transition-metal oxide physics.

7. Contrast

Contrast is one of the prime interests in the analysis and measurement of speckle patterns. It can be defined statistically as the ratio of the standard deviation in detected intensity to the average intensity in a speckle pattern

$$C = \frac{\sqrt{\langle I^2 \rangle - \langle I \rangle^2}}{\langle I \rangle} \tag{4.11}$$

This essentially is a measure of how pertinent the interference is between scattering from different regions of the heterogeneity mechanism. The ensuing diffraction pattern is a complex picture representing a reciprocal space function of the the disorder in the sample. Another way to measure the level of deviation from the average intensity is sometimes referred to as *visibility* in optics, or the *Michelson* contrast. This is defined as

$$C(\xi, \sigma, \mathbf{q}) = \frac{I_{max} - I_{min}}{I_{max} + I_{min}} \tag{4.12}$$

where I_{max} and I_{min} are the maximum and minimum intensity in the pattern over the region where one wishes to calculate the function. The variables ξ, σ, and $\mathbf{q}$ are to remind us that the contrast depends on the correlation length ξ of the photon beam at the sample, the degree of roughness σ, or measure of heterogeneity in the system, and the momentum transfer $\mathbf{q}$ defined as $\mathbf{k}_f - \mathbf{k}_i$ where the $\mathbf{k}$ represents the incoming and outgoing wavevectors of the x-rays.

With the flurry of laser physics over the last half-century, optical contrast became an important method of measuring different types of surface disorder [102, 103]. By observing how the contrast in a laser speckle pattern changes from laser light scattering from separate surfaces, one could derive the level of roughness for a comparison between the surfaces. In astronomy, typically the converse is done: by assuming some model of the *roughness* of the density variations in the index of refraction of the atmosphere, measuring speckle from starlight allows for a deduction of the coherence properties of the source. This is used to study many different types of extraterrestrial objects.

The dependence on $\mathbf{q}$, though slight, should be obvious because of the dependence on roughness. Measurements at different $\mathbf{q}$-values can be thought of as probes at different length scales, or spatial resolutions. A surface can be smooth optically, and exhibit no speckle pattern for optical wavelengths, while on a much shorter wavelength, the x-rays can be sensitive to the roughness. Though a much smaller effect, it becomes clear that for different spatial resolutions of the structure, the disorder would appear different for different momenta. To demonstrate the dependence of speckle on ξ, we have captured different patterns as a function of coherence length in Figures 4.6 and 4.7. The images in 4.6 show the same image for different magnifications. The size of each individual coherence area is around 7 square pixels on average. As discussed, the contrast varies slightly with $\mathbf{q}$, but across the entire pattern is about 45%. Figure 4.6 is has all the same experimental parameters, but is using about a 3 μm pinhole. This gives a coherence area of about 15 - 20 square pixels and a contrast of about 65%. Typically, speckle size is thought to be governed by the spatial filter d, but this is only because it usually defines the transverse coherence lengths in Equation 4.8, where $\xi \approx d$. However, in dynamics measurements, signal-to-noise becomes more important that the contrast, and spatial filters are used to increase ξ, but not define it. In Figure 4.6, the correlation length is smaller than the pinhole, by about a factor of two, assuming about a 5 μm coherence length. The increase in speckle size and contrast is not dramatic in Figure 4.7, because the aperture used there is on the order of $\sim 3\mu$m. However, the reduction of ξ by 40 % is certainly enough to see the changes clearly by eye. The two sets of images in figures 4.6 and 4.7 have been scaled to represent structure on the same level.

Here it is worth noting that we have been assuming symmetric coherence lengths, as this is legitimate since we usually use circular spatial filters. However,
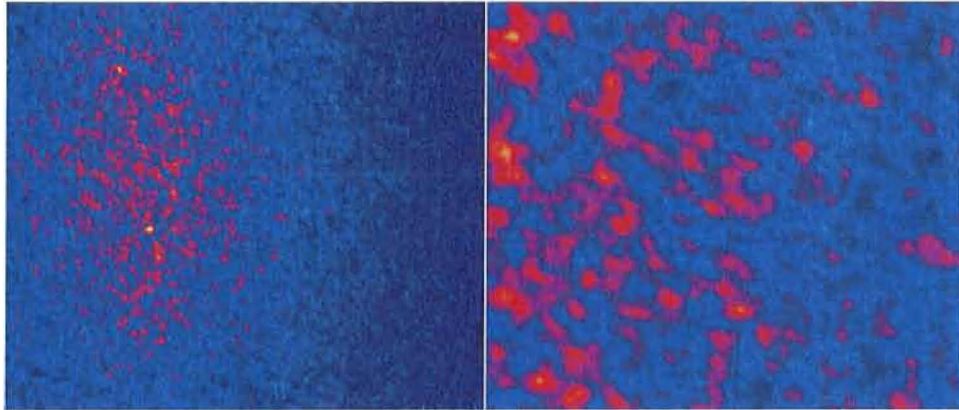
Fig. 4.6: **Contrast as a function of** ξ. A and B show the same image at different magnifications. This image shows much smaller coherence areas, about $\sim 7 \times 7$ pixels. The contrast level in this image is about 45%.
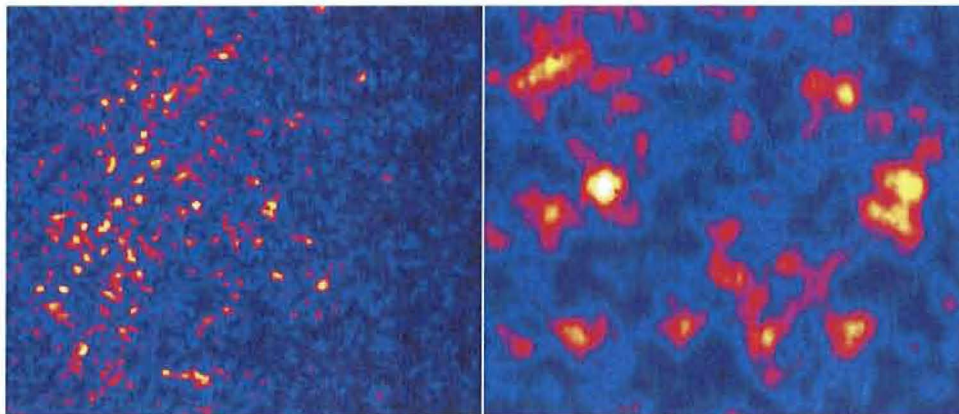
Fig. 4.7: **Contrast as a function of** ξ. A and B show the same image at different magnifications, to compare with in Figure 4.6. This image shows much larger coherence areas, about 15-20 square pixels. The contrast in this image is calculated to be near 65%.

the exact dependence of the coherence area is in fact a function of the shape of the filter. Because of the high degree of coherence in the beam prior to a spatial filter, we are able to form speckle patterns with a highly asymmetric beam. This fact is demonstrated by elongated coherence areas.

Theoretically, when partially coherent, or largely incoherent radiation is used as a probe, the contrast will effectively be zero since the resultant diffraction should be averaged over. In other words, the amplitudes from different regions of the sample will add incoherently. Contrast then is only a useful function as the x-rays approach full coherence.

i.   Coherent Extraction

One last note about the contrast is that theoretically, the trade off between contrast and the signal-to-background ratio (incoherent background) cancels in most cases for dynamics measurements. An example is for spatially filtered light that has a much smaller correlation length then the natural correlation length of the unfiltered, uniformly distributed beam. In this example, increasing the spatial filter diameter by a factor of two $(d' = 2d)$ gives an increase by a factor of four in the new signal estimate s', since signal goes as the area:

$$\pi(r')^2 \sim \pi(2r)^2 \Rightarrow s' \sim 4s$$

However, the S/N increase is only by a factor of 2, since by Poisson counting statistics

$$\frac{(S/N)'}{S/N} = \frac{s'}{\sqrt{s'}} \frac{\sqrt{s}}{s} = 2 \tag{4.13}$$

where the ratio scales as the square root of the areal increase, since the number of photons is also proportional to total area. Similarly, it is well known [85] that the contrast scales as the inverse square root of the number of coherence areas or for this example,

$$C \sim \frac{1}{\sqrt{n}}$$

For the increase of 2 in diameter, the contrast and S/N exactly cancel, yielding no net gain in overall in the signal to background despite 4 times as much intensity. The total signal or intensity does play an important role however in acting as a limit in the dynamic range of the detector, and determining acquisition times. For this reason, this cancellation is sometimes used to justify altering

the spatial filter to allow more signal (though less coherent), even though it leaves the overall signal-to-background unchanged.

CHAPTER V

SPECKLE STATISTICS

> If your experiment needs statistics, you ought to have done a better
> experiment.
> - Ernest Rutherford

Many experiments emerging as of late exploit coherence to solve new mysteries. Techniques such as lensless microscopy, dynamic light scattering, and spectral holography are just a few examples which all rely on interference effects of highly coherent photons. This chapter presents some general tools for analyzing coherent diffraction patterns. A general form of correlation functions of random variables has recently been applied to images for the purpose of metrology [104]. By generalizing this formalism, we apply it to dynamics experiments in order to measure time-correlation functions.

First, we describe a brief history of the related field of dynamic light scattering, followed by an introduction to the basic physics. Then there is a detailed description of two different methods of treating time-correlations analysis using speckle patterns that differ in statistics: with the focus set on the cross-correlation method used in this work. As a largely contrast-independent metric, the cross-correlation method discussed here seems to give an alternative option in dealing with the plague of normalization issues that arise in conventional time-correlation analysis. The discussion progresses with the strength and weaknesses of both types of calculations, while giving examples of each. Finally, momentum-dependent statistics is delineated, including an appendix of the details of the transformation.

1. Brief History and Basic Physics

The last 50 years has brought many fruitful applications in science, technology, and medicine based on the invention of the laser. The idea is generally

recognized as stemming from the microwave version of 'amplified stimulated emission of radiation', sometimes called the *maser*. In 1954, three scientists from Columbia University published work on the construction and operation of the first device [105, 106]. This was soon pushed to the optical regime where a flurry of success in technological applications soon followed. Now the laser has become commonplace in everyday life, from scanning groceries at the supermarket or printing pages from a computer, to more sophisticated applications such as eye and knee surgery or military weaponry.

i. *Dynamic Light Scattering*

As a result of the increased flux and the large increase in coherence, many novel scientific techniques have been implemented: from interferometry to holography. One example that utilizes these features, only possible with the invention of the laser, is dynamic light scattering (DLS). This technique is also known as intensity fluctuation spectroscopy (IFS), photon correlation spectroscopy (PCS), or the older synonym quasi-elastic scattering (QES) [107]. DLS takes advantage of the the coherent attributes of the laser to measure time-dependent phenomena. When using a laser as a coherent source, a heterogeneous system will scatter light differently, as the scattering cross-section will depend strongly on the region of the non-homogeneity being illuminated. This difference will be amplified through interference of scattered amplitudes from these different regions, forming the so-called 'speckle' pattern, described previously.

By studying fluctuations in this interference pattern, DLS can be used to study the dynamics of the system. Just how the dynamics is studied and under what conditions this technique is justifiable will be discussed in the following pages. In particular, DLS has made some great advances in a number of fields, allowing unprecedented opportunities to study behavior near phase transitions, such as in critical opalescence and critical slowing down [47]. Two conditions must be met regarding the length scale of the disorder for this technique to apply. The first is it must be smaller than the correlation length of the laser light being used to probe the system. The second is the length scale of the disorder must be larger than the wavelength. For different reasons, when these two conditions are met, the ensuing speckle pattern forms based on the first condition and can be studied easily by the second.In addition to the laser, another key factor to the birth of DLS was the availability of first-rate detectors in the optical regime. The photomultiplier tube (PMT) was developed about a decade prior to this

time period and was ideal for optical photon detection, producing gains as high as 10^8 [108].

DLS involves the idea of measuring a window about a single coherence area of the speckle pattern. The detected light over this region is read out into a digital autocorrelator for real-time computation of autocorrelation functions, performed with established, commercial software. This process will be discussed further in more detail in Section 2.. Correlation functions are automatically measured, and the process must be repeated over any coherence area, or region of coherence areas, enough times to conclude a statistically significant measurement for a given q-value. The measurement of multiple coherence areas *simultaneously* however, with a photon counting method, has not proven to add any advantage for dynamics. For each added coherence area that is collected, the contrast decreases at the same rate. This idea was discussed mathematically at the end of the last chapter. In terms of the signal-to-noise ratio, it should be clarified that there is not much gain in adjusting the total accumulation area of the detector for measuring a single correlation function.

ii. DLS with X-rays

The next significant progression of DLS came with the extension of DLS to x-ray wavelengths, sometimes referred to as x-ray photon correlation spectroscopy (XPCS) or even x-ray intensity fluctuation spectroscopy (XIFS). This was pursued to probe smaller length scales which were previously impossible with the long wavelengths of optical light. Unfortunately, without an x-ray laser, the analog to the x-ray energies was extremely challenging. Synchrotrons and recent detector development have started to improve the situation for high energy DLS, or XPCS. These two attributes, major contributors in our work in the soft x-ray regime, will be described in the following chapter in some detail, but here we will just focus on one aspect of the latter: large area detection.

iii. 2d Detection

With the development of area detectors [109], one advantage is to measure large regions, and sometimes even the full speckle pattern simultaneously. The data is saved to disk and repeated, for correlations to be computed at a later time. The difference in this option from the multiple coherence area measurement noted above is that the latter is computing time correlations in real time over the *entire* region at once. That is, there is no spatial resolution within

the detected area. The total intensity at a given time is the quantity that is automatically correlated together with the total intensity values for other times.

Another concern that has arisen in DLS is the amount of data that can be collected at a given time. While time-correlation functions can be measured for a given speckle, many of these coherence regions must be measured through the course of a given experiment. This extends experiment durations to long periods of time, as correlation functions must be measured over the duration of the needed time window per speckle, and repeated for many coherence regions of a given speckle pattern under some given experimental conditions, such as applied fields or temperatures.

The benefit of area detection is that a large amount of the information in the speckle pattern is retained in an image file. By applying post-experiment spatial correlation analysis described in detail in Section 3., we can retrieve the speckle information from the entire pattern. Therefore, by implementing this general correlation analysis, we are able to overcome the limitations of single-speckle measurements, and concomitant long experimental duration.

It should be noted that this process instead comes with a different limitation: long-time correlations due to the extended readout time of the entire detector array. The choice of incorporating a CCD detector is limited to slow-time physics because of the additional time it takes to readout the entire detector. Due to this limitation, in certain cases it becomes useful to impose a smaller active area of the CCD for a trade-off of shorter readout times.

iv. Noise, Complex Phasors, and Statistics

The beauty of speckle is that though it involves extreme complexity, by careful consideration of the statistical properties, many ideas from random noise and statistics can be applied to the data to make definitive quantitative conclusions. This takes place by considering the electromagnetic scattering amplitudes in the Fraunhofer plane. The amplitudes in this plane can be modeled as complex phasors for each component of the field, where the random walk prescription can be implemented appropriately in two dimensions [85].

The intensity in the observation plane is given by the square modulus of the complex wave field $A_\alpha(x, y)$:

$$I(x,y) = A^\alpha(x,y)A^*_\alpha(x,y) = |A(x,y)|^2 \tag{5.1}$$

where the x and y coordinates describe the Cartesian image plane, α describes the polarization component, where it is understood that repeated indices are summed (the Einstein convention). The autocorrelation function can be written as

$$\langle I(x+\eta, y+\xi)I(x,y)\rangle - \langle I(x+\eta, y+\xi)\rangle \langle I(x,y)\rangle \tag{5.2}$$

The second condition mentioned in Section i. is based on necessary assumptions that must be made about the speckle pattern. When the length scale of the roughness mechanism responsible for the speckle pattern is large compared to the wavelength of light, we can assume we have a Gaussian amplitude process. Statistically, this refers to how the random phases of the complex scattered wavefields vary. If the medium is characterized by this type of a roughness mechanism, this implies a zero mean complex amplitude fluctuation. The term 'Gaussian' means that the phases are normally distributed on a $(0, 2\pi)$-interval in the complex plane. This is necessary to derive the results exact mathematically. Then, according to Gaussian statistics Equation 5.2 reduces to

$$\langle I(x+\eta, y+\xi)I(x,y)\rangle = |A^\alpha(x+\eta, y+\xi)A^*_\alpha(x,y)|^2 \tag{5.3}$$

where the square modulus term on the right is the mutual intensity of the amplitude. This condition will surface again in later discussion of ergodicity and its implications.

2. 'First-Order' Spatial Statistics: The Intensity-Intensity Autocorrelation

In this section, we will discuss the intensity-intensity autocorrelation function. This is the typical measurement in a dynamic light scattering or x-ray photon correlation spectroscopy experiment, and a large amount of information about the system can be calculated based on its measurement.

i. The Function

In DLS and especially XPCS, field detection is extremely difficult. What is typically done is measurement of intensity for a computation of the intensity-

intensity autocorrelation function:

$$g_2(\tau) = 1 + \left(\frac{n}{n-\tau}\right)\frac{1}{N}\sum_{t=1}^{n-\tau} I(t)I(t+\tau) \tag{5.4}$$

where N is a normalization constant equal to

$$N = \sum_{t=1}^{n} I(t)^2$$

where the intensity $I(t)$ is measured for some time t, and multiplied by the intensity at some different time $I(t + \tau)$. This product is averaged over all intensity products with the same separation time between quotients, τ. This inherently assumes that the process responsible for the scattering is stationary, a common assumption made in statistical mechanics. Some examples of some $g_2(\tau)$ functions are shown in Figure 5.1. They were measured by DLS to study diffusional behavior of polystyrene latex spheres in a polyacrylamide gel [9].

The beauty of the measurement of $g_2(\tau)$ is that under certain conditions, it can be directly related to the 'ensemble-averaged' intermediate scattering function, also known as the dynamic structure factor F($\mathbf{q}$,t). This is known, historically as the 'Sigert relation', though it seems to have been derived separately by several independent authors [110] and can be written as

$$g_2(\mathbf{q}, \tau) = \frac{\langle I(\mathbf{q},t)I(\mathbf{q},t+\tau)\rangle}{\langle I(\mathbf{q},t)\rangle^2} \tag{5.5}$$

$$= 1 + \beta\left|\frac{F(\mathbf{q},\tau)}{F(\mathbf{q},0)}\right|^2 \tag{5.6}$$

where in Equation 5.5 we have just re-written Equation 5.4 in a short-hand notation where the brackets represent a temporal averaging and Equation 5.6 is the Siegert relation where β is a coherence factor between zero and one. One subtlety is that we have implicitly assumed ergodicity here. We will discuss this condition in detail in Section 4..

ii. An Example: The Dilute Macromolecule Solution

One example to showcase the extraordinary insight that can be gained from DLS is in the textbook example of particle diffusion in a macromolecular solution, assumed to be spherical particles [107], summarized and reproduced here. From the $g_2(\mathbf{q}, \tau)$ measurement, such as the ones shown in the example in Fig-
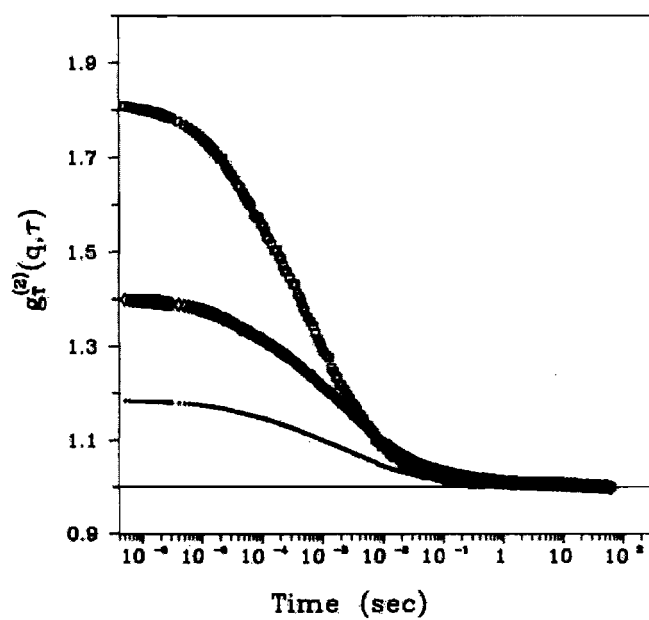
Fig. 5.1: **The Intensity-Intensity Autocorrelation Function:** $g_2(\tau)$. A few examples of some intensity-intensity autocorrelation functions taken from Joosten et al. [9]. The curves are calculated from scattering due to Brownian particles trapped inside polyacrylamide gels as a function of angle.

ure 5.1, we can extract the intermediate scattering function $F(\mathbf{q}, \tau)$ through the Siegert relation. This is also the characteristic function of the probability density function $G(\mathbf{R}, \tau)$, also known as Van-Hove self space-time correlation function discussed by Leon Van Hove in 1954 with regard to neutron scattering [111]. This describes the probability that a particle i will suffer a displacement in the vicinity $d^3\mathbf{R}$ about the point $\mathbf{R}$ at time t. Though the Van-Hove function can be retrieved simply through an inverse momentum Fourier transform, some care must be taken in the interpretation as $F(\mathbf{q}, \tau)$ is not known for all $\mathbf{q}$, but only for a certain range. From the simple model assumed, we can use simple diffusion theory to describe the system. The diffusion equation correctly describes the probability of the random walk – which here, is the probability for a particle to diffuse into the d^3R–neighborhood of the particle at time t. Taking the Van-Hove function as the solution to the diffusion equation

$$\frac{\partial}{\partial t} G(\mathbf{R}, \tau) = D\nabla^2 G(\mathbf{R}, \tau) \tag{5.7}$$

where D is the diffusion coefficient. Transforming to Fourier space, the solution can simply be written down:

$$F(\mathbf{q}, \tau) = e^{-t/\tau_c}$$

for an appropriate assumption of initial conditions. The definition of the relaxation time would then be given by $\tau_c = (q^2 D)^{-1}$. Now from the Einstein equation, the constant D can be related to the friction constant through

$$D = \frac{k_B T}{\zeta}$$

where the $\zeta = 6\pi\eta R$ for the viscosity of the solvent η and the radius of the particle R. In conclusion, when the viscosity η of the solution is known, a DLS measurement for known $\mathbf{q}$-values can be used to extract the diffusion constant, and hence the average radii of the spherical particles can be directly measured. This is a truly remarkable result and even though in a simplified model of identical particles, really displays the power of gleaning physical characteristics of a system through coherent scattering.

3. 'Second-Order' Spatial Statistics:
The Cross-Correlation Coefficient

The cross-correlation method uses a different approach to measuring temporal correlations between speckle patterns through 'second-order' spatial statistics. This is the only circumstance where this method has been used to measure dynamics in connection with speckle pattern images known to the author. Its usefulness has been applied to recent metrology work in magnetic films, where speckle patterns were compared along different points of the hysteresis loop to study the memory of the magnetic domain configuration [104]. In this section, we show how to generalize this to the time-domain. That is, by measuring 'second-order' spatial statistics, we can instead compare speckle patterns in time to measure changes in this domain. In a sense, this method is a calculation of 'temporal memory' which is then used to study dynamics. While conventional XPCS measurements must deal with parasitically fluctuating signals which can contaminate analysis, this method has an added benefit that the normalization is built-in. To further generalize this computation, we will leave in the q-dependence as this method can be applied to any region in the speckle pattern and finally averaged over regions with the same q-values. We will discuss the details of this important aspect in Section 5..

i. Coherent Background Subtraction

The first step to calculating a cross-correlation coefficient applied to images is to extract a reasonable approximation of a fully coherent image from the speckle pattern. The speckle patterns consist of two components: a coherent part and a incoherent background, shown as panel (A) of Figure 5.2. The latter is the result of the size of the scattering distribution determined from the correlations in the sample. Namely, incoherent addition of coherent scattering amplitudes from different regions of the illumination volume. This is usually referred to as 'incoherent' scattering, but to be precise, must involve some degree of coherence. For instance, in Bragg diffraction, scattering from Bragg planes must interfere to result in an accentuated scattered intensity.

To approximate the incoherent part from the speckle pattern, a functional fit is performed on the raw data. This can be thought of in two different ways. The first is simply the result of a small amount of averaging in reciprocal space. The result is to smear the speckle out, such as is done automatically when incoherent
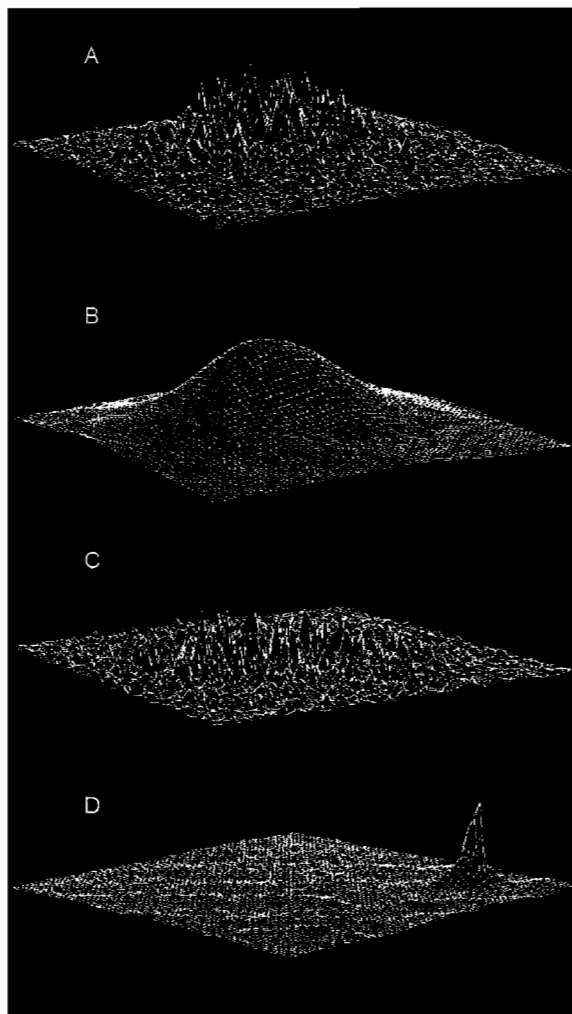
Fig. 5.2: **Surface Function Images** This array of images gives a sample of some of the surface functions discussed in the text. The first three images are rotated to 33° while each pixel represents 32×32 real pixels from the image. (A) The surface plot of a speckle pattern. Note that each pixel here represents a large number of pixels from the actual image, giving an illusion of a noisier image than in reality. (B) A 'tight' surface plot to the speckle pattern in A. The fit is a 2d polynomial fit, five terms in x and up to nine in y, including cross-terms. (C) The residual from the original speckle pattern (A), and the fit (B). (D) Speckle peak from the correlation of two copies of (C). The speckle peak will always appear in the middle of the correlation function, but here is translated to the corner to emphasize the flatness of the region surrounding it. This plot is zoomed in to six square pixels per plotted pixel and is oriented to 45° to measure both directions of the width more easily.

electromagnetic radiation is used and the scattered signal does not interfere with itself. In fact, if incoherent x-rays were used in the same experimental set-up, the fit would represent exactly what data would be collected. It represents the scattering distribution due to any deviations from long range order and an example is shown in panel (B) of Figure 5.2. A second way to illustrate the physical meaning of this fit is in coherent scattering: when long acquisitions are taken over time periods much longer than the temporal fluctuations of the system. We will use the first illustration below.

To emphasize either type of averaging, we denote the result of the incoherent component of the image acquired at time τ as:

$$\widetilde{I}(\mathbf{q}, \tau) = \langle I(\mathbf{q}, \tau) \rangle_{\delta \mathbf{q}}$$

where the $\widetilde{I}$ denotes incoherent and the $\delta \mathbf{q}$ is used to remind the reader of the first illustration: that the spatial speckle structure is being averaged over. This momentum-averaged image, here termed the 'incoherent' image, is subtracted from the raw speckle pattern to create a purely coherent pattern, to first order, shown in panel (C) of Figure 5.2. This subtraction is necessary to attain the zero-mean statistical characteristic of the intensity as discussed for amplitudes previously. This removal isolates the speckle structure due to local topology of the system from the average scattering, which we denote by I_C where

$$I(\mathbf{q}, \tau)_C = I(\mathbf{q}, \tau) - \langle I(\mathbf{q}, \tau) \rangle_{\delta \mathbf{q}}$$

This is also sometimes known as a type of 'background' subtraction, a term which is not used here due to the many different types of background subtractions that take place in this type of analysis.

ii. Fourier Transform Extraction

Another method used to perform the incoherent subtraction is by Fourier analysis. This also provides a clear way to understand the subtraction process. The speckle pattern consists of two major Fourier components: the high frequency components related to the speckle, and lower frequency components related to the average, or incoherent scattering distribution. By using a Fourier transform on the raw speckle data, we can usually retrieve two separated components in Fourier space. Implementing the use of a step- or $\theta(\omega)$-function, we can subtract the frequencies related to the incoherent component. The result is

transformed back to display only the coherent fraction of the original data. This new transformed image can then be assumed to be isomorphic to the coherent component extracted by spatial averaging.

iii. The Correlation Coefficient

The next step is to cross-correlate two of the transformed coherent speckle patterns at different times. By comparing the spatial structure of two speckle patterns taken at different times, we can measure the relative changes from one to the other. The typical method of measuring temporal dynamics, for instance in dynamic light scattering (DLS) or x-ray photon correlation spectroscopy (XPCS) is through first-order spatial statistics. Mathematically, this refers to how the speckle changes at a single point. In practice, this is calculated by measuring intensity over a single speckle, one unit of spatial resolution, and calculating the intensity-intensity autocorrelation function for that particular speckle. By studying the spatial extent of the structure of the speckle distribution, we can measure how the system evolves in time. This method offers a new way to measure dynamics, spatially.

Q-space Cross-Correlations

The measurements are projected into the $(\mathbf{q}_\perp, \mathbf{q}_\parallel)$-plane of the detector, where the two orthogonal vectors are with respect to the scattering plane: we take cross-correlations with respect to this coordinate system:

$$I(\mathbf{q}, t)_C \otimes I(\mathbf{q}, t + \tau)_C \tag{5.8}$$

$$= \int_{a_1}^{b_1} \int_{a_2}^{b_2} dq_\perp dq_\parallel \, I(\mathbf{q}, t)_C I(\mathbf{q} + \delta\mathbf{q}, t + \tau)_C \tag{5.9}$$

$$= h(\delta\mathbf{q}, t, t + \tau) \tag{5.10}$$

where $h(\delta\mathbf{q}, t, t + \tau)$ is the cross-correlation function of the two images, and a_i and b_j are the limits of integration over the region of the image being correlated. Computationally, this is done by taking a discrete Fourier transform (DFT) of each image in a pair of speckle patterns, multiplying the first with the complex conjugate of the second, and calculating the inverse DFT on the product. This is just, the convolution theorem:

$$F[I(\mathbf{q}, t)_C] * F[I(\mathbf{q}, t + \tau)_C] = F[h(\delta\mathbf{q}, t, t + \tau)] \tag{5.11}$$

where the Fourier transform of x is represented by $F[x]$ and the correlation function by $h(\delta \mathbf{q}, \tau)$.

Correlation Function Interpretation

The cross-correlation function $h(\delta \mathbf{q}, \tau)$ between two coherent images has a maximum at zero displacement, unless of course one of the images has been shifted with respect to the other. In fact, in practice, measuring this shift allows the ability to decipher if there are system instabilities, another benefit of this formalism. This function is a two dimensional surface function and its maximum is represented by a peak where its volume sheds light on the properties of the speckle: the width represents the average width of the speckle in the image while the height represents the contrast. This is referred to as a speckle, or coherent peak. The lateral size of the speckle can be of particular importance when designing experiments, from beamlines to detectors, and sets the speckle resolution. In the previous chapter, we discussed how to estimate this size, while the discussion here pertains to the *exact* calculation, where of course *exact* has a statistical meaning only. This is simply the full width at half-maximum of the peak in panel (A) of Figure 5.3, about 15 pixels. Panel (B) of the same figure is zoomed in enough to see the pixelation. Though the size of each speckle varies widely in this image, and this is some arbitrary region of the image, it demonstrates the statistical robustness of using the speckle peak to define the speckle width.

The contrast is another quantity of importance, a measure of how well we can calculate correlations in speckle patterns, and indeed must be maximized in calculations such as the intensity-intensity autocorrelation function, where it determines how well the measurement can be made.

To demonstrate this, it will be shown how to measure quantities such as the contrast and average speckle width using the speckle peak in Figure 5.3. The inset shows a speckle peak of two raw speckle images, which appears as a small peak atop a larger, broader contribution from the scattering distribution (correlations must be done before the functional fits in contrast measurements or else the contrast will have an infinite or undefined value since $\langle I \rangle \rightarrow 0$ after the spatial averaging is performed). Panel (A) shows just a close-up image of the speckle peak. According to the equation

$$C^2 = \frac{\langle I^2 \rangle - \langle I \rangle^2}{\langle I \rangle^2} \tag{5.12}$$
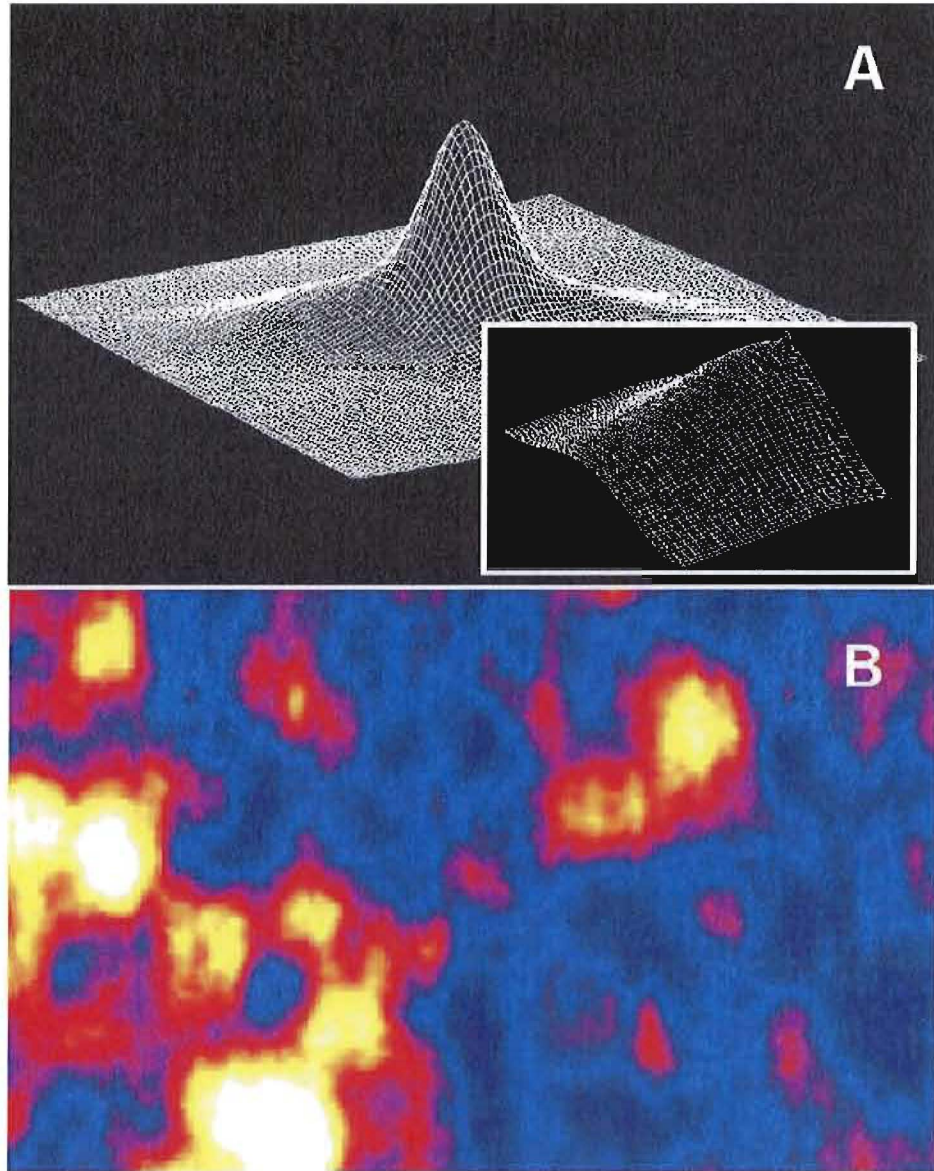
Fig. 5.3: **Speckle Peak as a Metric** This figure demonstrates how to use the speckle peak of a cross-correlation function between two speckle patterns to measure quantities of interest, such as the average extension of the coherence regions within the pattern as well as the contrast. (A) A speckle peak from a cross-correlated speckle pattern. (Inset) Half of the full cross-correlation function that the peak is extracted from in panel (A). The speckle peak is the small half peak shown at the top edge, while the broader peak represents the 'average' scattering. (B) A pixelated region of the pattern to compare the speckle structure with that as computed by the speckle peak.

To calculate this, we simply use the value at the central pixel of the peak and of a small region around the peak where the function becomes flat locally. For the image shown, this gives values of 4.33×10^{13} and 3.5×10^{13} for $\langle I^2 \rangle$ and $\langle I \rangle^2$, respectively, or a contrast of 40% after taking the square root. Using the definition from previous chapter, we get contrast values slightly higher, about 65% averaged over 20 different regions of the image. This can be understood on the basis of the fact that using the minimum and maximum pixels in a given region can lead to errors due to 'dead' regions on the camera, or 'burned' pixels, yielded 0 or 2^{16} ADC counts, respectively.

Speckle Peak Integrals

To measure average spatial correlations, we must integrate the speckle or *coherent* peak

$$h(\tau)_c = \int_{c_1}^{d_1} \int_{c_2}^{d_2} dq_\perp dq_\parallel \, h(\delta \mathbf{q}, \tau) \qquad (5.13)$$

where the c_i and d_i limits are over the speckle peak of the correlation function. For any given cross-correlation function, the limits can be deduced by inspection. To demonstrate this, Panel (D) in 5.2 shows a speckle peak translated to the edge of the surface plot to emphasize the flat region around the peak. The integral is performed over this region just outside the peak, where the limits are flat in the image, or where the average intensity is zero. As noted before, the boundaries will be set by the average speckle size in the data. The integral $h(\tau)_c$ then is a real-valued scalar.

iv. Normalization

In order to calculate the final cross-correlation coefficient, the value must be properly normalized. The integral of the cross-correlation coherent peak must be divided by some constant and there are two ways to go about this that will be discussed here. The first is intuitive, and comes from the definition of a covariant variable in statistics. The second is more practical, and removes some of the issues that the first introduces.

Autocorrelation Integrals

To calculate the necessary constant, integrals should be performed on auto-correlations taken of each of the two images in the cross-correlation pair. This is the same method as discussed above, but is between identical images, one

autocorrelation function from two copies of the first and one from the second. Coherent peak integrals are calculated in the same way for autocorrelation functions as they are for cross-correlations. Mathematically,

$$I(\mathbf{q}, \tau)_C \otimes I(\mathbf{q}, \tau)_C = \int_{a1}^{b1} d^2\mathbf{q} \ I(\mathbf{q}, \tau)_C I(\mathbf{q} + \delta\mathbf{q}, \tau)_C \tag{5.14}$$

$$= a(\delta\mathbf{q}, \tau) \tag{5.15}$$

or computationally, using again the correlation theorem:

$$F[I(\mathbf{q}, t)_C]^2 = F[a(\delta\mathbf{q}, t)]$$

to calculate $a(\delta\mathbf{q}, t)$ from image $I(\mathbf{q}, t)_C$. For both normalization schemes, the idea is to reduce the coefficient to a value with limits of $[0, 1]$. This is performed so that this coefficient is a scalar metric of the degree of correlation between two images, or regions of images. For the autocorrelation method, the square-root of the product of two auto-correlation function coherent peak integrals is used as the normalization constant:

$$\rho(\mathbf{q}, \tau, t + \tau) = \frac{h_c(\delta\mathbf{q}, \tau)}{\sqrt{a(\delta\mathbf{q}, t) * a(\delta\mathbf{q}, t + \tau)}} \tag{5.16}$$

Dividing by this constant yields the needed result such that for a pair that are completely uncorrelated the coefficient is zero and equals one for exact replicas.

Cross-Correlation Integrals

Mathematically sound, using autocorrelation integrals for normalization can be problematic in practice. Regardless of any aspects of the speckle pattern, every point in the image will give a contribution to the autocorrelation, whether from real signal or noise. This observation is solely based on the fact that each point in the pattern will by definition be correlated with itself: a real dynamic speckle, contributions from electronic noise, or even an imperfection or a burn mark for instance on the detector. This leads to an autocorrelation coherent integral that is larger than it should be in the zeroth channel only. Without a proper way to extract the real signal from the noise, the two are merged to give larger normalization constants, and hence, coefficients that have a maximum *less* than one. This is problematic as it introduces systematic offsets in the computation of cross-correlation coefficients. Since signal always varies with q,

a main challenge to conduct measurements as a function of q is to solve this noise issue satisfactorily.

One method used to battle this issue is to conduct a cross-correlation normalization. This seems counterintuitive since the cross-correlations are the end goal of the calculation. In situations where we are measuring correlations that decay over many separation times between images τ, the change between image n and $n + 1$ is minimal. The idea is to use integral values of cross-correlations between 'nearest' neighboring pairs (nn-CCF) *only* to retrieve proper normalization. This removes the zero channel spike for image pairs of the same image, but by the nearest neighbor constraint, approximates the contribution for an autocorrelation integral.

The idea is displayed qualitatively in Figure 5.4, in panels A through F. The autocorrelation method works beautifully for images that have a large amount of S/N, such as those shown at the top of Figure 5.4, panels (A) and (B). These are the ACF and nn-CCF, respectively. Because the S/N is so large, the correlated noise does not play a significant role. This is evident in the similarity between the two functions. In panels (C) and (D), the S/N is lower and the differences start to emerge. The panel shown in (D) is the nn-CCF and represents the real speckle peak contribution, with a width of about 5 pixels or so. Similarly, (C) is the ACF of the same image where we can start to see a sharp, 1 pixel wide peak that starts to dominate the rest of the structure. In the speckle pattern represented by (C) and (D), an ACF normalization would begin to have the correlated noise affect the coefficient. The bottom panels are from an image with noise-dominated statistics. Panel (E) is the ACF that is scaled to fit in the panel, but it is evident that the central channel is dominating all other points drastically. Panel (F) shows how the nn-CCF normalization can solve the S/N issues, giving the speckle contribution under the noise peak. Because the signal is so low, and the speckle peak not much stronger, structure in the noise floor starts to appear in the surface function.

The objection to this method might be that for a system that is changing rapidly, much faster than the accumulation time of each image, this method could be problematic. Indeed this could be an issue for rapidly changing systems, or even systems where the correlation times are not much larger than the accumulation times in the data set. If either one of these is the case, this methodology is difficult to justify. However, both these situations can be remedied by taking smaller acquisition times, with S/N allowing.
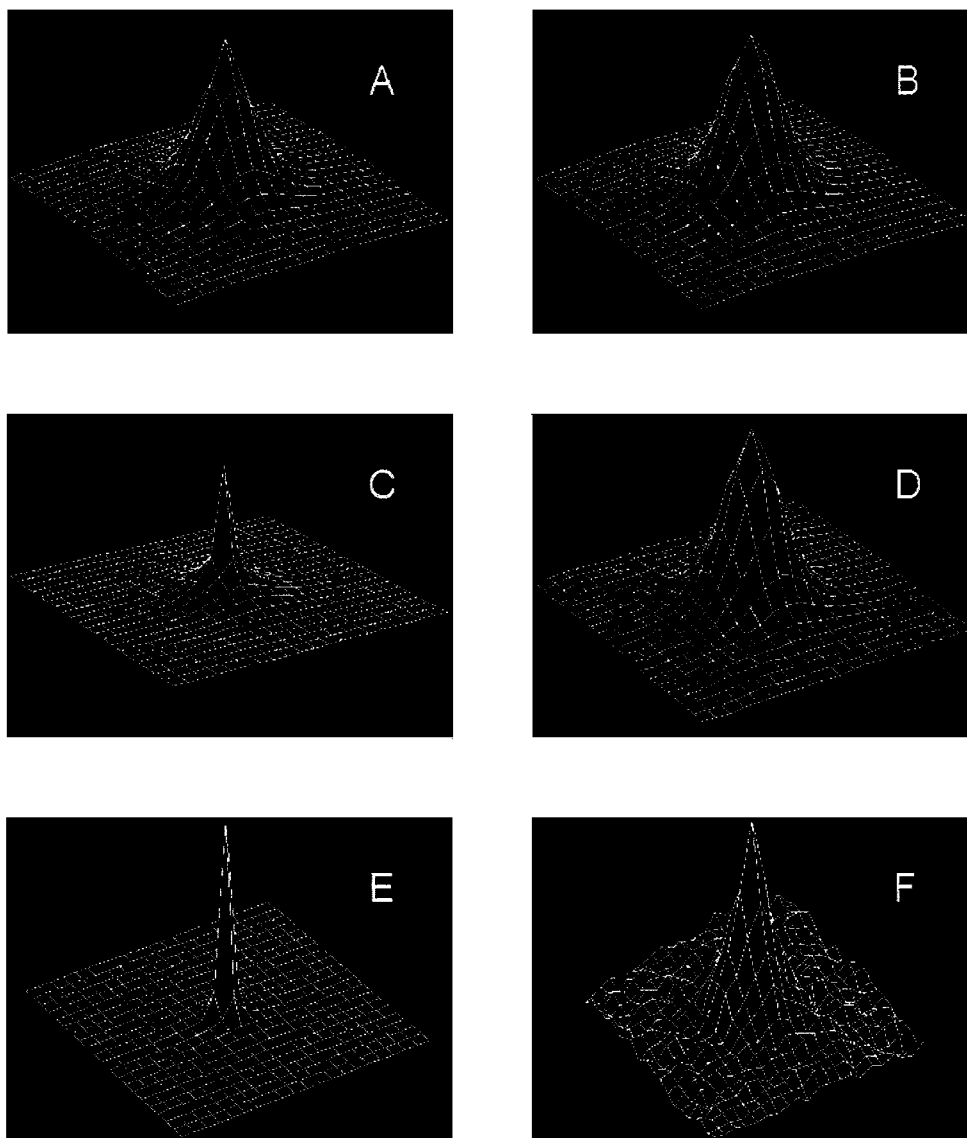
Fig. 5.4: **Normalization From Correlation Function Integral Comparison with S/N**
This set of panels displays the issues that arise with an auto-correlation function (ACF)
normalization (left column) when the signal-to-noise ratio becomes low as well as how using
a 'nearest-neighbor' cross-correlation (nn-CCF) method (right column) solves the problem.
The top row is images that have a large S/N ratio, the middle row is medium count rates,
and the bottom two have just barely resolvable signal. Each region is a 20x20 pixel area just
around the speckle peak, culled from the total surface function which is $(2 \times 2048)^2$ pixels in
total. (A) and (B) do not appear to be much different as the signal is adequate to make the
different normalization techniques negligible. (C) An ACF for a medium count rate speckle
pattern. Note the slight bi-modal nature of the surface. The sharp peak on top of a slightly
broader version is about 1 pixel wide FWHM. (D) A nn-CCF showing the removal of the noise
peak, and a similar speckle peak as in (B). (E) Shows how drastic the noise peak is with very
low signal-to-noise ratio. The severity of the central pixel in the ACF completely drowns out
the true speckle peak. (F) The low signal nn-CCF shows how small the true speckle peak is
under the shot noise portion. As all figures are scaled to be equal, the structure on the noise
floor is evident since the peak height is so small.

Situations where this is not the case, such as ergodic systems where the dynamics are limited, or where the accumulation times of the images are much smaller than typical correlation times of the system, the option of the cross-correlation scheme works well. An easy way to check this notion is to note that if there are subtle changes from one image to the next, correlations between nearest neighbors would give correlation coefficients of this normalization method slightly *larger* than one. By confirming that coefficient values do not exceed the upper limit of one (to a desired precision), we can justify this normalization calculation.

More formally, we can write a cross-correlation pair between image n with a nearest neighbor in one of two ways

$$I_n(\mathbf{q}, t)_C \otimes I_{n+1}(\mathbf{q}, t+1)_C \tag{5.17}$$

$$= \int_{a_1}^{b_1} \int_{a_2}^{b_2} dq_\perp dq_\parallel \ I_n(\mathbf{q}, t)_C I_{n+1}(\mathbf{q} + \delta\mathbf{q}, t+1)_C \tag{5.18}$$

$$= h(\delta\mathbf{q}, t, t+1) \tag{5.19}$$

or with the other neighbor as

$$I_{n-1}(\mathbf{q}, t-1)_C \otimes I_n(\mathbf{q}, t)_C \tag{5.20}$$

$$= \int_{a_1}^{b_1} \int_{a_2}^{b_2} dq_\perp dq_\parallel \ I_{n-1}(\mathbf{q}, t-1)_C I_n(\mathbf{q} + \delta\mathbf{q}, t)_C \tag{5.21}$$

$$= h(\delta\mathbf{q}, t-1, t) \tag{5.22}$$

where it is understood that the integer 1 in the equations is referring to an image that is one unit of τ from the image with index t. We now define $c(\delta\mathbf{q}, t \pm 1, t)$ as

$$c(\delta\mathbf{q}, t \pm 1, t) = \frac{1}{2} \left[h(\delta\mathbf{q}, t-1, t) + h(\delta\mathbf{q}, t, t+1) \right] \tag{5.23}$$

Here it should be noted, that with this normalization, the first coefficient that can be calculated is one for a pair with a minimum separation of $\tau = 2$.

v. *Time-averaged Coefficients*

To measure time structure, we need to get an average $\rho(\mathbf{q}, \tau)$, where the average is taken over all correlation pairs with the same spacing of time τ

between them. Auto-correlatively, this becomes

$$< \rho(\mathbf{q}, \tau) >= \frac{1}{N - \tau} \sum_{t=1}^{N} \frac{h_c(\delta\mathbf{q}, t, t + \tau)}{\sqrt{a(\delta\mathbf{q}, t) * a(\delta\mathbf{q}, t + \tau)}} \tag{5.24}$$

The t-dependence drops out of the equation because by computing this average over all pairs separated by the same τ, this makes the assumption that the system is stationary. Stationarity does not put too strong of constraints on the statistics of the system, and is the most general of assumptions for a system exhibiting equilibrium fluctuations. Similarly, we can write the time-averaged coefficient with a cross-correlated normalization as

$$< \rho(\mathbf{q}, \tau) >= \frac{1}{N - \tau} \sum_{t=1}^{N} \frac{h_c(\delta\mathbf{q}, t, t + \tau)}{\sqrt{c(\delta\mathbf{q}, t \pm 1, t) * c(\delta\mathbf{q}, t + \tau \pm 1, t + \tau)}} \tag{5.25}$$

where Equation 5.23 is used to define the c's for the normalization constants. These two final results, used in the right cases, should always be between zero and one. The time-average can be plotted as a function of τ to connect with the intensity-intensity autocorrelation function.

4. Statistical Method Comparison

The two forms of analysis that we have discussed here both have different strengths and weaknesses. We will compare and contrast those attributes in the following section.

i. *Intensity-Intensity Autocorrelation Function*

The real strength of the intensity-intensity autocorrelation function is to measure the ensemble-averaged intermediate scattering function, $\langle S(\mathbf{q}, \tau) \rangle$ where it is understood that the brackets here are not for time, but ensemble averaging. This offers a connection to theory through particular models based on the system under study as well as other physical properties, such as diffusion coefficients for polymer and silica spherical particles near a glass-transition [112]. This intermediate scattering function can be calculated from time correlations for a single Fourier component through the 'Siegert relation' shown in an Equation 5.4. This connection to theoretical models is an incredible advantage, as it offers a way to measure properties that can not be measured by other techniques. The weakness is that it can be challenging in terms of normalization

and that it is only valid when the ergodicity theorem holds. To understand the repercussions of this statement, we will delve into the meaning of the ergodicity theorem briefly in the next section.

Ergodicity Theorem

The ergodicity theorem states that as time approaches infinity, the time-average of a system of microstates is equal to the ensemble-average (See for instance [113] for a short review). The discussion in Section 2. made this assumption, that the ergodicity theorem held for the system under study. This can be seen clearly by inspecting the limits of the function. For the time averaged version, when the intensity is completely constant, $\langle I(\mathbf{q},t)I(\mathbf{q},t+\tau)\rangle_T = \langle I(\mathbf{q},t)\rangle_T^2$ and

$$g_2(\mathbf{q},\tau) = \frac{\langle I(\mathbf{q},t)I(\mathbf{q},t+\tau)\rangle_T}{\langle I(\mathbf{q},t)\rangle_T^2} = \frac{\langle I(\mathbf{q},t)\rangle_T^2}{\langle I(\mathbf{q},t)\rangle_T^2} = 1 \qquad (5.26)$$

As shown in the example in Figure 5.1 however, the function $g_2(\mathbf{q},\tau)$ always starts between one and two for ergodic systems. In short, this is due to a number of assumptions made about the medium. This result can be seen algebraically, and we will briefly review the main concept here. For a more extensive derivation, see the work by P. N. Pusey [114].

Ergodicity Measurements

If we can model the system as a group of N identical point particles, all non-interacting in a liquid suspension, we can write the total scattering amplitude from the system as

$$A(\mathbf{r},t) = \alpha \int_V d^3r \sum_{i=1}^{N} e^{i\mathbf{q}\cdot\mathbf{r}_i(t)} \delta[\mathbf{r} - \mathbf{r}_i(t)] \qquad (5.27)$$

summed over all N particles in the illumination volume V, where α is a proportionality factor that depends on the dialectric constant of the medium and drops out of the following illustration. A scattered component of the electric field is proportional to this by a factor of $-E_0 k^2 e^{-i\omega t}/4\pi R$. The average intensity can then be written as

$$\langle I(\mathbf{q},t)\rangle = \langle |\mathbf{E}(R,t)|^2 \rangle = \alpha' \sum_{i=1}^{N}\sum_{j=1}^{N} \langle e^{-i\mathbf{q}\cdot[\mathbf{r}_i(t)-\mathbf{r}_j(t)]} \rangle \qquad (5.28)$$

where the factors of E_0, 4π, etc. have been absorbed into a new constant α'. For independent, non-interacting particles, these terms all average to zero except for when $i = j$. Since the particles are independent, the exponential can be factorized to $\left\langle e^{-i\mathbf{q}\cdot\mathbf{r}_i(t)} \right\rangle \left\langle e^{i\mathbf{q}\cdot\mathbf{r}_j(t)} \right\rangle$ which is zero for oscillatory functions that are randomly distributed over 2π. This gives a simple result:

$$\langle I(\mathbf{q}, t) \rangle = \alpha' N$$

as there are N times when the indices are equal, $i = j$. Similarly,

$$\langle I(\mathbf{q}, t) I(\mathbf{q}, t + \tau) \rangle = \alpha'^2 \sum_{i=1}^{N}\sum_{j=1}^{N}\sum_{m=1}^{N}\sum_{l=1}^{N} \left\langle e^{-i\mathbf{q}\cdot[\mathbf{r}_i(t) - \mathbf{r}_j(t+\tau) + \mathbf{r}_m(t) - \mathbf{r}_l(t+\tau)]} \right\rangle \quad (5.29)$$

There are $N(N - 1)$ times that both $i = j \neq m = l$ and $i = l \neq j = m$, and of course the same factor of N when $i = j = m = l$. The result is $2N(N - 1) - N$. With the further assumption that $N \to \infty$ which is usually made,

$$\frac{\langle I^2 \rangle}{\langle I \rangle^2} = \frac{1}{(\alpha' N)^2}(2\alpha'^2 N(N - 1) - N) \sim 2 \quad (5.30)$$

This shows that there is an upper bound for ensemble-averaged intensity-intensity autocorrelation functions of two, but more importantly, emphasizes the fact that in situations where the time-averaged quantity is not the same as the ensemble-average, the $g_2(\tau)$ formalism gives different results. Situations where this is commonly overlooked with experiments such as these is with 'non-ergodicity' parameters. In systems such as fluids or colloidal solutions, the particles responsible for the scattering of laser light execute Brownian-type motion. The particle fluctuations can be expected to sample all of phase-space in times comparable to experimental times. Hence, these Brownian-type systems are systems where the ergodicity theorem holds. Soon after the demonstration of DLS, systems such as glasses were found to exhibit non-ergodic behavior. Fluctuations could still be found to be present, yet were accompanied with some degree of frozen-in disorder. The only known way to deal with this was to directly measured the ensemble 'by hand'. That is, to exhaustively sample the entire system by translating the laser illumination through the sample, physically. This creates the condition to measure separate sample volumes, and the number of iterations needed precludes practical experiments to conform to the standards of the central-limit theorem.

A method developed to combat this issue theoretically was an approach by Pusey and van Megen. They calculated a way to recover analogous equations for the ensemble-averaged intermediate scattering function by measuring a *time*-averaged correlation function and an *ensemble*-averaged intensity. Experimentally, this translates to only having to measure one single correlation function in the usually way for one Fourier component, and merely taking an average over the ensemble of the intensity. The removal of the condition to measure ensemble-averaged correlation functions replaced with the condition to measure ensemble-averaged intensities was a considerable achievement, especially in terms of the central-limit theorem, where N is a subset of the true ensemble and must approach infinity.

Ergodicity and Heterogeneity

Something that has not been touched upon until now, is that the Pusey-van Megen formalism is only helpful for a globally homogeneous system. There certainly must be a non-homogeneity as the speckle pattern would not form in a purely well-ordered system, but this must be a local effect. The system must be homogeneous enough to attain a reasonable measurement of the ensemble-averaged intensity by sampling different regions of the scattering volume with the incoming beam.

In highly heterogeneous systems (that is, globally), the intensity can vary radically from one sample spot to the next. Even certain regions of the system can scatter much more strongly and make the task of measuring even an ensemble-averaged intensity difficult. It is in these cases that this formalism is challenging to incorporate. Measurements can still be conducted in terms of $g_2(\tau)$, but the connection to the intermediate scattering function through Siegert's relation is lost.

As already mentioned previously, the challenge of measuring one Fourier component lends itself to many measurements in any given experiment. Recently, measurements have been made with area detectors in XPCS. The $g_2(\tau)$ functions are then calculated per pixel, and averaged over many Fourier components. One practical drawback is in normalization of this method. Many works have been published [115] just in dealing with these normalization issues that plague the correct formulation of $g_2(\tau)$.

ii. Cross-Correlation Coefficients

As in some of the situations discussed above, the cross-correlation coefficient does not explicitly map to a theoretical quantity for easy predictions. Also, the computational power needed to correlate a series of full-frame images is excessive.

However, the method is robust. There are no constraints to what can be correlated except that there must be a fair level of contrast and signal. The biggest argument in favor of using the cross-correlation coefficients is in the normalization. With this method, normalization properties do not arise. The reason is the difference in how the terms are averaged. In this method, the normalized coefficients are averaged after they have all been calculated. It is a type of 'internal' normalization. This can be advantageous experimentally in many respects. For instance, with a varying incoming flux such as with the decay constant in electron storage rings in synchrotrons or with thermal loading on mirrors that are not adequately cooled constantly, the incoming flux can vary adding more parameters to the necessary normalization. The way the coefficients are calculated removes this uncertainty.

Another aspect is the coefficients are contrast independent. The intensity-intensity autocorrelation function has a resolution that is based on the contrast. In other words, the limits determine how well decays can be measured. For the cross-correlation coefficient, the limits are always the same, making it straightforward to measured the degree of change.

5. Momentum-dependent Statistics

We now turn to the momentum-dependence of speckle statistics. Here we will briefly discuss and show examples of the dimensionality dependence that can occur for both cases of the 3d and 2d forms of the photon momentum $\hbar k$. We will simply outline the process of calculating the q-dependence measured from the detector plane and state the transformation, leaving the detailed derivation to Appendix A for the interested reader. After demonstrating the momentum transform, we end the section with a discussion of dynamics as a function of momentum.

i. Geometry

Up until this point, we have kept the more general q-dependence in the equations that makes the above equations correct for any geometry, or experiment. We would like to digress momentarily here for the special case of the experimental geometry of our current experimental apparatus. We probe a special section of **q**-space since the detector is flat and $\mathbf{k}_f$ is always parallel to the normal of the detector plane for Bragg or specularly reflected x-rays. In what follows we will calculate the momentum explicitly, taking our geometry as an example.

The geometry of our typical experimental set-up is shown in Figure 5.5, where the momentum **Q** is given by $\mathbf{Q} = \mathbf{k}_f - \mathbf{k}_i$ and the k's are the final and initial wavevectors of the x-ray beam, respectively. The wavevetors have an absolute value of $2\pi/\lambda$ and give the direction of photons in momentum-space. In conventional diffraction experiments, **Q** is the main variable measured. From a more theoretical perspective, **Q** can be thought of as the transform variable, which gives the scattering amplitude as the Fourier transform of the charge density.

ii. Transformation

The momentum can be calculated by first performing a coordinate transformation of the initial momentum k_i to the final position k_f and simply taking the difference $\mathbf{Q} = \mathbf{k}_f - \mathbf{k}_i$. This consists of three rotations: γ, referring to the sum of the detector and chamber angle (usually referred to as the variable 2θ), and two small-angle rotations labeled as $\delta\alpha$ and $\delta\beta$, referring to the two orthogonal axes of the detector. All three angles are labeled in Figure 5.5. Note that $\delta\alpha$ and $\delta\beta$ are small angles, even though they are not drawn to scale in the figure.

It is worth noting here that this calculation is only valid in the small angle approximation, as the angular acceptance of the detector is about 30 mrad. We make this approximation using the two angles that the outgoing photons make with the specular or Bragg reflection. The scattering considered here is considered to be *Fraunhofer* diffraction since the distance from the sample to the detector distance L obeys the relation

$$kd^2 << L$$

where the approximate size of the region responsible for the scattering is denoted by d. In fact classically, L must always be much greater than d, as a diffraction
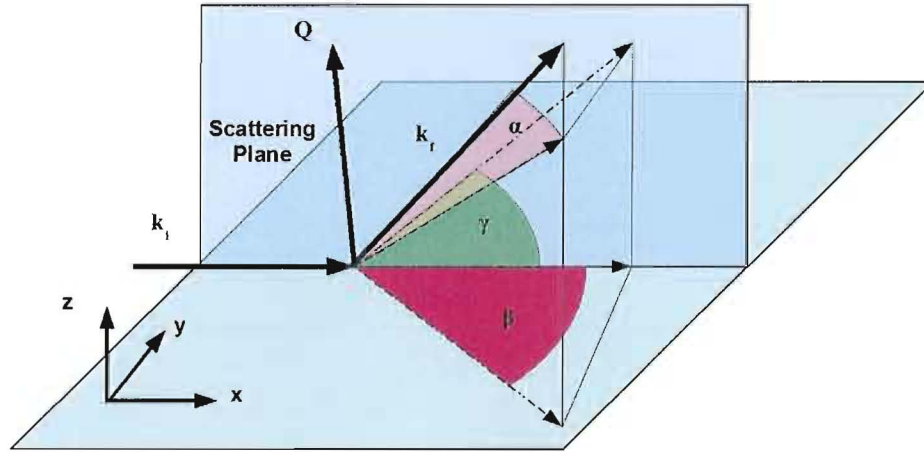
Fig. 5.5: **Q-space Geometry in the Laboratory Reference Frame** The figure shows the Q-space geometry for the incoming beam in the positive x-direction, where $\mathbf{Q} = \mathbf{k}_f - \mathbf{k}_i$. The incoming and final momenta are shown in the figure as well as their difference vector $\mathbf{Q}$. The dotted lines show vectors in the respective planes for clear demonstration of the angles involved in the transformations. The translucent plane (x-z) represents the scattering plane, constructed from the two momenta shown. The opaque plane (x-y) represents a Bragg plane of the sample (or surface plane in reflectivity). The figure is expanded to emphasize the angles and is not drawn to scale. For instance, in the text the angles α and β are small compared to γ, and are termed $\delta\alpha$ and $\delta\beta$. They are expanded here to clarify the geometry.

pattern will only become manifest in this limit [116]. Fraunhofer scattering sets an additional constraint based on the wavelength.

The result of the three coordinate rotations mentioned above is a momentum transfer $\mathbf{Q} = \mathbf{k}_f - \mathbf{k}_i$ of

$$\frac{\mathbf{Q}}{|k|} = \cos\delta\beta \begin{pmatrix} \cos\delta\alpha * \cos\gamma - \sin\delta\alpha * \sin\gamma - \sec\delta\beta \\ -\tan\beta \\ \cos\delta\alpha * \sin\gamma + \sin\delta\alpha * \cos\gamma \end{pmatrix} \tag{5.31}$$

where the upper case notation $\mathbf{Q}$ is for the total momenta and the lower case will be reserved for *relative* momenta. The standard notation is used for the vector components with x, y, and z labeled from top to bottom.

This gives the full relative 3d momentum in the small-angle approximation as a function of angle. To get $\mathbf{Q}(x, y)$ with position on the detector, we must again invoke the small-angle approximation, $\tan\delta\alpha = (y/L) \sim \delta\alpha$ and x/L for $\delta\beta$.

Lastly, to calculate the $\mathbf{Q}$ in the sample frame of reference, one last rotation must be performed by the negative sample angle about the y-axis, which of course leaves the y-component the same $q_y' = q_y = -\tan\frac{x}{L}$. Since we are interested in the magnitude of the *relative* $\mathbf{Q}$, we must take the difference in $\mathbf{Q}$ from the center of the Bragg peak, or specular reflection which is defined as $\mathbf{Q}_0 = (4\pi/\lambda)\sin\gamma$, before computing the magnitude. This involves a subtraction of the z-component only from the equation for $\mathbf{Q}(x,y)$, or

$$q = |\mathbf{Q} - \mathbf{Q}_0| \tag{5.32}$$

The result of this last rotation, the transformation of angle to detector plane coordinates, and conversion to $\mathbf{q}(x,y)$ is:

$$q_x' = \cos\theta\,(\cos Y\cos\gamma - \sin Y\sin\gamma - \sec X) \tag{5.33}$$
$$+ \sin\theta\,(\sin\gamma\cos Y + \cos\gamma\sin Y) \tag{5.34}$$

$$q_y' = q_y = -\tan\frac{x}{L} \tag{5.35}$$

$$q_z' = \cos\theta\,(\cos Y\sin\gamma + \sin Y\cos\gamma) - 2\sin\gamma \tag{5.36}$$
$$- \sin\theta\,(\cos Y\cos\gamma - \sin Y\sin\gamma - \sec X) \tag{5.37}$$

where we have used the short-hand notation of $\frac{y}{L} = Y$ and $\frac{x}{L} = X$. The second term in q_z' is the $\mathbf{Q}_0$ term. Note also that the $\cos\delta\beta-$factor in Equation 5.31 has been omitted in the component equations. A map of the q-dependence as seen by the detector is shown in Figure 5.6 according to

$$q = \sqrt{\sum_i q_i' * q_i'} \tag{5.38}$$

where the plotted magnitude is just the normal square root of the sum of the squares of all the components listed above.

iii.   Momenta in 2d

We have calculated the 3d momentum, but some systems only require a 2-dimensional functional dependence. This changes Equation 5.38 by removing the third component q_z completely, and changes the functional form considerably. Two comparisons are shown in Figure 5.7, for the same detector angle γ. The top is 3d while the bottom shows the 2d form. At this angle, near $\sim 60°$,
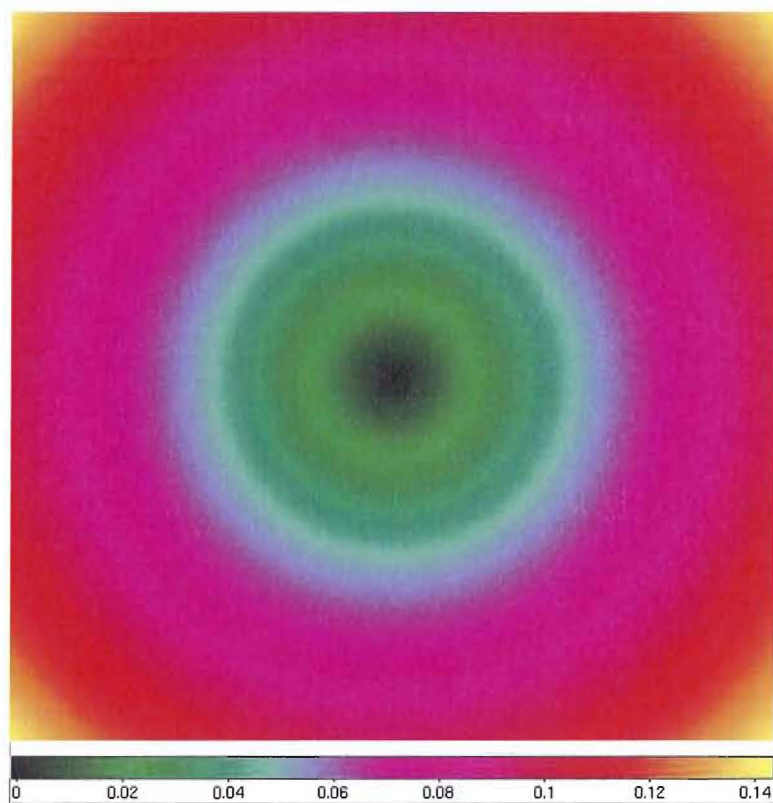
Fig. 5.6: **Map of q-dependence** A plot of the 3-dimensional momentum magnitude. The coordinate system is in x and y pixels for the detector, giving an effective q-dependence exactly as would be detected on the camera for a detector angle γ of $\pi/4$. A color map of the q-values is given below the figure, which is the same for all q-plots shown in this chapter. They have been scaled the same to emphasize functional form with respect to each other. The plot shown is for the calculation using Equation 5.38, where γ was chosen to correspond to a specular reflection illuminating the center of the detector.
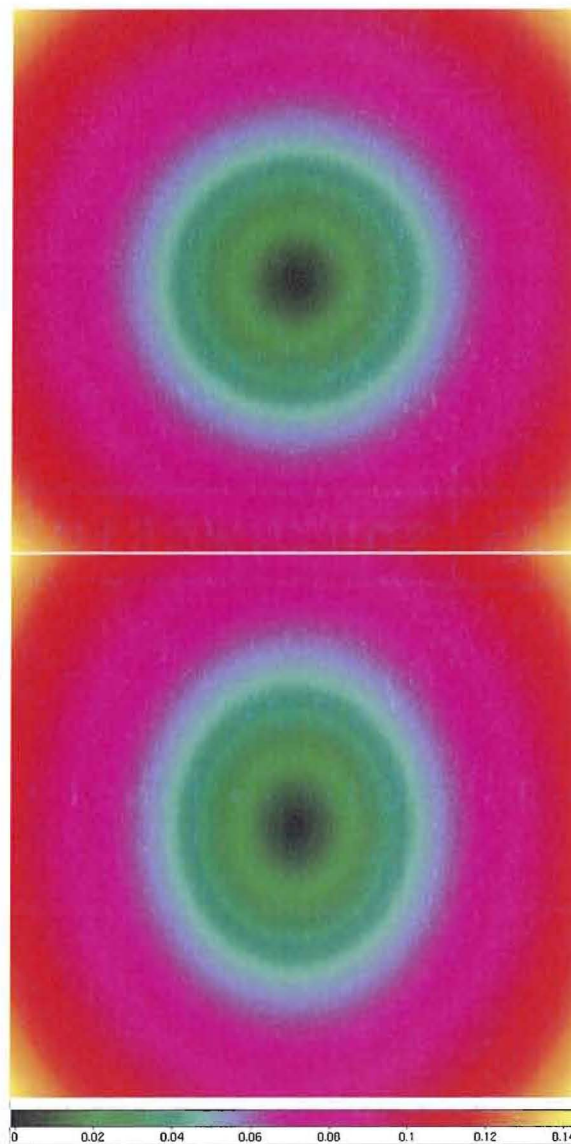
Fig. 5.7: **Q-dependence Map Comparison** Plots of the q-dependence for both 3-dimensional (top) and 2-dimensional (bottom) momenta. Coordinate systems are in detector coordinates with the color map below giving the magnitude of the total vector. These plots are both calculated for high detector angle $\gamma \sim 60°$. The 2d case is only shown to be slightly *stretched* in the vertical direction, the same direction as the scattering plane.

the form is similar. One can just make out the slight vertical elongation in the 2d case. The orientation is such that for a detector angle that goes to zero, this is the view seen by the direct beam, where positive y is vertical in the figure. The 2d dependence is much more strongly affected by the γ-dependence of the detector (See Appendix A for details). Figure 5.8 shows how large this difference is for two different detector angles. In fact, based on the difference in 2d and 3d momentum dependence, we have started to measure dynamics for both cases as a check on 2-dimensionality. For systems that behave like 2d materials, strong length scale dependent dynamics would not be apparent in the third dimension. For 2-dimensional systems, one would expect the dynamics to vary with the functional dependence shown in Figure 5.8.

In addition to 2d materials, another application where the 2d momentum can surface is technique driven as well. For instance, in a transmission geometry, or even to a large degree a grazing incidence reflection mode, momentum conservation can only be measured as 2d. In thin films, where small-angle x-ray scattering (SAXS) is usually used in transmission, q can even be assumed to be 1d, where the scattering is isotropic. As a result of the above transformations, data in the x-y plane of the detector collected during an experiment can be computed in terms of either type of simplified form.

iv. Q-dependent Dynamics

Another attribute q-dependent dynamics offers is the ability to decipher between physics and instabilities. For instance, Figure 5.9 shows the correlation map calculated by the formalism discussed earlier in this chapter. The vertical axis is τ, and here each unit of τ is two minutes. The horizontal is given in units of $|q|$, with each pixel of $\sim 0.01\,\text{nm}^{-1}$. The color map below gives the magnitude of the correlation coefficient. This series of images was taken while heating the system up by $10°\,\text{K}$. This image shows the drop in the coefficient to zero as a result of the system heating. The expansion of the apparatus as small as a micron can expand and translate the pinhole slightly across the sample. Even though slight, this motion can give correlations from frame to frame that decrease quickly. This figure not only confirms that illuminating a slightly different region of the system will produce a different speckle pattern, but we can deduce the instability by the lack of q-dependence. Note in the figure how straight, horizontally, the decay is. In real systems, it becomes possible to measure a difference for fluctuations at different q-values, as we will see shortly.
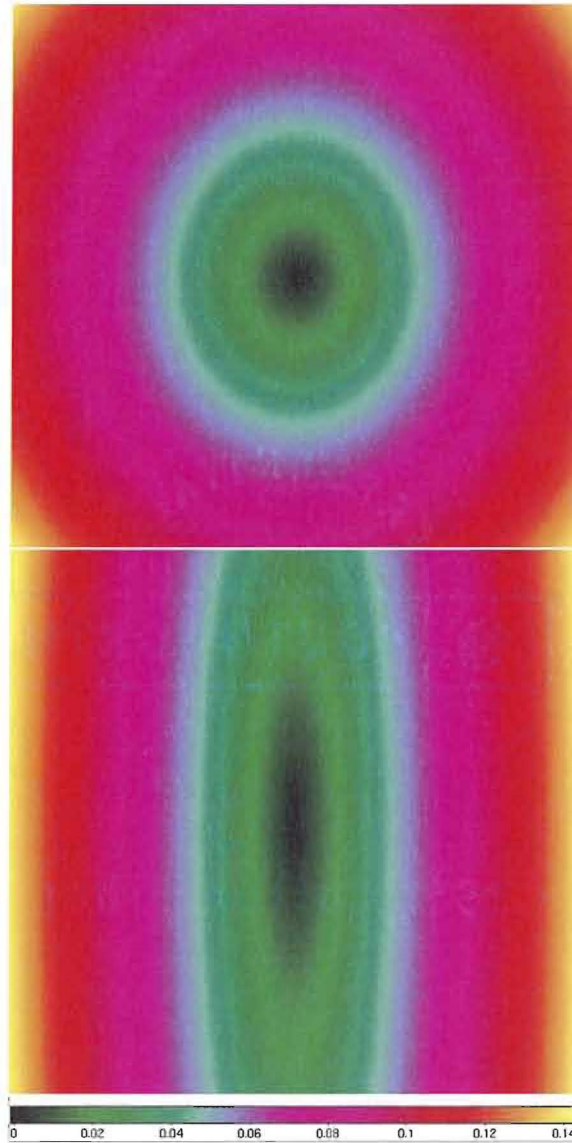
Fig. 5.8: **Two-dimensional Momentum γ-dependence** Plots are of the 2d q-dependence calculated for $\gamma = 62°$ (top) and $\gamma = 12°$ (bottom). The top is the same as in Figure 5.7 and is reproduced merely for comparative purposes. The demonstrates how strongly γ-dependent the momentum is when the system can be assumed to be two-dimensional.
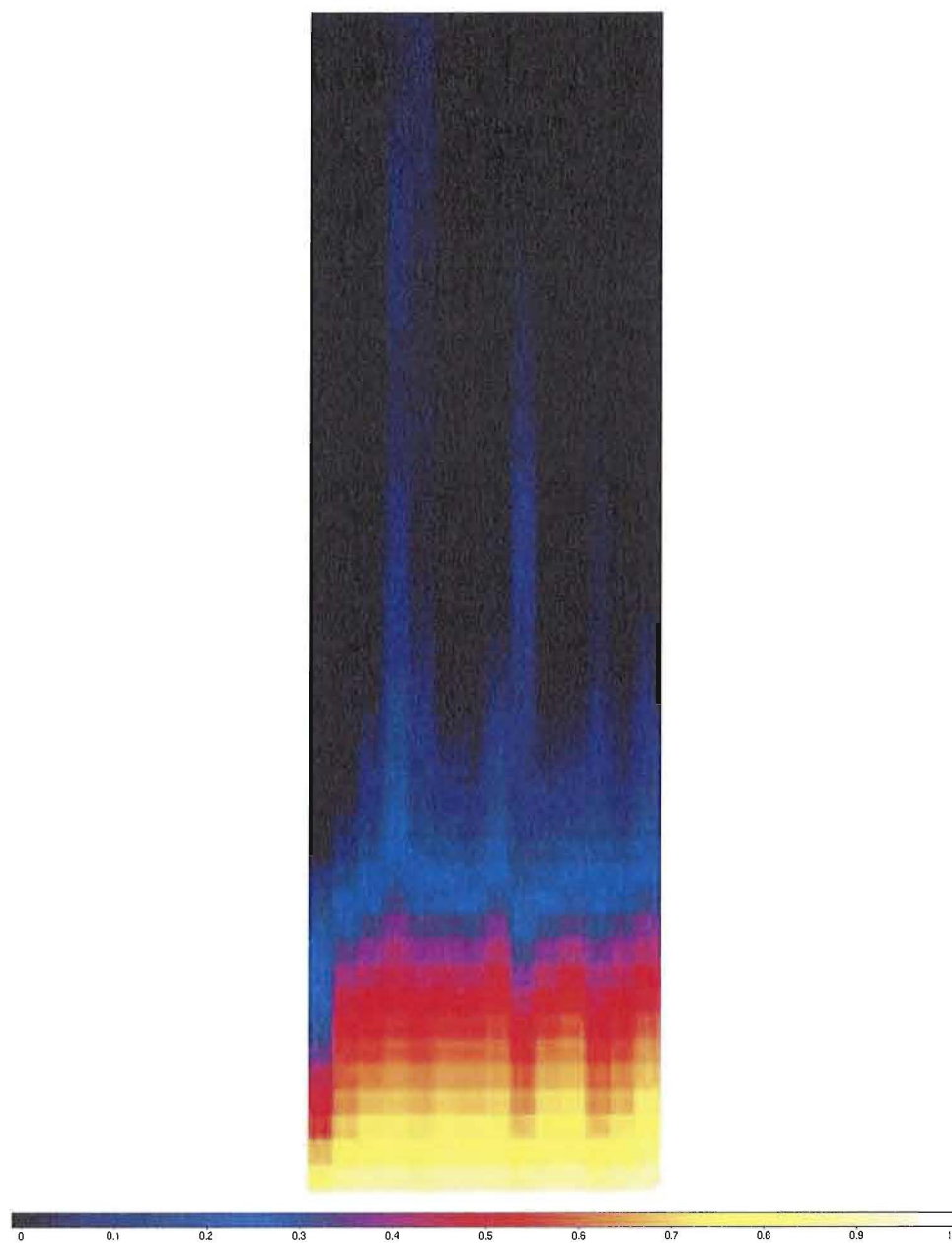
Fig. 5.9: **Correlation Coefficient Decay due to Thermal Expansion** Correlation-coefficient decay for speckle patterns as the system is heating up. This shows the coefficient not only going to zero, but a lack of q-dependence. The decay seems to be constant across q - the horizontal axis. Since each pixel represents a total accumulation of two minutes, it seems that after 20 minutes or so on average, the system has moved enough to fully decorrelate from images greater than $10\,\tau$ away.

CHAPTER VI

EXPERIMENTAL

> It doesn't matter how beautiful your theory is, it doesn't matter
> how smart you are. If it doesn't agree with experiment, it's wrong.
> - Richard P. Feynman

Coherent x-ray scattering experiments are extremely challenging and incorporate many aspects to make them possible. Only with the remarkable advances in synchrotron facilities and advanced instrumentation is the work described here conceivable. A number of those aspects are described in this chapter. First, we briefly comment on the source: the description and generation of synchrotron radiation. Next we will describe the beamline, which is how the photon beams get from the source to the experiment. Lastly, we will describe the endstation, the effective termination of the beamline and location of all experiments. A large number of people are responsible for many of the details described here as this part of the experiment includes an excessive amount of development and an enormous array of expertise in the the design, engineering, and construction at all of the different phases along the way.

1.   Synchrotron Radiation

The entire experiment is hinged on the generation of x-rays of considerable brightness created at synchrotron facilities. Without this source of x-rays of which presently, there are only a handful around the world, none of these types of experiments would be feasible. The basic idea will be briefly summarized here, with a more detailed account left for Appendix B.

The basic formulas of synchrotron radiation can be derived from classical electromagnetic theory, Heisenberg's uncertainty principle, and special relativity. Because any charged particle undergoing acceleration must emit radiation, synchrotron facilities are based on harnessing the radiation that gets emitted

when an electron or other charged particle undergoes some type of acceleration. In contrast, to particle colliders, or 'atom smashers', synchrotron facilities accelerate particles in vacuum which are never bombarded into each other or a target. By simply accelerating electrons in different ways, a wide spectrum of electromagnetic radiation can be created and used for a large array of experimental techniques. The radiation is transported, again still in vacuum, to the experiment through the beamline. The experiment is finally conducted in the endstation placed at the termination of the beamline, where the photons finally arrive. These endstations vary wildly from experiment to experiment based on the enormous range of types of experiments that are conducted at these types of facilities.

2. Beamline

Beamline 12.0 designed by the Center of X-ray Optics at Lawrence Berkeley National Laboratory started construction in 2002. The beamline has two branches, 12.0.2.1 which is used for testing x-ray coherence from specially fabricated optics and spatial filters, and 12.0.2.2 which is used for coherent soft x-ray scattering from magnetic and disordered samples. While the former is focused on the optics, the latter is mainly concerned with the use of the properties of the radiation to understand the systems being studied. Figure 6.1 shows a schematic of the two branchlines, with an inset giving the spectral coherent power for the 1st and 3rd harmonics. Some of the beamline characteristics have been published though mainly focused on the coherent optics branch, and a excerpt of some of the basic design principles of the coherent scattering beamline has been published in Chesnel *et al.* [117]. Here we give a comprehensive overview of the coherent scattering branchlines. Some of the numbers and details have been measured or worked out by our group as they can differ significantly between the two branches.

i. Pre-Monochromator

The first component the radiation from the source impinges is a four-jaw filter. This is a beveled edge in the direction of the beam on four sides, two vertical and two horizontal, that allows the central cone of the undulator to pass, while taking an enormous heat load from the beam. Because of its shape, the radiation has a larger footprint, absorbing a greater amount of the heat.
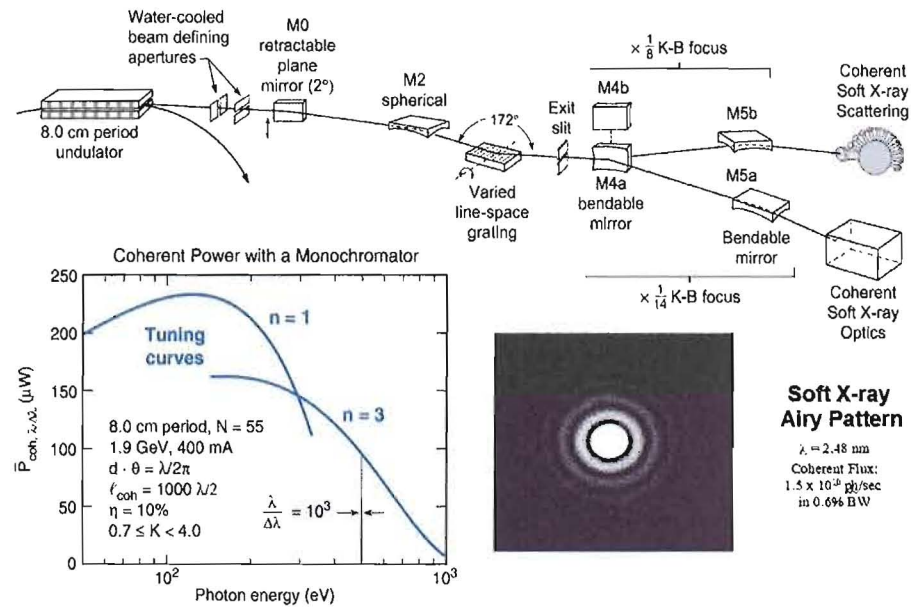
Fig. 6.1: **Coherent Soft X-ray Branchlines** The two branchlines for beamline 12.0.2 at the Advanced Light Source in Berkeley, CA. The schematic shows the optical layout and some of the beamline design characteristics. The two insets below show the tuning curves of the undulator and an example of an Airy pattern from a 2.5 μm pinhole at 500 eV. This represents the first example of coherence at this wavelength (Rosfjord *et al.* [119]).

By preserving the most important part of the emitted radiation, this does not affect the coherence properties or brightness of the x-rays, but just filters all the additional off-center radiation. This is important as it does not reduce any useful part of the beam for the experiments described here, but only affects a large and unneeded fraction of the x-ray beam that presents a considerable load on the optics. The four-jaw is water-cooled as the load being dumped from the direct beam is quite large. The positioning is important of this aperture as is its variable size. Each edge can be adjusted to be a beam defining aperture, but not a *coherence* defining aperture. In other words, it should allow the entire cone to pass, on the order of 60 microradians.

The second element before the monochromator is the M_0 mirror. This is simply a plane gold coated mirror. The deflection angle is small, on the order of 2° and deflects the beam from the 12.0.1 branch into the coherent science pair of endstations in 12.0.2. This serves to re-direct the beam while not affecting the focusing properties as well as absorbing unwanted power in the higher harmonics.

ii. Monochromator

The monochromator consists of a spherical focusing, grazing incidence mirror and a varied-line spacing grating. The mirror focuses the beam vertically through the grating onto a fixed exit slit. One of the features of the varied line space grating is to allow wavelength tunability without changing the focus at the fixed exit slit [97, 118]. The grating was a new version designed as a joint project by CXRO and Hitachi. It was created by the deposition of a low roughness gold film which was characterized, and shown to increase the efficiency by a factor of four [97]. To measure the energy resolution, we can insert a titanium thin film. This is followed by measuring the absorption spectrum of the transmitted light through the film on a photodiode or by measuring the photocurrent off of a metal coated mirror down stream of the film. Because the derivative of a theta-function is a delta-function, we can measure the width of the derivative as a function of energy to get a measure of the energy resolution. Here, this means physically, how much of an energy bandwidth must be scanned above the Ti absorption edge in order to absorb a given fraction of the beam. Theoretically, the monochromator should produce a resolving power of R = 1000 [119]. With much care, alignment, and effort, the largest resolving power that could be produced and measured for our beamline to date is 500. At present, this factor of two is thought to be due to large spherical aberrations on the spherical focusing mirror.

iii. Focusing Optics

The next set of optics is a pair of Kirkpatrick-Baez (K-B) mirrors, named after the two scientists who envisioned a way to overcome the obstacle of x-ray optics in the focusing of short wavelength radiation in 1948 [120, 121]. These are spherical mirrors coated in tungsten that are placed orthogonal to each other to focus the x-rays in each direction [97]. There are electronics allowing a slight bending to control the precise shape of the curved mirror. There is one for each direction transverse to the beam direction. Because these are also grazing incidence components, they externally reflect, and act like mirrors (analogous to total internal reflection with optical light when the index of refraction is always larger than one). The curvature determines the degree of focusing. The beamline demagnifies the source size by a factor of eight in each direction and by the square of that in depth. The vertical mirror, M_5 images the virtual source at the exit slit onto the focal plane at the center of the end station. The

exit slit is set to the desired energy resolution, and usually can vary anywhere between 5 and 30μm. Horizontally, the K-B optic M_4 images the source size, which is 10 m or so upstream. As discussed in Appendix B, the virtual source, given by the RMS dimensions of the beam emitted from this undulator is about 15 x 250 μm at the ALS. Naively, this would seem to yield about a $\sim$ 2 x 30 μm spot size at the focal plane with a 15 μm exit slit size. In reality, due to the depth of the source size (dependent on the undulator characteristics) and the grazing incidence focusing of the monochromator mirror, among other subtleties, it is not as straightforward to calculate. The focal area is about 30 x 250 μm and with only minor aberrations of the optics, represents an excellent spot size formation due mainly to exceptional x-ray optics.

Between the K-B system and the endstation is a multilayered mirror for measuring the focal spot of the beam. It consists of a 45° plane multilayered mirror that reflects at 250 eV due to Bragg-like diffraction. It gets inserted transversely into the beam. The beam is reflected vertically down another beam pipe to a YAG crystal attached to a transparent, glass view port where the beam can be observed as the crystal fluoresces. Mounted on top of the view port is a video camera mounted to a 3-axis translational stage. The two directions perpendicular to the beam direction allow alignment of the camera to the center of the focal spot, while the third gives the ability to focus. The image is captured on a video screen, with the option to convert to an image file via *MATLAB*. This diagnostic is extremely helpful because the actual focus is unaccessible inside the chamber. It allows a viewing and to be able to finely focus the beam while watching its shape in real time. Because of the strict confinement of the available space in the endstation, this focusing must be done outside the chamber. The beam focal spot is always minimized in area, and optimized in shape before removal of the mirror for the beam to enter the endstation.

iv.   Coherent Flux and Signal/Speckle

One of the main goals in the design of the beamline was to maximize the number of photons per second per speckle. One obvious attribute is to minimize the number of optics in the beamline. Two such optics for the focusing (in each orthogonal direction), and a spherical mirror for the purpose of increasing the resolution are necessary (although current designs are in progress to combine these in the next generation coherent scattering beamline at the ALS). The only other optic that is not needed is the first, but this is merely due to the need

to maximize physical space at the synchrotron by branching sectors to include multiple beamlines that share the same insertion device.

Another design goal aimed at maximizing this flux/speckle attribute was to demagnify the focal spot of the beam sizably at the center of the endstation. As discussed, the K-B mirrors image the beam onto the focal plane. Decreasing this image size by focusing rather than filtering, the signal per speckle is maximized.

In other experiments, the overall coherent flux may be of more importance. For instance, in some of the work we have done, we collect full speckle patterns instead of measuring time correlation functions per speckle. It depends on what physics one wishes to understand and consequently, what type of technique will best suite that goal. Coherent flux measured for the experiments performed on the manganites (near the L-edge of Mn) range from $\sim 2 - 5 \times 10^{11}$ photons/s for partially coherent flux, or about 700 photons/s per speckle. The former is comparable to incoherent flux available at 2nd generation sources.

3. Endstation

Figure 6.2 (A) shows the 'Flange-osaurus' for its comparison to Figure 6.2 (B), named by Dr. Stephen Kevan as a result of his research efforts focused in herbivorous reptiles of the orders Saurischia that were chiefly terrestrial and existed during the Mesozoic Era. It is a titanium ultra high vacuum scattering chamber embedded inside an electromagnet that applies magnetic fields through the chamber from outside vacuum. The chamber was designed by Jason Akre and detailed by Mike Wingert. The sample is inserted from the side using a sample manipulator and stage designed by Tom Miller. It includes a cryostat for liquid nitrogen or helium cooling. It is motorized by four degrees of freedom and includes a separate mechanism to control the pinhole mount. This mount has two additional piezoelectric mechanisms that control each direction of the pinhole perpendicular to the beam. The mount hangs off the end of the manipulator arm to filter radiation prior to the illumination of the sample. The flanges all along the spine nearly span the scattering plane and allow a series of detectors to be attached at any angle, depending on the type of measurements. The two ports along the chamber rotation vector are held on rotary seals, so the chamber can be rotated about the manipulator axis to span the small angles that are not able to be reached from the immovable chamber ports. This chamber rotation allows, theoretically, the full scattering plane to be covered. These details will be covered more in-depth in the following sections.
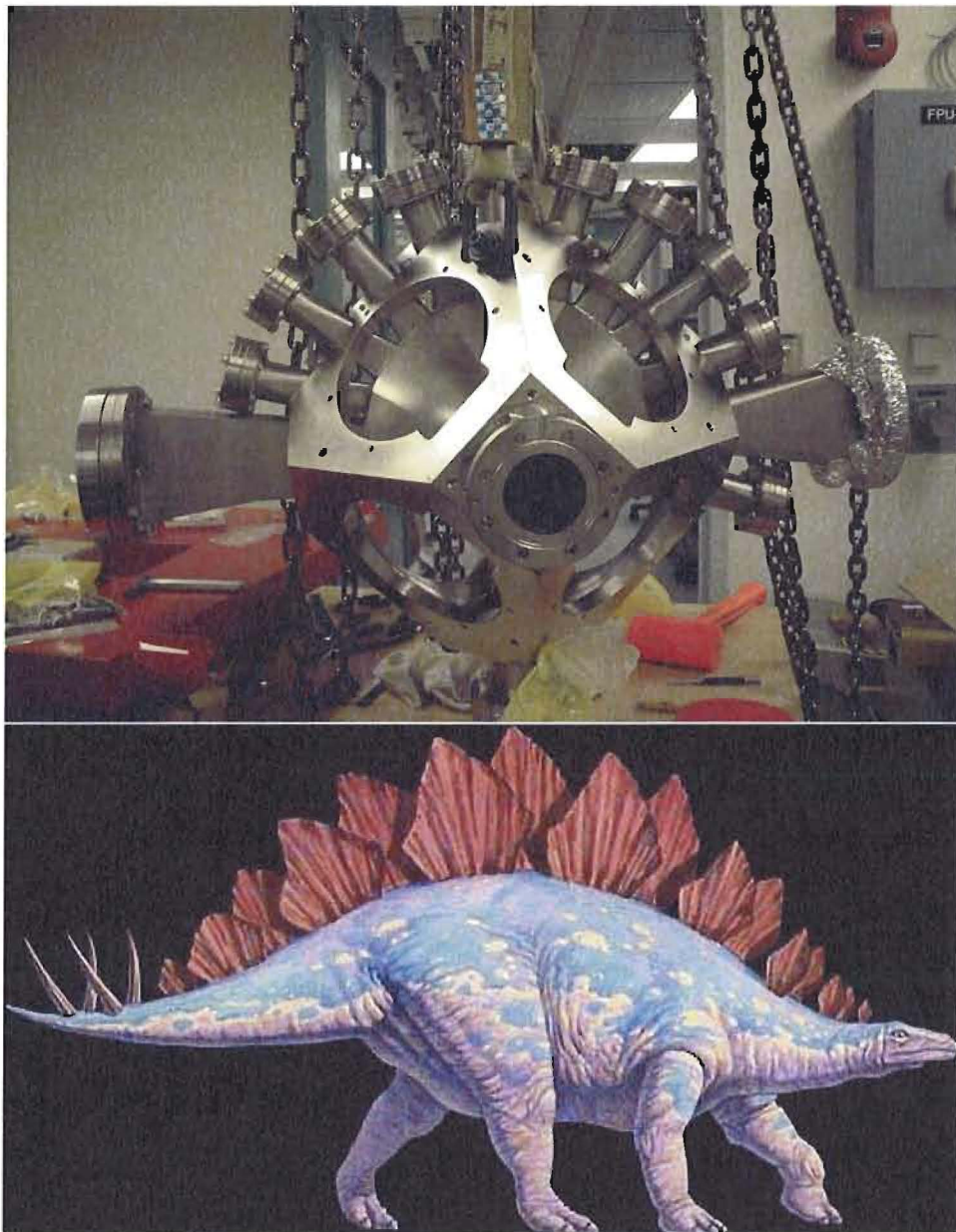
Fig. 6.2: **'Flange-osaurus' Coherent Soft X-ray Scattering Chamber** (A) The skeleton only of the 'Flange'-osaurus. The Ti chamber is shown with the steel yoke encompassing it. The magnets are not present to show the internal structure of the chamber. The yoke serves to support the chamber weight as well stabilize against large magnetic forces. (B) The Stegasaurus dinosaur that the chamber takes its name after. It ranged from about 25-30 feet in length, weighed about 7000 pounds, and displayed up to seventeen plates made of bone along the spine, usually in two rows (the chamber only has eleven).

i. Chamber

The chamber is shown in Figure 6.3 (see Appendix C for a more detailed sketch including dimensions). It was hand-formed from titanium sheets due to its non-magnetic character, and its robustness. The actual central portion of the chamber where the sample is studied is very small, which is important for the external magnet poles to be as close as possible to the center of the chamber to get the highest possible field density per magnet. This is a challenging constraint, as inside the magnet there must allow for a sample, sample mount, pinhole mechanism, and a cooling system to change the temperature of the sample. In addition is the needed ability to move the sample a fair amount to allow for alignment with both the beam and for the separate alignment of the pinhole to both the beam and sample. To compromise all these needs, the diameter of of this small central portion of the chamber was fabricated to be 41.15 mm. This distance becomes crucial in the design, as the magnetic field varies strongly with the pole-to-pole distance. It is so important, that this is even another reason for the use of titanium for the chamber material. For a given strength needed, Ti allows thinner walls to be used, and to gain slightly more in sample positioning volume.

Each flange is welded to the end of a tube originating from the center portion of the chamber that extends far enough away from the center to allow a detector to be mounted outside vacuum, and outside the magnet. The large, horizontal flanges are where the incoming beam comes in, and where a detector is set up to measure the outgoing flux or direct beam, when a sample is not present. The eleven flanges along the spine of the chamber, including the horizontals, are all equally spaced by 18° measured from the port centers. The chamber flanges are dispersed at specific points along the scattering plane, but with an area detector (or point detector when it includes an in-plane degree of motion), this only leaves a small region unaccounted for along the plane. The diameter at the flanges is 1.38" distanced 10 3/16" from the center of rotation, giving about a maximum 7.7° acceptance for detectors that are mounted at this first flange.

The chamber also has the ability to rotate. The chamber, magnet, and magnet yoke are all supported through rotary seals perpendicular to the scattering plane. This is the front and back ports with respect to the image shown in Figure 6.3. These joints support the weight of the chamber and against the vacuum load, while allowing to pump a small chamber outside the seals, assuring good pressure even with moving components. All pumping is done with
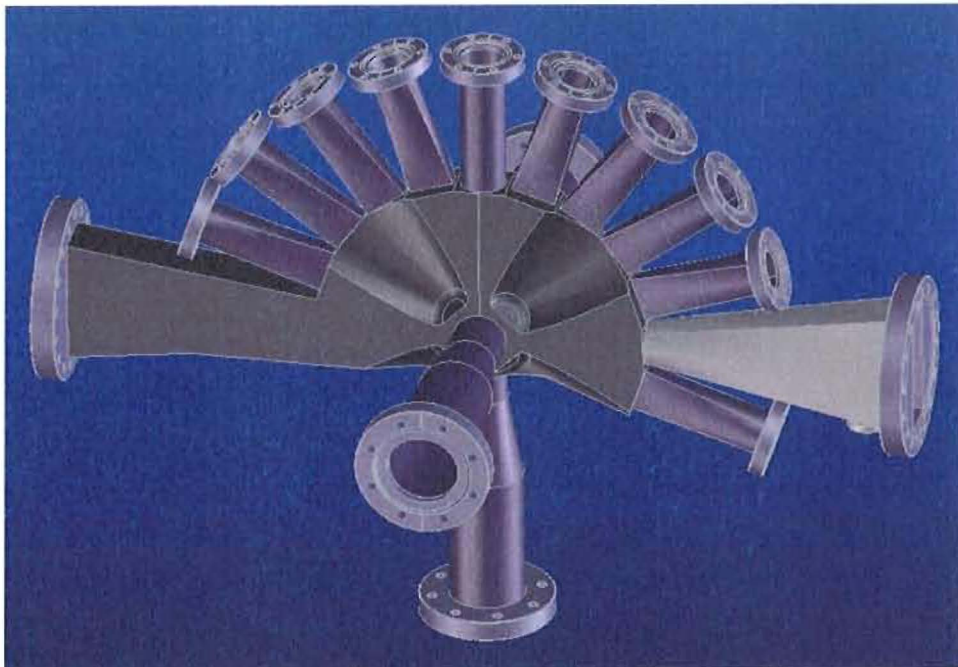
Fig. 6.3: **Titanium Chamber** The design of the vacuum chamber for the endstation. The large, beveled horizontal ports are for the incoming and outgoing x-ray beam when no sample is present to redirect the radiation. The series of ports along the semi-circular arc or for detectors along the scattering plane, and the transverse ports give the sample manipulator access to the center of the chamber. Note the grooves for a close fit of the magnet poles to be as close as necessary to the chamber origin.

turbomolucular pumps backed by roughing or mechanical pumps, typically dry, oil-free vacuum pumps. The range of chamber rotation is $\sim \pm 6$ degrees giving the possibility to span the entire scattering plane. However, in practice, the limit is set by upstream bellows and depending on the alignment of the beam, the edge of the upstream flange cutting the beam. There are only very few points along the plane that can not be reached with the apparatus.

ii. Magnet

What follows is a summary of the magnetic considerations of the octopole magnet. This is not meant to be exhaustive, but only a summary of the basic attributes. For a more detailed design account for a similar model and data on performance, see Elke et al. [122].

The magnet consists of eight electromagnets oriented on four corners of a cube. They are wired as four parallel dipoles in parallel, where each dipole pair is in a series configuration with one another. They are energized by four separate 80 V bi-polar power supplies, that produce up to 120 A of current. The bi-polar nature is necessary so the field can be applied in all directions. Just as a current loop provides a magnetic field transverse to the loop plane, these poles consist of current *coils* (for an increased field) directed towards the center of the magnet. In Appendix iv. the field calculations will be described in detail, but it is important to note here that the field vector is oriented from the each corner to the magnet origin.

For increased field strength, the coils are wrapped around 1010 steel, a ferromagnetic material. As is typical, the field strength is increased by a large factor for low currents, until the pole approaches saturation. Geometrically, the shape is important as the most efficient use of the ferromagnetic core is to have the Cu wire coils encompassing the most material possible. For the piece of the pole nearest the center chamber, the shape must be tapered off as they come to an almost 'close-packed' structure, where the poles fill most of the space outside the center chamber. This is shown in the photograph in Figure 6.4 of how the magnets, secured in the steel yoke structure, fit together without the chamber present. Magnetically, the tapered geometry is also important as the pole tips must be the first region of the pole volume to saturate first. This puts the highest field region generated by the magnet at the tips of the poles, and hence across the sample. Aside from geometrical considerations, without the largest volume of the pole near the surface of the magnet yoke, small excitation currents

would saturate the poles in this region first, affecting both the maximum field attainable and the field homogeneity at the sample.

The details of the magnetic field distribution are complex and the $\sim r^{-3}$ rule here does not apply because of the 3-dimensionality of the magnetic surfaces. The table below shows some typical values used [11] to design the volume of the central part of the chamber

gap [mm]	$B_{max}[T]$
15.84	1.1275
35.84	0.99958
50.8	0.81796

Tab. 6.1: **Field Strengths as a Function of Pole-to-Pole Distance** Numbers displayed are calculations [11] for the change in magnetic field strength as a function of the gap in mm between the ends of the electromagnetic poles. It is evident how sensitive the maximum field attainable is with distance. This sets strong physical constraints on the size of chamber inside the magnet.

Measurements of the magnetic field are challenging to perform due to the space constraints inside the chamber. Typically, a 3-axis Hall probe is used to measured the 3d fields. This consists of three perpendicular elements that act as magnetic field to analog voltage transducers. By reading out three separate voltage measurements per point in space, the vector field can mapped out. Measurements show we can attain a maximum field of 0.6 T, and that the spatial variation in field is fairly homogeneous across typical sample positions. Up to about a 2 mm diameter the field is constant. Passed this diameter, the pole-to-pole interaction generates stray fields that vary near the edges of the sample space quite dramatically.

The heat generated by the four dipole electromagnets is another aspect to consider in the instrument. Each singular pole is constantly water-cooled to minimize the heat load provided by the high-current power supplies. Copper coils of water tubes are wound around the wires that cover the pole surface in multiple layers. Furthermore, there is an additional cooling tube that makes a complete circuit inside the metal pole itself, though this is only a singular tube. There is a trade off here, obviously as well, as each cooling element that must be placed in the pole takes ferromagnetic core material away from the magnet, and hence reduces the field strength. This is the reason for such a large density of water tube coils around the outer surface of the piece. Note that the coils in the photograph in Figure 6.4 are actually of these copper water tubes, and not the current coils. These coils are directly under the water tube surface.
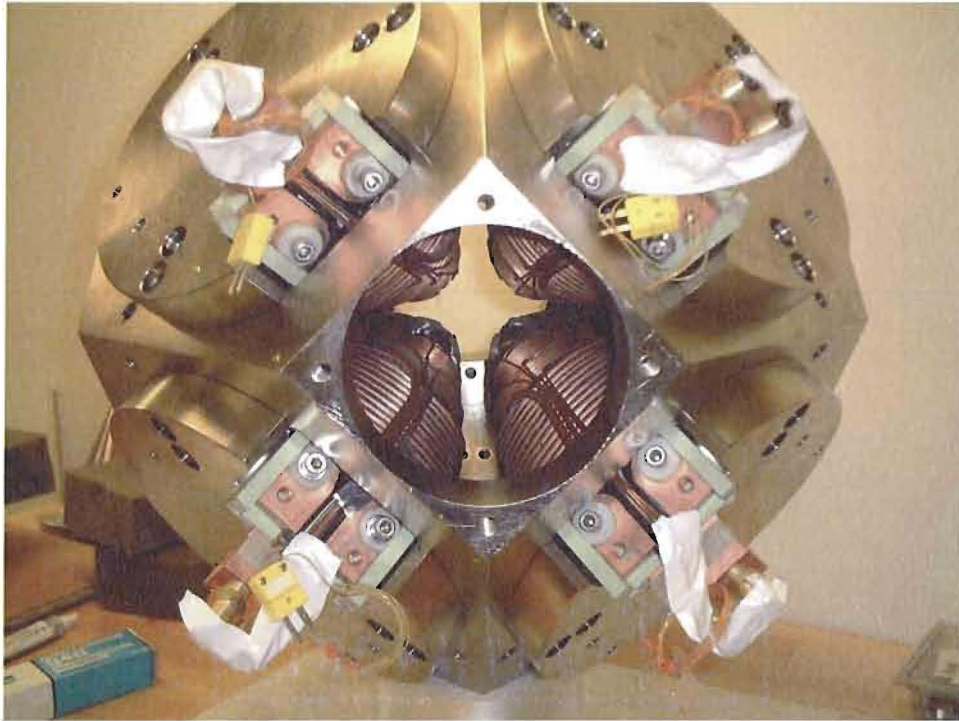
Fig. 6.4: **Internal Magnet Pole Configuration** The image shows how closely the magnets fit together around the chamber. The magnets were inserted into the yoke without the chamber present to emphasize the close proximity of the pole tips. This is important for maximizing the field with the given chamber constraints as much as possible.

So because the wire of the electromagnets heat up rapidly, there are cooling elements on both sides of the cone shaped pole surface. As discussed before, the magnet is designed to saturate first at the tip. Because this then means the tip should be the hottest part of the magnet, the measurement of the temperature at this point would be ideal. Due to space constraints however, the sensor can only be modestly close to the tip, and this must be taken into account for the temperature interlocking system. Typically, the current through each series element is limited to 80 Amperes. At this current level, the magnets heat up considerably fast, up to 90 K in a couple minutes. This provides another limit in dynamics studies in high-field, as we can only take measurements up to this length of time before the magnets are in danger of overheating, or melting crucial elements inside the coil packs. There is a temperature interlock system connected to the thermocouple readouts so that the power supplies will automatically shut down to protect the magnet from damage.
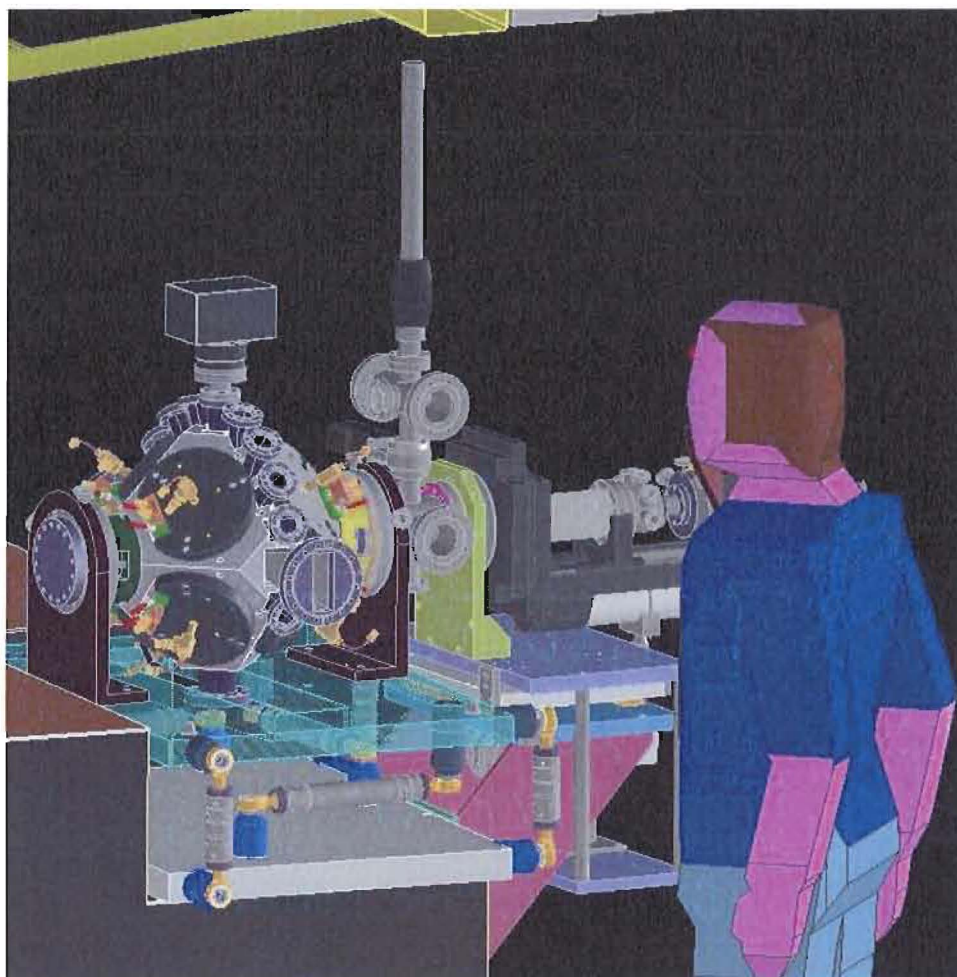
Fig. 6.5: **The Entire 'Flange-osaurus' System** The sample manipulator is shown attached to the side of the chamber through one of the rotary seal junctions. The vertical transfer moves the sample from its mounting chamber into the manipulator arm and is done by hand. The sample is then transfered into the chamber through motorized movements. The chamber also shows the magnet poles and yoke assembled. The whole system is atop a vibration sensitive table usually used in laser and optical physics to gain ultimate possible stability.

iii. Manipulator

The sample manipulator is used as the method of sample transfer to place the sample into the center of the chamber while under vacuum and is shown in Figure 6.5. It is constructed of all non-magnetic metals and includes a cryostat which allows for a removal of heat from the system down to liquid helium temperatures. In practice, the sample can only achieve about 15 - 20 K due to a lack of radiation shielding, impossible to include in the already tightly confined volume. Liquid helium is run through the inside of the manipulator and cools a copper element directly connected to a copper braid that the cools the sample. The sample holder has two diodes near it mounted to a copper block for a precise reading of the temperature, better than a degree for the diode closest to the sample.

There are three stages, for x, y, and z directions. These are controlled by M-drives, separate computer controlled motors for each orthogonal direction that can move the sample position to a few micron precision. There is a fourth degree of freedom also run by an M-drive motor that controls θ, the scattering angle of the sample. This is defined as zero for the orientation when the sample is inserted, before the sample is tilted, with respect to the floor. During the experiment, this definition is refined to be more precise by defining it to be when the the sample surface cuts the beam in half and is parallel to the beam.

Mounted vertically and transverse to the manipulator is a second chamber and transfer arm shown in Figure 6.6. This allows for a transfer of samples by hand. After the sample has been inserted into the sample transfer chamber, the chamber is pumped using a roughing pump-backed, Varian turbomolecular pump. Because of the small chamber volume and a dry nitrogen purge which is used prior to any venting of the chamber, a sample can be switched and transfered in a matter of minutes. The sample is placed into the sample transfer arm and pumped while isolated from the rest of the system. A valve is opened that connects the sample transfer chamber with the scattering chamber. With correct alignment, the sample is inserted into the manipulator sample holder effortlessly. The sample transfer arm can then be retracted and the chamber valved off. Once the sample is secure in the sample holder part of the manipulator, the remaining alignment is all computer controlled.

The sample is mounted inside a copper or silver coated copper puck that fits into a hole drilled from the center of the copper block piece shown in Figure 6.7 and in a close-up view in Figure 6.8. The hole has a spring around the
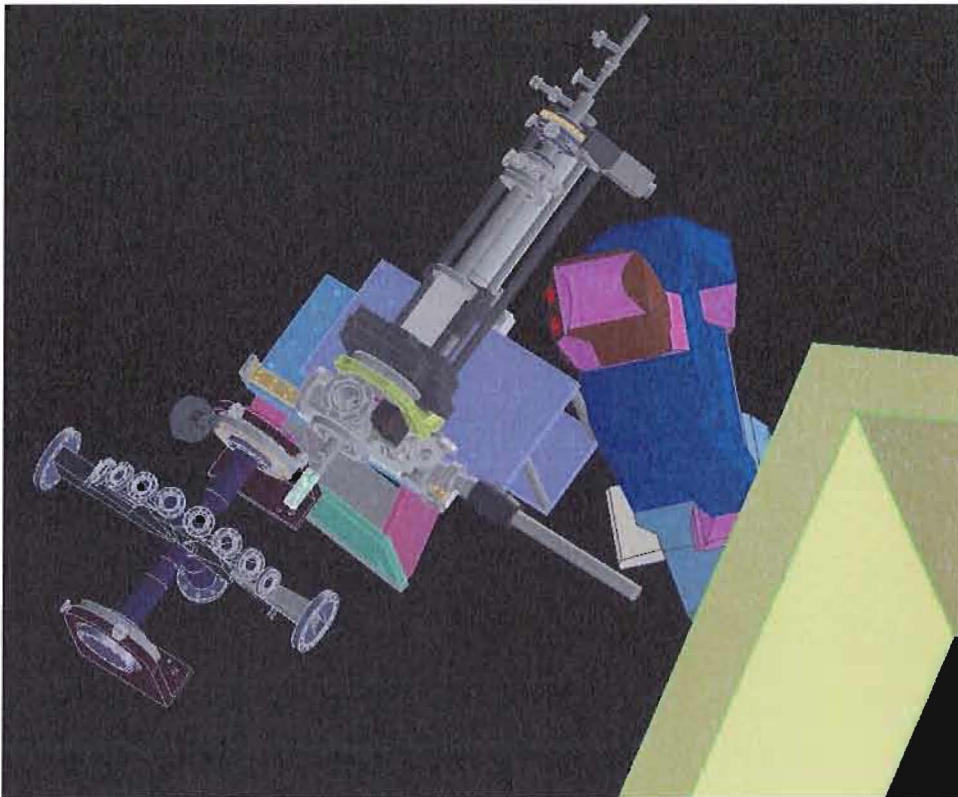
Fig. 6.6: **'Flange-osaurus' System without Magnet** The sample manipulator is shown disengaged from the chamber, a typical set-up for maintenance or for changing equipment. The whole manipulator comes completely out, and then is on a slide on the table so that inside can be reached and worked on from the beamline. This is typically how pinholes are changed for instance. The system is shown without the magnet and yoke to show how small the chamber actually is without the magnet covering it.

Fig. 6.7: **Manipulator** The sample manipulator is shown with the pinhole mechanism attached to the end. The large cylinder at the center of the manipulator is a 4.5 inch bellow needed when the sample is transfered into the center of the chamber. The cryostat is in the center of the cylinder and is connected to a liquid helium or nitrogen supply from the back end. The five feedthroughs near the back end are for bender and inchworm control, feedback for each, and a sample current readout.

circumference to hold the sample puck when it is inserted fully. The size of the disk the sample attaches to is 4 mm glued to a holder of diameter of 6.35 mm. (Note: the system has since been upgraded to a larger sample mounting system since the time of this work. The new numbers are now 6 mm and 8.38 mm for the sample size and holder, respectively). The sample puck also has a ridge around the circumference enabling it to be secured and transfered by the sample transfer arm (the vertical arm in Figure 6.5).

iv. Stability

As stability is crucial for coherent scattering experiments, measures were taken to ensure the best possible stability. One was the design of the sample and pinhole being confined to the same element. This was to ensure minimum relative motion between the two. Another thing is a vibration sensitive optical table, usually used for precision laser experiments. This has a damping coefficient designed specifically for the weight of the entire apparatus. Both endstations for the Coherent Science Beamline, as well as all the optics downstream of the monochromator, are all mounted to this optical table. The table can be seen underneath the chamber platforms supporting the endstation in Figure 6.5. Another effort for increased stability is in pumping. Turbo pumps are always used to minimize vibrations to the chamber, and even are sometimes mounted on special connections to increase stability even more.
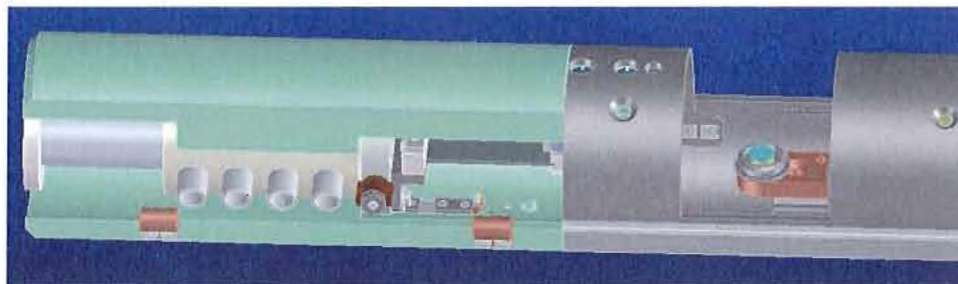
Fig. 6.8: **Sample Holder and Pinhole Mechanism** This image is the design of the end of the manipulator, showing a close-up view of the mechanism outlined in the red box in Figure 6.7. The sample in the figure is shown as the blue disk sitting on top of the copper sample holder. The pinhole can be see protruding from the end piece even though it is fully retracted. The four coils shown are the high voltage leads for the inchworm.

v.   Pinhole Mechanism

The pinhole mechanism is mounted off the end of the manipulator. The idea of having the pinhole and sample mounted to the same support was, as mentioned above, based on the cooling of the system. If each component was cooled through the same mechanism, the relative motion of the two should be minimal. The pinhole plane is mounted to two separate piezo-electric motors for high precision motion. The horizontal direction is controlled by a high precision inchworm motor with a spatial precision of tens of nanometers determined by its encoder, while the vertical is controlled by a bender, capable of a step size of better than a microns.

vi.   Pinhole Spatial Filters

Mounted to the pinhole plate are Si_3N_4 windows covered in $1.5\,\mu$m of gold. This was evaporated using a deposition system at LBL. The process involves attaching the windows to a flat table. A gold source is heated until evaporation and accelerated towards an aperture placed above the membranes. The table is then rotated rapidly in the presence of a evaporated gold gas particles, ensuring a homogeneous film deposition onto the silicon nitride membranes. The width of the film can be finely tuned by the rotation speeds and the voltages used.

Fabrication

Apertures were formed using a Focused Ion Beam (FIB) Microscope at the National Center for Electron Microscopy. Gallium ions are extracted from a
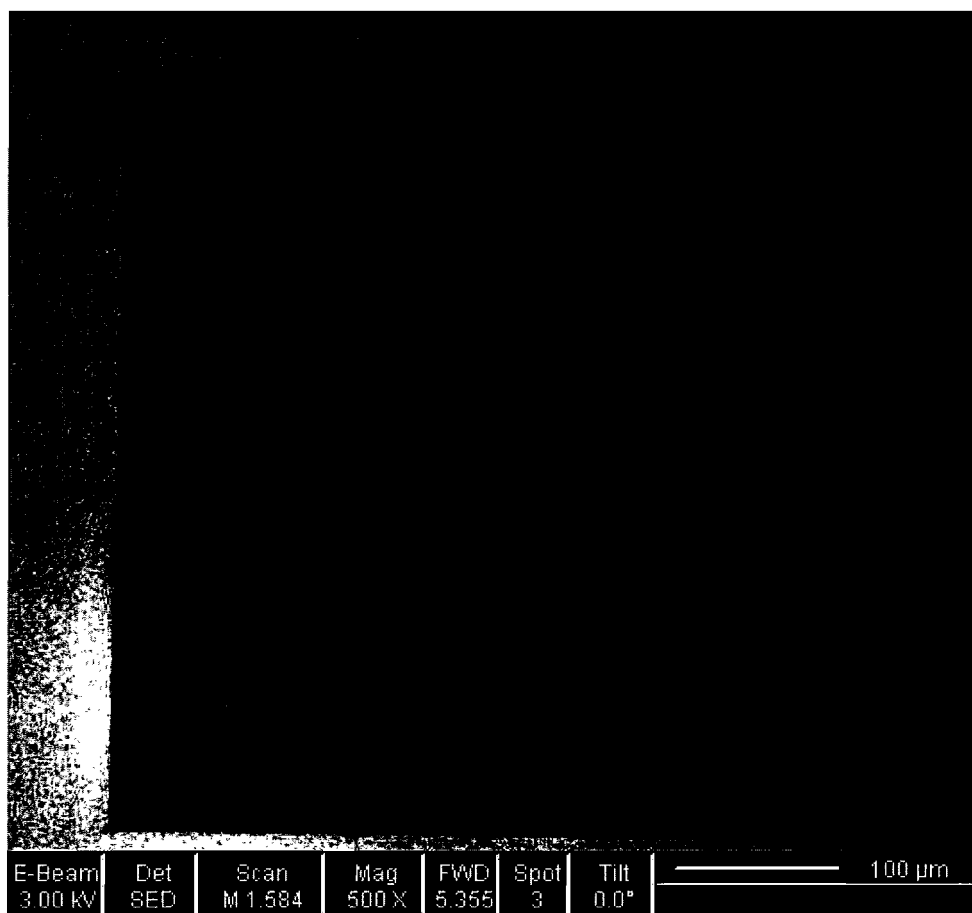
Fig. 6.9: **Pinhole Array** SEM image of gold pinhole array etched by molten gallium ion bombardment. The apertures here range from a few μm up to 25 μm, usually used as an indicator of the array.

sharp tungsten tip - as wide as a few nm - by application of an electric field. The source is molten Ga which is heated and extracted from the tip by a large bias voltage on the order of tens of kilovolts. The small source size opens the possibility of using a very narrow, well-defined beam size with the use of apertures and electrostatic optics. First FIB microscopes were originally used to both mill and image, but with the improvement of dual-beam microscopes, the ion beam can be used to etch structures while an electron source can simultaneously apply a beam of electrons to the same point. This way, images can be formed using an electron microscope in real time during mill sessions.
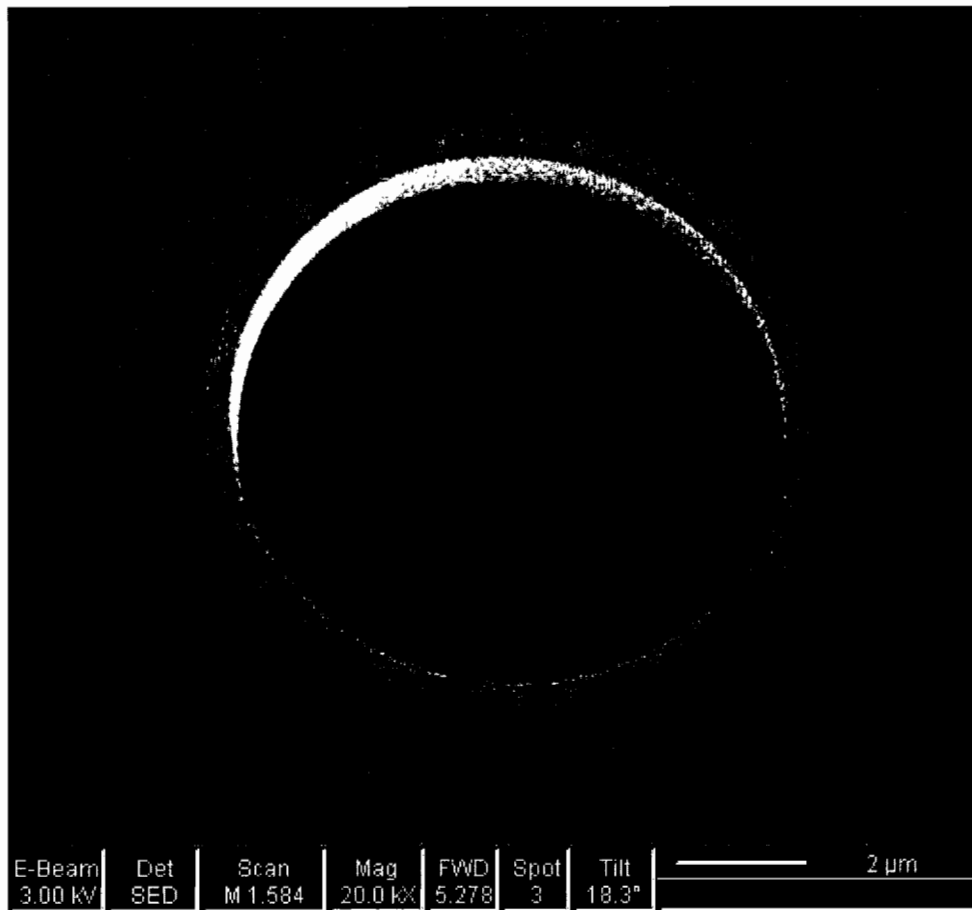
Fig. 6.10: **Sample Pinhole Close-up** An 8μm gold pinhole imaged by secondary electrons in the dual-beam microscope. The width of the gold film can be estimated from this image to confirm it is of order 1μm.

Examples

Figure 6.9 shows scanning electron microscope (SEM) images of gold pinholes etched by Ga bombardment. The present set-up contains two such arrays. A typical hole is shown in Figure 6.10. Usually because of the range of motion allowed by the piezo-electric stages, the pinhole plate consists of a series of pinholes of various sizes. The particular array in Figure 6.9 was chosen based on the fact that the beam is about $\times 100$ larger in the horizontal direction. This allows additional holes to be placed closer together vertically while still only illuminating one hole at a time. The horizontal are staggered for this reason. The figure shows six such holes, with a large aperture to find the array, usually of order $30\,\mu\text{m}$, and a incredibly small hole for imaging. This process is two-fold: both for holes that get clogged by hydrocarbons after long periods of time and for the additional options of changing the coherence length of the beam illuminating the sample. The pinhole mechanism is an important part of coherence experiments for the necessity the control the trade-off between contrast and coherent flux.

vii. Detectors

A variety of detectors are useful for the experiments described in this work. Here we will describe three: photodiodes used mainly for alignment and flux measurements, CCD cameras capturing the majority of the data, and channeltrons to be used for fast dynamics. A fourth measurement is made, but does not properly go under the definition of detectors. This is metal coated mirrors used as focusing lenses, where the photo-current can be measured from the thin, conductive tungsten mirror coating. These are used to check flux measurements in beamline alignment diagnostics and in measuring the degree of spectral resolution by the monochromator.

Photodiode

Photodiodes are semiconducting devices that create electron-hole pairs when illuminated with soft x-rays. The electrons are read out as a photocurrent proportional to the photon flux incident on the diode. They of course have a spectral response, and previously could only work in the soft x-ray regime when the commercial window is removed. This was a protective cover over the active area that is transparent for extreme ultraviolet photons. Soft x-ray photodiodes are now commercially available from International Radiation Detectors.

Charge Coupled Device

Charge Coupled Device (CCD) detectors have attained much popularity as of late for their high sensitivity and quantum efficiency. They consist of a large array of 'buckets' each able to collect charge in an isolated area. The idea for each element is similar to the photodiode in that the photons are converted to charge. However, in a CCD, the analog signal is not directly read out from the area element, or pixel. Instead each pixel accumulates a total charge over the accumulation time, determined by a mechanical shutter upstream that opens and closes in synchronization with the experiment. After one accumulation time, the first pixel at the edge of the array is read out, leaving an effectively 'empty' pixel. Each adjacent pixel then moves its charge to the neighboring pixel, followed by the same pixel being read out. The process is continued until the entire row is read out at which point the next neighboring row, one unit along the columns, is shuffled into the original row and the process repeated. This continues until the entire 2d array of pixels is read out and digitized. The data is saved into 2-dimensional images, usually of FITS format. To read out the entire available array without any binning usually take slightly under 2 s.

To reduce the thermal noise accumulated on the chip, the camera is cooled with a thermoelectric cooler. Additionally, there is a water cooling system attached to the cooling device of the detector to remove heat more efficiently. This is connected to a water supply system at the ALS and keeps a constant flow of water on the CCD. The detector is usually kept at about $-50°$C. In practice dark images are taken with the same accumulation time without x-ray illumination to be subtracted from the data to account for this. This is necessary when there is parasitical light in the chamber not related to the x-rays, or when there is any type of blemishes or defects from over-exposed pixels on the chip. However, the subtraction is also useful to remove additional counts accumulated from thermal and readout noise that are always present, when parasitical scattering or camera defects are absent.

The characteristics of the CCD used for the experiments described here are of extremely high quality, and are among the best available at the present time. The readout noise is of order 10 electrons per ADC count and the total active area of the CCD chip is 2.56 cm square, covered by 2048×2048 pixels. Each pixel measures 12.5 μm on each side. The software used to control the acquisition and readout time is made by Andor. The program also gives the ability to choose a special region of the chip for measurement, or for binning pixels. Binning is

to combine a given number of pixels together into a single pixel, or bin, in the sense that the charge collected for each pixel in the new bin of choice are all added together. This for instance can be used to 'create' pixels that are a factor of two bigger in each direction to get faster readout times at the cost of some spatial resolution. However, this only gives a readout time gain by a factor of two and not four based on the mechanism used for readout mentioned above.

The mode of choice common for using the CCD as a time correlation detector is kinetic series mode. Here, the active area, or special region of the active area chosen, is used to capture an image. After digitizing the information, the next image is captured. All images are saved in memory finally readout after the entire set has been acquired. This way, each image is separated by a precise time, the length given by the readout time of that particular region of the camera. In this way image sets can be taken, or movies, with not only the same acquisition time for each collected image, but with equal time spacing in between images as well.

Single Channel Electron Multipliers

Single Channel Electron Multipliers, or channeltrons, are detectors capable of measuring ions or photons based on the photomultiplier tube idea. That is, an avalanche effect. When a charge ion or a photon interact with the active area, one or more electrons is ejected from the surface. By applying a large bias voltage from the front of the detector the the back, the ejected electron is accelerated through the device to the back end where the signal is read out to fast electronics. The shape of the channeltron shown in Figure 6.11 accentuates the process. As the ejected electron hits the curved surface, it releases more electrons. Each ejected electron has the opportunity to channel the same process. This gives a large gain per detected particle, and can be tuned with the voltage. The voltage can either be a negative bias, grounded at the back terminal, or a positive grounded at the front of the cone.

For an increased efficiency, the surface can be coated with a potassium bromide layer. Typical efficiencies for different coatings are shown in Figure 6.12. Data were taken by Burle Electro-Optics engineering division. The specific coating we use is not shown on the graph, but has been shown to be even higher than the cesium bromide, estimated between 50-60 %.

The advantage with the channeltron is the exceptional gain, up to $\times 10^8$, and rapid readout times. In principle, separate pulses can be differentiated at
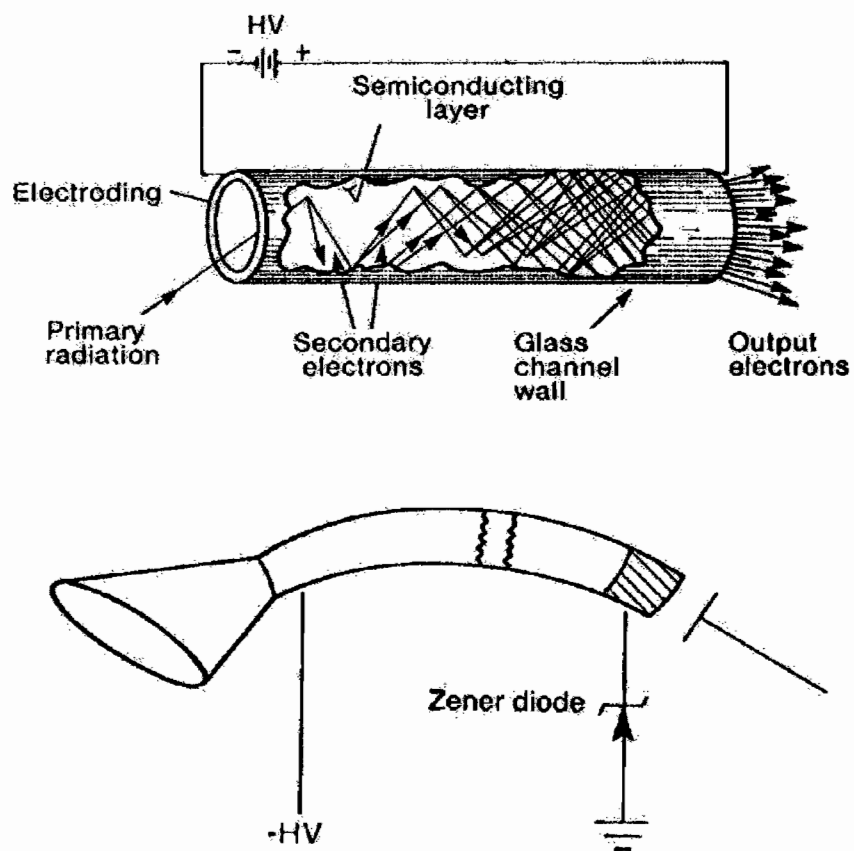
Fig. 6.11: **Channeltron** Top: The schematic of the process involved with a channeltron. The bias voltage accelerates any particles ejected by photons, which in turn create more ejected particles. The time constant for this process is extremely fast, on the order of tens of nanoseconds. Bottom: The shape of the channeltron. The curvature helps to accentuate the avalanche process described in the text.
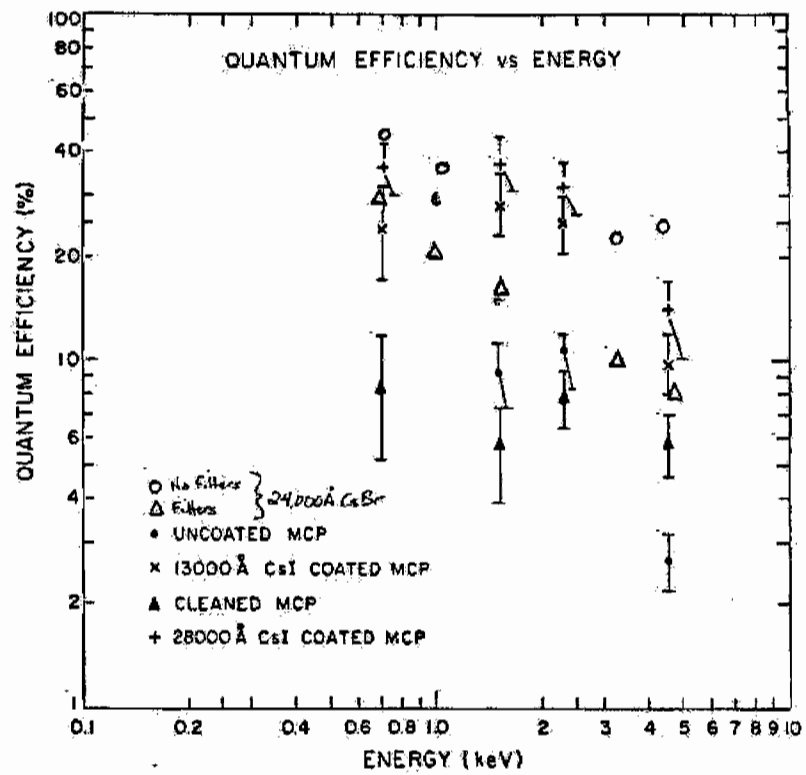
Fig. 6.12: **Channeltron Quantum Efficiency** Plots show quantum efficiency for an array of coatings for channeltrons made and tested by Burle. The level of gain with coatings is sizable.

tens of nanoseconds timescales (though electronics readouts typically limit us to about μs times). The difference though is that there is no spatial resolution as in an area detector. This fact then gave us the idea to use the CCD for spatial detection, window a given area measured on the CCD by using a pinhole aperture, and then to collect all photons through the detector aperture using the channeltron. This is limited by only allowing a measure of one speckle at a time, but advantageous in measuring fast correlation times. In principle then, one could measure fast correlation times per speckle, and measure multiple coherence areas as a function of momentum in this way.

The pulses are run through a pre-amp, and then directly into a digital auto-correlator. This correlates pulses from the detector in real time through commercial software. This automatic correlation is fast and easy, and removes the need to correlate everything 'by hand', as has been discussed at length in previous chapters.

CHAPTER VII

RESULTS

A man should look for what is, and not for what he thinks should be.
- Albert Einstein

In this chapter, we summarize some recent results from a half-doped manganite single crystal system: $Pr_{1-x}Ca_xMnO_3$. This system has a strong coupling between orbital, charge, magnetic, and lattice degrees of freedom, and is a puzzling system in manganite physics for its insulating ground state and its lack of a zero-field CMR transition.

We will describe the coherent soft x-ray resonant scattering experiment on this system in detail. By using the adsorption edges of the Mn L-edge to enhance the cross-section of elastic scattering from the electronic structure of manganese in $Pr_{0.5}Ca_{0.5}MnO_3$, we are able to measure scattering from the orbital ordering mechanism. The measurements allow us to make a number of conclusions about the physics of orbital ordering and the phase transition from the ordered state to a paramagnet. Near the transition temperature, we observe a small fluctuating component in the scattered signal. In addition, there is a rapidly decreasing total signal and orbital domain size correlated with the temporal fluctuations, as well as an abrupt onset of a broad background intensity. We attribute the latter to the production of correlated polarons, generated simultaneously as the melting of the orbital domain state. Our speckle results suggest that the transition is characterized by a competition between pinned orbital domains that remain static and mobile domain walls that exhibit slow, spatiotemporal fluctuations. We conclude with some discussion of the results that set the stage for a whole range of future directions in manganite and other complex oxide coherent experiments.

1. Disorder

In the last decade has there been a resurgence in interest due to the discovery of the colossal magnetoresistance (CMR) phenomenon [14], in which disorder has emerged as a key ingredient to understanding the magnetoresistance mechanism in these materials [14]. In fact, Akahoshi *et al.* has shown that without some amount of quenched disorder, the CMR phenomenon is absent [123]. We will briefly discuss two type of disorder here: a structural, as well as an orbital disorder. The structural is set by twin boundaries present from the growth of the single crystal. The measurement of orbital order is hinged on the structural as it is only possible to be measured in crystallographic domains which are oriented in the [010]-direction. We map this using microdiffraction at high energies. By zeroing in on crystallographic domains of this type, we finally use coherent x-ray scattering to study the heterogeneity due to *orbital* domain disorder.

2. Hard X-ray Microdiffraction

One example of this disorder that permeates these systems is in the crystallographic structure induced by twinning. Using a different set-up then the one described in detail in this thesis, housed at the National Synchrotron Light Source at the Brookhaven National Laboratory, we imaged the crystallographic domain structure by microdiffraction at the energy of 8 keV. The experimental set-up of this experiment is described more thoroughly in Appendix ix..

Bragg's law, simply stated, is just a relation between the outgoing phases of scattered photon amplitudes from a crystal. Because it inherently includes a degeneracy by the fact that it only keeps track of phases within one wavelength, different structures with different orientations can give rise to scattering at the same angle. There are three types of domains present in the $Pr_{1-x}Ca_xMnO_3$ system that can be measured for many orders, that all occur near the same Bragg angle. For the fourth order in $\hat{h}$ and $\hat{k}$ and 2nd order in the [112]-direction, the (400),(040), and (224) Bragg peaks can be accessed with the wavelength of $\lambda = 1.545\text{Å}$. This set was chosen because the higher the order, the more spread out in reciprocal space the separate peaks would be. The upper limit is set by the instrumental limitations in at the beamline. These Bragg peaks give angles 2θ of $70.134°$, $70.015°$, and $70.198°$, respectively. Remembering of course, that

to calculate d for an orthorhombic unit cell, we must use

$$\frac{1}{d^2} = \frac{h^2}{a^2} + \frac{k^2}{b^2} + \frac{l^2}{c^2}$$

where the right-hand side of the equation contains the usual reciprocal lattice vectors as numerators and Bravais lattice vectors as denominators.

The idea of this microdiffraction experiment then was to align to a certain Bragg peak and to scan the sample through the incoming beam. When the domain crosses the path of the beam for the given geometry, the result is a large scattered signal when the right domain is being illuminated. This way, the crystallographic structure could be mapped out in real space. Fig.7.1 shows two such maps, for the (040) and the (112) domains.
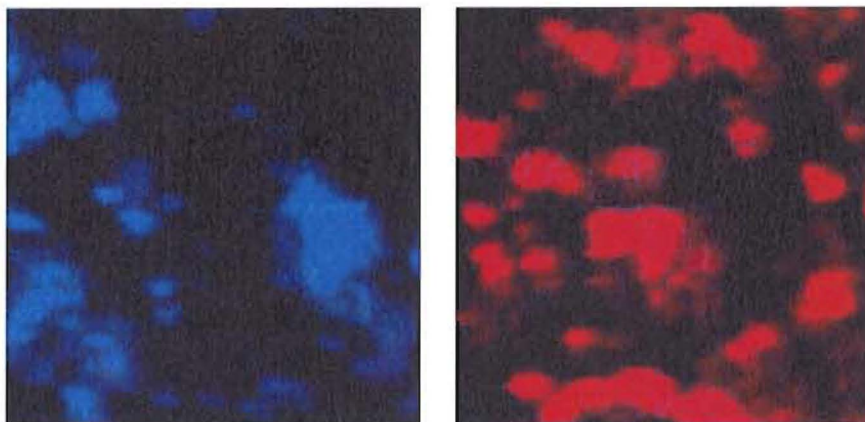
Fig. 7.1: **Hard x-ray microdiffraction imaging of crystallographic domains** Real space images from [010]-oriented (blue) and [112]-oriented (red) domains in PCMO.

Fig.7.2 depicts the addition of the two images to show the complementary structure to emphasize the fact that the region separates into distinct crystallographic domains. The empty regions near zero intensity in the image, could represent where the [100]-domains reside, or some combination of any of the three domains where mosaic may lead to reduced diffraction reaching the detector. These images demonstrate the challenge of aligning to the right domain when the separation of crystallographic domains becomes necessary in isolating the correct order parameter, as in the need to align to domains that give rise to magnetic scattering for instance, to study diffuse scattering from magnetic domains.

The difference of the two images for the same 250 x 250 micron region. Black here would represent the [010] while yellow, the [112].
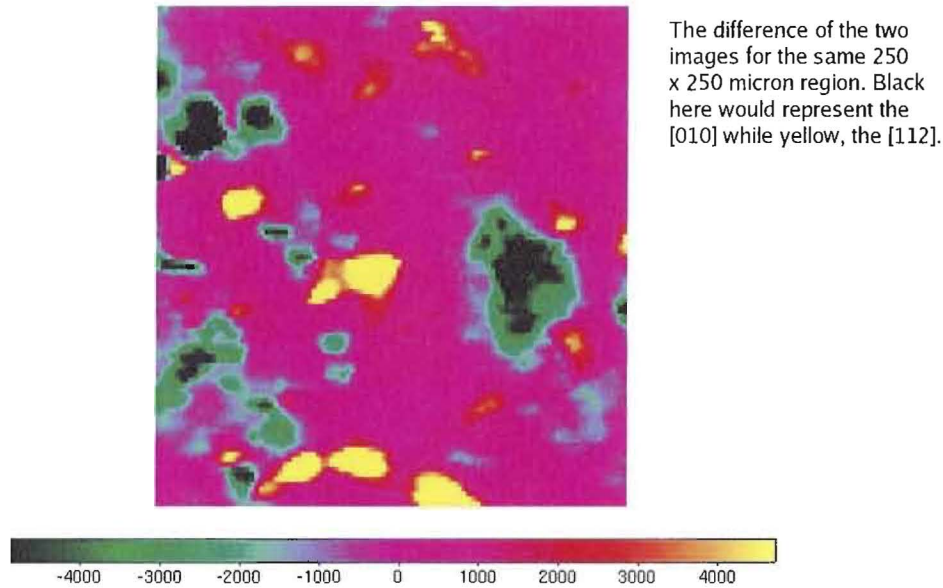
Fig. 7.2: **Microdiffraction images of the combined domains**. The [010]-oriented domains and the [112]-orientations are both shown to emphasize the complementary position of the domain structure. The black and green colors represent the [010]-oriented domains while yellow and red the [112] orientation.

In these systems, disorder plays an enormous role. This experiment serves as a demonstration of how widely structure can vary on multiple length scales in these types of complex systems [124]. For the remainder of this work, we will only be concerned with one single crystallographic domain. By focusing on one of the [010]-oriented domains such as those shown in Fig.7.1, we can then study the *orbital* domains that arise within one *crystallographic* domain.

3. Complex-valued Resonance Effects

We saw in Chapter III how the quantum mechanical amplitude is related to the measured x-ray cross-section. This can be connected classically to the complex value index of refraction

$$n = 1 - \delta + i\beta$$

where the two parts are related to the quantum matrix elements: a real part $1 - \delta$ related to how the illuminating electric field amplitude undergoes a phase shift through the medium, and an imaginary part β which is proportional to absorption. This relation is to the complex scattering factor $f_1(\omega) - if_2(\omega)$ for forward scattering ($\theta = 0$). At the resonance, there is sharp increase in absorption, and concomitantly a singularity in the real part of the scattering factor. So *near* this resonance, the cross-section is greatly enhanced. By measuring the scattered radiation and scanning the energy of the incoming photons, we are able to record the spectrum of the scattering factor for $Pr_{0.5}Ca_{0.5}MnO_3$. Fig. 7.3 shows the scattering spectrum, proportional to the resonant scattering cross-section.
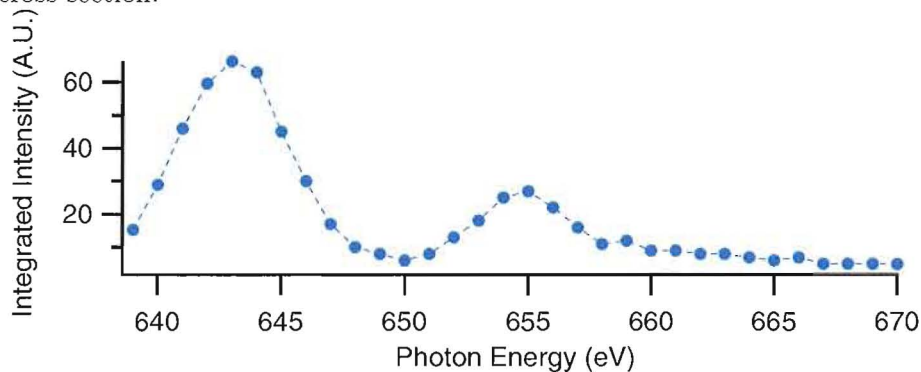
Fig. 7.3: **Energy spectrum from Mn in PCMO**. The plot was created by taking single-frame acquisitions for each energy and integrating the total intensity of the CCD for each image. The geometry used was off the Bragg condition to remove any angle dependent enhancement. The structure shows both the L_3- and L_2-edges, from left to right, due to the spin-orbital interaction.

To study the orbital ordering mechanism with soft x-rays, the $(0\frac{1}{2}0)$ orbital Bragg peak must be accessed. Because of the ordering of orbitals which doubles the unit cell in one direction, we can use the well-known Bragg's law $2dsin(\theta) = m\lambda$ to calculate the scattering angle 2θ where the largest signal would appear. Where the spacing d in this case is not given by the lattice spacing, but by the period of the orbital wave, or orbital unit cell. Here, d is equal to $2 * b$, where b is the lattice parameter $\approx 3.7\text{Å}$and $\lambda = 1.9\,\text{nm}$ for the L_3-edge of Mn. This gives a 2θ of $124°$.

One subtlety is that by setting the detector to the given 2θ we can then scan the energy of the scattering signal, but this will result in the energy spectrum convoluted with the Bragg peak. One way to deal with this is to position the

detector off of the Bragg geometry. This allows a measure of the energy spectrum that is not affected by the Bragg enhancement. After measuring the correct spectrum, the sample and detector can then be moved back to the approximate Bragg condition to maximize the two angles for the given maximum resonant signal. This was performed for the energy spectrum shown in Fig. 7.3. Since the given Bragg condition gives a sample angle θ of 62°, the angle was lowered by 4° to measure the spectrum.

At the present time, wiring is being set-up to measure the sample current during experiments. This will not give the resonant scattered spectrum, but the absorption of the sample. As discussed above, these are not always inversely related. But once the signature of the absorption can be compared with scattered signal and reproduced, this will speed up the process to find the desired resonance. The signal due purely from the resonant enhancement is increased by about a factor of three or so.

After tuning to the resonant peak in the Mn exchange scattering at the correct reciprocal lattice vector, the energy is chosen that maximizes the scattered signal, in this case, for dipole-dipole-type scattering in Mn. Once this value is set, a combination of sample and detector angles is optimized to maximize the signal due to orbital Bragg scattering. This is usually quite broad in angle, and fairly easy to accomplish. The importance of this step of the alignment process is two-fold: one is of necessity since the wavevector is fundamental to the physics we are studying, and must be correct to study the right physics. We will draw conclusions about this essential point later. The second is again related to S/N: Bragg enhancement here at this position offers about an order of magnitude in increased signal.

4. Multiple Scattering Mechanisms

There are two transitions for the half-doped sample: an antiferromagnetic transition at T $\sim$ 170K and both an orbital- and charge-ordering transition near T $\sim$ 235K. The antiferromagnetism takes place in all three directions as does the charge ordering. However, the orbital ordering only occurs in the [010]-direction. That is to say, not that the orbitals do not order with respect to each other in other directions, but this direction alone can give rise to scattering in the experiment. To be more precise, the orbitals are ordered in other directions, but it is concomitant with the periodicity of the Mn lattice and as we will discuss further, becomes impossible to measure anywhere over the entire Ewald

sphere. Fig. 7.4 shows a schematic of the CE-type orbital ordering in the a-b plane. The c-direction is directed out of the plane, showing that the a-b plane identical in this direction. This represents the orbital structure of a typical domain. Before we discuss the details of the orbital scattering experiment, we put forth convincing proof that this is indeed the structure that is being probed.

i. *Magnetic*

The magnetic ordering is displayed in Fig. 7.5 where the magnetic structure is given by the color scheme: green represents a spin orientation out of the plane, while green is in. The orbital structure is retained in the figure for comparing the orbital and magnetic pictures easily. We can see how intimately coupled the orbital and magnetic degrees of freedom are to each other. In fact, it can be seen clearly that both the OO and AF have the same modulation wave vector. The long-range antiferromagnetism is not present in our experiment discussed later because in the orbital study, all measurements were made above the Neel temperature. Also, it is worthy to note that the Neel temperature is defined in terms of long-range magnetic order. So while the experiment is performed above this temperature, there is still a large degree of magnetic structure present, just not observable using neutron or x-ray probes.

By temperature we can exclude the magnetic ordering from the orbital order study. This is problematic since the a and b axes are close in length. Due to the twinning of both [100]- and [010]-directed domains, one can easily imagine focusing on a [100] to observe magnetic scattering with or instead of orbital scattering from a [010]. This has been measured previously by us and others. The phase diagram enables us to use the sample temperature to exclude the possibility of magnetic *noise* on the orbital ordering intensity.

One last point about the magnetic scattering from the AF structure is the ϕ-dependence. As we saw in Chapter III, the dependence of the magnetic scattering is a function of the polarization and average magnetic moment vectors. As the sample is rotated about the $\mathbf{q}_z$ vector by angle ϕ, the dot product between the two changes as $\sim \cos(\phi)$ and the intensity as $\sim |\cos(\phi)|^2$. This gives another way to differentiate between the different order parameters: by studying the ϕ-dependence of the intensity.
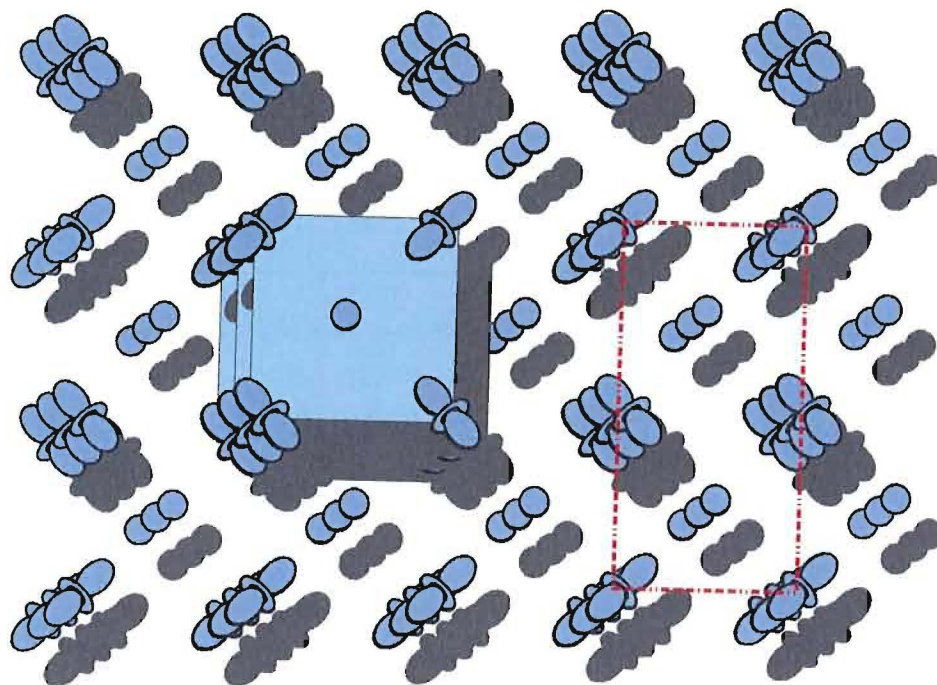
Fig. 7.4: **Orbital Structure**. The CE-type orbital ordering which takes place in the a-b plane. The blue squares represent the charge-ordered unit cell and display the third dimension to emphasize the fact that the a-b plane orbital structure does not change in the c-direction. The elongated and spherical icons represent one e_g electron (d^4 configuration) and the empty e_g orbital configuration (d^3). The red rectangle represents the orbital order unit cell.

ii. Charge

Charge ordering could be another source of orbital background in our experiment. By charge ordering, the difference between d^3 and d^4 ions is the mechanism that is referred to. Since this takes place at the same temperature, it can not be ruled out in the same way. Since the charge order scattered signal goes like the contrast of these two ions, it can be excluded based on **q**. In other words, because the charge order unit cell is one half the size of the orbital unit cell (along the third direction, the *c*-axis, they are actually the same), this moves the charge-order peak outside of the Ewald sphere completely, and in fact can not be reached physically with soft x-rays because of the long wavelength. The magnitude of the d-spacing for charge order is $d_{CO} = 7.64$ Å meaning that, at this energy, $\lambda/2d > 1$, so no real angles exist to see a charge order Bragg reflection.
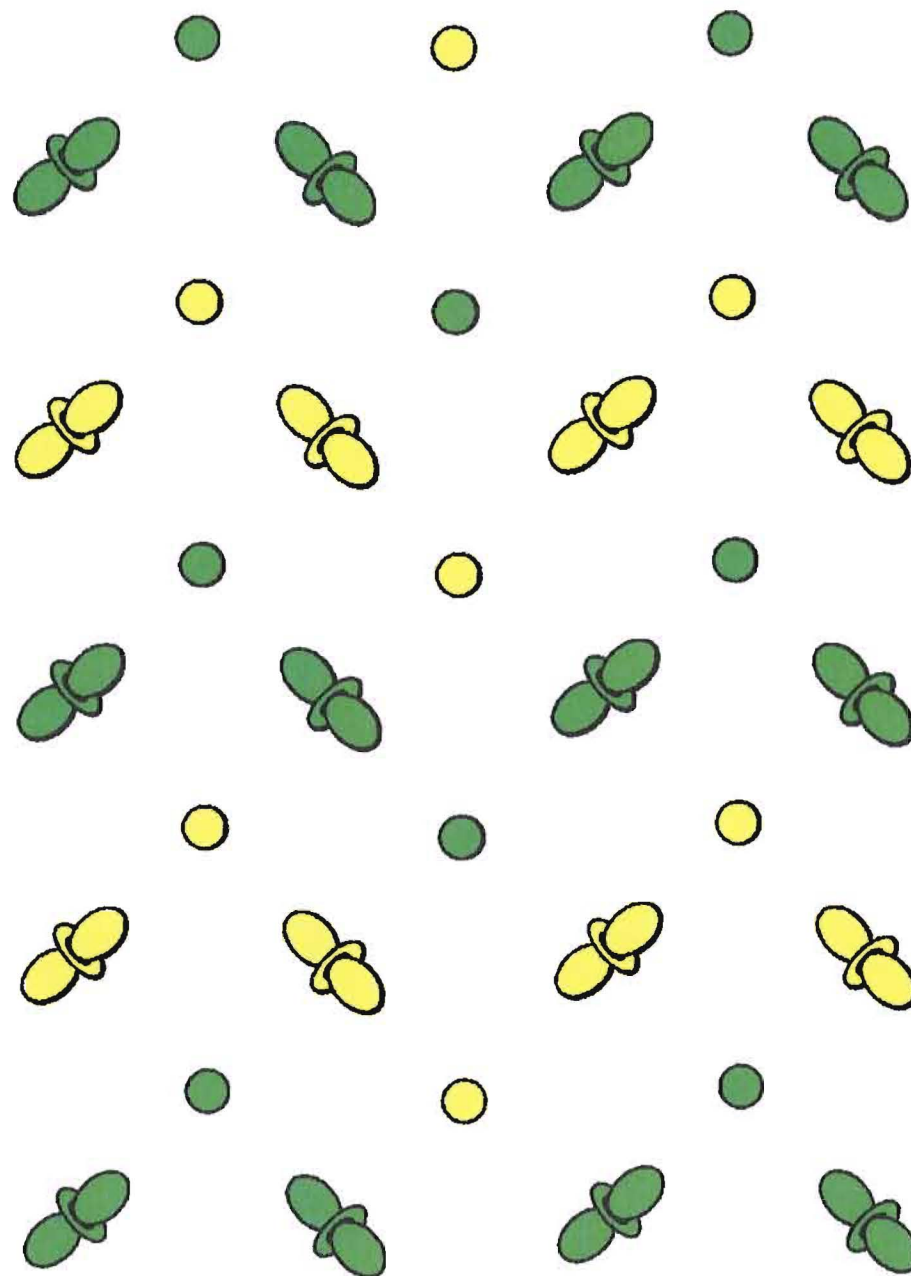
Fig. 7.5: **Magnetic Structure**. The CE-type orbital ordering diagram for the a-b plane with the magnetic structure given by the alternating color scheme. Green represents spin up (out of the page) and yellow is spin down (into the page).

iii. Bragg

Lastly, Bragg scattering could also occur at the same place as the orbital peak. Any type of periodicity that is used to diffract x-rays could in principle be called 'Bragg' scattering, but here we use the term to refer to the scattering solely from the atoms of the lattice. This is what is commonly referred to as 'Bragg' scattering, and is a consequence of the interaction between the electric field of the incoming photons and the charge on each Mn center in the lattice. This refers to all the actual positions of Mn atoms in the system, and not the overall charge differences resulting from the doping. This can be ruled out by the same argument as for charge ordering: $\sin(2\theta)$ could have to be larger than 1 for the lowest order reflection. In retrospect, it is actually a rarity that the OO is large enough to allow a reciprocal lattice vector of the ordering in the soft x-ray regime to be observed.

iv. Specular

There is one last contribution that could be incorporated into the orbital scattering and that is due to a possible surface reflection. This is a large increase in signal in the form of a rod in reciprocal space due to the abrupt change in the surface normal direction termed a 'crystal truncation rod'. This is argued to be absent due to the sample preparation.

The crystal was cut and polished with the [010]-axis normal to the crystal surface to reach the OO reflection using again the orthorhombic unit cell index. The lattice parameters are $a = b = 5.4\,\text{Å}$ and $c = 7.6\,\text{Å}$. We have measured the difference between the surface normal and the orbital Bragg plane normal using hard x-rays at Beamline X22A at the National Synchrotron Light Source. By measuring the incoming x-rays directly and cutting the beam with the surface of the sample we can measure how flat the surface is with respect to the Bragg planes. Scanning the angle of the sample θ with respect to the beam allows us to line up with the surface parallel to the beam. This angular scan, or θ-scan is typical in diffraction experiments.

Fig.7.6 shows a typical θ-scan taken at the ALS prior to a measurement. Comparing this θ-value with half of the 2θ-value detector angle for the [010] Bragg peak, we can get a good estimate of the miscut of the surface with respect to the orbital Bragg planes. This is of course only valid for the given orientation of ϕ of the sample. In the scan shown, the peak is shown to be at about 4°. This alignment is not related to that discussed above, but merely
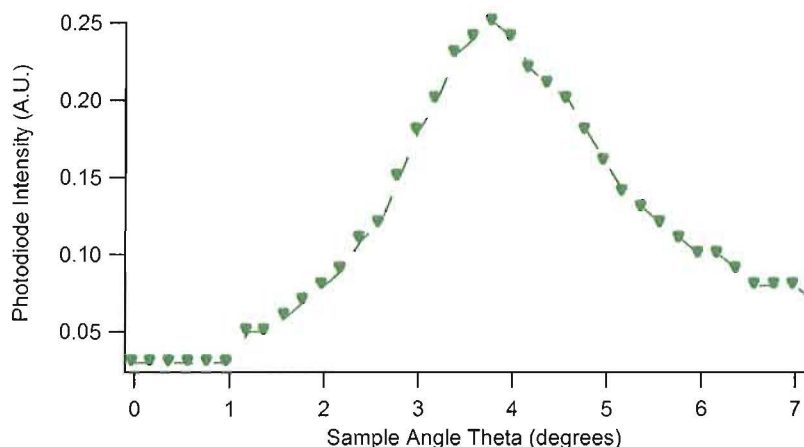
Fig. 7.6: **Theta scan**. The scan shows the direct beam intensity on a photodiode detector while scanning the angle of the sample θ with respect to the beam. The asymmetry could be related to the small sample and imperfect surface.

relates the position of the apparatus to the sample surface. In doing these types of scans, the angles get 're-zeroed' where $\theta = 0$ defines the sample surface to be parallel to the incoming beam. So for the scan shown above, $4°$ became the zero of the sample surface. We measure a misalignment of about $\sim 2°$ for this azimuth. This gives significant separation between orbital Bragg scattering and the specular surface reflection, which are separated in reciprocal space by about 2 or 3 * 10^{-2} nm^{-1}. These arguments become an important part of the experiment later as we will need to show convincingly that the scattered x-rays we collect at our detector are of purely orbital origin.

v. Azimuthal Dependence

The correct ϕ-angle to give maximum orbital scattering is with the c-axis - which is perpendicular to the surface normal - to be rotated into the scattering plane due to σ-polarized beam. This is because the ϕ-dependence described earlier is the same for the order parameter of OO as it is for the magnetic: $\sim (\cos\phi)^2$. Imagine the polarization vector of the x-rays parallel to the c-axis, or for our geometry with σ-light, perpendicular to the scattering plane. In this case, there is no contrast mechanism of the sample. Since the ordering takes place in the a-b plane, there is no differentiation between different orientations. The modulation is still present, the ordering wavevector for OO, but the amplitude is null. Since in this case, the scattering is the same from the two different

orientations, the difference in dot products between the polarization and the directional vector of the electron cloud is zero. If the polarization vector is orthogonal to the c-axis, this difference $\epsilon \cdot \hat{a} - \epsilon \cdot \hat{b}$ is at a maximum for the two orbital sites $\hat{a}$ and $\hat{b}$ rotated by $\pi/2$.

5. Incoherent Scattering

Before discussing the main focus of this work which is the coherent scattering aspect, we first turn our attention to the incoherent scattering results which can offer much insight. In theory, the two should really be studied in conjunction with one another, as they each have strengths and weaknesses. Also, according to coherence theory, there is no such thing as perfectly coherent photons, or perfectly incoherent for that matter. Here it is assumed that by incoherent we mean largely incoherent, since without some degree of coherence the Bragg scattering will not even survive. Coherence of course refers to partially coherent light, and to a much larger degree, such that we can form interference fringes with by illuminating a detector plane in the far-field diffraction plane of the sample.

i. Order parameter

Once the geometry is set-up, and we have found the orbital ordering Bragg peak convincingly, we can study the ordering directly through the temperature dependence of the cross-section. This dependence of the integrated intensity allows for a direct measurement of the order parameter. This type of measurement, as those discussed so far, does not require coherence of the incoming photons. By cooling down just above the antiferrogmagnetic temperature which is near T $=$ 170 K, we heat the system slowly while measuring the static structure factor.

Fig. 7.7 shows the integrated intensity with temperature. This measurement is a direct measurement of the order parameter for the orbital ordering mechanism, which goes like the difference in structure factors [61] for the two types of orbital orientations: $F(x^2 - r^2) - F(y^2 - r^2)$. This term goes to zero in both the limit where the orbitals are no longer ordered above the transition as well as if they are ordered, but all in the same direction. The plot shows the rapid decay of signal near T $=$ 233 K, where the transition occurs. Above this, the orbitals are disordered and orbital scattering becomes non-existent. This aver-
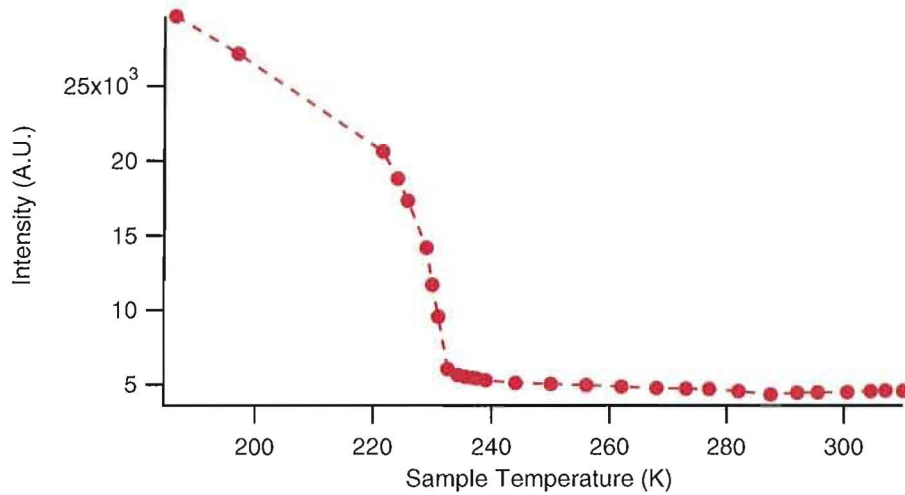
Fig. 7.7: **Order parameter with T**. The plot shows the integrating intensity of the orbital order Bragg reflection as a function of temperature. This give an estimate of the transition temperature and shows the character of the order parameter

age intensity experiment becomes important for measuring precisely where the transition is with respect to our instrument and thermometry, which we will show later becomes vital for the present experiment. Note the large value of the intensity even after the sharp decay. We will discuss the meaning of this background level at length in Section iii..

ii. Correlation Lengths

Another characteristic to be probed that is possible without a high degree of coherence is the correlation lengths of the orbital domains. These can be fit to the spatially averaged scattering distribution by Lorentzian functions for this particular experiment. This allows a measure of both the integral and width of the peak, which can be related to the order parameter and the average width of the domain, respectively.

One note about fitting functions of this form is the definition of the width of the domain is not precise due to the dependence of the correlation length on the functional form. For instance, by fitting a distribution to a Lorentzian function, i.e.

$$L(\zeta) = L_0 + \frac{A}{(\zeta - \zeta_0)^2 + \Gamma^2} \tag{7.1}$$

the parameter Γ is the half-width at half the maximum (HWHM) of the peak

and can be used to find the correlation length of the system. For a Gaussian or Lorentzian squared fit, these definitions will change. This translates to a slight error in defining 'average' domains, when the nature of the scattering can drastically effect what functional form is chosen to be fitted. Ideally, we would have an idea *a priori* from theoretical models and therefore a reason to choose a particular function. Issues such as these arise in complex systems like the manganites due to lack of theoretical models used to describe these types of systems. The same goes for the height of the function which gives us a measure of the order parameter. However, in that case a more general way of describing the structure factor is solved by using a total integration of the intensity to sidestep the absence of functional form models (as was shown in Fig. 7.7).

In Figure 7.8, we have plotted the horizontal widths from Lorentzian functional fits to images collected on the CCD detector. That is, an out-of-scattering-plane fit to the distribution. With our experimental set-up, we are only able to measure two directions: the horizontal shown above, and the vertical or in-plane width, which is a mixture of both domains in the q_z- and q_x-directions. By comparing the two, there seems to be an anisotropy of the domain shape for the two directions. After transforming the data to a constant $\mathbf{q}$ space (Appendix A), the widths become symmetric. The conclusion is that the anisotropy is a geometric effect and the domains actually retain an isotropic overall shape, to a large degree.

The widths plotted here are inversely related to the character of the order parameter drop-off of the OO, shown earlier. Both plots clearly demonstrate that as the domains are melting, they are both scattering less strongly due to a volume decrease (shown in Fig. 7.7) as well as a decreased lateral length scale (shown in Fig. 7.8). Well below the transition, the orbital domain size is around 30 nm and is on the same scale to be consistent with recent measurements of 40 nm on identical samples of different doping [125] and of 50 nm in completely different manganites [126]. We can see that the width gets larger with an increase in T as the domains start to shrink in the close proximity of the transition, as one would expect.

iii. Polaron 'Background'

Finally, we also plot the polaron background L_0 from the Equation 7.1 shown in Fig. 7.9. We can see that there is an onset of a flat background in the same vicinity as both where the order parameter starts to drop off and where the
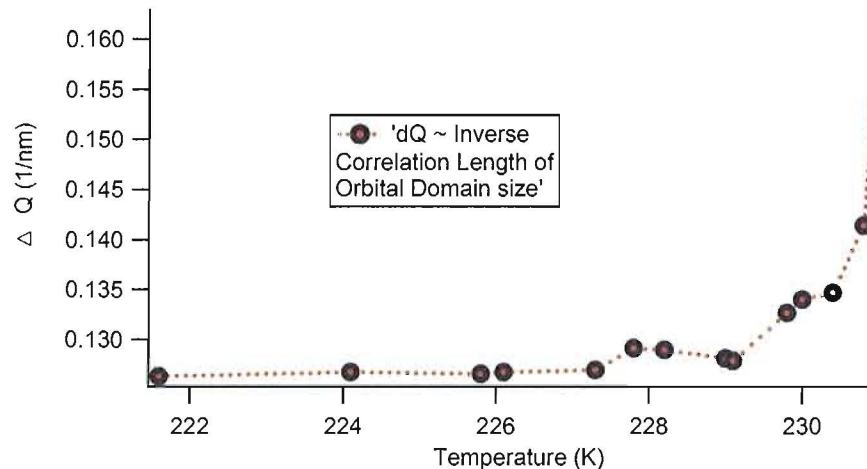
Fig. 7.8: **Correlation lengths**. From this plot of the inverse correlation length, the average domain size can be deduced as a function of temperature. The domain volume starts to decrease as the temperature approaches the transition from below, appearing as an increase in the width of the orbital peak. In terms of the peak width dQ, the correlation length ξ is π/dQ. Well below the transition, the orbital domain size is on the order of 300Å.

peak broadens. Based on previous work, we think this is proof of broad, diffuse scattering from polarons. As discussed earlier, polarons are quasi-particles created from electrons which get trapped in a Mn octahedra due to Jahn-Teller distortions. The distortion causes the e_g orbital to lose its degeneracy, and the electron become localized. In some cases, polarons retain the quasi-particle-like characteristics with a renormalized charge and mass, but become delocalized and act like conduction electrons, as has been shown in some experiments. As was discussed earlier, this was an idea thought up in 1995 by Millis and coworkers to explain the low resistivity at high temperatures [39].

In our experiment, the lattice-spacing size particles would scatter at the same orbital wave vector, which offers a hint that these are not the usual polarons. Because of the position in reciprocal space of the measurement, these must be *orbital polarons*. In other words, these can be thought of as having the same orbital domain structure, but are only one orbital unit cell wide. The idea being the same as mentioned above, but the unit particle has the right orbital orientation to give rise to scattering. Because of the small length scale, the production of the scattering distribution spans a much larger area in reciprocal space than our detector width. Not only are we detector limited, but there is also a physical limit set by the available region of q-space. The correlation length
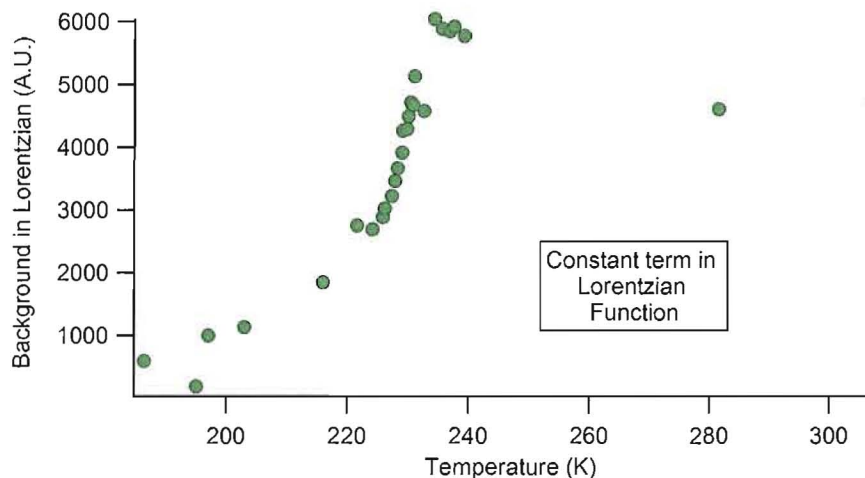
Fig. 7.9: **Polaron background**. The background plotted here is the constant term given by L_0 in the Lorentzian function (Equation 7.1), used to fit the orbital Bragg peaks as a function of temperature through the transition. It seems to suggest an onset (saturation) of diffuse scattering from polarons in the vicinity of the transition (at higher temperatures).

given by a single polaron is of order $\xi_{pol} \sim 2\pi/5\,\mathring{A} \sim 1\,\mathring{A}^{-1}$. Thus they can not be directly resolved without much higher energy x-rays. Polarons have been studied at hard x-ray wavelengths where the limit of **q**-space does not present an issue. However, to confirm a polaron background in the measurement, the sample was warmed passed 300K to ensure consistent results with Nelson *et al.* [127] and indeed, we find the signal to be constant. This can be noticed here in Fig. 7.9 and also is confirmed in the earlier discussion of the order parameter in relation to Fig. 7.7. There it was not emphasized, but one should note the values of the total integrated intensity above the transition is quite high, near 5000 ADC counts, where there is approximately 30 counts per photon. On average, the signal from this diffuse component is about an order of magnitude higher than the dark counts that register on the CCD chip due to electronic readout noise.

So without yet discussing speckle, we have conglomerated some preliminary results on PCMO. We have measured a decaying order parameter that is consistent with a broadened 1st-order-like phase transition. This is in conjunction with a shrinking domain size that is also what is expected near a order-disorder transition. In the same vicinity, we see an onset of a constant, isotropic background due to scattering from polarons which occurs at the same wavevector as

the orbital ordering. This can be thought of as due to single orbitally ordered unit cells: the wavevector is unchanged, but with the addition of an incredibly large diffuse component. This can also be compared to magnetic scattering, and is reminiscent of broad diffuse scattering that occurs when ferromagnetic domains, for instance, become disordered above the Curie temperature.

The implication here is that there are two dominant competing phases: a liquid-like polaron phase and a frozen orbitally ordered domain state. To emphasize this more clearly, Fig.7.10 shows the ratio of to the polaron background to the Lorentzian height of the peak. This plot only is valid for $T \leq T_{OO}$ because above the transition, the amplitude goes to zero and the ratio becomes infinite. This figure serves to emphasize the onset of the background scattering at the cost of the orbital domain amplitude. As the domains reduce and shrink in volume, the polaronic sea fills the gaps. This seems consistent with the 1st-order-like idea of phase separation near discontinuous phase transitions.
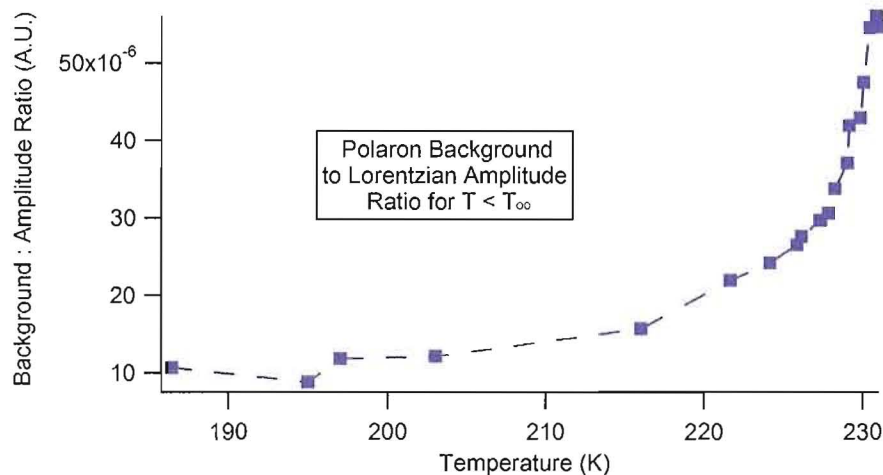
Fig. 7.10: **Ratio of flat background to peak amplitude.** The ratio of the flat background in each image to the amplitude extracted from a Lorentzian fit. The validity is only for the orbital domain phase because at the transition the amplitude goes to zero. Here we define zero to be where one standard deviation of the fit parameter of the amplitude is on the same scale as the parameter itself. This emphasizes the competition between two types of phases.

6.   Coherent Scattering

Coherent scattering can be used to take a closer look at the structure and disorder of the orbital domain state in the PCMO system. Because there is a large

distribution in sizes of orbital domains, the domain walls act as the interference mechanism giving rise to speckle, similar to the role surface roughness played in Chapter IV with a specular reflection due to charge scattering. Here we can take advantage of the *roughness* of orbital domains to explore the structure through obtaining speckle patterns due to phase differences at domain walls.

The first measurement was to obtain low temperature speckle patterns of the orbital domain structure near the region of the phase diagram where the orbitals have the most stable configuration. Here it was assumed that the structure would be more stable, in case there were temporal fluctuations near the transition. Displayed in Fig. 7.11 is the speckle pattern collected from PCMO and is of the the the entire $(0 \frac{1}{2} 0)$ orbital ordering Bragg peak collected in a reflection geometry at 200K. A high quality three micron pinhole was used as a spatial filter for the soft x-rays to increase the level of contrast depicted in the figure. For all dynamics measurements pinholes used were larger by a factor of three or four to count on shorter timescales. This is not so important in other types of experiments, imaging for instance, since count times in that case do not represent a limit. To count long enough to gain necessary statistics is quite common, so long as the times do not exceed normal experimental times. When studying dynamics in different types of systems, the time becomes crucial as there is one or more specific time constants to measure, and the experiment must be sensitive to the requisite scale.

To appreciate the exceptional level of contrast in this image, Fig. 7.12 shows a close-up view of the previous speckle pattern. Notice the large average area of each particular speckle, the *approximate* diameter s of which is set by

$$s = 1.22\frac{\lambda R}{\xi} \tag{7.2}$$

where ξ is the coherence length of the light at the sample and R is the sample to detector distance. The 2d solution to this equation is shown in the inset as an illustration of the average coherence area. Not realized in the equation, the small pixel size of the detector used compared to this size is largely responsible for the exceptional speckle resolution displayed here. Also, note the large variation in intensity from bright to dark regions in the pattern (Fig. 7.12). This gives a qualitative picture of the contrast, which for this pattern was computed to be about 80%. To the author's knowledge, this represents the first soft x-ray speckle pattern measured from any type of transition-metal oxide or even single
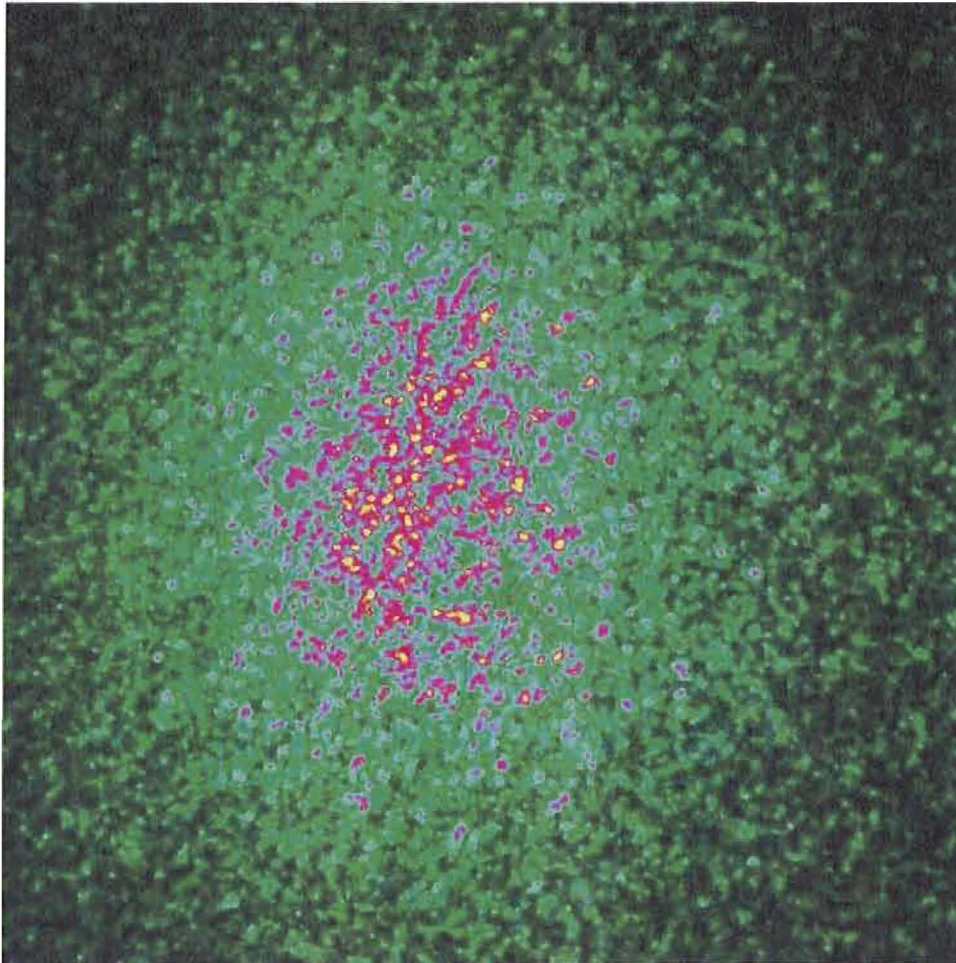
Fig. 7.11: **Orbital order speckle patterns**. Speckle pattern of the $(0\frac{1}{2}0)$ orbital ordering Bragg peak collected in a reflection geometry at 200 K for a 3 μm pinhole. As can be seen, the peak is so broad that it essentially fills the full angular acceptance of the detector.

crystal for that matter, and arguably the first direct display of orbital ordering speckle in the manganites.

i. Dynamics - qualitative

To answer the question on dynamics of the orbital domain state, the domain behavior was studied via speckle patterns as a function of time. As a first approximation, sets of images are collected and compared by eye for any noticeable changes. This was completed by taking time scans. That is, line scans taken across the image for multiple frames and plotted together to study structural
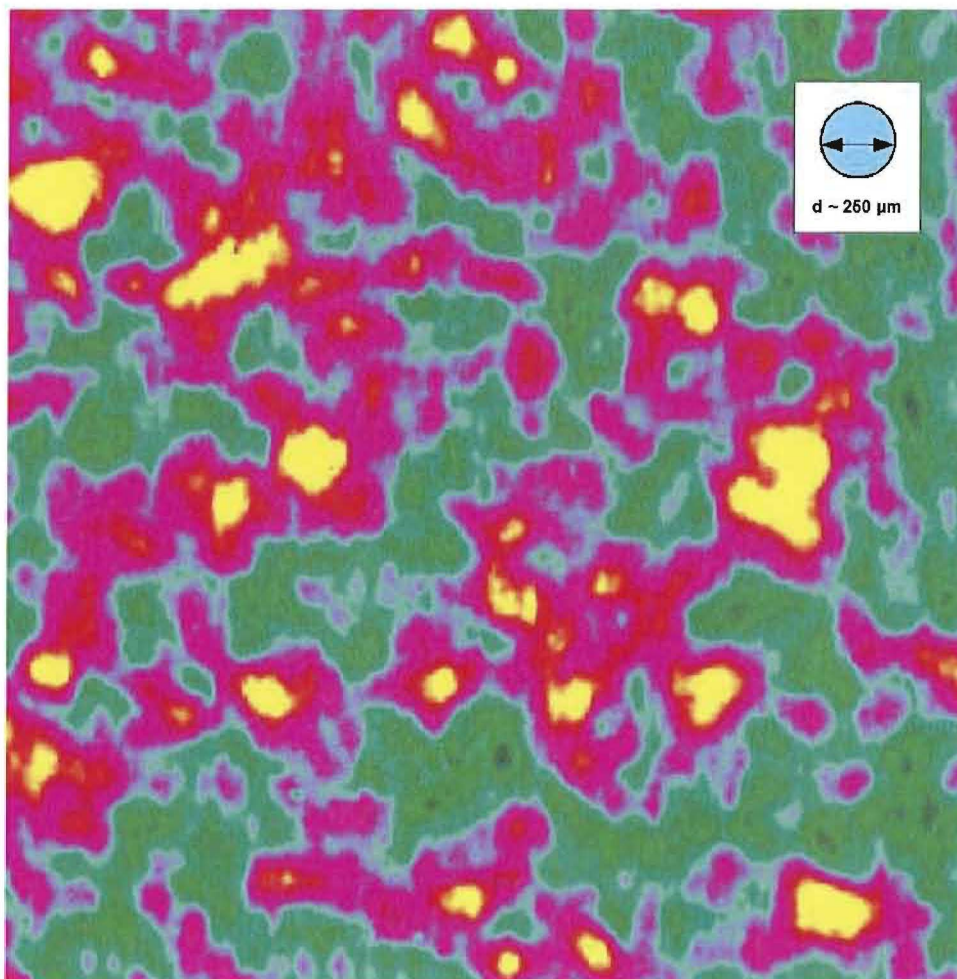
Fig. 7.12: **Orbital order speckle structure.** Close-up view of the speckle pattern in Fig.7.11. The inset shows the average size of the speckle size calculated from Equation 7.2 for comparison. The contrast level in this image is about 80%.

differences. A series of one hundred separate images were recorded wherein a vertical line through the pattern for each image is plotted for comparison. Because of the number of images, we chose to arrange one hundred line scans into a single image (Fig. 7.13).

The image shown is the orbital Bragg peak for 200K using a $\sim 10\,\mu$m pinhole alongside the time scan for the same image. The time scan is a 1d line scan down the center of the image performed on each image of the set, spanning a ~ 20 minute period. This picture helps to visualize the evolution of the speckle intensity as a function of time on the horizontal axis for a vertical cut through
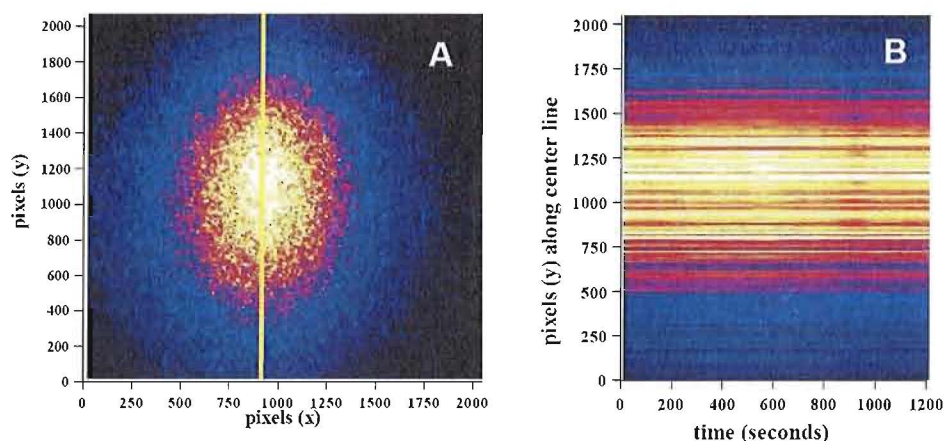
Fig. 7.13: **Time evolution of speckle for 205 K.** (A) Speckle pattern taken at the orbital Bragg peak deep within the orbital ordering phase at T = 205 K. (B) Time evolution of the speckle pattern in (A) for a vertical slice (yellow line) through the center of the image. This figure represents the evolution of a 1d scan through the image like that shown in (A) of a 100-image set, taken over a 20 minute period. The speckle structure is static as evidenced by the straight horizontal lines.

the middle of the Bragg peak. The line plotted in time is given by the yellow line in the down the center of the image.

The lines look reasonably constant and horizontal, as one would guess because of the position in the phase diagram. One can imagine, if the coherence areas were fluctuating in intensity, that the lines would remain horizontal, but not constant: there would be a modulation of the intensity for each horizontal line. Furthermore, if the coherence areas moved, the line would remain constant, but no longer straight horizontally. In this case, the lines would have some curvature. Here it is worth noting that this explanation is correct only for the 1d case. In other words, since we are only interested in a pictorial idea here, we only show 1d scans which mean curvature would only be present if coherence areas moved along the line shown in the speckle pattern. A constant intensity coherence area could move in and out of the 'line of sight' which would give an impression of the modulation mentioned above, and not show up as curvature. One can imagine generalizing this method to more dimensions, but for our purposes here, this will suffice. We will return to a more thorough, quantitative method of measuring dynamics shortly.

For T = 232 K, Fig.7.14 shows the same set-up: a CCD image of the Bragg peak with a time scan for a similar set of 100 images. This is with the same size
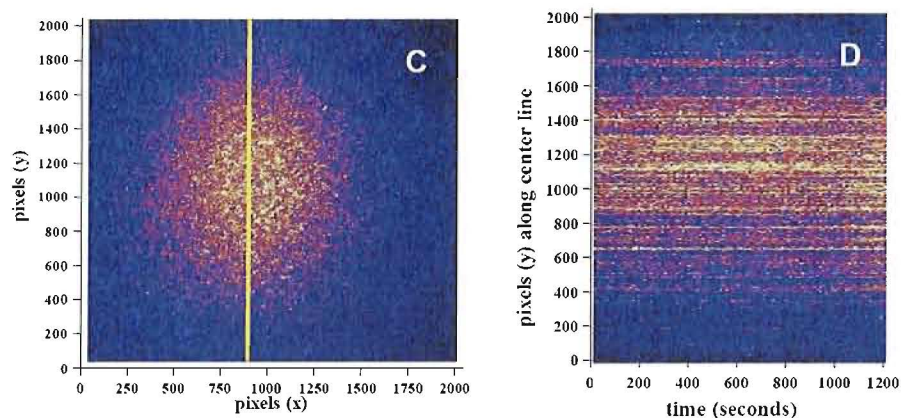
Fig. 7.14: **Time evolution of speckle for 232 K**. (C) Speckle pattern taken at the orbital Bragg peak near the phase transition at T = 233 K. (D) Time evolution of the speckle pattern in (C) for a vertical slice (yellow line) through the center of the image. Although much higher in temperature and with close proximity to the transition, the time scans still shows evidence of overall static structure.

pinhole and should have all the same experimental attributes, but is nearer to the transition. Surprisingly, this time scan shows straight, constant horizontal lines as well. One may argue about the constant aspect since the signal has dropped dramatically. But overall, there is not a large deviation from the earlier time scan at lower temperature. A similar test was done previously with coherent scattering at the K-edge (6.55keV) to get qualitative understanding of the dynamics, but the signal rates were too low to obtain good statistics and the results were inconclusive. Further, K-edge measurements have been controversial to the study of orbital ordering as theoretical studies have shown that they are two orders of magnitude less likely to probe the actual ordering of the d-orbital wave as they are to a collective Jahn-Teller distortion that results from the actual oxygen displacements around the Mn ion.

These figures taken together indicate that the domains are largely static on the time scale of the data set. This is in contrast to recent results in a 1st-order transition in the CDW spectrum of a magnet [128]. The low temperature behavior seems intuitive because the order-disorder transition is > 30 degrees Kelvin higher in temperature, but the static structure close to the transition seems at odds with what one would expect. By conducting a more quantitative speckle analysis however, we can explore the implications of the orbital ordering static structure somewhat further.

ii. Dynamics - quantitative

To approach this question of dynamics quantitatively, the temperature was systematically changed from low to high for every degree through the transition - with at least two hours of time spent waiting for the system to stabilize for each point. For each temperature we calculate cross-correlation coefficients that again, yield $\rho \sim 0$ for uncorrelated images, and $\rho \sim 1$ for two speckle patterns that are exactly the same. This method serves as a metric of how much the domain state is changing from image to image. At each degree, we again took multiple sets of image for a total duration of 20 minutes each. Each 20 minute set consisted of 100 images at 10 s per acquisition, for a total time of 20 minutes including readout times of the detector.

Q-integral Dynamics

The first result is a q-integrated coefficient averaged over tau, and is plotted in Figure 7.15. This is a correlation coefficient for the entire image averaged with other images at the same temperature. It provides insight into how the full speckle patterns are changing in time with temperature. We can see that at low T, the value is extremely close to one, confirming that the low-T speckle patterns are in fact static and, not incidentally, that the experimental set-up is stable enough for the detailed measurements outlined here. Each coefficient represents an average coefficient, both in τ as discussed in Chapter V, but also in temperature. We took multiple 100-image data sets for each T, and then averaged the same-T coefficients to get a more thorough statistical analysis, $< \rho >_{\tau,T}$ for each temperature measured. The data points depict the slight decrease of the coefficient near 232 K. Upon computation of correlation coefficients, we see that there is actually a small degree of temporal orbital fluctuation near the transition. This level of detail is not visible in comparing line scans, but only through a careful measure of correlations statistically. There is an onset here near the transition, or a point where the fluctuations seem to 'turn on'. The increase of coefficients at 233 K seem to suggest that at higher temperatures the dynamics slows down. We believe this is simply due to the lack of good statistics at these temperatures and that this simply affirms that the window where these dynamics are accessible is quite narrow in temperature.

To be more thorough, we completed a extensive analysis to gain insight into length scale dependencies by computing cross-correlation coefficient maps, not only as a function of time, but also now of **q** [129]. These maps serve as a
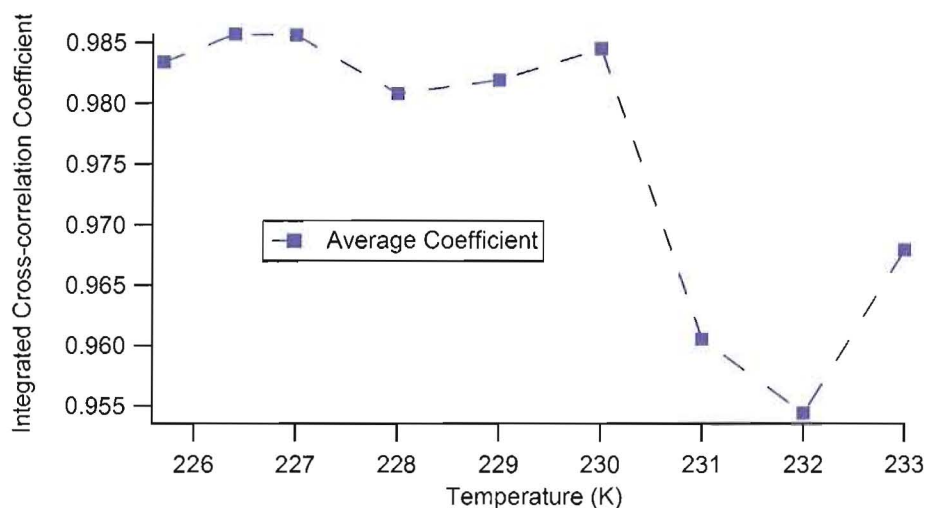
Fig. 7.15: **Time correlation near transition**. The following plot demonstrates how well speckle patterns are correlated from frame to frame for a given temperature, never changing temperatures during a acquisition of a set of images. There is a large drop near the transition, where after the decay, the correlation coefficient seems to rise again. This could be due to the fact that at such high temperatures, the S/N drops considerably, and we do not have adequate statistics on the small time scales that are most likely needed for these temperatures.

visualization of the length-scale-dependent dynamical behavior in the vicinity of the transition and help to characterize the fluctuations more thoroughly by reflecting any q-dependence.

An array of panels is shown in Fig. 7.16 that shows the time dependence we saw in the **q**-integrated coefficients with the second dimension of the image portraying a length-scale dependence for each temperature. In the coefficient maps for 231 K and 232 K, the fact that at higher q-values the coefficient drop more quickly reaffirms that smaller length scales that are being probed have shorter correlation times, as is consistent both intuitively and is observed in dynamic light scattering and x-ray photon correlation spectroscopy experiments.

Though the map for 231 K is not as robust as the others due to the lack of data for that temperature, the behavior seems to agree largely, with its 232 K counterpart. These usually measure diffusion constants of compact objects in a fluid. With some given energy in the system, quantum fluctuations or Brownian motion of the particles will be larger for smaller particles, and less for small. The T = 233 K is again questionable for reasons mentioned in the q-integrated plot.
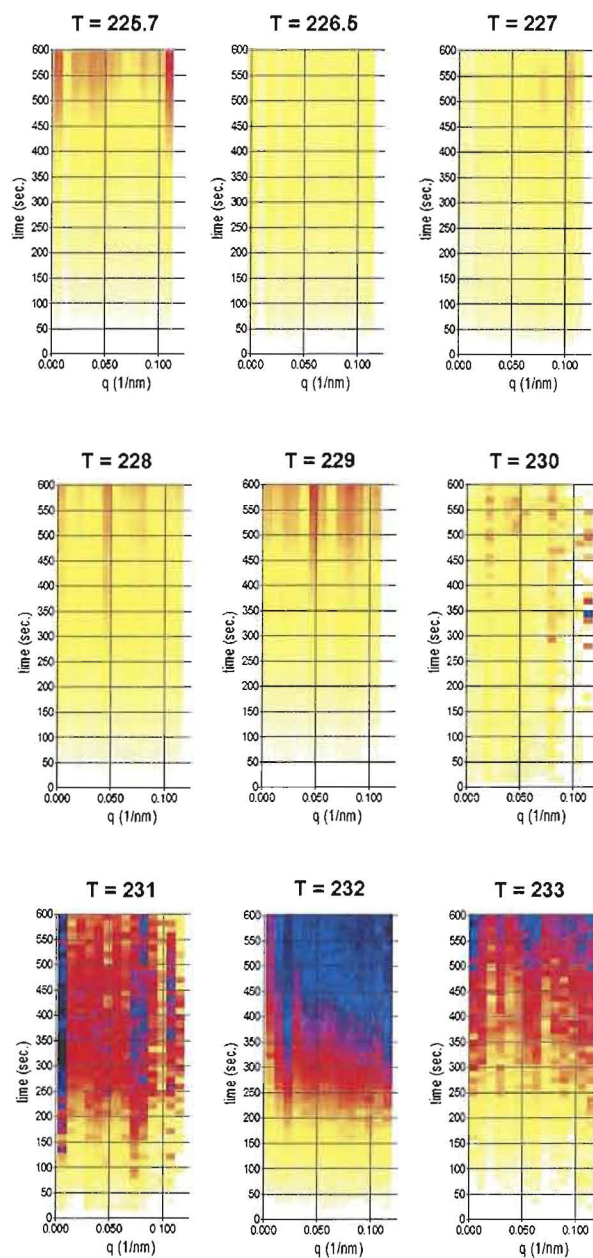
Fig. 7.16: **Cross-correlation coefficient maps.** Each frame represents the average of three separate maps for a given temperature. Time is on the vertical axis and momentum transfer on the horizontal with the coefficient given by the color chart shown below the images. Time is given in seconds, and calculated by averaging over all permutations of pairs separated by delay time τ. The q-resolution is 0.01 nm^{-1} per pixel. The quantity q was calculated by computing all three components of the wave vector transfer $\mathbf{Q} - \mathbf{G}$ and taking the magnitude, where the wavevector magnitude $|\mathbf{k}|$ is $2\pi/\lambda$, $\mathbf{Q}$ is given by $k_f - k_i$, and $\mathbf{G}$ is the orbital ordering reciprocal lattice vector. Even for the $\mathbf{q}$ and τ dependence shown above, the absolute changes are small.

7. Summary

To reiterate, as the temperature of the material approaches the OO transition, the system exhibits simultaneous decay of the OO Bragg intensity, decrease of the correlation length, and a pronounced diffuse background. This seems at odds with the fact that the domain structure is largely static. This is clarified by noticing that the q-integrals (Fig.7.15) and correlation coefficient maps (Fig.7.16) do not drop below about 10% for all times, wavevectors, and temperatures measured. The same conclusion that was drawn from the time scans of the images, albeit much more convincingly so.

What is more, there is a small component that is fluctuating. Hidden in the overall static structure of the speckle evolution scans (Fig.7.13 and Fig.7.14), only with our more statistical analysis does the appearance of a small-amplitude fluctuating component emerge near the order-disorder transition. The fact that such a small region of the OO domain volume is attributed to these types of spatio-temporal fluctuations is surprising.

But most puzzling is that this dynamic component occurs on a timescale on the order of hundreds of seconds. Not only is this small volume of the orbital domain structure dynamic, but on scales that seem so slow as to almost imply the behavior is very much unlike what would be expected in any kind of transition-metal oxide. One thing should clarified on the static structure, which remains an open and important question: the origin of the pinning of the orbital domains.

i. Static Structure

Although soft x-rays only penetrate 500-1000 Å into the sample, we believe it is unlikely that the pinning is due to defects at the surface. In particular, we note that the size of the domains observed here and the temperature dependence of the order parameter are both comparable with the results of neutron and hard x-ray measurements, which probe the bulk of the material [5, 50, 51, 130]. In addition, as has already been noted previously, short-range OO, with orbital domains of ~300-500 Å, appears to be a general result [126, 131] from L-edge scattering studies on a variety of manganite materials prepared in different laboratories. These arguments suggest that a more general mechanism is responsible for pinning the of domain walls that may not be related to surface morphology.

ii. Discussion

The behavior is quite interesting of the OO mechanism near the transition. The main result is that there are two competing tendencies in the orbital domain structure: a widespread static component, and a smaller, dynamic component. The majority of the domain volume remaining static as discussed above can again be seen from the fact that even at the longest times measured, $\langle \rho(q, t, T) \rangle$ does not decay by more than 10%. The system behaves as though it has frozen-in disorder that prevents any sizable fluctuations in the orbital domains on the timescale of the experiment, even very close to T_{OO}.

These observations and the static arguments discussed in the last section suggest that the pinning of the domain walls is not surface related, but is intrinsic to the system. Given this, domain walls may be expected to be pinned at points where the cost in elastic or electronic energy for having neighboring OO wavefunctions out of phase is lowest. One candidate for such a location is the Ca dopant ions and the strain fields they produce. At half doping the average separation between dopants is much smaller than the orbital domains, so if this is the responsible mechanism, then clearly the pinning is not very energetically relevant. It is possible however that this is a cumulative effect associated with a local statistical deviation from the average calcium concentration which produces a strain field that pins the domain walls. Another issue that may be related to the static structure is the level of hole doping. With an equal number of divalent and trivalent sites, the ordering is thought to be more robust with respect to perturbations, and hence, to equilibrium domain dynamics. It would be interesting to conduct the similar measurements for the same system for different doping to check this notion.

We now turn to the small-amplitude fluctuating component that emerges only near the phase transition. Here the dynamics are related to limited domain wall motion, which exhibit fluctuations that occur on the order of hundreds of seconds. These long time scales are slower than any measured mechanism that we know of at this time. These results provide a clue that understanding the orbital ordering transition in the manganites may be through mesoscopic, rather than microscopic physics. Furthermore, not only are the dynamics slow, but they occur on large length scales, of order one domain, or about 50 lattice spacings.

An interpretation that is consistent with our results is a picture in which, at a given temperature, the bulk of a domain volume is static. The domain walls are

pinned except for temperatures very close to the transition where the domain walls are able to execute small-amplitude motion [129]. Such behavior contrasts, for example, with the domain wall dynamics associated with charge density waves in the simple antiferromagnet Cr [128]. In chromium, the domains are a few microns in size and fluctuate on a length scale comparable to the domain size itself, resulting in speckle patterns that become completely uncorrelated at long times [128]. Thus, it appears that in contrast with these systems, the manganites possess a source of quenched disorder which couples to the OO order parameter. This coupling pins the domain walls, and though critical fluctuations are absent in this regime, may demonstrate that the manganites are more analogous to recent observations in the displacive, $SrTiO_3$ antiferrodistortive transition [132, 101], a 2nd-order structural phase transition. However, the onset of the unusual, slow orbital domain wall motion is a completely novel observation, unlike either of these systems.

Another of the unsolved problems is the large correlation length difference in the orbital ordering than in all the other order parameters. It was recently shown that, though modulation wave vectors are similar, the correlation length in the d^4 magnetic superlattice is a factor of two larger than the OO [131]. The short-range order in the orbital ordered phase seems as though it is unique to the other ordering phenomena. We believe this is related to this frozen-in disorder. Current investigations are under way to measure dynamics in the magnetic phase to see if dynamics are correlated with this hypothesis.

In the manganites and other complex oxides, the coupling of multiple degrees of freedom charge, spin, and lattice has mostly been considered at the microscopic level. Here, we argue that a thorough understanding of the mesoscopic physics is also needed to shed light on the governing mechanisms of the macroscopic properties. Indeed, the interactions between order parameters are complex and involve a range of length scales. Our results show that a great deal of information can be collected by probing these systems in the time-domain. In particular, we have shown a number of new results regarding the orbital transition, including that short-range orbital correlations are largely static with only small-magnitude, domain wall fluctuations that become manifest only as the transition is approached. This highlights the importance of quenched disorder in this system for determining its ground state properties. It is also interesting to note that the short-range orbital order is not universally observed in doped manganite single crystals. For instance, in some layered manganite systems, the

domain size has been shown to be much larger. As in the discussion on magnetic correlation lengths, it seems intuitive to assume that these longer-ranged orbitally ordered systems may lack appreciable quenched disorder, giving a larger probability that motion associated with domain walls will be more considerable. Finally, if the domain wall dynamic measurements reported here can be applied to other complex oxides, such as the dynamic stripe correlations in the high-temperature superconductors [133], then many forms of time-dependent heterogeneity may be readily probed, helping to reveal a new understanding of the interconnection between mesoscopic physics and complex order parameters.

CHAPTER VIII

OUTLOOK

Any fool can make things bigger, more complex, and more violent. It takes a touch of genius - and a lot of courage - to move in the opposite direction.
- Albert Einstein

In conclusion, we have completed a number of novel studies and analysis in the $Pr_{0.5}Ca_{0.5}MnO_3$ system. Some of the data presented here is the first coherent soft x-ray scattering from a transition-metal oxide system. We have measured orbital ordering dynamics of the domain state in a cubic manganite system and gained new insight into the phase transition from an orbitally ordered domain state to a high-temperature paramagnet. The half-doped $Pr_{0.5}Ca_{0.5}MnO_3$ system is important because of the complex relationship exhibited between differing order parameters. In fact, this system is such that these multiple mechanisms are all present, and the relationships are actively competing energetically at this doping level to produce a richness in the phase diagram. Orbital order is thought to be a big player in some of the elusive physics that governs these types of strongly correlated electron oxides.

These speckle measurements are only the beginning. There is a voluminous body of work and plethora of questions waiting to be answers by novel speckle techniques. Phase transitions in complex systems will be key to many future studies. In particular, the mesoscopic world as it relates to the manganites may very well be on the verge of being understood, or at least observed in great detail. Soft x-ray speckle has emerged as a new tool with which to attack some of these unsolved problems involving the 'middle-way' and the manganite system is the perfect arena for applying these new tools. It is an iconic system epitomizing our limited knowledge, and posing some of our greatest challenges in condensed matter physics. Many unsolved problems lie on the horizon and manganites represent a ideal testbed for many competing issues to be solved by studying them simultaneously.

Secondly, we have generalized a metrology speckle analysis method to handle momentum and time dependent measurements conveniently. This is mainly to approach some technical details more readily, but could become more useful as the coherent x-ray scattering field opens to a wider array of subjects such as the complex and intrinsically heterogeneous systems discussed here.

Lastly, we have summarized the construction and commissioning of new end-station and Beamline 12.0.2.2 at the Advanced Light Source. This is obviously a enormous joint-project involving many people, but the instrument has enabled us to make measurements that are only possible at very few places in the world.

1. Future

The future is extremely bright for both the manganites and in the field of coherent x-ray scattering. Just recently, there was a conference held solely for the purpose of discussing the use of manganites in technological applications [134]. The importance in magnetic sensors, or in novel types of electronics can not be overlooked. Recently, there was success in making nanotubes out of the manganite materials [135] and electronic transport junctions between epitaxial manganites and carbon nanotube structures [136]. Indeed, there has been an uprising of activity in these systems and it seems as though the field is not cooling down.

Furthermore, the elusive physics is what makes these systems most intriguing. There have been at present, five full length books published in the last few years just to keep up with the rapid development in the field. One even states [14] that the trend in the manganites may be overtaking the cuprates and high temperature superconductivity. In addition, the broader class of strongly correlated electron physics also seems to be an ever so hot topic. With the use of coherent scattering to study temporal physics, an entire world is opening to possibilities in the transition metal oxide and other self-organizing systems, but also in a broad class of heterogeneous, mesoscopic systems.

The technique of coherent x-ray scattering is having its own explosion as well. There are now bi-annual international workshops to discuss its development [137]. With new ways to study dynamics, a plethora of directions becomes available of where the take this in the future. From the dynamical measurements, there are enumerable places to study fluctuations near phase transitions, especially in the esoteric systems that can not be probed in other ways. Furthermore, there are additional branches of coherent scattering that are

also becoming popular as well, including using the speckle patterns measured to perform imaging or memory experiments.

Lensless imaging for instance, can be used by measuring the far-field speckle pattern and recovering the phase through algorithms, eventually producing the real space structure. This avoids the limits set by x-ray lenses in the soft x-ray regime, or the depth of focus issues brought about by zone plates. Holography is also a version of this diffraction microscopy that has recently been shown at these energies. These two aspects have the potential to break open an entire new way of studying physics by being able to image soft matter and hard condensed systems with only the diffraction limit of the x-rays determining ultimate spatial resolution in reconstructed real-space images.

Speckle metrology is a fourth aspect that coherent x-rays makes possible. This is the comparison of speckle pattern with some external parameter such as electric field, magnetic field, or temperature. This enables a study of microscopic memory effects in ways not possible by other methods [104].

In addition, many places around the world are just beginning to build programs to conduct these types of experiments. Argonne National Laboratory has recently proposed to apply many resources to build the coherent scattering program and diffraction imaging program considerably. There are also new facilities proposed or under construction to be optimized for these types of experiments such as the National Synchrotron Light Source II [138] at Brookhaven which will be the world's brightest synchrotron, and the Linear Coherent Light Source [139] at Stanford, which will boast the world's first x-ray free electron laser.

In conclusion, this field is only beginning. The future is bright, and there is many more experiments to be done.

APPENDIX A

TRANSFORMATION

This appendix details the derivation of the transformation of the Cartesian coordinate system of the detector plane into 3d as well as 2d momentum space. An important aspect of scattering experiments is focused on the geometry. Understanding and correctly evaluating the photon momentum is paramount. For instance, in reduced geometries or systems, such as in the bi-layer manganite materials where the system is effectively 2-dimensional, the relevant momentum also becomes effectively 2d. The geometry is shown in Figure A.1 and is the geometry used in the majority of this work, where $\mathbf{q}$ is denoted by $\mathbf{q} = \mathbf{k}_f - \mathbf{k}_i - \mathbf{Q}_0$. The coordinate system shown in Figure A.1 is different than earlier in the text in Figure 5.5 by a single rotation by the sample angle: the final coordinate system we wish to know the momentum in. As discussed earlier, in conventional diffraction experiments, $\mathbf{q}$ is the main variable. Each component can be varied and scanned by adjusting the experimental geometry. For the coordinate system given in Figure A.1, the q_y component can be varied by scanning χ, the out-of-scattering-plane sample angle. Similarly, q_x can be measured by scanning the in-plane sample angle, θ. Both of these variables are sample dependent and are based on keeping the detector in a fixed position during the scan. The q_z variable on the other hand is a reflectivity scan, and is measured by scanning both the sample angle θ, and the detector angle γ, simultaneously. Each component of $\mathbf{q}$ then can be measured through adjusting the correct combination of sample or detector angles. These relationships will become clearer when we compute them shortly, explicitly.

i. Q-space

One final note is that in typical diffraction experiments, parameters are not measured in units of 'q', but in reciprocal lattice units. The reason is that most diffraction consists of crystallography, in which the notation is that of the
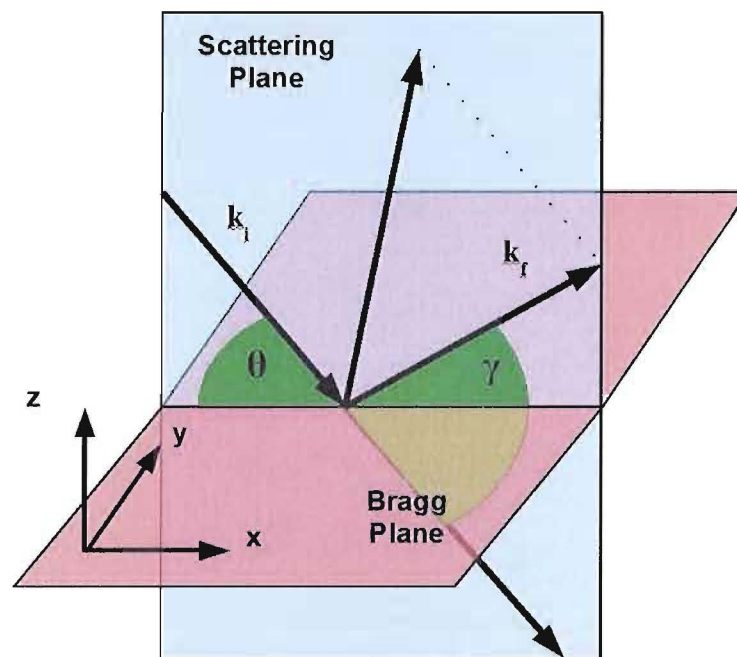
Fig. A.1: **Q-space Geometry in the Sample Reference Frame** The figure shows the q-space geometry, where $\mathbf{Q} = \mathbf{k}_f - \mathbf{k}_i$. The incoming and final momenta are shown in the figure as well as their difference vector $\mathbf{Q}$. The dotted line shows the addition of $-\mathbf{k}_i$ with $\mathbf{k}_f$. The blue plane (x-z) represents the scattering plane. The salmon colored plane (x-y) represents a Bragg plane of the sample or surface plane in reflectivity. The angle θ represents the angle of the incoming beam with respect to the sample. The angle γ is the total angle of the outgoing photon with respect to the incoming. The coordinate axes are shown in the bottom left corner.

reciprocal lattice vectors h, k, and l. These are the values of the components of the reciprocal lattice vector, $\mathbf{b} = (b_1, b_2, b_3)$ where the b_i vectors are related to the crystal structure of the direct lattice by:

$$\mathbf{b}_i = 2\pi \frac{\epsilon^{ijk} \mathbf{a}_j \mathbf{a}_k}{\epsilon_{ijk} \mathbf{a}_1{}^i \mathbf{a}_2{}^j \mathbf{a}_3{}^k} \tag{A.1}$$

where the $\mathbf{a}_i$ vectors are the three Bravais lattice vectors, ϵ_{ijk} is the Levi-Civita symbol where the Roman indices represent 1-3, and we have invoked the Einstein convention. This of course changes, depending on the sample orientation and crystal symmetry. The terminology of $\mathbf{q}$-space is mainly taken from the SAXS/WAXS community where average length scales are the relevant quantity to study and crystal structures are rarely dealt with. For the experiments described here, a type of 'unconventional' x-ray diffraction experiment is performed on crystals, where we do not measure the reciprocal lattice scans. We adopt the $\mathbf{q}$-coordinate system language as it is *geometrically*, and not *crystal*, dependent.

An example is a diffraction experiment on a [100] versus a [010] oriented crystal structure. Geometrically, since both scans are reflectivity scans, they would be referred to as q_z scans, when either the [100] or [010] vector is parallel to the surface or Bragg planes. A reflectivity scan is regarded with respect to the surface or Bragg plane(s) and is not specific to how the crystal lattice is oriented. In crystallography, these two measurements would be referred to as either an h or k scan, respectively. In other words, the scan is performed in the *sample* reciprocal space with reference to the crystal structure, and the geometry is not relevant. This preserves the notion of a certain reciprocal scan without the need to understand anything about the geometry or experimental set-up. This language difference is subtle, but can lead to some misunderstanding.

ii. Unconventional Scattering Attributes

Because of the experimental apparatus, the geometry discussed here is slightly unconventional. The $\mathbf{q}$-scans can not be performed as in normal x-ray diffractometers where there are usually degrees of freedom to scan each variable.

One issue is that there is no χ degree of freedom, only the in-scattering-plane sample angle θ. Another thing is the chamber does not have the ability to scan the position of the detector angle γ. These two facts prevent reciprocal lattice-type scans using this apparatus. The idea in these types of coherent experiments

is to go to a specific point in $\mathbf{q}$-space and measure time correlation functions. This is opposed to typical diffraction experiments where intensity is measured, sometimes averaged over long periods of time, as a function of one or more of these angles.

iii.   Derivation in 3-dimensions

As discussed briefly in Section 5., the momentum calculation can be thought of as a coordinate transformation of the initial momentum k_i to a final position, k_f. Once this quantity is calculated, the problem is essentially solved. The result is simply the magnitude of the difference vector $\mathbf{q} = \mathbf{k}_f - \mathbf{k}_i - \mathbf{Q}_0$. Because the detector position is limited to the scattering plane, there is no out-of-plane degree of freedom for the camera, as is common in diffractometers. All out-of-plane diffuse scattering data is limited to the acceptance of the detector in that direction. Hence, we only need one large-angle rotation where the order must be kept track of. This angle γ is the sum of both the detector and chamber angles. The other two rotations can both be described with the small-angle approximation and are considered infinitesimal rotation matrices, referring to the two orthogonal axes of the detector. As is common in matrix algebra, the order always matters, except with 'differential rotations', since these commute to first order. We will start with the differential matrices first:

$$\mathbf{k}_f = A_{lm}\mathbf{k}_i \qquad (A.2)$$

where A_{lm} is a matrix element equal to $\hat{e}_l \cdot \hat{e_m}'$ where the primed notation refers to unit vectors in the final frame of reference. Note that here the l and m Roman numerals are indices and the i and k simply label the initial and final wavevectors. These matrices can be written as

$$A(\delta\beta) = \begin{pmatrix} \cos\delta\beta & \sin\delta\beta & 0 \\ -\sin\delta\beta & \cos\delta\beta & 0 \\ 0 & 0 & 1 \end{pmatrix} \qquad (A.3)$$

$$B(\delta\alpha) = \begin{pmatrix} \cos\delta\alpha & 0 & -\sin\delta\alpha \\ 0 & 1 & 0 \\ \sin\delta\alpha & 0 & \cos\delta\alpha \end{pmatrix} \qquad (A.4)$$

Here the two infinitesimal rotation angles $\delta\alpha$ and $\delta\beta$ refer to the angles made between the specular wavevector and to the data point in question for the two

directions in the detector plane. Usually, in geometries such as this, the incoming momentum can be chosen to have the direction of one of the principle axes. However, this does not make calculations such as this any easier as we eventually must attain the momentum transfer in the coordinate system of the sample, and not the laboratory. This involves rotating by the sample angle θ at the end of the calculation. We will transform to the lab frame first, followed by the last rotation to achieve the momentum in the sample frame, shown in Figure A.1.

The momentum k_i in the laboratory system is $|k| * (1, 0, 0)$. Conventionally, the beam direction is chosen to be $\hat{z}$, but here we use a q-coordinate system where q_z is the momentum transfer oriented out of the sample plane. This gives a momentum in the new coordinate system after the two infinitesimal rotations

$$k_f = \begin{pmatrix} \cos \delta\alpha * \cos \delta\beta \\ -\sin \delta\beta \\ \sin \delta\alpha * \cos \delta\beta \end{pmatrix} \tag{A.5}$$

Now, the last step to get the lab momenta is to transform this final momentum state by the rotation of the detector position

$$T(\gamma) = \begin{pmatrix} \cos \gamma & 0 & -\sin \gamma \\ 0 & 1 & 0 \\ \sin \gamma & 0 & \cos \gamma \end{pmatrix} \tag{A.6}$$

giving us the final momentum in the laboratory frame.

The final result for this third rotation is a total momentum $\mathbf{Q} = \mathbf{k}_f - \mathbf{k}_i$ of

$$\frac{\mathbf{Q}}{|k|} = \cos \delta\beta \begin{pmatrix} \cos \delta\alpha * \cos \gamma - \sin \delta\alpha * \sin \gamma - \sec \delta\beta \\ -\tan \beta \\ \cos \delta\alpha * \sin \gamma + \sin \delta\alpha * \cos \gamma \end{pmatrix} \tag{A.7}$$

This gives the full 3d momentum as a function of angle. Again as discussed earlier in Section 5., what is useful in terms of physics is to know q-values as a function of the detector plane coordinates x and y. The small-angle approximation for $\tan \alpha = (y/L) \sim \alpha$ gives

$$\frac{\mathbf{Q}}{|k|} = \left(\cos \frac{x}{L}\right) * \begin{pmatrix} \cos \frac{y}{L} \cos \gamma - \sin \frac{y}{L} \sin \gamma - \sec \frac{x}{L} \\ -\tan \frac{x}{L} \\ \cos \frac{y}{L} \sin \gamma + \sin \frac{y}{L} \cos \gamma \end{pmatrix} \tag{A.8}$$

Just from using the identity $\sin^2(x)+\cos^2(x) = 1$, we can reduce the magnitude to:

$$\left|\frac{Q}{k}\right| = \sqrt{1 - 2\cos\left(\frac{x}{L}\right)(C_1 + C_2 + C_3)} \tag{A.9}$$

for the coefficients:

$$C_1 = \cos\left(\frac{y}{L}\right)\cos\gamma$$

$$C_2 = \sin\left(\frac{y}{L}\right)\sin\gamma$$

$$C_3 = \cos\left(\frac{x}{L}\right)\sin^2\left(\frac{y}{L}\right)\sin^2\gamma$$

giving the total $\mathbf{Q}$ as a function of detector coordinates, $\mathbf{Q}(x,y)$.

To get $\mathbf{Q}$ in the sample frame of reference, one last rotation must be performed by the negative sample angle about the y-axis. If we denote the components in Equation A.8 as q_i for x, y, and z, the result is simply the following components:

$$q_x' = q_x * \cos\theta + q_z * \sin\theta \tag{A.10}$$

$$q_y' = q_y' \tag{A.11}$$

$$q_z' = q_z * \cos\theta - q_x * \sin\theta \tag{A.12}$$

where the prime here denotes the sample coordinate system.

The last step is to calculate the relative momentum, denoted by q for consistency. This quantity is simply the magnitude of the difference between the momentum in the sample coordinate system and $\mathbf{Q}_0$, which equals the reciprocal lattice vector $\mathbf{G}$ for Bragg scattering, or the specular momentum value for surface scattering

$$q = |\mathbf{Q} - \mathbf{Q}_0| \tag{A.13}$$

We can just take $\mathbf{Q}_0$ to be equal to Equation A.8 at the origin of the scattering distribution, when $(x,y) = (0,0)$

$$\mathbf{Q}_0 = \sqrt{(\cos\gamma - 1)^2 + \sin^2\gamma} \tag{A.14}$$

or also equal to the familiar form of $Q = \left(\frac{4\pi}{\lambda}\right)\sin\gamma$, the normal form of $\mathbf{q}$ with no diffuse scattering. This only changes Equation A.12 in the last component, giving q_z an additional term:

$$q_z' = q_z * \cos\theta - q_x * \sin\theta - 2\sin\gamma \tag{A.15}$$

The final equation is

$$\mathbf{q} = \sqrt{\sum_i (Q^i - Q_0^i)^2} = \sqrt{\sum_i q_i' * q_i'} \qquad (A.16)$$

A map of the q-dependence as seen by the detector is reproduced here from Section 5. shown in Figure A.2. This result is the relative momentum magnitude in three dimensions.

iv. *Derivation in 2-dimensions*

As mentioned in the text, since some systems only require a 2-dimensional functional dependence, the corresponding momentum must be changed accordingly. This changes Equation A.16 by removing the third component q_z, and changes the functional form considerably. The result is

$$\frac{\mathbf{q}_{2d}}{|k|} = \left(\begin{array}{c} \cos \frac{x}{L} \cos \frac{y}{L} \cos \gamma - \cos \frac{x}{L} \sin \frac{y}{L} \sin \gamma - 1 \\ - \sin \frac{x}{L} \end{array} \right) \qquad (A.17)$$

The 2d dependence is much more strongly affected by the γ-dependence of the final momenta as shown in the 2d discussion of Section 5.. The result for $|\mathbf{q}_{2d}|$ is

$$|k| * [\cos^2 X \cos^2 Y \cos^2 \gamma - \cos^2 X \sin^2 Y \sin^2 \gamma - \sin^2 X \qquad (A.18)$$
$$+ 2(\cos X \sin Y \sin \gamma - \cos X \cos Y \cos \gamma - \cos^2 X \cos Y \sin Y \sin \gamma \cos \gamma)]$$

v. *Validity*

Recall that the validity of this calculation is in the small angle approximation, as the angular acceptance of the detector is approximately $30\,\mathrm{mrad}$ for the sample-camera distance of $0.4\,\mathrm{m}$. In situations where the diffractometer has the detector position not limited to the scattering plane, this approximation would not hold. The β-angle would not necessarily be constrained to the small values set by the detector size.

One way to view this approximation is to look at the section of the Ewald sphere that is being probed. For this geometry, it is essentially a 'Ewald plane', as the surface of a sphere looks like a plane locally and the energy resolution changes near the edges of the detector. Another, but equal way to look at this is that we are measuring higher energy x-rays near the edges of the detector: the only way to make a plane equal to a section of a sphere in k-space.
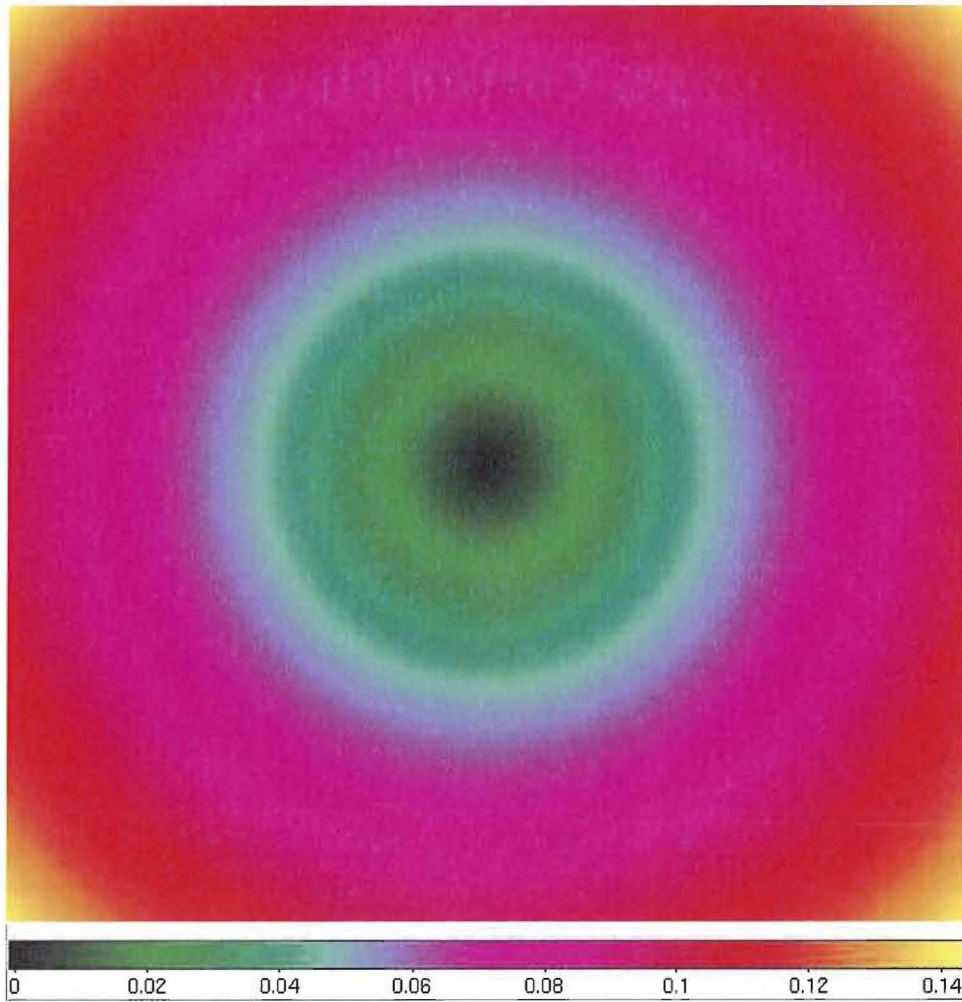
Fig. A.2: **Map of q-dependence** The momentum dependence in 3d. The coordinate system is in x and y units for the Cartesian detector plane, giving an effective q-dependence for γ of $\pi/4$. This figure is reproduced from Figure 5.6 of Section 5. to demonstrate the q-dependence of this more involved derivation.

APPENDIX B

SYNCHROTRON RADIATION

In this appendix we will discuss synchrotron radiation and how it is generated. The discussion will follow work from the synchrotron chapter from Atwood [97] and the Undulators and Wigglers for Synchrotron Light Sources section in Jackson's chapter on radiation [116] in *Classical Electrodynamics*. We will only focus on the radiation generated from undulators as that is what is used for all the work in this thesis, and the choice of insertion device used for most experiments that rely on a high degree of x-ray coherence. Additionally, we will describe some of the properties of undulators, focusing on the specific characteristics that are relevant to coherent scattering.

i. *Main Idea and Brief History*

The basic formulas of synchrotron radiation can be derived from classical electromagnetic theory, Heisenberg's uncertainty principle, and special relativity. The main idea is to take advantage of radiation that gets emitted when an electron or other charged particle undergoes some type of acceleration. A typical example of this is the Bremsstrahlung radiation that occurs when electrons slam into a material with a high atomic number, Z. As the ions have a much larger mass then the incoming electrons, they abruptly stop, or scatter strongly (or a combination of the two). When this happens, high energy photons are emitted proportional to the large acceleration.

In synchrotrons, the acceleration is controlled by a magnetic field. By the Lorentz force law, anytime an electron trajectory is perpendicular to a magnetic field, the resultant force will be felt by the particle in the direction orthogonal to the plane containing the trajectory and field direction vectors. Just as a planet is held in orbit by a force that is orthogonal to the velocity vector of the planet and directed toward the star it is orbiting, a particle can be held in a circular orbit by a magnetic field orthogonal to its direction of travel. In fact, this is

the general model of the first 'cyclotron', invented by Orlando E. Lawrence in 1929, the scientist who won the Nobel prize for his work in 1954 and now has a United States Department of Energy National Laboratory name after him in his honor [140].

Synchrotrons developed soon after, though dedicated sources (2nd generation) did not arrive until the 1970s and 80s. The earlier versions (retroactively coined '1st generation' sources) were parasitical, utilizing otherwise wasted energy loss radiation from high energy particle colliders. With continuous range of energies, first generation sources gave an increase in brightness of five orders of magnitude, and seven for second generation sources [141]. The second generation sources were the first to be dedicated, and were created to contain a series of magnets that could be placed in the appropriate configuration around the circumference of the trajectory to 'steer' the beam in the circular path, giving access to the radiation all along the circumference of the accelerator.

Finally, the birth of third generation sources came with the demonstration of insertion devices [142], discussed in depth in the next section. Here we just remark that as long as the electron beam can be stabilized, the continual acceleration of particles along the circumference of the storage ring - as it is called - allows a constant stream of photons generated in a wide range of energies, depending on the energy (and hence the diameter of the ring) of the electron beam. One issue that arises is keeping the energy constant of the electron bunch since they are constantly loosing energy due to the radiative process. This is in fact, the exact same problem that arose with thinking of atoms as small solar system models, where there are many planets revolving around the sun. In this naive model, the nucleus kept a constant attractive force perpendicular to the tangential electron velocity vector to hold the particle in orbit. By the same reasoning, this was inconsistent with the fact that any electron undergoing acceleration must radiate. This question arose in the 1920's as a paradox, and was one of the reasons for the formulation of 'new physics' in the understanding of the atom and was a corner stone of quantum theory. Without a quantum mechanical analog in synchrotron beam physics, the problem is solved in particle accelerators by a radio frequency cavity. This is a section of the storage ring that produces a axial electric field in the direction of electron travel that gives a boost to the high velocity particles. This of course oscillates with the same frequency as the arriving electron bunches.

Lastly one may ask, how do the electrons start? The whole process is begun with a low work-function material. This function describes how hard it is to ionize the material. That is, the energy needed to strip the system of one electron must be low, like it is in tungsten (used for light bulb filaments). By applying a large positive voltage to a grounding plate possessing an aperture in it a short distance away, electrons are accelerated through the aperture to form a 'electron gun'. Once the stream of electrons is attained, it is passed into a linac. This linear accelerator ramps the speeds up increasing the energy before dumping the beam into a booster ring. The is where the electron beam is focused and stabilized before injection into the main storage ring, and where the beam reaches its full capacity, approaching the speed of light. The booster ring consists of magnetic lenses where the goal is to confine the beam diameter into a small a cross-sectional area as possible. A magnetic lens can be thought of as alternating poled magnet. One version would 'squeeze' the beam in the vertical direction while adjacent to that 'lens' is a magnetic dipole ring that would focus the horizontal. By a series of similar devices, the beam can be focused down to incredibly small regions of phase space. The same magnetic lensing is used in high energy particle colliders and in the optics of electron microscopes.

ii. Insertion Devices

The aspect that sets 3rd generation synchrotron facilities apart is the development and implementation of insertion devices. The invention and use of these spawned a new generation of facilities with unprecedented flux and brightness. The two most notable devices are the wiggler and undulator. We will focus on the undulator as it is the basis of the experimental endstation and beamline we have run all the experiments described here. Wigglers give a broad range of energies but differ from previous bending magnets in that they peak at much higher energies. They are particularly useful in applications where a broad range of energies is needed. With regard to coherence properties, the wiggler is a not a optimal device.

iii. Undulators

A picture of an undulator is shown in Figure B.1. An undulator is a device with a series of magnets which force the electrons traveling through its center to *undulate* periodically. As shown in the diagram, this is only a slight acceleration in a transverse direction to the average direction of travel of the electrons,
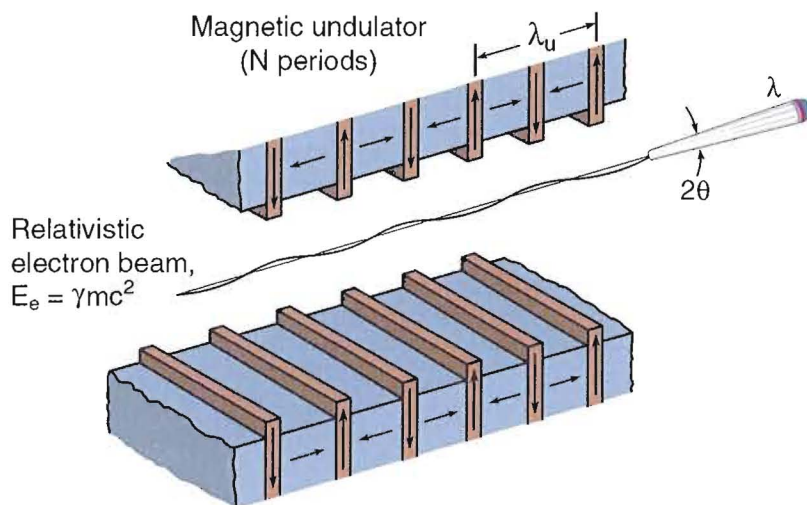
Fig. B.1: **Magnetic Undulator** A typical insertion device found in 3rd generation synchrotron facilities: the undulator. The magnet arrays are set up such that they induce a periodic magnetic field on the electron beam traveling through the center of the device. The causes a force in the transverse direction according to the Lorentz force law. The small angular excursions cause a beam to be radiated that emits the majority of the power in a narrow forward cone. These waves are partially coherent and have a reasonable energy resolution. Starting from the center of the radiated beam on axis, the spectrum of energies get lower for angles further from the forward direction [10].

followed immediately by an acceleration in the opposite direction. In fact, the magnet structure is such that the magnetization rotates by $\pi/2$ for each magnet, projecting a smooth, periodic magnetic field on the electron beam. The result is an oscillation of the electron beam about the original directional vector through the course of the device. Each undulation emits tangential radiation to the original path, which is precisely collinear with the electron beam velocity for small electron excursion angles. The periodicity of the magnet array forces the new radiation generated at the $i\,th$ magnet pair to occur in phase with previous electromagnetic radiation generated at the $(i-1)\,th$ pair. The result is after the electron bunch has completed the journey through the device, the radiation that is available at the termination of the device is highly coherent and has a large flux over a small area. One thing that sets it apart from its counterpart wiggler, is when the electron beams are tightly confined, an idea usually optimized at synchrotron facilities, the emitted radiation that occurs is in a narrow spectral range and small angular cone with concomitant angular divergence. The median of the radiation produced is centered at soft x-ray wavelengths, as we will see,

and these straight section devices are placed at intervals along the circumference around the storage ring.

Angular Divergence

One thing already mentioned is the small angular divergence of undulators that makes them ideal for coherence based experiments. Here we will look into the divergence more closely. A clever method can be used to calculate the radiation patterns in undulators. Namely, to use classical dipole radiation considerations, which would be the case for the rest frame of the relativistic electron bunch, and Lorentz transform back to the laboratory frame of reference. We will estimate this first for a bending magnet (only one magnetic structure), and then see how this changes for an undulator.

This is similar to a common problem in standard text book problems in undergraduate relativity courses: the search light effect. What happens to the headlights of a relativistic train as seen by a stationary observer? If the angle from the direction of travel is given by θ in the laboratory frame (stationary observer) and θ' by the relativistic frame (according to the train passengers) the Lorentz transformation is give by:

$$\tan \theta = \frac{\sin \theta'}{\gamma(\beta + \cos \theta')} \tag{B.19}$$

For the small angle approximation, $\tan\theta = \sin\theta \sim x - x^3$ and $\cos\theta \sim 1 - x^2$ we have

$$\theta - \theta^3 = \frac{\theta' - \theta'^3}{\gamma(\beta + 1 - \theta'^2)} \tag{B.20}$$

or for $\beta \sim 1$, to first order, this is just

$$\theta = \frac{\theta'}{2\gamma} + O(\theta'^2) \tag{B.21}$$

If fact, a definition exists of undulator radiation in the laboratory frame that defines any angular divergence of the *electron* beam to be

$$\theta_e < \frac{1}{2\gamma} \tag{B.22}$$

Any device which contains electron angular excursions θ_e smaller than this magic number, is dubbed an 'undulator'. For a divergence of milliradians, this gives a divergence in the laboratory frame of microradians for γ-values of typical rela-

tivistic electron beam speeds for lower to medium energy storage ring facilities in the soft x-ray regime.

Dipole Radiated Power

We can make some simple arguments to justify the choice of definition in the last section. Starting from Maxwell's equations only, where the conservation law of charge can be directly derived, we can calculate the solution to the radiated fields from an accelerated point charge. The result is:

$$\mathbf{E}(\mathbf{r}, t) = \frac{e\hat{\mathbf{k}} \times \ddot{\mathbf{r}}}{4\pi\epsilon_0 c^2 r}$$

and

$$\mathbf{H}(\mathbf{r}, t) = e\frac{\mathbf{k} \times (\hat{\mathbf{k}} \times \ddot{\mathbf{r}})}{4\pi\mu_0 c^2 r} \tag{B.23}$$

where the second equation just comes from

$$\mathbf{H}(\mathbf{r}, t) = \frac{\epsilon_0}{\mu_0}\mathbf{k} \times \mathbf{E}(\mathbf{r}, t)$$

The Poynting vector can be calculated from here, $\mathbf{S}(\mathbf{r}, t) = \mathbf{E}(\mathbf{r}, t) \times \mathbf{H}(\mathbf{r}, t)$, the magnitude of which can be used to get the power per solid angle

$$\frac{dP}{d\Omega} = \frac{e^2\ddot{r}^2}{16\pi^2\epsilon_0 c^3}\sin^2\phi \tag{B.24}$$

which can also be solved using Lamor's formula. The crucial dependence is that the power goes as $\sin^2\phi$ where the angle ϕ is taken to be between the acceleration $\ddot{r}$ and point of measurement. The complementary angle to ϕ is θ' as we have been calling it, the angle between observation and the plane orthogonal to $\ddot{r}$. In terms of θ', the power goes as $\cos^2\theta'$, where we choose the direction of electron travel to define the vector in the orthogonal plane. A reasonable measure of total power radiated into a given angular acceptance is the cutoff for which acceptance is one half. This is precisely when $\cos\theta' = \frac{1}{\sqrt{2}}$, or for $\theta' = \pi/4$. Substituting into Equation B.19, this gives

$$\theta \sim \frac{1}{2\gamma} \tag{B.25}$$

So after calculating the radiation cone encompassing half of the radiated power we Lorentz transform back to the laboratory frame to estimate the angle within

which we have access to half of the power of the radiation, given by Equation B.25.

Undulator Narrowing

For a large array of permanent magnets such as is found in an undulator, the emission solid angle reduces to

$$\theta \sim \frac{1}{\gamma \sqrt{N}} \tag{B.26}$$

where N is the number of periods the electron undergoes. The higher the number of magnets, the smaller divergence in the radiation source properties, and hence the higher degree of coherence. We will see where this angle comes from in the next section. Suffice it to say, here we just note that this angular divergence of the beam can be controlled by the undulator device parameters.

iv.   The Undulator Equation

One of our greatest concerns is increased coherent flux from undulators. We have looked at the source size and divergence properties which we know is related to ultimate transverse coherence. We now turn to the temporal coherence of the central cone of radiation. We just saw how the source size is dominated by Lorentz transformed dipole radiation, which sets the spatial and angular limit of the central cone. Now we discuss spectral resolution, which is proportional to the longitudinal coherence.

The Lorentz Force Solution

With a special relativity, we can derive the full undulator equation which is paramount to the spectral resolution and the longitudinal coherence attainable. We can write the force law

$$\partial_t \mathbf{p} = q(\mathbf{E} + \mathbf{v} \times \mathbf{B}) \tag{B.27}$$

where the momentum is understood to be relativistic. Also, since the length of the undulator is typically $5\,\mathrm{m}$ or so, far from free electron laser action, the radiated field from the undulation has negligible effect on the electron beam

motion, reducing the electric field term to zero. The result is

$$m\gamma \frac{\partial}{\partial t}\dot{x} = e\frac{\partial}{\partial t}zB_0 \cos\left(\frac{2\pi z}{\lambda_u}\right) \qquad \text{(B.28)}$$

where we have pulled the relativistic factor γ outside the derivative, as it is constant in a magnetic field since it only is a function of the magnitude of the electron velocity. This can also be seen since the dot product of the velocity and the force, or $\mathbf{v} \times \mathbf{B}$ is zero by definition, giving a constant electron energy. We also have assumed the beam is traveling in the z-direction with the periodic magnet array applying fields in the y-direction, giving the cross-product a x-component only, to first order. To a very good approximation, the magnetic fields felt by the electron bunch is periodic, denoted above by λ_u, the period of the undulator which differs from device to device. Integrating both sides gives

$$\dot{x} = \frac{Kc}{\gamma}\sin\left(\frac{2\pi z}{\lambda_u}\right) \qquad \text{(B.29)}$$

for a convenient choice of the constant K given by

$$K \equiv \frac{eB_0\lambda_u}{2\pi mc} \qquad \text{(B.30)}$$

Note that the simplified version of the equation solves exactly, but the x-component of the velocity is a function of z. This physically demonstrates that there is a speed modulation of the electron beam with position in the undulator. The electron beam velocity is largely fixed to the plane then spanned by the axial velocity $\dot{z}$ and transverse $\dot{x}$. The ratio of these gives the maximum excursion angle of the beam

$$\tan\theta_e \sim \frac{\dot{x}}{\dot{z}} \sim \frac{Kc}{\dot{z}\gamma}\sin\left(\frac{2\pi z}{\lambda_u}\right) \qquad \text{(B.31)}$$

or for axial velocity near c and for small angles

$$\theta_e \sim \frac{K}{\gamma}\sin\left(\frac{2\pi z}{\lambda_u}\right) \qquad \text{(B.32)}$$

This demonstrates the reason K is usually referred to as the magnetic deflection parameter, giving the maximum excursion of the beam horizontally. Thus, as mentioned earlier in equation B.22, for angular electron excursions smaller than the radiation emission angle θ, the emitted radiation will be confined to a narrow cone. Based on the above derivation, we can see that this is for any

magnetic field strength and magnet periodicity combination that gives $K \leq 1$, or weak-field limit.

Harmonics

Using $\gamma(\dot{x}, \dot{y})$ as any motion in the vertical direction is negligible, we can solve B.29 to get $\dot{z}(z)$

$$\beta_z^2 = 1 - \frac{1}{\gamma^2} - \frac{K^2}{\gamma^2} \sin^2 \left(\frac{2\pi z}{\lambda_u} \right) \tag{B.33}$$

To first order in the binomial expansion, using the weak-field limit of undulators, we retrieve

$$\beta_z = 1 - \frac{1 + \frac{K^2}{2}}{2\gamma^2} + \frac{K^2}{4\gamma^2} \cos(2k_u z) \tag{B.34}$$

with the help of the double angle formula. Here we see that the axial velocity is itself a periodic function of z, giving rise to harmonics. These become important for expanding the available range of energies and/or for exploiting polarization phenomena. For the *average* axial velocity, the sinusoidal term is irrelevant, and the velocity change is given by the 2nd term in equation B.34. For comparative purposes, we will write this as

$$1 - \overline{\beta_z} = \frac{1}{2\gamma^{*2}} \tag{B.35}$$

for a definition of an effective γ^* of

$$\gamma^* = \frac{\gamma}{\sqrt{1 + \frac{K^2}{2}}} \tag{B.36}$$

So although the total magnitude of the electron beam velocity stays constant in the magnetic field, on average, the axial direction of the electron speed is decreased a small amount, giving an reduction factor to the z-component of the Lorentz factor. We will return to this in a moment.

Relativistic Doppler Shifted Wavelengths

In the electron frame, the beam perceives an effective wavelength λ' of λ_u/γ. Recall the Doppler shift for frequency f, after substituting for $f' = c/\lambda'$ is given by

$$f = \frac{c}{\lambda_u(1 - \beta \cos \theta)} \tag{B.37}$$

where θ here is the angle of observation from the direction of the motion. We can use the power series expansion for $\cos\theta$ for small angles

$$f = \frac{c}{\lambda_u(1 - \beta + \frac{1}{2}\beta\cos^2\theta)} + O(\theta^3) \tag{B.38}$$

or

$$f = \frac{2c\gamma^2}{\lambda_u(1 + \gamma^2\theta^2)} \tag{B.39}$$

with $1 - \beta = 1/2\gamma^2$ for $\beta \sim 1$. This is because $1 - \beta^2$ can be written as $(1 - \beta)(1 + \beta)$ or equivalently $2(1 - \beta)$ when β approaches the speed of light. The result is

$$1 - \beta = \frac{1}{2\gamma^2} \tag{B.40}$$

Finally, this gives an observed wavelength from equation B.39 of

$$\lambda = \frac{\lambda_u}{2\gamma^2}(1 + \gamma^2\theta^2) \tag{B.41}$$

We note here that on-axis radiation is decreased by a factor of $1/2\gamma^2$. For the ALS with electron energy of 1.9 GeV and an 8.0 cm undulator period such as the one used in our experiments, this gives an observed wavelength peaked on axis of 2.85 nm. Thus the given magnet periods have been chosen to generate electromagnetic radiation peaked in the soft x-ray regime for the given source energy.

In our study of harmonic generation, where we saw oscillatory solutions to the Lorentz force law, we denoted the reduced Lorentz factor by γ^* given in equation B.36. This work now demonstrates that axially, the observed wavelength given in Equation B.41, gives a further Lorentz contraction by the same factor. For γ^* written explicitly, this yields the undulator equation

$$\lambda = \frac{\lambda_u}{2\gamma^2}\left(1 + \frac{K^2}{2} + \gamma^2\theta^2\right) \tag{B.42}$$

which simply translates to an extra term in the observed wavelength contraction in the laboratory frame. It now becomes clear how the energy spectrum emitted from the device is strongly dependent on the undulator period, the energy of the storage ring of the facility, the magnetic field strength, and the angle off-axis where the radiation spectrum is being detected.

As we saw in Equation B.34, the 2nd harmonic arose from the fact that we only expanded the solution out to first order in K/γ. By keeping higher order

terms, we can generate solutions for every power. This gives radiation for each integer multiple n of fundamental frequency $n\omega_u$ and amplitudes which scale as K^n. For harmonic n, the observed wavelength for that harmonic then scales as λ/n, where the fundamental is given by B.41.

Undulating Energy Bandwidth

We can calculate the bandwidth within any given angular region by subtracting the $\lambda(\theta)$ for $\theta = 0$ from $\lambda(\theta)$, or λ from $\lambda + \Delta\lambda$. The result is

$$\Delta\lambda = \frac{\lambda_u \theta^2}{2} \tag{B.43}$$

By taking the ratio $\Delta\lambda/\lambda$ we are left with

$$\frac{\Delta\lambda}{\lambda} = \frac{\theta^2 \gamma^2}{\left(1 + \frac{K^2}{2} + \gamma^2 \theta^2\right)} \tag{B.44}$$

for small K, always true for undulators, and substituting in Equation B.26 for the angle θ, we get a relative spectral bandwidth of

$$\frac{\Delta\lambda}{\lambda} = \frac{1}{N} \tag{B.45}$$

where N is the number of magnet periods in the undulator. Remember that the angle $\theta = 1/\gamma\sqrt{N}$ was defined as the half-angle in section iii. for the central radiation cone. To be more precise, the spectral bandwidth of $1/N$ is chosen to define the central cone, and from our bandwidth generated from the undulator Equation B.44, we then estimate the angle of this 'central cone'.

One more note on harmonics: not only are they useful for the different range of energies available and for the differing polarization properties, but the energy resolution differs as well. By the comment earlier on how the wavelength scales with harmonic number, we can conclude that the spectral resolution for harmonic n is given by

$$\left(\frac{\Delta\lambda}{\lambda}\right)_n = \frac{1}{nN} \tag{B.46}$$
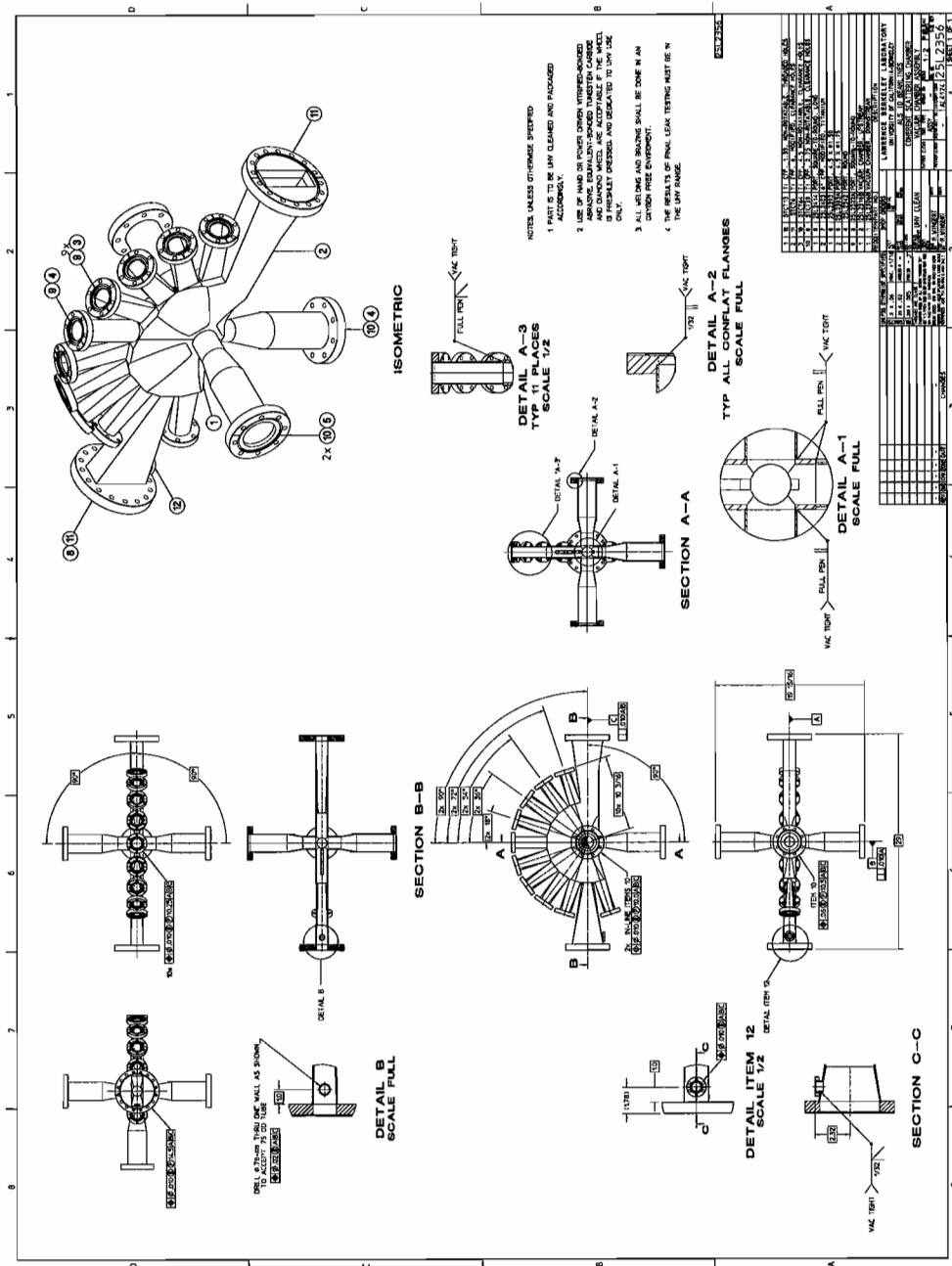
This can be seen because the velocity arguments discussed above lead to the fact that there are many harmonics developed (velocities of alternating polarizations), essentially a mixing process driven by the periodic magnetic field in the cross-product term of the force equation. There the velocity mixes with the magnetic period to produce the fundamental velocity in the x-direction, which

mixes with the periodic field to give a second harmonic on axis in the z-direction. This mixes again with the field to produce a third harmonic, again now transverse to the average velocity. The repeats indefinitely. By Fourier analysis, the electron will execute n oscillations for every one period of the magnetic field. The resultant wavelength will be n times shorter and the resultant wave train will be $n * N$ oscillations long [143]. Therefore, we can expect the wave train to define a relative spectral bandwidth n times narrower than Equation B.45, as shown in Equation B.46.

APPENDIX C

CHAMBER DIAGRAM

The diagram on the following page is a sketch of the coherent scattering chamber, or 'flangosaurus' which was drawn by Mike Wingert, from the Engineering Division at Lawrence Berkeley Laboratory. This diagram shows some of the details and the precision necessary to construct the titanium, thin-walled chamber.

APPENDIX D

LINEAR **H**-FIELD CALCULATIONS

The following appendix on linear **H**-field calculations was largely written by the author in the summer of 2002 in collaboration with Dr. Soren Prestemon in work related to a similar eight-pole electromagnet apparatus, and some of the results have been partially published [122]. This was the original version of the magnet, which was designed for soft x-ray magnetic dichroism and magnetic spectroscopy experiments at the Advanced Light Source. The instrument is currently available and running on Beamline 4.0.2 of the ALS at Lawrence Berkeley Laboratory. This original version has a smaller chamber, and corresponding higher maximum field strength, and includes different pole sets for higher resolution measurements at low-field. The scattering chamber octapole magnet described in this thesis includes many differences, but is based on the that design. One obvious adjustment for this instrument was to include access to the full scattering plane which puts constraints on the chamber, and hence magnet design. The calculation remains largely the same but is modified from the original manuscript where necessary, as it applies to the current instrument.

i. *The 4d Current-coordinate Subspace*

In the case where the poles are non-ferromagnetic, the fields can be plotted for any given current distribution based on a linear mathematical model. The main issue is that to conduct an experiment with a homogeneous magnetic field distribution across the sample, there needs to be knowledge a the **H**-field with respect to the 3d Cartesian coordinate system of the sample. The fields are created by four dipole electromagnets directed towards the origin of the chamber. This can be envisioned as eight current loops based at the corners of a unit cube, with the current area vectors oriented towards the center. Hence the current distribution that is responsible for the fields is given by a 4-dimensional, non-orthogonal space.

Assuming we can take the distribution in the coils to yield linear field distributions, we must then compose a transformation that will take a 3d Cartesian matrix $(\hat{\imath}, \hat{\jmath}, \hat{k})$ and convert it into a 4-vector distribution in current coordinates $(\hat{e}_1, \hat{e}_2, \hat{e}_3, \hat{e}_4)$.

We define the $\hat{\imath}$, $\hat{\jmath}$, and $\hat{k}$ vectors as the three orthogonal directions where the possible field attainable is maximized. When the currents are at a maximum limit for the coils, the net field distribution will point along one of these principle axis, based on symmetry considerations.

ii. The Transformation Matrix

The above prescription means the field strengths are described by a fraction between zero and one. The basis vectors in euclidean space are defined to have unit length when the *maximum* possible distributions generated with the magnet are used; any magnetic field can be described by a 3-vector (H_1, H_2, H_3) where $0 \leq \mid H_i \mid < 1$. Next we define the four current-coordinates to be the directions pointing from the origin to the four corners of one of the faces of the cubic structure. This face is chose to be the one in which the negative y-axis intersects through the center of the face. The negative y-axis is chosen to be congruent to the sample coordinate system. Note that both the 3d and 4d coordinate systems have a common origin. With this orientation, we can now write $\mathbf{H} = \Gamma \widetilde{M} \mathbf{I}$ and define a coordinate transformation map

$$\widetilde{M} = \begin{pmatrix} 1 & -1 & -1 & 1 \\ -1 & -1 & -1 & -1 \\ 1 & 1 & -1 & -1 \end{pmatrix} \tag{D.47}$$

Where Γ is some conversion factor that relates the current density to the B-field, $\mathbf{I}$ is the four dimensional current distribution, $\mathbf{B}$ is the 3-d magnetic field, and $\widetilde{M}$ is the matrix for mapping the field to the 4-dimensional space.

iii. Parameter Variations of the Solution

In general we have four degrees of freedom to create a 3-component field, implying that there are infinite ways to choose how to distribute the current while producing the same field. However, one solution to $\mathbf{I}(I_1, I_2, I_3, I_4)$ exists that will allocate the current to the four dipole magnets the most evenly. We devised a way to systematically do this with an algorithm that adds all the basis vectors together to get one solution, selects another solution based on the

outcome of the summation, and then adds the two linear solutions. The final solution is found as we adjust all the parameters to both sub-solutions accordingly to yield the final, most efficient result. This method could be repeated, but using the two solutions to generate the final solution returns a distribution that is sufficient for the purposes described here.

iv.   The $\mathbf{S}^0$ solution

The first solution is trivial. Since each sample coordinate system basis vector is a superposition of a maximum current configuration, i.e.

$$(1,0,0) \rightarrow (I_1^{max}, -I_2^{max}, -I_3^{max}, I_4^{max}) \tag{D.48}$$

we can easily get the first solution in current-coordinates just by this superposition, even though this almost always is not the most efficient choice. Hence the first step can always be calculated immediately, $\mathbf{S}^0(I_1, I_2, I_3, I_4) = (A^0, B^0, C^0, D^0)$.

v.   The Sub-Matrices

The first step to get the second part of the final solution, $\mathbf{S}^\mu$, where μ is an integer between one and four, is to look at the four different cases of an extremity: where one pole has no contribution. With at least one entry in the current 4-vector zero, this is favorable mathematically, giving a square matrix expression and allowing a unique solution. The motivation behind this idea is that by zeroing the entry of that corresponding to the maximum current in the $\mathbf{S}^0$ solution, the addition of the two solutions will be more favorable regarding power output of each magnet. The current supplied to each dipole will be more evenly distributed, yet the field will be the exact same. Take the $I_1 = 0$ case:

$$\begin{pmatrix} H_1 \\ H_2 \\ H_3 \end{pmatrix} = \Gamma \begin{pmatrix} 1 & -1 & -1 \\ -1 & -1 & -1 \\ 1 & 1 & -1 \end{pmatrix} \begin{pmatrix} I_2 \\ I_3 \\ I_4 \end{pmatrix} \tag{D.49}$$

The problem now is 3-d, $\mathbf{B} = \Gamma \widetilde{M_1} \mathbf{I}$, where the one denotes the matrix corresponding to zeroing out the first current entry. Now we can easily calculate

the inverse, M_1^{-1} and get the current *3-vector* as a function of the B-fields:

$$\begin{pmatrix} I_2 \\ I_3 \\ I_4 \end{pmatrix} = \frac{1}{2\Gamma} \begin{pmatrix} 0 & -1 & 1 \\ -1 & 0 & -1 \\ 1 & -1 & 0 \end{pmatrix} \begin{pmatrix} B_1 \\ B_2 \\ B_3 \end{pmatrix} = \begin{pmatrix} B^1 \\ C^1 \\ D^1 \end{pmatrix} \tag{D.50}$$

This enables us to construct a four dimensional solution, $\mathbf{S}^1(I_1, I_2, I_3, I_4) = (A^1, B^1, C^1, D^1)$, where of course A^1 is zero by our assumption. Similarly, the other 3×3 inverse matrices are

$$M_2^{-1} = \frac{1}{2} \begin{pmatrix} 0 & -1 & 1 \\ -1 & -1 & 0 \\ 1 & 0 & -1 \end{pmatrix} \tag{D.51}$$

$$M_3^{-1} = \frac{1}{2} \begin{pmatrix} 1 & 0 & 1 \\ -1 & -1 & 0 \\ 0 & -1 & -1 \end{pmatrix} \tag{D.52}$$

$$M_4^{-1} = \frac{1}{2} \begin{pmatrix} 1 & -1 & 0 \\ -1 & 0 & 1 \\ 0 & -1 & -1 \end{pmatrix} \tag{D.53}$$

The inverse matrices above now give the explicit matrices needed for the final computation. These 4 possible options make it straightforward to calculate the final 4-d current $\mathbf{S}^\mu(I_1, I_2, I_3, I_4) = (A, B, C, D)$ for any μ.

vi. The Algorithm

The algorithm must first calculate the maximum current entry for the solution $\mathbf{S}^0(A^0, B^0, C^0, D^0)$. For instance, define it to be the X^0th entry. A linear combination is constructed between S^0 and the $\mathbf{S}^\mu$th solution vector calculated previously, where the μth distribution was precisely the one with zero current at the X^μth position. We then have a solution $\mathbf{S}^0$ with a maximum at some X^0 and a corresponding solution $\mathbf{S}^\mu$ which is selected based on the fact that it has a minimum at the X^μth position. Our final solution $\mathbf{S}^\mathbf{F}$ is some linear combination of the two:

$$\alpha \mathbf{S}^0 + \beta \mathbf{S}^\mu = \mathbf{S}^\mathbf{F} \tag{D.54}$$

Furthermore, let us call the maximum of the $\mathbf{S}^\mu$th solution Y^μ. Note the index refers to what solution vector the value belongs to, while the character

refers to the component of the vector. So X^0 and X^μ refer to the same component of the 4-vector for the two different solutions. We then want to find when

$$\alpha X^0 = \alpha Y^0 + \beta Y^\mu \tag{D.55}$$

where again X^0 is the maximum to the original solution, the corresponding X^μ is zero by definition, Y^μ is the maximum of the $\mathbf{S}^\mu$th equation, and Y^0 is the entry in the $\mathbf{S}^0$th equation which corresponds to the same component as the maximum in $\mathbf{S}^\mu$.

vii. Alpha

In the ideal case, the magnetic field requested will be applied in the chamber and the solution 4-current will exactly solve the transformation equations, but more importantly, will do so in the most efficient way. For this scenario, there is only one variable to solve for, based on the fact that the solution combination field must be of the same magnitude. These means the α and β from the algorithm then satisfy $\alpha + \beta = 1$. This yields

$$\alpha = \frac{Y^\mu}{X^0 - Y^0 + Y^\mu} \tag{D.56}$$

One problem that may occur is that if two poles have the same maximum in the $\mathbf{S}^0$ solution. But with only 4 sources, 2 sources with the same maximum already accomplishes the goal the original algorithm was set to achieve.

viii.   Symmetry Considerations

The maximum field for the instrument is 0.6 Tesla, but this is only in the one of the three principle axis directions. For a given maximum current density per dipole that is set by the melting temperatures of the components used to construct the system, when all four electromagnets are applying the maximum, the direction will be in one of the 6 directions, always pointed through the center of one of the faces of the cubic structure discussed earlier. Any direction other than these will suffer a loss in magnitude because of the symmetry. When a field is specified which is unattainable by the vector magnet, due to the linearity, the software can just multiply by an overall constant to decrease the magnitude to the maximum field that the magnet can produce in that direction. Figure D.1 shows the maximum field that can be obtained as a function of angle, where the maximum field of unit magnitude in the figure corresponds to 0.6 Tesla. This
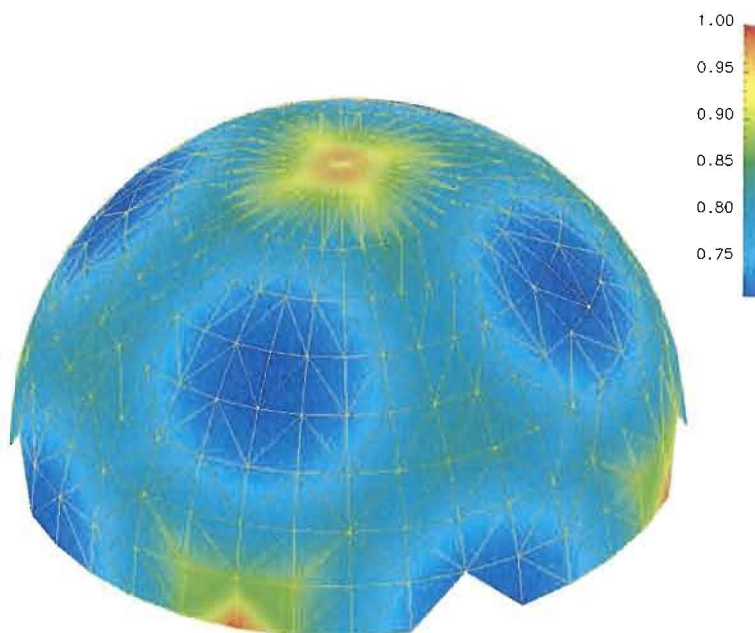
Fig. D.1: **Field Distribution** The calculated fraction of the peak magnetic field as a function of angle. The magnitude is show in the color map at the right. The calculation makes evident how peak fields are only available in principle axis directions [11].

symmetry issue must be taken into consideration when devising experiments for arbitrary angle magnetic field application, as angles for which the field vector is axial to one of the dipoles can suffer a loss in magnitude of up to 25%.

ix. *Non-Linearity*

The second reason for the algorithm discussed above is the non-linearity of the magnets. The poles used inside the coils for increased field strengths are ferromagnetic, which comes with a cost that the current to H-field relationship is highly non-linear for high fields. The reason is that the ferromagnetic core gives a large increase in field for currents applied, but past some critical current, the curve starts to flatten. This is true in general for ferromagnetic materials where the non-linearity occurs because the ferromagnetic poles become saturated. This problem makes the algorithm of distributing the currents as evenly as possible even more pertinent.

In this high field regime, instead of using the matrix defining our coordinate system in Equation D.47, the transformation must consist of entries that are not just real numbers, but functions themselves. It is only in this regime that the curve differs considerably from the linear model. Because this region is minimal compared to the range of fields we are able to produce, we assume our matrix entries are functions of only one current coordinate. This ignores the coupling of other dipole magnets, but this effect will only be a small perturbation to our first non-linear term. This give a new transformation matrix only in this high-field region

$$\widetilde{M}^{ij} = \widetilde{M}^{ij}[f(I_j)] \tag{D.57}$$

where the ± 1 terms are replaced by functions of $f(I_j)$ that neglect the pole-to-pole interactions, and only account for field corrections as

$$H^i = \sum_j f(I_j)I_j \tag{D.58}$$

By measured data elke, it has been shown that the this non-linear fit is needed to get the true relationship for the high-field regime, which is almost at the limit of the magnet. The data falls somewhere between the linear fit to the low field region and the S^0 equation.

APPENDIX E

HARD X-RAY MICRODIFFRACTION

In this appendix, we use high energy x-rays to study the crystallographic disorder in this sample. The crystal used in this study is a twinned single crystal with [100], [010], and [112]-oriented domains. The sample was cut and polished to give a [100]-oriented normal to the crystal face.

The arrangement of these crystallographic domains are on the length scale of tens of microns. By using the larger beam spot and the Bragg scanning capabilities at the National Synchrotron Light Source at the Brookhaven National Laboratory, the crystallographic domain structure was imaged by microdiffraction.

In this appendix, we describe microdiffraction, or micro-topography, which we use to study the structural disorder of the single crystal, $Pr_{0.5}Ca_{0.5}MnO_3$. This technique is well suited for sample characterization because it avoids the difficult, and potentially destructive, sample preparation procedures necessary for electron microscopy, and because an arbitrarily large field-of-view can be attained. In addition, x-rays penetrate several microns into the sample, allowing for the observation of the crystallographic domains in the bulk of the sample. Despite these advantages, no work has yet been conducted on these systems to map out the full structural disorder of the system.

The X-ray microdiffraction work was conducted at the National Synchrotron Light Source at Brookhaven National Laboratory on beamline X20A, at an x-ray energy of 8 keV. The samples used were pure, single crystals [64]. Absent in the literature is a comprehensive characterization of the structural twinning of crystallographic domains in manganese-oxide systems. There exists in many of the pseudocubic single crystals of manganites three types of domains observed [144] with normal directions quasi-parallel to a [100]-type surface: Specifically, [100], [010], and [112]-oriented domains.

A tapered, parabolic glass capillary was used as a incoming x-ray condenser, producing a beam size diameter of $\sim 3-4\,\mu m$ [145]. The actual spatial resolution of the experiment however is slightly larger as it is a convolution between the beam divergence at the sample and the precision of the scanning motors. The detector used was a Si avalanche photodiode 0.9 m from the sample and the motor step size was $1\,\mu$m. The optics and endstation have been described elsewhere [146, 147]. Room temperature lattice constants of 5.395 Å, 5.403 Å, and 7.612 Å have been measured previously for the a, b, and c axes of $Pr_{0.5}Ca_{0.5}MnO_3$ by neutron scattering [6]. The crystal was cut and polished with a [100] surface normal. For these studies, the (400),(040), and (224) peaks were selected with Bragg angles (2θ) of 70.134°, 70.015°, and 70.198°, respectively. This set of reflections was chosen to maximize the momentum transfer, and hence the separation in reciprocal space given the instrumental limitations in 2θ at X20A.

Microdiffraction imaging consists of collecting a diffracted signal for a given reflection using a microfocused incoming beam. The same region of interest of the sample is then scanned through the beam in 2-dimensions for each particular Bragg peak. This way, by measuring the Bragg intensity over a given area, a real space image can be constructed of the crystallographic structure so that each domain orientation can be mapped.

Two motors raster the sample in two orthogonal directions in the plane of the sample surface, and are reproducible to within a micrometer. This allows images of the same region of the sample to be formed for each of the Bragg peaks in Fig. E.1. We measured both low resolution scans over the entire sample (or order millimeters) and high resolution over much smaller regions. Two examples of high resolution maps were shown in panels A and B of Fig. 7.1 in Chapter VII for the (040) and the (224) domains. The green and red regions were high intensity parts of the image where the Bragg condition is met for the beam while that particular part of the sample is being illuminated. The entire image spans a 250 μm x 250 μm region of the sample, using a step size of $2\,\mu$m to compose the map. We measure an average domain size distribution of order 10 μm, comparable to twinning in other systems, such as in ferroelectric lead magnesium niobate for instance [148]. The details of the disorder of these twinned domains and the effect it may have on the CMR results in discussed in a short paper by J. J. Turner et al. [124].
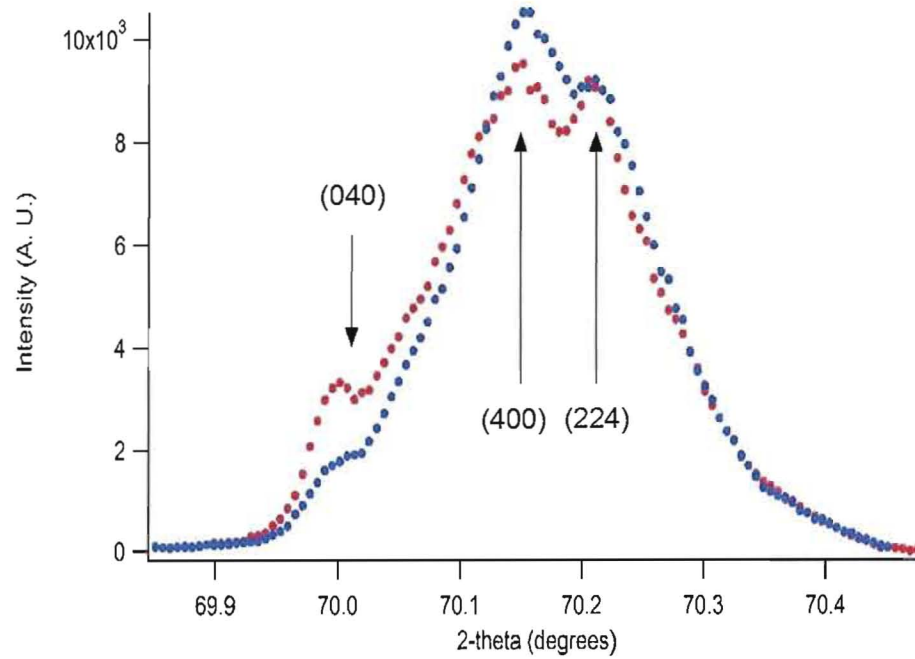
Fig. E.1: **Bragg Scans** Two typical scans are shown for the three Bragg peak set taken at the same sample spot for each scan. Each peak represents different crystallographic domains, narrowly separated in reciprocal space. By adjusting χ, θ and 2θ angles, the contributions of a particular peak can be maximized with respect to the others, as can be seen by comparing the two plots. Once maximized, the peak is selected by using a narrow aperture in front of the detector.

BIBLIOGRAPHY

[1] P. Schiffer et. al. *Phys. Rev. Lett.*, 75:3336–3339, 1994.

[2] E. Dagotto, T. Hotta, and A. Moreo. *Phys. Rep.*, 344:1, 2001.

[3] Y. Tokura and N. Nagaosa. *Science*, 288:462, 2000.

[4] C. D. Ling et. al. *Phys. Rev. B*, 62:56096 – 56111, 2000.

[5] J. P. Hill et al. *Applied Physics A*, 73:723–730, 2001.

[6] Z. Jirak et al. *J. Magn. Magn. Mater.*, 53:153 – 166, 1985.

[7] Image taken from http://stochastix.files.wordpress.com/2007/02/newport-beach-at-sunset.jpg.

[8] A. Schawlow. *Sci. Am.*, 219:120, 1968.

[9] Jacques G. H. Joosten, Erik T. F. Geladé, and Peter N. Pusey. *Phys. Rev. A*, 42:2161 – 2175, 1990.

[10] This image was taken from David Atwood's EECS 213 class notes at UC Berkeley, found at http://www.coe.berkeley.edu/AST/sxreuv/.

[11] These calcualtions were perfomed by Dr. Soren Prestemon (private communication).

[12] Y. Tokura. *Phys. Today*, 56:50, 2003.

[13] E Saitoh et al. *Nature*, 410:180, 2001.

[14] E. Dagotto. *Nanoscale Phase Separation and Colossal Magnetoresistance: The Physics of Manganites and Related Compounds.* Springer, Berlin, 2003.

[15] Tapan Chatterji. *Colossal Magnetoresistive Manganites.* Kluwer Academic Publishers, Dordrecht, Netherlands, 2004.

[16] Y. Tokura. *Colossal Magnetoresistive Oxides.* Gordon and Breach Science Publishers, New York, 2000.

[17] J. Burgy et al. cond-mat/0308456.

[18] N. Mannella et al. *Phys. Rev. Lett*, 92:166401, 2004.

[19] M. Mayr et al. *Phys. Rev. Lett*, 86:135, 2001.

[20] R. M. Kusters et al. *Physica (Amsterdam)*, 155B:362, 1989.

[21] K. Chahara et al. *Appl. Phys. Lett.*, 63:1990, 1993.

[22] R. von Helmolt. *Phys. Rev. Lett.*, 71:2331 – 2333, 1993.

[23] S. Jin et al. *Science*, 264:413, 1994.

[24] E. H. Hall. *American Journal of Mathematics*, 2:287, 1879.

[25] N. W. Ashcroft and N. D. Mermin. *Solid State Physics*. Harcourt Brace College Publishing, Fort Worth, 1976.

[26] A. Abrikosov. *Fundamentals of the Theory of Metals*. North-Holland, Amsterdam, 1988.

[27] http://www.physics.gatech.edu/advancedlab/labs/hall/hall-1.html.

[28] http://www.chembio.uoguelph.ca/thomas/cmr_research.html.

[29] http://physics.unl.edu/~tsymbal/gmr/gmr_origin.html.

[30] G.H. Jonker and J. H. Van Santen. *Physica*, 16:599, 1950.

[31] P. G. de Gennes. *Phys. Rev.*, 118:141, 1960.

[32] J. B. Goodenough. *Phys. Rev.*, 100:564, 1955.

[33] C. Zener. *Phys. Rev.*, 82:403, 1951.

[34] C. Zener. *Phys. Rev.*, 81:440, 1951.

[35] C. Zener. *Phys. Rev.*, 83:299, 1951.

[36] P. W. Anderson and H. Hasegawa. *Phys. Rev.*, 100:675, 1955.

[37] N. Mathur and P. B. Littlewood. *Physics Today*, 56:25, 2003.

[38] P. W. Anderson. *Phys. Rev.*, 115:2, 1959.

[39] A. J. Millis. *Colossal Magnetoresistive Oxides*. Gordon and Breach Science Publishers, New York, 2000.

[40] Y. Tomioka. *Colossal Magnetoresistive Oxides*. Gordon and Breach Science Publishers, New York, 2000.

[41] A. J. Millis et al. *Phys. Rev. Lett.*, 74:5144, 1995.

[42] Steven S. Zumdahl. *Chemistry*. Houghton Mifflin Publishers, Boston, Ma, 1997.

[43] Steven S. Zumdahl. *Chemical Principles*. D.C. Heath and Company, Lexington, Ma, 1995.

[44] K. Terakura, I.V. Solovyev, and H. Sawada. *Colossal Magnetoresistive Oxides*. Gordon and Breach Science Publishers, New York, 2000.

[45] D. S. Dessau and Z. X. Shen. *Colossal Magnetoresistive Oxides*. Gordon and Breach Science Publishers, New York, 2000.

[46] G. Morandi, F. Napoli, and E. Ercolessi. *Statistical Mechanics: an Intermdiate Course*. World Scientific Publishing, Singapore, 2001.

[47] H. E. Stanley. *Introduction to Phase Transitions and Critical Phenomena*. Oxford University Press, New York, 1971.

[48] Jorn Gores. *The Hubbard Model*, 1998. (unpublished).

[49] E. Nazarenko et al. *Phys. Rev. Lett.*, 97:056403, 2006.

[50] M. v. Zimmermann et al. *Phys. Rev. B*, 64:195133, 2001.

[51] P. G. Radaelli et al.. *Phys. Rev. B*, 55:3015, 1997.

[52] H. J. Jahn and E. Teller. *Proc. Roy. Soc.*, A161:220, 1937.

[53] K. I. Kugel and D. I. Khomskii. *Sov. Phys. Usp.*, 25:4, 1982.

[54] T. Hotta. *Rep. Prog. Phys.*, 69:2061–2155, 2006.

[55] T. Hotta and E. Dagotto. *Physica B*, 312:700–702, 2002.

[56] E. O. Wollan and W. C. Koehler. *Phys. Rev.*, 100:545, 1955.

[57] A. J. Millis. *Nature*, 392:147, 1998.

[58] J. van den Brink, G. Khaliullin, and D. Khomskii. *Orbital Effects in manganites*. Kluwer Academic Publishers, Dordrecht, 2004.

[59] J. B. Goodenough. *Magnetism and Chemical Bonds*. Intersciene Publishing, New York, 1963.

[60] S. B. Wilkins et al. *J. Phys. Condens. Matter*, 18:L323, 2006.

[61] C. W. M. Castleton and M. Altarelli. *Phys. Rev. B*, 62:1033, 2000.

[62] Y. Moritomo et al. *Nature*, 380:141, 1996.

[63] C. Frontera, J. L. Garcia-Munoz, A. Llobet, M. Respaud, J. M. Broto, J. S. Lord, and A. Planes. *Phys. Rev. B*, 62:3381 − 3388, 2000.

[64] Y. Tomioka, A. Asamitsu, H. Kuwahara, Y. Moritomo, and Y. Tokura. *Phys. Rev. B*, 53:R1689, 1996.

[65] T. Asaka, S. Yamada, S. Tsutsumi, C. Tsuruta, K. Kimoto, T. Arima, , and Y. Matsui. *Phys. Rev. Lett*, 88:097201, 2002.

[66] Y. Tokura. *Rep. Prog. Phys.*, 69:797851, 2006.

[67] R.B. Laughlin et al. *PNAS*, 97:32, 2000.

[68] A. J. Millis. "theory" opening talk at strongly correlated electron systems conferenc. 2001. (unpublished).

[69] A. Moreo et al. *Phys. Rev. Lett.*, 84:5568, 2000.

[70] Y. Murakami et al. *Nature*, 423:965, 2003.

[71] M. Fath et al. *Science*, 285:1540, 1999.

[72] M. Uehara et al. *Nature*, 399:560, 1999.

[73] A. Moreo et al. *Science*, 283:2034, 1999.

[74] Heffner et al. *Phys. Rev. Lett.*, 85:3285, 2000.

[75] Y. Tokura. *Physics Today*, 56:50, 2003.

[76] M. Blume. *J. Appl. Phys.*, 57:3615, 1985. Also see articles by the same author in 'Proceedings of the New Rings Workshop', Stanford, 1983; and *Resonant Anomalous X-ray Scattering*, edited by G. Materlik, C. J. Sparks and K. Fischer, Elsevier Publishing, North-Holland, 1994.

[77] H. D. Young and R. A. Freedman. *University Physics*. Prentice Hall Publishing, New York, 2000.

[78] W. Friedrich, P. Knipping, and M. von Laue. *Sitzsungsberichte der Bayerischen Akademie der Wissenschaften*, pages 303–322, 1912.

[79] D. Gibbs, D. R. Harshman, E. D. Isaacs, D. B. McWhan, D. Millis, and C. Vettier. *Phys. Rev. Lett.*, 61:1241, 1988.

[80] D. B. McWhan, C. Vettier, E. D. Isaacs, G. E. Ice, D. P. Siddons, J. B. Hastings, C. Peters, and O. Vogt. *Phys. Rev. B*, 42:6007, 1990.

[81] J. J. Sakurai. *Modern Quantum Mechanics*. Addison-Wesley Publishing Company, Reading, Massachusetts, 1994.

[82] Gordon Baym. *Letcures on Quantum Mechanics*. Perseus Books, Cambridge, MA, 1990.

[83] D. Gibbs, M. Blume, D. R. Harshman, and D. B. McWhan. *Rev. Sci. Instrum.*, 60:1655, 1989.

[84] C. W. M. Castleton and M. Altarelli. *Phys. Rev. B*, 62:1033, 2000.

[85] J. C. Dainty. *Laser Speckle and Related Phenomena*. Springer-Verlag, Berlin, 1975.

[86] J. W. Goodman. *Speckle Phenomena in Optics: Theory and Applications*. August, 2005. (unpublished).

[87] Sir Isaac Newton Knt. *Opticks: or, A Treatise of the Reflections, Refractions, Inflections and Colours of Light*. printed for William Innys at the Weft-End of St. Paul's. MDCCXXX, 4th edition, 1675.

[88] K. Exner. *Sitzngsber. Kaiserl. Akad. Wiss.*, 76:522, 1877.

[89] K. Exner. *Wiedemanns. Ann. Phys.*, 9:239, 1880.

[90] M. von Laue. *Sitzungsber. Akad. Wiss.*, 44:1144, 1914.

[91] M. von Laue. *Mitt. Physik. Ges.*, 18:90, 1916.

[92] M. von Laue. *Verhandl. Deutsch. Phys. Ges.*, 18:90, 1916.

[93] W. J. de Haas. *Ann. Phys. IV*, 57:568, 1918.

[94] J. D. Rigden and E. I. Gordon. *Proc. IRE*, 50:2367–2368, 1962.

[95] B. M. Oliver. *Proceedings of the IEEE*, pages 220–221, 1962.

[96] R. F. Jurgens M. A. Slade J. L. Margot, S. J. Peale and I. V. Holin. *Science*, 316:710–714, 2007.

[97] D. Atwood. *Soft X-rays and Extreme Ultraviolet Radiation: Principles and Applications*. Cambridge University Press, 1999.

[98] J. W. Goodman. *Introduction to Fourier Optics*. McGraw-Hill, Boston, MA, 1996.

[99] S. K. Sinha, E. B. Sirota, S. Garoff, and H. B. Stanley. *Phys. Rev. B*, 38:2297–2311, 1988.

[100] J. X. Ma, D. T. Gillaspie, E. W. Plummer, and J. Shen. atomic resolution. *Phys. Rev. Lett.*, 95:237210, 2005.

[101] M. Holt, M. Sutton, P. Zschack, H. Hong, and T.-C. Chiang. *Phys. Rev. Lett.*, 98:065501, 2007.

[102] L. C. Leonard and V. Toal. *Optics and Lasers in Engineering*, 30:433, 1998.

[103] U. Persson. *Optics and Lasers in Engineering*, 17:61, 1992.

[104] M. S. Pierce et al. *Phys. Rev. Lett.*, 94:017202, 2005.

[105] J. P. Gordon, H. J. Zeiger, and C. H. Townes. *Phys. Rev.*, 95:282–284, 1954.

[106] J. P. Gordon, H. J. Zeiger, and C. H. Townes. *Phys. Rev.*, 99:1264 – 1274, 1955.

[107] B. J. Berne and R. Pecora. *Dynamic Light Scattering*. Dover Publications, Inc., Mineola, New York, 2000.

[108] For instance, see: http://elchem.kaist.ac.kr/vt/chem-ed/optics/detector/pmt.htm.

[109] J. W. Boyle and G. Smith. *IEEE Transactions on Electron Devices*, 23:661 – 663, 1976.

[110] P. N. Pusey. *Photon Correlation Spectroscopy and Velocimetry*. Plenum, New York, 1976.

[111] L. Van Hove. *Phys. Rev.*, 95:249, 1954.

[112] W. van Megen, T. C. Mortensen, S. R. Williams, and J. Müller. *Physical Review E*, 58:6073, 1998.

[113] P. Bocchieri and A. Loinger. *Phys. Rev.*, 111:668 – 670, 1958.

[114] P. N. Pusey. *Photon Correlation Spectroscopy and Velocimetry*. Plenum, New York, 1976.

[115] D. Lumma, L. B. Lurio, S. G. J. Mochrie, and M. Sutton. *Rev. Sci. Instrum.*, 71:3274–3289, 2000.

[116] J. D. Jackson. *Classical Electrodynamics*. John Wiley and Sons, Inc., New York, 1999.

[117] K. Chesnel, J. J. Turner, M. Pfeifer, and S. D. Kevan. *Applied Physics A*. (accepted for publication).

[118] M. Hettrick, J. Underwood, P. Batson, and M. Eckart. *App. Opt.*, 27:200, 1988.

[119] K. Rosfjord, Y. Liu, and D. Atwood. *IEEE J. Sel. Top. Quant. Electr.*, 10:1404, 2004.

[120] P. Kirkpatrick and A. V. Baez. *J. Opt. Soc. Amer.*, 38:766, 1948.

[121] P. Kirkpatrick. *Sci. Amer.*, 180:44, 1949.

[122] E. Arenholz and S. O. Prestemon. *Rev. Sci. Instrum.*, 76:083908, 2005.

[123] D. Akahoshi, M. Uchida, Y. Tomioka, T. Arima, Y. Matsui, and Y. Tokura. *Phys. Rev. Lett.*, 90:177203, 2003.

[124] J. J. Turner, M. Upton, J. P. Hill, J. Jordan-Sweet, Y. Tomioka, Y. Tokura, and S. D. Kevan. *Applied Physics Letters*, 2008. (accepted for publication).

[125] K. J. Thomas. (private communication).

[126] S. S. Dhesi et al. *Phys. Rev. Lett.*, 92:56403, 2004.

[127] C. S. Nelson et al. *Phys. Rev. B*, 64:174405.

[128] O. G. Shpyrko et al. *Nature*, 447:68, 2007.

[129] J. J. Turner, J. Thomas, J. P. Hill, M. Pfeifer, K. Chesnel, Y. Tomioka, Y. Tokura, and S. D. Kevan. *New Journal of Physics*, 2008. (accepted for publication).

[130] C. S. Nelson et al. *Phys. Rev. B*, 66:134412, 2002.

[131] K. J. Thomas et al. *Phys. Rev. Lett.*, 92:237204, 2004.

[132] S. Ravy et al. *Phys. Rev. Lett.*, 98:105501, 2007.

[133] D. Reznik et al. *Nature*, 440:1170, 2006.

[134] See: http://icfm.crimea.edu/Prg03.htm.

[135] J. Curialea, R. D. Sanchez, H. E. Troiania, A. G. Leyva, and P. Levy. 254:368, 2007.

[136] Luis E. Hueso *et al.* cond-mat/0511259.

[137] For the latest workshop, see for instance: http://www-als.lbl.gov/coherence2007/index.htm.

[138] See for instance: http://www.bnl.gov/nsls2/.

[139] See for instance: http://www-ssrl.slac.stanford.edu/lcls/.

[140] http://nobelprize.org/nobel_prizes/physics/laureates/1939/lawrence-bio.html.

[141] R. E. Watson and M. L. Perlman. *Science*, 199:1295, 1978.

[142] H. Winick. *Sci. Amer.*, 257:88, 1987.

[143] D. Atwood. (private communication).

[144] J. P. Hill. (private communication).

[145] J. L. Jordan-Sweet. *IBM J. Res. Develop.*, 44:457, 2000.

[146] I. C. Noyan, P.-C. Wang, S. K. Kaldor, J.L. Jordan-Sweet, and E. G. Liniger. *Rev. Sci. Instr.*, 71(5):1991, 2000.

[147] I. C. Noyan, S. K. Kaldor, P.-C. Wang, , and J. Jordan-Sweet. *Rev. Sci. Instr.*, 70(2):1300, 1999.

[148] J. S. Wallace, J.-M. Huh, J. E. Blendell, and C. A. Handwerker. *J. Am. Ceram Soc.*, 85 [6]:1581–84, 2002.